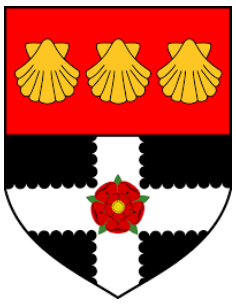

Bio-Mimicry and Self-Organisation of the Belousov Zhabotinsky reaction

A thesis presented for the degree of
Doctor of Philosophy in Cybernetics

Oliver Back

Department of Biomedical Engineering

School of Biological Sciences

University of Reading

February 2023

0.1 Abstract

Introduction: The Belousov Zhabotinsky (BZ) reaction is commonly used as a proxy for biological systems in physical-chemistry experiments. The BZ reaction is well known to be influenced by environmental perturbations, very much like biological systems. The mechanisms of which have been studied to understand how this relates back to biology.

Aim: There is a lack of knowledge regarding the effect external electric fields (EF) and surfactant concentration have on the BZ reaction, and how this relates to biological function in cells. We aim to use the BZ reaction as a model of how biological systems interact with one another, along with the interaction with their environment.

Methods: Ferroin catalysed BZ solutions were prepared and pipetted in droplet form into an oil phase. The droplets were subjected to various external perturbations and recorded using a DSLR camera recording at 60 frames per second. The environmental stimulation involves varied power AC and DC fields, along with a range of concentrations of surfactant dissolved in the oil phase.

Results: Firstly, the discovery of BZ droplet electrotaxis was reported and quantified, where the static EF was found to create an inhomogeneous distribution of ions within the droplet, which leads to a bias in the formation of leading centres (LC) across the droplet. The phenomena was then deployed as a form of push-pull mechanism on oscillating BZ droplets to cause their division. Finally, continuing from the division experiments, we study the synchronisation between the periodicity in a pair of droplets. We found that the oscillating droplets had an influence on one another, and would synchronise their beating behaviour according to one another.

Conclusion: We have found that the ferroin-catalysed BZ droplets can be used to simulate biological redox signalling, and as a proxy for understanding processes from environmental signal detection to cell division, where our experiments have shown that an external EF can induce the electrostatic behaviour, and contribute to the droplet division event.

0.2 Declaration

I confirm that this is my own work and that the use of all material from other sources has been properly and fully acknowledged.

Oliver Back

0.3 Acknowledgements

I would like to give a big thank you to the following people, without them the following thesis would not have been possible.

I would like to start by thanking my **family** and **friends**, for the love and support that has driven and motivated me to complete this project. I would like to especially thank my mum and stepdad, along with my mother and father-in-law, for their kindness and understanding throughout this journey.

I would especially like to thank my wonderful wife, **Amelia Back**, for the love and support they gave me, they truly motivated me to keep grinding out my thesis.

I am grateful to **Dr Alaa Al-Dibouni**, and **Simeon Adejumo** for their support and encouragement throughout the course of my PhD, I would not have been able to complete this journey without them.

I am thankful for the supervision I have received from **Dr Yoshikatsu Hayashi**, **Dr Zouwei Wang**, and **Dr Nandini Vasudevan** over the past 4 years.

The friends I have made at the gym deserve particular thanks, for the encouragement to push myself harder and further has led to discipline that I have been able to apply to all areas of my life, especially with the work for my PhD.

A special thank you to **Professor Simon Sherratt** for their continual pastoral support throughout my journey through my undergraduate degree and also graduate school, and for helping me not only grow as a researcher, but as a person, I would not be who I am today without them.

I would like to especially thank **Calvin Smith** for his generosity in support and kindness, especially throughout COVID.

0.4 Scientific Meetings and Publications

Some of the results presented in this thesis have been presented at scientific meetings and published in scientific journals.

Peer-reviewed Publications

Some of the results in this thesis have been published in peer-reviewed publications

- **Scientific Reports, accepted:** Back, O., Asally, M., Wang, Z. et al. Electrotaxis behavior of droplets composed of aqueous Belousov-Zhabotinsky solutions suspended in oil phase. Sci Rep 13, 1340 (2023). https://doi.org/10.1038/s41598-023-27639-8

Presentations and Scientific Meetings

- **Oliver Back** (2019) Investigating the non-linear dynamics of the BZ reaction in an electric field. Poster presentation at the School of Biological Sciences Symposium, University of Reading. United Kingdom.
- **Oliver Back** (2020) Electrotaxis Effect On Droplet Motility. Oral presentation at the School of Biological Sciences Symposium, University of Reading, United Kingdom.
- **Oliver Back** (2021) BZ reaction as a model of biological redox signalling, Oral presentation at the School of Biological Sciences Symposium, University of Reading, United Kingdom.

Along with these presentations, many of the results presented in this thesis were demonstrated and presented in a series of outreach lectures to undergraduate and A-level students throughout the course of the PhD journey.

Contents

List of Figures

List of Tables

Chapter 1

Introduction

1.1 Bio-mimicry

Bio-mimicry, also referred to as biomimetics, and self-organization are important areas of focus for many research communities as they have led to the advancement of materials engineering, development of complex systems, better design of robotics and their control systems, and a better understanding of biological processes [1, 2]. Bio-mimicry can be defined as the imitation of natural biological processes and designs, in engineering and invention [3, 4]. Bio is taken from biology and refers to a living organism, and mimicry means to imitate. Put simply, bio-mimicry is borrowing factors from evolution to expedite the design process, due to the wealth of knowledge that can be attained from studying biological systems after having undergone the process of evolution over millions of years to perfect their design [5]. As a source of inspiration, bio-mimicry offers millions of years of evolution can that provide performance and efficiency benefits to the engineering design process. An example of this is the comparison of the fabricated needle tip to a bee's stinger. The degree of detail in a bee's stinger is imperceptible to the naked eye and requires a great degree of magnification for the detail to be apparent. The perfection of the design in the bee stinger has led to many studies into the best removal strategies to avoid human harm, whether it be immediately, or performed surgically. Particularly in cases where the sting occurs in sensitive anatomy, great care is paid to avoid any retention of the stinger inside the patient [6, 7, 8]. This comparison highlights the importance of bio-mimicry in a research context, as not only can the studies of biological systems help to develop new technologies directly modelled after biology, but the

fabrication process as well can be a source of new knowledge. Bio-integrated processes are often chosen as they allow components to have innate biocompatibility, or include the desired features and biological ingredients.

The aim to draw inspiration from nature has led to developments in drug delivery systems (DDS) which use bio-mimicry to develop safer and non-invasive DDS technologies. A DDS can be developed to formulate or deliver an active pharmaceutical ingredient to a patient. Traditionally, a transdermal introduction of the drug is the best non-invasive method for drug delivery (DD). The current challenge for non-invasive DD is the specific targeting of the delivery of the active compound. Invasive techniques are able to directly target specific tissues but can come with tremendous drawbacks. Non-invasive DD is preferable because there is no recovery time or discomfort for the patient. The issues presented with the non-invasive DDS' involve lower efficiency in the absorption of the active compound by the desired tissue due to a lack of specificity in targeting and also with decreased efficiency in the administration of the drug [9, 10]. DD is one aspect of pharmacology that benefits from bio-mimicry. The weak interactions that occur between receptors and ligands have been ignored in the drug-discovery process and could harness powerful uses in a patient's medical care. Using bio-mimicry as an inspiration to search for natural products and metabolites with drug-like features has proven to be a promising avenue for drug research to take. On such study was able to find a metabolite that mimics drug effects potently in vitro and in vivo [11]. Another challenge in drug development that bio-mimicry can help to overcome is peptide assembly. Traditionally, it can be very difficult and expensive to synthesize long chains of proteins, whereas short chains of peptides can be conveniently synthesised at low cost on large scale. Research is being carried out on the use of smaller chain peptides that can self-assemble within a patient at physiological pH and temperature, to then act on protein receptors in the same manner that a traditionally developed drug would. This is carried out by approaching the development of peptides with positive and negative charges to promote the co-assembly process via electrostatic interactions between the peptides [12].

Pharmacology isn't the only chemistry-related field of research that utilises bio-mimicry in its design. Chemical engineering also looks to biology to discover how nature can guide

the engineering process in developing new methods and materials. Nature-inspired chemical engineering (NICE) is a process where materials and processes are redesigned to supersede conventional technology, with an approach to creating a sustainable and better solution to classical engineering problems. The advantage NICE has to nature-integrated, or nature-imitating design, is the focus on mechanistic features of the natural systems, rather than superficially generating a resemblance to the natural counterpart. NICE also does not incorporate any natural, or living systems, as to not merely copy nature out of context. The NICE approach to bio-mimicry has led to the development of bio-inspired materials, mimic bone growth, to create a bone replacement technology. The new method develops the nano-material in a system using bioactive glass nanoparticles, in a multilayered coating, inspired by marine mussel nacre [13].

One of the most famous examples of bio-mimicry comes from Leonardo da Vinci, who was famous for the blend of art and mathematics in his work. He famously attempted to create a flying machine, using nature's rules as a preset for his design [14]. There have been more studies where the biologically designed wing has been the focus of invention. For example, in a recent study, Win *et al.* designed a wing based on the biological design of maple leaves, functioning by switching from diving and auto-rotating, and is capable of flying to its destination [15]. In a similar study, a microrobot equipped with biologically inspired wings was found to be capable of both swimming actions, and at transitioning from water to air. The insect-scale robot weighs only 175 milligrams and has strategies to efficiently locomote in both fluids, and fluid-air transitions. The main challenge to overcome in the air-liquid transition is the interfacial tension at the interface between the water and air. This was overcome by employing electrolytic plates which produce oxyhydrogen from the surrounding water at the interface, which provides enough buoyant force to help the microrobot to 'escape' [16].

The ability of any biological system to detect environmental stimulus is paramount for survival. The evolution of such systems forms a so-called biological arms race, where predator and prey both adapt to survive [17]. One of the best examples of This type of evolution is the development of the eye, where the common precursor, the proto-eye evolved in parallel across many species as a great example of convergent evolution to produce photoreceptors

that we identify today as biological vision [18, 19]. Moving away from the eye, and onto the ear, echolocation in bats has been found to drive the predator-prey model pushing evolution to advance in both animals. Echolocation evolved in bats as a method of hunting for prey at night, where the auditory sensory system is active, rather than using vision to determine the presence of prey. To do this, the bat ear has evolved in such a manner that they are capable of detecting high-frequency signals which they emit as part of the echolocation. Bat predation drove the evolution of certain insects for bat-detecting ears, as well as non-auditory means to detect such frequencies being emitted by bats whilst hunting. The high-frequency sensitive ears introduced bat-avoidance behaviours into the insects, allowing them a better chance to survive whilst out at night, meaning the genes for the bat-hearing can be passed down to next of kin [20, 21, 22]. The evolution of hearing within prey has brought up an interesting unanswered question when it comes to the silent flight of birds. Has quiet flight originated as a response to self- masking, or as an increase in stealth? Self-masking would decrease the noise generated by the bird itself and allow it to hear prey more easily, whilst quiet flight would also inhibit the prey's ability to detect the bird in the first instance[23].

Biological systems develop the ability to sense the environment and stimulus to avoid danger and to locate sources of nutrients. Another example of this is bacterial chemotaxis, where chemical gradients are sensed via tumbling motion, which will be acted on to determine the swimming direction to locate nutrient sources [24]. The role of chemotaxis has largely been assumed to be purely used for foraging for resources. Still, doubt was cast on this assumption when it was learned that less nutritious sources of resources often present as very strong drivers for chemotaxis [25]. A possible explanation for this is that these less nutritious sources once were a greater source of nutrients for the bacteria, but as the organisms evolve over time, the nutrient needs change [26]. Then when a new source takes over as the best food source, the chemotactic response remains the same for the older source, which could explain why such a great chemotaxis response is granted from a poor nutrient source. Other research presents a possible explanation for the taxis behaviour in sub-optimal conditions, where chemotaxis is used for a 2-way chemical signalling [27].

The coevolution between predator and prey is often seen as analogous with an arms race,

where an advancement, or evolution on one side, is met with a response from the other, hopefully with the aim of evading the previous advance [28]. The predator-prey arms race as a model has limitations, however, as described by Ambrams [29] in their work. Prey will increase investment in predator avoidance in response to a predator increasing investment into prey detection and capture. Where the model of the arms race does break down, is that predators have no response to the prey increasing investment in predator avoidance. Instead, it is proposed that stability between predator and prey interactions comes where coevolution has a bi-directional axis in prey vulnerability [30]. Some supporting evidence for this plays out where abiotic disturbances impact the population ratios of predators and prey in fish species. It was discovered that physical changes to the environment allowed the prey fish to flourish, due to the decreased numbers of the predators, which allowed for population regrowth in the prey, before they would have died out, as a result of too many predators [31]. If the 'arms race' theory was valid, no environmental conditions would need to be considered in the predator-prey model. This is where the 'arms race' analogy breaks down, however, the biological significance does not, as in either circumstance environmental detection is still paramount to survival.

The information processing capabilities of the brain have long been studied to garner more information regarding its ability to adapt to new information, along with novel stimuli. This led to new techniques in the laboratory being developed to ensure the culturing of neural cells would remain healthy and stable over long-term studies [32]. Demarse *et al.* were able to use this technique to culture dissociated cortical neurons on a multiple electrode array (MEA) with the aim of producing an animat. The research carried out was motivated by the hope of gaining the ability to read signals in the newly forming neural network. The MEA was also capable of providing electrical impulses akin to those found in the brain via ordinary brain function. The cultured cortical neurons were taken from day 18 embryonic rats and allowed to develop and grow on the MEA for one month. The MEA was capable of detecting signals as small as +/- 600mV within a timeframe of 400μs. A clustering algorithm was incorporated into the digital control, which could recognise pattern formation in neuronal firing. After 8 minutes of detection, the number of patterns seems to stabilise at approximately 27 patterns. At this point, a feedback system was incorporated into the animat testing procedure and was

allowed to run for a further 40 minutes. At this point, a total of 51 patterns were detected. Interestingly, the researchers found that routines would form where sequences of patterns would present as the animat interacted with its virtual environment. Further studies have shown the direction animat research is going to take, where the biological processing unit is being thought of as a replacement for traditional silicon processors due to the intrinsic fault tolerance built into a self-repairing biological system [33].

Recent advances have shown that interest in bio-mimicry is even present in industries like construction. Bio-mimicry can offer greater sustainability and lower energy cost to current construction techniques, while also offering unity between built environments, people, and the environment. Using biomaterials with better mechanical properties is the main focus for such research currently, as the durability of current biomaterials is not up to the standard that construction companies would require. On top of this, the materials cannot be readily mass-produced which adds another barrier to entry [34, 35, 36]. With bio-mimicry taking traction in research and development of the built environment, more case studies will come up which can be analysed and improved in the long run. A major weakness in current studies is the lack of buildings currently using principles from bio-mimicry to improve design and sustainability [37].

The use of bio-mimicry, and using nature as a template for new design has taken hold in a lot of industries and research and will continue to grow in knowledge as more applications are discovered and created. To recap, the main advantages of bio-mimicry involve efficiency in design, sustainable design technologies, and environmentally friendly manufacturing. The benefits of using bio-mimicry in engineering and manufacturing processes involve the reliance on millions of years of evolutionary design to perfect the design process, along with using bio-materials which are more eco-friendly, more sustainable, and better suited to biomedical applications.

1.2 Self-organization

Self-organization can be defined as the production of spontaneous order forming from interactions in a disordered system [38, 39, 40]. Together, bio-mimicry and self-organization make up a powerful tool for researching the advancement in non-linear physics, biology and the advancements of robotics control systems. Self-organisation is linked with bio-mimicry, where many self-assembly mechanisms are biologically inspired, and many biological systems show self-organisation. Systems with transient function have developed from self-regulated structural control, where fibres and gels will self-assemble into desired structures. Self-organisation has similarities with emergence, where the sum of the parts is greater than the individual on their own. That being said, it refers to a structure forming, that the constituent parts do not possess singularly. For self-organisation to manifest, according to Bonabeau, some basic principles are required to be met [41]. These principles are: Strong dynamic non-linearity, generally through positive and negative feedback loops; A balance of exploitations and exploration; Components must have many interactions; and the availability of energy, the free energy must be maintained to overcome entropy. Self-organisation can occur in many types of systems, from physical to chemical, biological or robotic. The phenomenon is present in crystallisation, chemical oscillation, swarming behaviour, and convection flows. The spontaneous order that forms can provide order is a disordered system or aid in homeostasis in another. The first in-depth study of self-organisation was research into the laser. The term stands for light amplification by stimulated emission of radiation and incorporates a set of mirrors which bounce the light beams back and forth, and only allow very specific light wavelengths to leave the device in a steady beam of photons [42].

Multifunctional nanoparticles have been recently used to address challenges with distributing nanomedicine in patients [43]. Bio-mimicry has inspired many types of drug delivery systems (DDS), where self-organisation plays a tremendous role in its application. Engineering nanoparticles (NP) to mimic the cellular microenvironment to be used as a system to deliver nanomedicine non-invasively to specific regions within the body is now a large focus within medicine. The current challenge to this axis of research is incorporating the use of nanoparticles in a non-toxic capacity [9]. Other works have found that the use of NPs can increase

circulatory time for a DDS, and reduce off-target drug transmission. NP can entrap therapeutic molecules, especially ones with poor solubility, and can carry the medicine more closely to the desired target location within the body[44]. Many organic-based NPs use weakly binding noncovalent interactions to self-assemble, which means that they are prone to external stimuli. This is advantageous in DDS applications of nanotechnology, as the self-assembled nanostructures can be guided to locations within the body where targeted drug treatment is required, and where the drug can be delivered effectively. This is especially applicable when the drug has poor solubility in a pharmacological environment, or if it has poor selectivity between different types of tissue [45]. Self-assembly of peptides opened the door to a new class of DDS using a new class of materials. The peptide self-assembly process allows for drug delivery to be tuned across length scales and has increased the DDS capacity for transporting a wider range of small-molecule drugs to targeted biological sites. Hydrophobic inclusion within peptide nanofibres has increased the drug incorporation weight by 6.8% in drugs with poor solubility. The peptide self-assembly process has superior biocompatibility compared to the traditional NP approach, along with high efficiency in drug loading, and a better-sustained drug release behaviour [46]. It was discovered, that a complex system resulting from the combination of passive and active particles leads to the activity-driven organization [47, 48]. The minority present active particles produce hydrodynamic flow in surrounding space, which interact with other active particles along with passive particles, leading to pattern formation acting as a so-called 'force field', which leads to the particles' self-organization. In other work, self-organization has been studied within bacterial colonies, where quorum sensing is invoked as a method of regulating motilities in run-and-tumble bacteria [49]. Dinelli *et al.* were able to observe the emergence of travelling waves forming from non-reciprocal interactions.

Self-organisation is important in the field of robotics too. Swarm robotics is a branch of control systems where many individual 'agents' have a specific role to complete a task, and do so by communicating with others in their network. Swarm robotics lends itself heavily to self-organisation because of the distribution of control and processing that the individual robot gets [50, 51]. Experimentation has been conducted on the self-organisation aggregation in swarm robotics, where some agents are considered to be uninformed, with others being informed. The aim of this research is to illustrate how a swarm of autonomous robots can

self-organise and aggregate a desired site chosen by a human controller. Introducing informed robots can help to improve the efficiency of the aggregation, and with the navigation of the environment. The informed robots will act as a method of communication for the humans, which correspond to the informed robots, which then interact with the uninformed robots as a method of communication [52]. Self-organising swarm robots have been used to battle the devastating destruction of wildfires. Wildfires have become more frequent and severe worldwide, so a team produces a swarm intelligence robotic drone system to combat wildfires. The drones take advantage of the distributed computing resources made applicable with the swarm intelligence design in the fire alert system. The drones are capable of monitoring a wider range of areas compared to the traditional approach using a series of trucks patrolling known risk areas. The future work involved in this field includes extending drone range and improving battery life [53]. A mathematical model of swarming robots that synchronise their internal states has been developed and named the 'swamalator' This simulated robotic control system was then developed for the Robot Operating System 2 (ROS 2). The robots are capable of synchronisation and swarming due to the internal phase and location data shared with the connected network of robots. The sync behaviour observed in the robots is remarkably similar to the syn found in fireflies, where each insect behaves as an agent within a multi-agent system, updating, and synchronising with the neighbouring agents via the light pulses emitted [54, 55]. Ecologists have discovered self-organisation across the food system. The self-organisation that occurs spans between the food chain, communities, and geographical regions [56]. The feedback systems observed in the ecological self-organisation relate to the theories presented in Gaia theory where it is proposed that every living organism interacts with its surroundings and other organisms in a synergistic self-regulating system that perpetuates the conditions for life on earth [57, 58].

The study of self-organization within schools of fish has led to the development of models for fish growth [59, 60]. Demonstrating how research in self-organization can be applied to bettering the understanding in greater research areas. Distributed, self-organised decision-making is a phenomenon found in schools of fish. This collective emergence of behaviour that arises from larger groups interacting is referred to as swarm intelligence, where the so-called 'pool of competence' statistically allows for greater numbers of motivated and intelligent indi-

viduals to increase the collective cognition of the group[61]. Self-organisation is commonplace to be found in social systems, so much so that it is presumed to be very 'cheap' from a behaviour optimisation standpoint when considering evolution [62]. It seems so intrinsic and obvious as to *why* fish school, in fact, most studies focus on the mechanisms at play that allows the fish to work together to produce emergent properties. One study found that over 25% of elfish will school throughout their lives, with more than 50% schooling as juveniles. A common 'tactic' found within schooling fish is the repulsion ability. This strategy involves creating an open space around the source, such as a predator, which repels the external source [63]. The pattern formation of schooling fish has been studied on a mechanistic front, as the same collective patterns produce the same behaviour under different conditions [64]. Physiological alterations have been shown to affect the way collective behaviours manifest within zebrafish. Little is known about the role that genes play in the regulation of social behaviour, however, when genes linked with human psychiatric disorders were introduced to zebrafish using CRISPR-Cas, observations were made regarding changes in schooling behaviour. Behaviours differed to the wild-type fish, where the changes to the individual interactions lead to scattering, uncoordinated, and huddled behaviour. The huddled behaviour occurs when the fish form dense and disordered groups. The genetically altered fish exhibited a weaker distance-dependant attraction and instability in group dynamics [65].

Flocks of birds typically fly in a formation known as an echelon which is a form of self-organisation that governs the collective emergence of intelligent behaviour governing their actions. The use of the echelon formation allows for long-distance flights to be carried out with under predation have been studied for their abilities to organize into a defensive arrangement to increase the odds of survival [66, 67, 68]. Variability in the behaviour of the birds will correspond with variance in the global pattern formation in the flock of birds. Increased speed can produce a more oblong shape in a flock of starlings, for example, where the increase in speed will correspond with an increase in volume, and a decrease in density, in their flock. Experiments on computer simulations of flocks of birds have found variability in the flock shape which depends on local differences in behaviour, showing that there is a degree of free agency from bird to bird, within the flock. It was also found that there is no current relationship known between group size, and flock density [69]. The pattern formation within

flocks of birds is not the only example of self-organisation in birds. The emergence of pattern formation in cellular self-organisation was found to be produced by stochastic fluctuations in developing tissues in feathered birds and penguins. live imaging and ex vivo perturbations were used to find that cell anisotropy (a property in which a cell's growth rates are not equal in all directions) optimised the motility for sharp and precise formed arrangements in the cell growth. This leads to a collective property in which the cells undergo pattern formation through self-organisation to optimise the fitness function of the organism for evolutionary purposes. It is posited that this arises from a mechanism that optimises the collective cellular properties developing pattern formation across many forming cells [70].

It is apparent that self-organisation is prominent in many different fields of research. The study of pattern formation in systems outside of thermodynamic equilibrium is crucial to understanding the self-regulation and pattern formation that govern many systems in physics, biology, and chemistry. Many of the thermodynamics principles that govern self-organisation are described in Herman Haken's theory, Synergetics [71, 72]. The interdisciplinary theory outlines how microscopic interactions within the system lead to macroscopic order. The systems lie outside of thermodynamic equilibrium and act to reduce entropy. This means that a self-organising system is converting enthalpy into the opposition of entropy. Self-organisation has been found to occur naturally in many fields of research, including both animate, and inanimate studies [73, 74, 75]. This has led to an increased awareness of self-organisation due to its application in creating systems that are more adaptive and robust, with the ability to reconfigure themselves, they are an important field of study for many reasons. Researchers are particularly interested in self-organisation because of the dynamic ability that a system can have when it is able to self-assemble and adapt to different environments, along with the importance that self-organisation plays in crystal growth and developing intelligent robotic systems.

1.3 Taxis effects

Taxis behaviour is the movement of an organism in response to a stimulus such as light, chemical reaction, or the presence of food, for example. The motion is found to align the mo-

tion and orientation of the agent towards, or against (negative-taxis) the source of stimulus. Taxis is distinguished from kinesis in that directional changes are common in taxis effects, whereas they are not in kinesis. Taxis is also differentiated from tropism, as tropism is simply the turning response of a biological system towards a stimulus, with no movement [76]. The phenomena can be described as positive or negative depending on whether the movement is towards, or against the stimulus. Which is an important distinguishing factor in how the taxis phenomena presents in biology. Taxis can be the essence of nutrition-seeking behaviour [77], or for predator avoidance behaviour [78]. Many types of taxis phenomena occur in nature and physical systems with a variety of different presentations and classifications. **Galvanotaxis**, or **Electrotaxis** refers to motion induced as a response to electric field presence. **Chemotaxis** refers to the detection of a chemical, or chemical gradient, and the motion that is observed as a result of its detection. Bacillus subtillis is a type of bacteria and has been observed to undergo the taxis phenomena when exposed to a pH gradient, known as **pH taxis** [79]. It was discovered that four critical amino acids are utilised in the detection process, which involves a type of receptor called a chimeric receptor. This discovery is being utilised in a new technology for pH detection. Other types of taxis include: **Aerotaxis**, stimulation by oxygen; **Anemotaxis**, stimulation by wind; **Barotaxis**, stimulation by pressure; **Durotaxis**, stimulation by stiffness; **Gravitaxis**, stimulation by gravity, which is also known as **Geotaxis**; **Hydrotaxis**, stimulation by moisture; **Magnetotaxis**, stimulation by a magnetic field; **Phototaxis**, stimulation by a light source; **Rheotaxis**, stimulation by fluid flow; **Thermotaxis**, stimulation from changes in temperature; and **Thigmotaxis**, stimulation from physical contact.

Kilnotaxis refers to organisms that have specific receptors to detect changes in the environment but do not have a specific organ paired with this receptor. The taxis motion occurs after a series of measurements are made, where the receptors are repositioned in the environment, and a comparison is made between the different states. This is then used in a decision process to determine the direction in which the organism should travel in. After making a decision about the direction that the gradient of stimulus occurs in, the organism will travel purely in a direct route. Tropotaxis is displayed by certain organisms which do have the pairing between the receptor, and a specific organ, unlike in the kilnotaxis presentation. This means that the organism can continue to detect stimulus and gradients in the stimulus whilst moving, leading

to directional changes much more frequently than in the previous example. Mnemotaxis is referred to the action of the use of memory to determine the organism's path. This is present in ants, where the path from a food course, for example, back to their home, is not marked by any taxis phenomena, but rather by the memory of the initial route taken [80, 81].

A simple model of taxis behaviour can be related to the writings of Valentino Braitenberg, in their book *Vehicles: Experiments in Synthetic Psychology* [82]. Valentino proposed the basic model of the Braitenberg vehicle. A simplistic vehicle with 2 sensory units, and 2 motor units. The sensory units detect environmental changes, and the motor units are responsible for driving the vehicle. If the right motor has a larger signal than the left motor, the vehicle will steer to the left, if both units receive the same magnitude of the signal, the vehicle will continue in true course. The sensory units can be connected to the motor actuators in an ipsilateral, or contralateral configuration, and be either excitatory or inhibitory. In this regard, ipsilateral connectivity refers to when the sensory unit and actuation unit are on the same side of the vehicle, and contralateral aligning refers to the opposing wiring. Excitatory connectivity refers to when the sensory units detect a stimulus and will respond by increasing the speed at the motor unit, inhibitory will slow down the unit. There are 4 possible wirings for this type of vehicle.

Figure 1.1 details a schematic representation of the four different types of Braitenberg architecture. The behavioural characteristics observed in the architectures have been named fear, aggression, liking, and love. The first pair shows the excitatory configuration, where the detection of external stimuli results in an increase in motion in the actuation unit. The left-hand vehicle is wired in the ipsilateral configuration, which will result in stimuli-avoidance behaviour. This is the exact mechanism of negative-taxis phenomena in biology and physical sciences. The right-hand vehicle depicts the contralateral configuration, which shows the positive taxis or sensory-seeking behaviour [83]. The second pair of vehicles display the inhibitory configurations of the Braitenberg vehicles. The left-hand vehicle shows the ipsilateral wiring, where the sensory information fed into the right-side sensory unit, is wired into the right-side actuation unit. This results in the sensory-seeking behaviour associated with the contralateral wiring in the excitatory model. There are some differences in reality, however, which are introduced when simulations or practical applications in hardware are developed

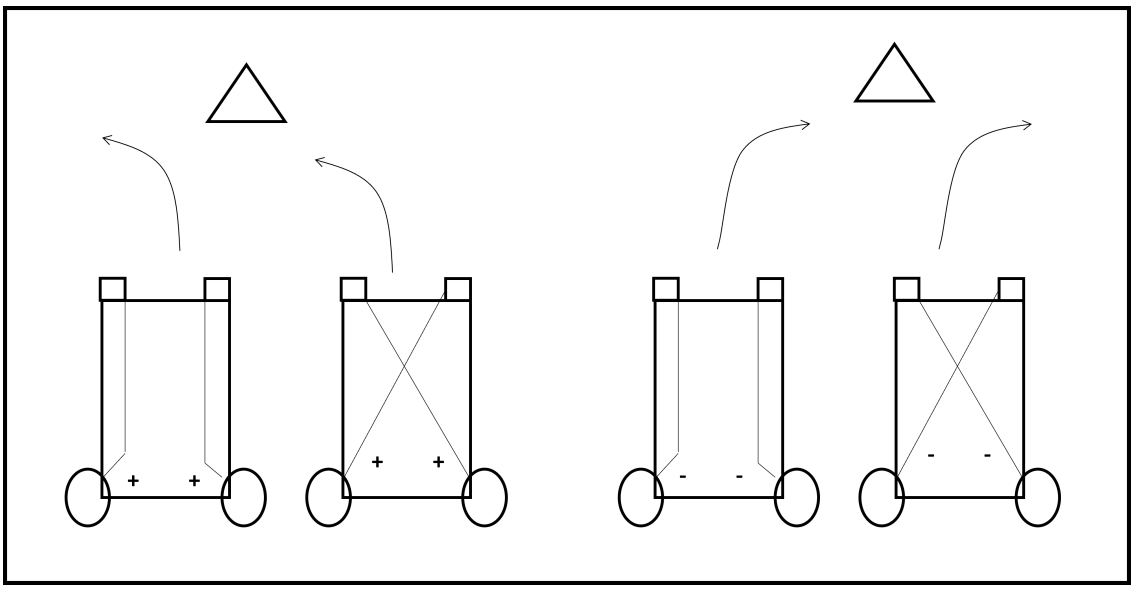

Figure 1.1: Schematic diagram of the 4 arrangements of the Braitenberg architecture. Displaying the excitatory, and inhibitory arrangements of the ipsilateral and contralateral architectures. In this diagram the triangle represents a source of environmental stimuli, the boxes at the front of the vehicle represent the sensory unit, and the circles are the back represent motor actuation units.

for these models. But there is still great overlap in the basic premise behind the behavioural traits garnered from these wirings. Lastly, the rightmost vehicle shows the contralateral wiring with the inhibitory construction. This causes the negative taxis response we have previously seen in the ipsilateral wiring in the excitatory pair. A key distinction between the excitatory and inhibitory schema is that the speed will accelerate in the excitatory configuration, as the vehicle approaches the source of stimuli, whereas the speed will decrease in the inhibitory arrangement. This will lead to the contralateral excitatory vehicle accelerating towards and overshooting the stimuli, whilst the ipsilateral inhibitory vehicle will come to a rest as it approaches the source. Alternative vehicles have been proposed with a multitude of sensory units on each vehicle. This can produce many types of dynamic complex behaviours as small shifts in the positioning between the sensors will feed different input signals to the actuators and deliver wildly different behaviours. Some interpretations will employ multiple sets of sensory units with different sensitivities to stimuli and have different wiring schemas to the neighbouring sensors. Some sensory units will be inhibitory, some excitatory, some ipsilateral, and some contralateral. This will lead to complex and possibly intelligent behaviour, similar to that which we observe in 'simplistic' organisms like bacteria. The interesting dynamics of the behaviour observed in the sensory-seeking and sensory-avoidance vehicles have been remarked

as appearing complex or even intelligent. This relates very strongly to the taxis response to stimuli found in biological systems being a driving force for adaptation, evolution, and survival.

Braitenberg vehicles have been studied further due to the simplistic nature of their adaptation to environments, along with adaptability at being implemented within new models. Improvements on the Braitenberg architecture has allowed for better speed control of the robots, along with smoother transitioning when detecting stimuli [84]. other studies have implemented Braitenberg architecture onto wheeled mobile robots to compare the trajectory mapping with similar hardware controlled by PID controllers. The simple design of the Braitenberg was used to illustrate the complex behaviour that can emerge from such a system where the potential to improve algorithms for auto-following robotics. The potential that the Braitenberg architecture brings, that the PID-controlled robots do not, is the autonomy and complex behavioural patterns that can emerge [85]. Other work inspired by the Braitenberg vehicle architecture includes the development of a memristive neuromorphic circuit vehicle. This vehicle was developed using this circuitry as opposed to the traditional Von Neumann architectures, to develop smart robots that are capable of achieving autonomy in their environment, making them better adapted to changing circumstances than traditional robotics. The team were able to reduce the latency in the microcontroller unit in response to the input signals, which could allow for a more responsive vehicle in unknown conditions [86, 87].

As taxis is an innate behavioural response of an organism or a particle. Taxis research is fundamental to understanding the laws of nature and biology, including the origin of life. Nutrient seeking is such a priority in all living systems that it is one of the best-adapted systems in all organisms. So much so, that the taxis behaviour in bacteria is so well optimised it takes very little energy for the bacterium to realign towards a food source in response to its detection [88]. Considerable focus has been spent researching the application of taxis phenomena in physical systems. Water in oil systems are often the focus due to its relation to the biological cell in a modelling capacity. Phototaxis was exhibited by a controllable self-propelled water droplet. Continuous wave (CW) laser irradiation was utilised as the laser power was able to generate a local temperature gradient which drove the motion of the water droplet [89]. In a related study, Iron nanoparticles were dispersed in the water droplet which absorbed the light

rays from the laser and produced a photocatalytic Fenton reaction. This caused an uneven ion concentration within the droplet. The gradient of ions caused changes to the interfacial tension, which induced Marangoni flow. As the flow state is in either phase, a passive friction force occurs, resulting in a momentum transfer, and therefore the translational motion of the liquid robot [90].

Taxis phenomena play a role in biological development, where mechanisms for detecting nutrient gradients are favourably chosen through selective breeding to enhance the survivability of a species [91, 92]. Bacteria have 3 modes of action for movement patterns: Swimming or gliding; run and tumbling; and twitching. Where the mechanism for movement is a propeller-like action of the flagellar motor at the base of the cell [93]. The motion observed in the tumbling phase is random and uncoordinated, and it is believed to be due to the bacteria searching for a more nutrient-rich environment [94, 95]. When bacteria are exposed to a nutrient gradient in their environment, the motion switches from the random motion observed in the tumbling behaviour to the controlled directional motion observed in the swimming [96]. This is an example of chemotaxis within bacterial communities, however, bacteria are known to exhibit many types of taxis behaviour. Phototaxis behaviour is observed in some bacteria, however, the mechanism for detecting light stimulus is very different in nature to that for the chemotaxis effects. As the bacteria are so small, the light detection is incapable of locating a source of light, instead, the intensity is measured, and movements are made to detect an increase in such intensity. Then the cell will make movements to navigate towards the light source through a series of such measurements [97, 98].

More recently, taxis phenomena in bacteria have been studied for designing biologically inspired algorithms [99]. The deployment of bio-mimicry involving the study of taxis phenomena can have advantageous outcomes in the development of new technologies. One such example utilising such technology is the development of an artificial nose [100]. The key advantage of the artificial nose, over a generic particle detection device, is the degree of selectivity and high sensitivity that it can have. Mimicking the sense of smell has great potential to improve the detection of volatile organic compounds, for a variety of different applications. One such application is the utilisation of an artificial dog nose as a method for detecting trace vapours

in a commercial setting. This technology has applications in medicine as well as security and law enforcement [101]. The artificial dog nose uses a sniffing technique, which agitates the airflow, and allows for a much greater efficiency in aerodynamic sampling than in conventional tests. This was made capable due to the 3D-printed dog nose. Flow pattern analysis created a visualisation of the airflow around the artificial nose, to confirm that it produces the same environmental action as found in real dog sniffing.

1.4 Physical Chemical Mechanisms

Physical chemistry is important because it is one of the most fundamental sciences which explains how nature works. Understanding the phenomena in this field can have applications in other areas of science. The applications usually involve understanding the mechanisms behind new phenomena, or understanding how systems will react and interact with one another. Research into the mechanisms behind physical-chemical phenomena has extended to the theoretical level, where modelling and analysis methods have been devised to validate experimental findings and to help explain phenomena. Knowledge created around these phenomena has led to insights into further discoveries that have produced new technologies, along with opening the door to wider fields of research. Understanding these mechanisms will also allow for proxies or models to be developed, which can lead to further discoveries along with greater experimental and theoretical validation.

The emergence of hydrogels became an intense subject of study for many different research groups upon their first instance in literature. A hydrogel is a cross-linked polymer, that cannot dissolve in water, along with being hydrophilic. Hydrogels fall into 2 categories: Chemical hydrogels; and physical hydrogels. Chemical hydrogels are connected via covalent bonds, whereas physical hydrogels have non-covalent bonds. Due to the covalent bonds in the chemical hydrogels, the gels are very strong, and irreversible, but unfortunately are unfavourable for medical applications, because the covalent bonds result in harmful properties to biological organisms. Physical hydrogels have very high biocompatibility due to the lack of toxicity and ease of reversibility. To reverse the crosslinks, external stimuli like temperature, or

a pH change can be applied. Depending on the preparation, hydrogels can be considered to be natural or synthetic. The properties of the hydrogel can change depending on the preparation and whether the hydrogel is physical or chemical.
The applications of hydrogels are a growing field of research. These can include: Drug delivery systems; Regenerative medicine; Soft robotics; Biomimetic engineering; and Bioanalytical chemistry. The term transformer gels is used to describe gels that are capable of swelling and deswelling as a response to external stimuli, and capable of performing a task. These gels can be sensitive to the stimulus on their own, or a gradient, and exhibit tactic behaviours such as: Chemotactic response; Photosensitivity; Electrical or Magneto sensitivity; and Thermosensitivity. These external conditions can be manipulated to use the hydrogel for performing specific tasks as previously mentioned [102].

Hydrogels can also be sensitive the perturbations from within. These types of hydrogels are commonly known as self-oscillating gels. The self-oscillating gels are often used to model biological motility, where the gel can undergo swimming actions similar to the biological organisms, driven by the internal reaction [103]. Mechatronic engineers using hydrogels with internal reaction-diffusion systems have produced mechanical work harnessed to drive pumps, simply through the incorporation of a self-oscillating BZ hydrogel. The researchers argue that the redox reaction powering the hydrogel to act as a pump for oil flow can be adapted and refined to act as an artificial heart for soft machines [104].

Many physical chemistry mechanisms are the subject of study, both in the wet lab and in the computer lab. Mathematical modelling has become a very powerful tool for testing experimental data, validating results, and running sensitivity testing which can increase efficiency in lab work. The mathematical basis for pattern formation due to the signalling of morphogens was proposed by Turing in 1952 [105]. Where the signalling molecules react and diffuse through a tissue and produce the phenomena of biological pattern formation. Morphogen gradients were later studied within a rodent model by Kondo *et al.*, where pattern changes were observed in the skin tone of a genetically modified mouse [106, 107]. Research into the nature of the periodic patterns that form in nature has led to the understanding of how the spatial models produce pattern formation autonomously from homogeneous states

[108, 109].

Reaction-diffusion systems in chemistry have been studied and modelled due to their biological significance in pattern formation. Gray *et al.* modelled such systems to produce a mathematical model of target patterns that form in reaction-diffusion systems [110, 111]. The Gray-Scott Reaction-diffusion model allowed the simulation of chemical systems to become more systematic, as the reproducibility of simulations drastically increased accuracy in theoretical experiments. The theoretical analysis allowed for more edge cases in experiments to be investigated, along with impractical conditions to be met.

Investigations into the construction of artificial cells have utilised fatty acids as a boundary structure, much like biological cells employ. Hancyc *et al.* experimented with an oil phase loaded with a fatty acid precursor, this was then introduced into an aqueous fatty acid micelle solution. Autonomous sustained motion was observed in the oil droplets moving through an aqueous media. A positive feedback loop was created by the internal convection flow which pushed fresh precursor to the surface, which became hydrolyzed, creating more internal convective flow. The oil droplets moved along the chemical gradient, exhibiting a form of chemotaxis behaviour [112]. other research discovered that hydrophobic anions can generate periodic motion in a droplet involving a water-oil interface. The interface can be controlled by the chemical reaction of a cationic surfactant and a hydrophobic anion. The hydrophilic anions induce the Marangoni instability, whilst the hydrophobic anions generate periodic motion [113]. Using principles from physical-chemical mechanisms along with taxis effects generates a strong resemblance to biological cells and their motile behaviour. Studying these systems as a proxy can help to uncover the nature of the physical mechanisms and laws that govern biological life.

The study of the physical mechanisms has led to the mathematical and objective modelling of the phenomena. An exhaustive list and explanation of every model concerning the topics covered in this thesis would be impractical, so instead a select few will be touched on, as they were either paramount in the development of a statistical model used in the thesis, or will either be brought up in discussion to explain a phenomenon presented in the results chapters.

The study of fluids is important in biology, as many living systems rely on liquid exchange for survival. The Navier-Stokes equations were developed to describe the motion of liquids, and other viscous fluids (including gases) [114, 115]. The equations are a set of partial differential equations and are used to describe the both compressible and incompressible flow. The equations differ from the Euler equations, where the viscosity is taken into account in Navier-Stokes, whilst Euler equations only model inviscid flow. Solutions to the Navier-Stokes equations produce a fluid flow velocity field, represented by a series of vectors. These vectors detail the motion at every point in the fluid field, at any moment in a time interval. The vector represents the velocity of the fluid at that particular moment in time and space. A breakdown in the equations lies in no smooth solution existing for 3 dimensions, which is now the current focus for many mathematicians [116, 117]. The Navier-Stokes equations are important as they fundamentally describe how a fluid flows through the environment. Many engineers use the Navier-Stokes equations to model water flow in sand banks as a computational model prior to starting work on engineering developments. Another example of the Navier-Stokes equations being used in science involves biomedical researchers using the equations to model blood flow around the body [118].

As the Navier-Stokes equations are incredibly computationally expensive, other models have been developed to accomplish similar results, using computational efficiencies and taking different approaches to produce solutions to understanding fluid flow. The lattice Boltzmann methods (LBM) are a class of computational fluid dynamics methods for the simulation of fluids and gases [119, 120]. The practical application of LBM is to construct simplified kinetics models using only essential physics laws on a mesoscopic level. Mesoscopic refers to the intermediate stage between macroscopic, and microscopic. Rather than simulating every possible detail and particle on a microscopic level like with the Navier-Stokes equations, the LBM method utilises simulation of a fluid density on a lattice, where the particle collisions and relaxation processes average out onto the macroscopic level, producing a mathematical description that follows physical laws at the macroscopic level, without losing detail like other coarse-grained techniques tend to. On the mesoscopic level fluids are represented as a probability density as opposed to discrete particles and molecules as depicted on the microscopic

scale. The probability density gives an estimate for finding a particle at a given position in space at a given time, with a given velocity. This description is an application of kinetic theory, a cornerstone of fluid dynamics.

A plethora of techniques have been developed for simulating fluid or gaseous flows. A key inclusion is the lattice Boltzmann method (LBM) [121]. In phase space, the LBM's convection operator is linear. The properties: space time; and particle velocities are discrete in the lattice gas automaton, which is an abstract, simplified molecular dynamic model. The LBM uses microscopic models and kinetic equations instead of typical numerical schemes based on discretizations of equations describing physical laws used to describe mass transfer and forces in a coarse-grained model developed from continuum equations.

For supercritical shallow water flow, a new 1D LBM has been developed for steady and unsteady flows [122]. Existing LBM schemes are restricted to subcritical flows or a limited range of Froude numbers which are ineffective for predicting engineering fluid mechanics. Froude numbers are a dimensionless value used to describe the flow regimes in different open channel flow states. The Froude number is the ratio of inertial and gravitational forces subjected onto the flow. Using this approach, the limitations of existing schemes were overcome. There is a complete set of general equilibrium functions, boundary conditions, weights for external forces and new stability conditions derived from these equations. When used in conjunction, these parameters enable the selection of lattice parameters for modelling subcritical and supercritical free surface flows. LB models for free surface flow can be significantly extended with the new generalized LBM scheme. Using a simple first-order scheme, this research describes how to model a wide range of supercritical flow conditions with high accuracy using the new generalized LBM. As a moving reference frame, the new model generalizes the LBM model into a generalised Galilean transformation.

1.5 Active Matter

Active matter as a field of research is important due to the nature of understanding a system's ability to consume energy in a way to drive itself away from thermodynamic equilibrium [123]. To begin with, in science, 'active' is characterised by movement and action, and matter is defined as a physical substance in general, with distinct mass, and energy, and occupies space. Active matter is defined by its composition of 'active' particles, which are free agents able to demonstrate motility. A particle with motility is a particle with the ability to perform mechanical work, such as motion, at the expense of some energy input, either metabolic or environmental for example [124, 125]. Active matter can be composed of nanometer-scale active particles, such as Janus particles, or on a macro-scale, agents like fish within a school, or birds within a flock. Active matter is often considered to be composed of a series of active 'agents' which are expending chemical energy to exert mechanical forces. These systems are intrinsically maintaining stasis outside of thermal equilibrium. Active matter will cease to be considered 'active' once the thermal equilibrium is met. This is akin to a vehicle running out of fuel. Schools of fish, flocks of birds, and bacteria colonies are examples of more well-known active matter, where the constituent elements each use energy to perform actions, within a large group of self-similar agents. Lesser thought of examples of active matter includes self-organising polymers, microtubes, and actin. Research of active matter is important because it can reveal the underlying physics and statistics of out-of-equilibrium systems. This can be used as a framework to generate and develop systems utilising similar methodologies to arise in similar conditions.

Janus particles, so named after the Roman god, depicted with 2 faces, are a form of active matter, concerned with reaction with its environment. The particles have generated interest due to their outstanding properties and applications. Janus particles are interconnected by solid-state interfaces, where one face has different properties from the other. A commonly used example of such an effect is presenting a Janus particle where one interface is hydrophobic, with the other being hydrophilic. An arrangement like this can present interesting properties like self-organisation and self-assembly. It has been shown that synthetic Janus particles can share a multitude of similarities and features of organic Janus particles, leading

to more research in colloidal chemistry due to the availability of reproducible results from the synthetically produced architecture [126]. The development of Janus particles historically involved powder coating one material with another, such that the exposed side has differing properties to the enclosed. Generations of different permutations of properties have led to advancements in their construction. Microfluidic devices have been utilised due to the nature of fabrication from such a device offering many more unique characteristics which cannot be obtained through the traditional batch synthesis processes [127]. Due to their robust and versatile nature, Janus particles have been utilised within biomedical research with a special focus on their application for cargo delivery and bio-imagine. the self-propelled particles have been used to deliver multiple drugs to patients, due to their ability to function autonomously and penetrate biofilms [128, 129]. Precise targeting of specific tumours and other biological barriers have been overcome through the use of Janus particles [130]. Calcium carbonate particle micromotors were deployed, with a half Au shell to develop the Janus particle structure. The schema was important for the delivery of curcumin to cancer sites in in-vitro studies. Using this strategy guaranteed controllable trajectories of the drug delivery device, which was guided to the target location where the distribution of the drug was carried out. PSS was employed as a surfactant in the one-pot emulsification to generate the $CaCO_3$ microspheres. The surfactant was sued to control the size and morphology of the microsphere formation. The uniformity of the distribution of calcium was verified using energy-dispersive X-ray spectroscopy, which mapped the distribution within the particle. The Au coating was applied via the ion sputtering method [131].

Biological motility is often studied as an approach to understanding the nature of biological systems. The motion of oil in water droplets has been studied as a way to replicate amoeba-like motion in a simplistic system, where a surfactant dissolved in the water creates Marangoni stress that acts as stimulation on the droplet leading to autonomous motion [132].

Liquid droplets are often used as a mechanism to study real biological phenomena, as they can act as a very good proxy for biological systems, allowing for repeatability in experiments, as well as allowing for better control of environmental conditions. An active droplet can be defined as a material forming a droplet, existing outside of non-equilibrium environments. Dwivedi *et al.* [133] explain the breakdown of active droplets into the subsequent categories:

Reaction [134]; Solubilization [135]; Phase separation [136]; Droplet swarms [137]; Droplet pairs [138]; Under confinement [139]; External flow [140]; Addition of solutes [141].

Droplet motion driven by a chemical reaction is commonly found in a system with a phase separation between the droplet and the liquid phase it resides in. Common experimental setups involve an aqueous droplet inside an oil phase, as the aqueous droplet can contain chemical compounds capable of undergoing a chemical reaction. This is not always the case, as oil droplets have also been experimented on. The mechanism driving motion of the droplet driven by reaction typically involves the generation of Marangoni stress, which induces flow within both the liquid phases. These flows then impart a momentum transfer onto one another, which causes the motion of the droplet within the liquid phase [142]. Reaction-driven droplet motion can also exist as a reaction between the droplet and a chemical in its environment. This is the essence of chemotaxis, where environmental conditions are detected by the droplet, and the reaction induces motion according to how the gradient of the chemicals are presented [143].

Solubilization is the process of making a substance more soluble and has been found to drastically increase the velocity of Janus particles [135]. The fluid motion driving the motion of droplets which have undergone solubilization is in the Stokes flow regime, also referred to as creeping flow or creeping motion [144]. Stokes flow forms in a squirming motion that is much akin to that found in bacterium and is generated when advective internal forces are much smaller than viscous forces. Droplets driven by such mechanisms have been studied as they offer great potential to guide further research in soft matter and engineering. The complex behaviour observed in these squirmers is also exhibited in living systems which undergo morphogenesis [145].

The study of droplet motion due to phase separation mechanics has become more and more studied as it is believed that phase separation plays a key role in the spatial organisation within bacterial communities [146]. For this reason, phase separation has been studied as a mechanism of droplet motion, where the separation can exist as 2 (or more) liquid phases intercept, or in the form of evaporation, solidification, dissolution, or where a liquid

phase meets a solid phase. The interface between the separated phases is a source of energy transfer which can maintain the droplet being kept out of equilibrium. When there is a non-equilibrium body, there will be a gradient in concentration, which generates mass transit and flows. This phenomenon is prominent within nature and is commonly found to drive motion within bacterial colonies [147, 148]. Another study of droplets interacting with a phase separation was conducted on oil droplets, where an air-liquid interface presented attractive and repulsive forces between the droplets. The self-motion interactions of the droplets were driven by convective flow derived from heat exchange between the two phases. the study revealed a 'capture' motion, where an unbalanced impact force forms fluid flow around the droplets [149].

The mechanisms driving droplet swarms are often different, many arise from internal reactions, or through phase separation effects. Droplet swarms are studied to research self-organisation using physical-chemical phenomena as the driving mechanism. In one study, the path of which the droplets take is determined by their size and the volume fraction of the dispersed phase. This led to a 95% packing rate in a 3-dimensional bilayer structure [137]. The droplets in this study produced minimal inter-droplet forces and formed the structure through the motion generated by a depletion force which arises between colloidal particles in a solution. In another study, a swarm of droplets was used to study the kinetics of phase separation so that a model of the coalescence process could be produced [150]. To support the data gathered from tracking the moving droplets at the phase separation interface, the interfacial tension was measured with a droplet-volume tensiometer. This allowed the first-order model to be developed, describing the kinetics of the phase separation in liquid-liquid systems.

Motion derived from droplet pair interactions is often derived from electrostatic forces, or from attractive or repulsive charges induced on the droplets [151]. Droplet-droplet interactions involving motion readily are important in the regulation of self-organisation in droplet clusters. The autonomous collective motion of droplets has been found to impact the interfacial tension between droplets, which acts as a feedback mechanism to continue the self-organisation regime [152]. Interactions between droplets can drastically alter the dynamics of the velocity profile, and the makeup of the droplet itself. A study was conducted to find the collision regimes resulting in the agglomeration of droplets, along with the stretching separation of

droplet-droplet collisions, droplet-particle, and droplet-substrate collisions [153].

Droplets moving under confinement are an example of external conditions causing directed motion. A simple example of this could be a rod simply pushing a droplet to move it from one point to another. This is related, but different to confined droplets, as it is something in the environment causing the motion, the motion is not derived from the environment itself. Confined droplets can be confined physically by apparatus in its environment, or by the generation of a convective flow. Droplets held in a convective flow will often demonstrate periodic cyclic motion, or motion directed towards an enclosed centre [154]. The elongated formation of droplets within a microfluidic system is assumed when the droplet diameter is greater than the diameter of the circular channel they reside within. Controlling the droplet velocity by altering the initial length of the said droplet, the viscosity ratio between the droplet and the continuous phase, the interfacial tension between the phases, and the flow rate of the continuous phase can allow for selective merging of the droplets. The merging of transported droplets in the same carrier fluid was proven to be triggered precisely in space and time, on demand. This has advances in drug delivery, where extremely precise margins are required to be achieved, along with pathogen detection in clean facilities [155].

Droplets moving under external flow follow the basic principle of F=ma, where the momentum transfer of the external flow is directly proportional to the motion of the droplet. The physical law F=ma has been expanded into the Navier-Stokes equations which depict fluid motion with greater sophistication. The external flow can be in the form of airflow against a droplet held on a slide, or partially suspended within an oil phase, where the exposed region of the droplet is in contact with the airflow which causes its motion [156, 157]. Alternatively, the flow can be within the oil phase itself, which could be generated from a number of effects. Pulsatile flow is commonly found in microfluidic systems, where the precise motion of fluids needs to be accounted for [158]. The pulsatile nature of the flow allows for a calibrated flow rate to exist in the structure. A practical application of millifluidic devices being used to control droplet flow is in the food industry, where extremely precise measurements are imperative when it comes to food safety control and the detection of pathogens in production facilities [159]. Another phenomenon where droplets are set in motion is in Faraday wave

systems. In these systems an external vibration causes droplets to rebound off a free surface and move. The frequency is a source of vibration causing droplet motion. The frequency of the wave should be tuned in to the natural frequency of the droplet to induce the greatest velocity. Droplets moving under such stimulus have been coined 'walking droplets'. Research into walking droplets has led to much larger and faster walking droplets which have been named superwalkers. The superwalkers are much larger, more than double the size, and are capable of moving up to 3x as fast [160].

The addition of solutes can drive the motion of droplets, in a similar mechanism to the reaction-diffusion-driven droplets, where the internal chemical reaction decreases the interfacial tension between the droplet and the liquid phase it resides within, the addition of solutes can cause the same effect [161, 162]. Solutes forming a reaction with chemicals within a droplet can create interfacial flows within the droplet and the residing phase, this will generate Marangoni flows, also responsible for the motion in the RD-driven droplets [163]. In the same vein, the deformation of droplets has been simulated under a solute gradient, where rather than motion being induced, shape changes occur in the viscous droplet [164].

Interest in moving droplets has led research into many pathways, in both mechanism and objectives. Droplets can be used as a proxy for studying how biological life interacts with its environment, especially with how organisms are able to convert chemical energy into mechanical work. This comparison has led to advances in mobile droplet research, involving many different regimes of droplets, in a variety of different environments. This has produced a greater understanding of fluid dynamics which has pushed the field of microfluidic devices further, along with uncovering biological mechanisms and a general understanding of physical chemistry.

1.6 The Belousov Zhabotinsky Reaction

1.6.1 Background of BZ reaction

The Belousov Zhabotinsky (BZ) reaction is one of my most widely known and researched examples of non-equilibrium physical chemistry phenomena [165, 166]. The reaction-diffusion system is famous for producing beautiful target patterns due to the propagating chemical waves when run in a quasi-2D system. A quasi-2D system refers to the bottom of a dish being covered in a thin layer of BZ solution, such that the height of the reaction is negligible, but the system can still produce chemical wave forms. The system is unstirred. In such a system, propagating waves emerge from nucleation points, known as a leading centre (LC). The propagating waves will diffuse through the system, annihilating upon convergence with another wave, or the edge of the dish the reaction is performed within.

Originally, Belousov was formulating a simple model of the metabolism using chemical reactions to replicate the oxidation of organic models, akin to what is observed in biological cells. Organic acids are oxidised into H_2O, and CO_2. The physical-chemical model of the Krebs cycle was performed using citric acid as the organic component, cerium (3+) as the catalyst, and utilising bromate as the oxidising agent. The reaction was not received well due to political tensions, and the visibility of the colour change is difficult to make out. It wasn't until Zhabotinsky began replicating his work when ferroin (2+) was substituted for the cerium, and the striking colour change became visible, that the publication was picked up and many others began experimenting with the new-found Belusov-Zhabotinsky reaction [167].

The BZ reaction is a name for a family of reactions discovered by Boris Belousov and Anatol Zhabotinsky after Belousov was experimenting with Potassium Bromate, Cerium(IV) sulfate, Malonic acid, or Citric acid, in dilute sulfuric acid, as a means to discern a non-organic analogue of the Krebs cycle [168]. Zhabotinsky began work on understanding the mechanism of the periodic oscillations observed by Belousov, where he introduced the addition of Ferroin solution rather than the Cerium recipe for the metal catalyst, leading to the striking colour change from red to blue under oscillation [169]. Experimentation with the reaction has led to a greater understanding of how different varieties will have different effects on the reaction

dynamics. A common change to the original protocol, for example, in his book titled "The geometry of biological time", Winfree details a recipe using Sodium bromate rather than Potassium bromate as the source of bromine, and the use of Ferroin solution is employed rather than Cerium Sulfate as the catalyst [170]. With many variations of the reaction existing, researchers have made efforts to understand the underlying phenomena and mechanisms to explain how the reaction functions.

Mechanistic view of BZ reaction

It was Field, Korös, and Noyes that examined the reaction mechanism of the original BZ system in depth. This system contained bromate ions, malonic acid (MA), and cerium ions (Ce^{3+}/Ce^{4+}) which is characterized by bromide ions as the control mechanism. The self-named mechanism, taking an initial from each researcher was published after its formulation and verification [171]. Bromate ions and malonic acid are reacting with the metal catalyst (often cerium of ferroin), to produce carbon dioxide and bromomalonic acid. At this point, the intermediate chemicals (Br^- and $HBrO_2$) periodically increase and decrease. Positive feedback for the autocatalysis is provided by the $HBrO_2$ present, allowing for the accumulation of Br- ions which inhibit the autocatalysis by introducing a delay via negative feedback.

These processes are described by the FKN mechanism, where 3 processes compete for dominance within a solution of chemical reactions, producing the periodic behaviour we observe in experiments:

$$BrO_3^- + 5Br^- + 6H^+ \rightleftharpoons 3Br_2 + 3H_2O \quad \text{(A)}$$

$$BrO_3^- + 4Ce^{3+} + 5H^+ \rightarrow HOBr^+ + 4Ce^{4+} + 2H_2O \quad \text{(B)}$$

$$2Ce^{4+} + MA + BrMA \rightarrow fBr^- + \text{by-products} \quad \text{(C)}$$

In these equations, f is a stochiometric factor. The by-products listen in equation C contain CO_2.

Process A: Together, processes **A** and **B** constitute an inorganic subsystem of the BZ

reaction, which is characterized by a long induction period with low reaction rates followed by a quick autocatalytic event. Process **A** acts as the induction period where many sub-reactions all consume the Br^- ions simultaneously.

Here, the equations for the induction period can be written as:

$$HOBr + Br^- + H^+ \rightleftharpoons Br_2 + H_2O \quad \text{(D)}$$

$$HBrO_2 + Br^- + H^+ \rightleftharpoons 2HOBr \quad \text{(E)}$$

$$BrO_3^- + Br^- + H^+ \rightleftharpoons HBrO_2 + HOBr \quad \text{(F)}$$

Process B: Process **B** produces HBrO2 and oxidizes Ce^{3+} to Ce^{4+} in a fast, autocatalytic manner, which is part of the inorganic subsystem in addition to Process **A**. There is a specific threshold for the concentration of the bromide ions to maintain for process **A** to dominate. Once the concentration falls below the said threshold, other reactions are able to build up momentum and react. BrO_2 then oxidises the Ce^{3+} ion simultaneously to the production of $HBrO_2$.

The equations governing the dynamics of process **B** can be explained with the following:

$$2HBrO_2 \rightarrow BrO_3^- + HOBr + H^+ \quad \text{(G)}$$

$$BrO_3^- + HBrO_2 + H^+ \rightleftharpoons 2BrO_2 + H_2O \quad \text{(H)}$$

$$BrO_2 + Ce^{3+} + H^+ \rightleftharpoons HBrO_2 + Ce^{4+} \quad \text{(I)}$$

$$BrO_3^- + 2Ce^{3+} + HBrO_2 + 3H^+ \rightarrow HBrO_2 + HOBr \quad \text{(J)}$$

When the concentration of Br^- drops sufficiently below a threshold, equation H will dominate over equation E.

Process C: As the organic subsystem of the BZ reaction, Process **C** provides delayed negative feedback through the involvement of numerous organic intermediates such as oxalic acid

($C_2H_2O_4$), mesoxalic acid ($C_3H_2O_5$), and tartronic acid ($C_3H_4O_5$). In process **C**, the oxidised Ce^{4+} is reduced to Ce^{3+} again, through the reactions with organic compounds. Bromide ions are also produced in greater quantities.

The combination of processes **A**, and **B**, leading into process **C** forms a periodic cycle, where the consumption of Br- ions in process **A**, allows process **B** to take over (upon the threshold level being crossed). The autocatalysis in process **B** leads to the oxidation event of the metal catalyst. Then, process **C** will act as a 'reset', where the original states are reconstructed by increasing production of the Br- ions, which inhibit the process **B** reactions and allow process **A** to dominate the chemical processes once again.

These cycles will continue until the reaction reaches thermodynamic equilibrium. In the ferroin-catalysed reaction, this will be visible by the colour shift from entirely red, to entirely blue. This will be accompanied by a production of CO_2 bubbles which will form at the surface of the solution in unstirred experiments and will escape the solution in stirred experiments.

Computational Models of the BZ Reaction

A natural next step once the FKN model was developed, was to generate a computational model to depict the changing concentrations of the chemicals in the 3 processes governing the periodic behaviour of the BZ reaction. The most famous of the models is the Oregonator [172]. Developed by Field and Noyes, the Oregonator details the role of the inhibitor, Br^-, and the autocatalyst, $HBrO_2$. Involving the metal catalyst, the model demonstrates the periodicity of the reaction and allows for modifications to be made to the initial concentrations of the chemicals. A user can simply modify the initial concentrations of the chemicals, represented by variables, and use a computational tool, like MATLAB, to compute the simultaneous differential equations, which will produce a graphical output depicting the periodic cycles of the BZ reaction. The utility of the Oregonator is a great example of improving the efficiency and optimization of performing repeat chemical reactions. Computational validation is now an important part of many sciences but also allows for the efficiency of performing robust systematic studies to be carried out, as the theoretical model can outline experimental con-

ditions which will not produce oscillations in real chemical experiments. This is an important factor for experiments carried out to produce a phase diagram when changing multiple factors in experimental conditions. The Oregonator is commonly found in numerical studies of the 2-dimensional pattern formation of the BZ media. Studies into 3 dimensions generally use alternate models due to the lack of scalability in the Oregonator producing computationally inefficient time scales for computing times.

Continuation of the work developing models of the BZ reaction has produced a model for deterministic chaos in the BZ reaction [173, 174]. The researchers were able to produce aperiodicity, and transitions between periodic behaviour and chaotic behaviour. Bifurcations between steady state and oscillatory behaviour were modelled in a theoretical stirred tank reactor. Other researchers have developed fractional analysis, allowing for greater accuracy in simulating the BZ reaction, within finer time constraints [175]. These models have since been extended from 1-dimensional analysis of chemical concentrations, through to 2-dimensional analytical tools capable of generating BZ pattern formation, and even further into 3 dimensions [176]. Aqueous droplets containing BZ solutions have been modelled computationally to support experimental findings [177]. The symmetry breaking that results in autonomous self-propulsion was studied experimentally and replicated computationally where the velocity field and pressure variable are approximated using a numerical solution to the Stokes equation.

A computational model was developed with the aim of capturing the complex three-dimensional behaviour of chemoresponsive polymer gels saturated with BZ solutions.The model utilised finite difference, and finite element techniques to develop a two-dimensional lattice spring model of the gel. The two-dimensional model was extended to capture the complex behaviour of the BZ hydrogel [178]. Other studies have drawn comparisons between the BZ reaction, and biochemical processes in biology [179]. The BZ reaction is characterised as a functional model of biological phenomena. Many biologists are now using the BZ reaction as a model to study a variety of processes relating to excitable media. Boris Belousov himself had his roots in cell biology and was studying the oxidation of citric acid as a model of biochemical clocks. Cell rhythm plays a crucial role in cell-cell regulation and signalling, where periodicity governs the nature of the biochemical processes. Using the BZ

reaction, or models of the BZ reaction can help advance knowledge in areas of cell biology because of the overlap in function between the biological cell, and the periodic BZ reaction [180].

Modelling periodic spiking behaviour has been carried out for many years now. One of the earliest spiking models generated was the Hodgkin-Huxley (HH) model [181, 182]. Originally developed as a physical model, using electronic components in a circuit, the 4 variable HH model was developed to simulate neuronal signalling, where an electrical excitation is observed along the axon of a squid. The extracellular medium and intracellular medium are represented as voltage pickups on the circuit, which was defined mathematically at a later date. the electrochemical gradients which drive the flow of ions are represented as voltage sources, which determine the ratio of the intracellular and extracellular concentrations of the ionic species. The membrane potential can be plotted through time to determine the effect of the injection (or excitation) current. The distinct phases can be observed in the HH model as the injection current is increased through specific parameters whilst sensitivity testing the model. When the injection current is negative, the model produces no excitation wave and is said to be in the equilibrium stage. With an injection current between 0nA and 10nA, there is a singular peak, where only one excitation signal is generated. Then as the injection voltage is increased further, into the limit cycle stage with an injection current of 10nA, a periodic behaviour is observed. The periodic behaviour shows the production of many, routine spikings, which resembles the excitatory behaviour of the squid axon. Analysis in the phase space has found that the HH model is stable and has a closed limit cycle. This model has been extended and simplified by many other models. A simplification of the HH model was developed by Van der Pol [183, 184]. As with the HH model, an electrical circuit diagram was developed with a tunnel diode. This produced the oscillatory behaviour we observe when computing the second-order differential equations governing the behaviour of the circuitry. The non-linear behaviour is dampened to produce a stable limit cycle, and produce periodic excitation and relaxation cycles. The Van der Pol oscillator was extended by Richard FitzHugh as a simplification of the HH model, which then had the equivalent circuit produced by Nagumo *et al.* [185, 186, 187, 188]. The FHN model describes the action potential of an excitable system like a neuron [189, 190]. The FHN model is a relaxation function, which takes an external input. If the external input is of great enough magnitude and crosses the threshold value, the

voltage, and reset variables will exhibit an excursion in the phase space, before relaxing back to their rest values. This will be exhibited as spiking behaviour in the time domain. Sensitivity testing can be conducted to find regions where the periodicity is maintained, decays, or only exhibits a single excitation. For this reason, the FHN modal has been uptaken by scientists and mathematicians as a model to explain oscillatory and excitatory behaviour in many systems, from modelling real phenomena to incorporation within simulations [191, 192].
Parallels can be drawn between the modelling of the BZ reaction and the FHN model, where both are modelling periodic spiking activity. In a later chapter, we will discuss using the FHN model to simulate a pair of entrained oscillators that rely upon the use of the FHN model coupled with the Kuramoto oscillator to close the feedback loop between such entrained oscillators, producing synchrony as a function of distance.

Changing Reaction Concentrations

Experiments with varying concentrations of reactants have been conducted to show the varying results of the dynamical system. In their study of the BZ reaction, Wood *et al.* experimented with altered experimental conditions along with the concentrations of reactants [193]. This experimentation leads to a greater understanding of the frequency of which wave formation occurs in a quasi-2D solution, along with the study of chemical wave propagation speed, and the wavelength of the emerging wave. Chang *et al.* experimented in a similar manner, with the exception that a series of droplets within a network was the subject of study, rather than the original quasi-2D experimental set-up [194]. The experiments with droplets in series have been conducted with the approach of expanding biological knowledge of signal processing and propagation, using the networks of droplets as a model of how biological systems process and encode information. Progress was subsequently made in the development of large-scale networks of coupled droplets, where pattern formation and basic computer architecture was achieved [195, 196]. The networks of droplets are created through the clever use of 3D printing, or CNC-milled millifluidic devices which are filled with an inert oil, Oleic acid for example. The oil phase is often saturated with a surfactant like SDS, which acts to reduce the surface tension between the water, and the oil phase with the aim of immobilising the droplets. The droplets are then pipetted into the device either by hand or through the use of millifluidic devices. The

droplets are coated in a lipid layer to prevent merging from occurring. The hypothesis for the signal propagation involves the flow of chemical species between droplets, or alternatively a hydrodynamic coupling, whereas the mechanical forces exerted between droplets due to the deformation upon chemical wave propagation acts as mechanical perturbation onto the following droplets. Research conducted by Zauner's research group found that adjusting concentrations of the acid and metal catalyst used in the solution could impact the outcome of the periodic behaviour of the reaction. Droplets here were observed to show 3 stages of the 'lifecycle': the initial; main; and late stages [195]. To determine the chemical concentrations to compose their BZ recipe, multiple experiments were conducted, where the concentration of bromine donor, acids (malonic acid, sulfuric acid), and ferroin solution was changed. The observations were made about the lifetime of the reaction, the frequency of which the reaction produced a travelling wave, the number of waves produced in total, the amplitude of the propagating wave, and its area. This information was used to optimise the recipe for the networks of droplets and use different concentrations of BZ reaction for droplets within the same network. Experimentation on the chemical concentrations of the cerium-catalysed BZ reaction was undertaken to find the minimum number of cerium 4+ ions required to produce one Br^- ion in the oxidation of bromomalonic acid. It was determined that a ratio of 1:1 cerium to BrMA. was required in aerobic conditions, and 2:1 in anaerobic conditions. The team also found that malonic acid played no role in this catalysis, where its presence did not affect the result [197].

In related work, entirely chemical-based computation units have been created. Perez-Mercader *et al.* created a Turing machine possessing the ability to process Chomsky type-1 language[198, 199]. The 'one-pot' stirred reaction process has the ability to accept or reject chemical inputs forming word strings.

External perturbations have also been applied to the excitable solution to study the effect. It is well known that silver wire perturbation will instantiate a chemical wave's formation. The application of external DC fields has also been investigated in BZ solutions, in particular where spiral waves are concerned. [200]. The unpinning of spiral waves in the excitable medium was confirmed with simulation using a 3 variable Oregonator model, where it was discovered that the retarding force applied by the DC field was responsible for the unpinning [201]. The spiral

wave always unpins at a fixed phase whilst propagating away from the anode at a fixed field strength.

Experimenting with the change in concentrations of the BZ reaction can be an interesting study of nonlinear dynamics (NLD). The addition of the BZ reaction to a non-ionic self-assembling polymer was investigated, where changing the concentrations of BZ reactants to adjust the induction period (IP) had profound impacts on the assembly of such polymer, where the BZ reaction acts as a perturbation factor on the polymer self-assembly mechanism [202]. Other experiments involve adjusting not the BZ concentrations, but with surfactants dissolved in the solutions to aid in the absorption of the metal catalyst, ferroin solution [203]. A well-stirred closed BZ reaction had surfactants present, at above critical micelle concentrations to reduce the surface tension and altering hydrodynamic parameters. This perturbation to the reaction caused the absorption rates to increase, altering the BZ reaction kinetics. Due to the enhanced chemical kinetics due to the surfactants, the Br^- ions were able to fall below the critical threshold in the FKN mechanism much faster than a typical reaction, reducing the induction period drastically. A mixture of surfactants with different charge profiles was able to both drastically reduce the IP, but also the lifecycle of the reaction. Other experiments have been conducted to determine the effect of the initial concentrations of the chemical substrates had on the oscillatory dynamics [204]. Some changes in concentration will change the time for the induction period, where it was shown that the waveform during the oscillatory period can be changed also. The substrates that were experimented with were, $NaBrO_3$, Malonic acid, and the ruthenium metal catalyst. The effects were varied, from producing a sharper waveform, where the reduction happens very quickly after the oxidation process occurs, to producing a higher frequency oscillation, where more waves happen in a given time. Other changes produced a greater wavelength, where the oxidation process is not quickly reset, so the oxidised wave stays around for a much greater time, followed by its reduction, then quickly back into the oxidation process.

1.6.2 Self-Organization in BZ

One of the most visually appealing examples of self-organisation in the BZ reaction is the generation of spiral waves. The striking pattern formation can be generated from many excitable media which exhibit geometrically complex spatio-temporal formations. Spiral waves are the origin of a plethora of interesting questions about the BZ excitable media. A numerical approach to understanding the formation of the spiral waves was carried out using a network of van der pol oscillators [205]. Interlayer coupling of synchronised wave structures leads to the transition of bistable dynamics in the network of oscillators. The synchronisation between oscillators was observed, along with stable rotating spiral waves under the effect of shear strain included from the Oregonator model. Numerical studies are often employed for studying the 2D pattern formation of the BZ media. The reproducibility of the computational models makes them an attractive approach o studying such formation. One such study delves into the formation of spiral waves, and how they can be induced with the application of an external light source [206]. The photosensitive BZ reaction was studied, where photo illumination was altered periodically to induce the formation of a spiral wave into the excitable media. The computational results were complimented by experimental data, where the external perturbation as a source for inducing spiral waves was validated. Spiral waves are often studied in a quasi-2D solution but have been observed in BZ droplets. Agladze *et al.* found that passing a current through a hydrogel containing the BZ excitable medium could impact the formation of spiral wave formation [200]. The velocity of the induced spiral wave increased linearly with the increase in the current applied across the gel. The dependence on the current that was observed in the angle of the spiral wave was proportional to the current as well, where the increased current application was shown to decrease the angle. The researchers conclude that an increase in the current will produce a more compact, faster-travelling spiral wave. The spiral wave unpinning was developed by Amrutha *et al.*, where the application of a circularly polarized electric field (CPEF) was applied to the excitable medium [207]. The electric field exerts a retarding force onto the chemical wave front, which acts with the greatest force when the chemical wave front is travelling in the direction of the field. The field was only able to unpin the spiral wave when the frequency of the CPEF was greater than a cut-off frequency. Theoretical validation was completed, where the numerical solutions of the 2 variable Oreg-

onator model also produced the unpinning of spiral waves. In photosensitive BZ solutions, constant illumination was shown to influence the wave dynamics [208]. An active media can be controlled by modulating its excitability in a periodic manner to control spiral-wave dynamics. According to the specific reaction conditions, spiral cores trace circular or hypocycloidal paths. It is possible to control the dynamics of other excitable media by modulating their excitability with weak external forces [209]. A wide range of hypocycloidal trajectories can be described using the motion of spiral cores in phase with modulation frequency. A modified Oregonator was used to confirm findings where the dynamic control of the spiral waves were replicated using numerical solutions. The discovery of concentric and spiral waves in the Belousov-Zhabotinsky reaction nearly 30 years ago was reported in 'Inwardly Rotating Spiral Waves in a Reaction-Diffusion System' by Epstein *et al.* [210]. Observations of inwardly rotating spirals were reported by Epstein in a water-in-oil microemulsion containing water droplets dispersed in them. The team reports observations of inwardly rotating spirals found in the BZ system dispersed in water droplets of a water-in-oil microemulsion. Simulations were used to generate these "antispirals". In many chemical, biological, and physical reaction-diffusion systems, we have observed rotating spirals and target waves. All of these waves propagate out from the spiral centre or pacemaker.

Autowave generation in a kinetic system, like the BZ reaction, has been studied for its application in spatial and temporal self-organisation. Hanke *et al.* draw a comparison between the excitable BZ reaction, and the excitable medium, that the CNS is [211]. The propagation of a chemical wave in the BZ reaction is akin to the self-organisation and pattern formation of excitations within the neuronal structure. The effect of microgravity on wave propagation in polymer gels containing BZ solutions was investigated and used as a physiochemical model of biological activity. The properties of the gel were found to be the same as the theoretical spreading of depression and action potentials in the CNS.

The BZ reaction has been studied for its self-organization properties [212], where water-in-oil emulsions are the subject of observation. Wave generation and pattern formation have been observed in such systems, where wave generation in one droplet is followed by the propagation throughout the surrounding droplets. Spiral wave formation is often attributed to

the BZ reaction self-organising. the local and global geometry of the pattern formation was studied and mathematically modelled [213].

Zyrova *et al.* draw the parallel between biological pattern formation and self-organisation, and the BZ reaction [214]. The quasi-2D BZ reaction can be photographed with relative ease, a camera placed directly above the reaction vessel can encapsulate its spatio-temporal dynamics with remarkably high precision. On the contrary, aerial photography to capture the flight dynamics of a flock of birds, or a camera submerged within the water to record the motion of a school of fish presents difficulties where the 3-dimensional activity is translated down into a 2D image. The data loss in representing the 3-dimensional space as a 2D image can result in difficulties properly representing the group dynamics in the self-organising system. Whereas using the BZ reaction as a conduit for biological self-organisation reduces this error, as the wave propagation occurs in a quasi-2D state. The reliability of recording the BZ reaction, and being able to reproduce results with ease has pushed the BZ reaction into the focus of the scientific community when self-organisation is concerned.

Polyethylene and polytetrafluoroethylene powder coatings applied to a droplet of BZ solutions has been termed a 'liquid marble' (LM), and is a good vector for studying self-organisation in the BZ reaction due to its malleable form [215]. The hydrophobic powder coating allows for a stable liquid-solid interface where visual information can be recorded. A distributed network of LMs has been capable of wave transduction, where an excitatory wave propagated from one droplet to another. This compartmentalised network of BZ droplets could be an application for studying biological signal propagation, as well as a new method for unconventional computing. Following the discovery that a He-Ne laser with a wavelength of 632.8 nm acted as a mechanism to initiate wave propagation in the BZ reaction, Tsompanas confirmed this finding when they utilised photosensitivity for control of a mobile robot driven by a liquid marble [216, 217]. The LM was composed of an aqueous droplet containing BZ solutions, coated with polyethylene powder. The polyethylene powder (PE) was incorporated into the system due to its hydrophobic properties, inhibiting the wetting of nearby objects and allowing for the droplet to be manipulated by the apparatus. The loop is closed by using photosensors underneath the petri dish housing the LM. The electrical potential of the BZ reaction was investigated by piercing the droplet with a pair of iridium-coated electrodes. Following the

propagation of the oxidised wavefront, the changing electrical potential was measured. When the oscillation of the electrical output produced a negative reading, the laser was activated to initiate a new BZ wave in the droplet, and when a positive reading is achieved, the robot will steer left. Whilst primitive, this research is a stepping stone towards a more complex application of the BZ reaction, specifically droplets containing BZ solutions, in the field of self-organisation research. More research involving LMs has been conducted, where the LM acts as a reusable photosensor with an instantaneous response time [218]. The recovery time in the experiments was around 40 seconds, and the system could be deployed for up to 1 hour. The PE coating allows multiple photosensors to be placed in a compact region without merging. This will allow for new unconventional computational units to be devised based on voltage readings taken from an LM.

The emergence of self-oscillating hydrogels has helped to push research efforts into the BZ reaction due to the rapid advances made in the last few decades [219, 220, 221]. The properties of hydrogels can be manipulated depending on internal solutions. A novel self-walking gel was developed, where a hydrogel containing BZ solutions periodically undergoing cycles of swelling and deswelling creates mechanical work capable to produce mass transit of the BZ-hydrogel [222, 223, 224]. Another application found by Yoshida *et al.* is the development of BZ-hydrogels for drug delivery systems (DDS). Hydrogels are generally sensitive to temperature, pH, and electric field, but in their study, the BZ-hydrogel was also capable of detecting glucose levels. The on-off regulation of insulin was developed as a response to the increase and decrease of glucose concentration. This was achieved by utilising the reversible formation of a complex between glucose and Phenylboronic acid in the hydrogel [225]. Oscillatory drug release can be synchronised with the periodicity of the BZ-hydrogel, as one of many applications of hydrogels in biomedical contexts. Many biomedical applications of hydrogels, specifically self-oscillating hydrogels are focussed on mass transit for DDS [226]. Murase *et al.* investigated the role of AMPS feed ratio on the swelling properties of ruthenium-catalysed BZ hydrogels. The utilisation of peristaltic motion of poly(NIPAAm-co-Ru(bpy)3-co-AMPS) gel, with microphase separated structures, generated the motion of a cylindrical gel which was fabricated from poly-acrylamide on the surface of the original gel. The autonomous periodic peristaltic motion generated from the self-oscillating gel produced mass transit, which can

have applications in DDS systems, self-cleaning surfaces, and developments of nanomaterials. Bio-mimicry has been achieved using BZ hydrogels. A research team conducted a study where the oscillatory behaviour of sino-atrial (SA) cells was developed. SA cells are a type of cardiovascular cell, which are found to become coupled in frequency due to apparent reaction-diffusion. On its own, an SA cell will be shown to periodically oscillate, at a given frequency. However, when interconnected, the SA is found to become entrained and will oscillate at the same frequency as neighbouring SA nodes. Tabata *et al.* discovered that ciliary motion could be generated using self-oscillating gels [227]. Other experiments have devised control parameters for the oscillating gel, where the oxidation state of the ruthenium catalyst was synchronised with the swelling and deswelling states of the gel, where temperature-sensitive gels were utilised as a manner of inputting environmental perturbation into the reaction-diffusion system [228, 229].

1.6.3 BZ Droplets

Research on the BZ reaction led to the study of aqueous droplets containing BZ solutions suspended in an oil phase. It was discovered that a droplet undergoing chemical wave propagation can move translationally across the surface of the oil phase [230]. The motion was shown to be accompanied by a partial reset in position, in the opposite direction to the initial impulse. Kitahata *et al.* spent efforts to determine the mechanism of action causing the translational motion of the droplet across the surface of the oil phase [230, 231, 232]. The team uncovered the mechanism of spontaneous motion emerging from chemically driven external stress between the droplet and the oil phase. It was discovered that the translational motion is a result of a changing gradient of interfacial tension between the two liquid phases. The gradient of the interfacial tension is generated by the propagation of the oxidised chemical wave as it propagates across the body of the droplet. The ferroin solution in its reduced state has a 2+ charge but has a 3+ charge when in its oxidised state. The two states create a different interfacial tension between the oil and aqueous phases. The gradient of the interfacial tension causes Marangoni stress between the phases which induces flow. Due to the different viscosities in the phases, there is friction which exists coupled to the flow, which imparts a momentum transfer between the droplet and the oil phase. No explanation for the positional

reset is provided. Through the use of micro-spheres made from polystyrene, the flow within the oil and aqueous phases was mapped through time; as the chemical wave propagates across the body of the droplet, and when the droplet undergoes chemically driven translational motion. The team found evidence that the hypothesised Marangoni stress was inducing flow within the phases as the chemical wave propagates across the body of the droplet. This experiment was carried out by containing a body of oil next to a similar volume of water containing BZ solutions under a cover strip. The motion of the phases was tracked and recorded for analysis in correlation with the propagation of a travelling chemical wave. This work was supported by computer simulation using a mathematical model developed of the system.

Graphene nanoparticles (NP) have been developed to act as a catalyst for the BZ reaction [233]. The NPs were seeded with ruthenium, a catalyst for the BZ reaction, which was then laid into a structure for the BZ droplet to interact with. The droplet would absorb the catalyst, which would then cause the generation of a leading centre, leading to wave propagation, driving Maranogni stress through the droplet, and ultimately leading to the spontaneous motion of the droplet. The NPs could be arranged in 0D-2D structures, allowing many different arrangements to be produced. Mode switching was investigated in BZ droplets, where the concentrations of the initial reactants were systematically altered to determine the recipes for ballistic motion, and random motion, and the states required to spontaneously switch from one to another. It was discovered that increasing the oxidants, H_2SO_4, and BrO_3^- had the effect of increasing the random motion, whereas decreasing the oxidants had the opposite effect and produced more ballistic motion. The introduction of a higher concentration of malonic acid had the profound effect of mode switching in the droplet [234].

BZ taxis effects have been studied and described in a plethora of studies. The self-sustained motion presents in a random direction in many studies of the mechanism behind its cause. For studies of directed motion, the external stimulus is mainly used to control the motion of the BZ droplet. In their study, Chaithanya *et al.* found that the use of the environment itself could be utilised to control the direction of the self-propelled droplet [235]. The BZ droplet was confined within a 2-dimensional channel to study the multi-phase hydrodynamics as well as the BZ kinetics. They found that manipulating the degree of confinement on the droplet

was a crucial factor in controlling its self-propelled trajectory. Other factors included the BZ recipe itself, along with the surfactant concentration, use to alter the friction occurring at the fluid-droplet interface. The data was generated using the LBM techniques to model and simulate the moving droplet. This was suitable to produce PIV streamlines of the fluid flows within the droplet, as well as the oil phase it resides in.

BZ droplets are of interest in the research community, for the same reasons as liquid droplets in general. However, a remarkable difference is the bio-mimicry that is possible with the BZ reaction. The BZ reaction itself was initially developed as a model of cellular metabolism, which makes the study of BZ droplets a perfect candidate for studying biological mechanisms using physical chemistry as a proxy, due to their motile behaviour driven by the conversion of chemical energy into mechanical work. This is the principle of biological motion, where chemical energy gained by consuming food is converted into mechanical motion, either through cellular motility, or muscle actuation to move a larger organism. Confined droplets containing BZ solutions have also been employed to study the communication dynamics akin to those found in bio-physical systems. Studies involving compartmentalised BZ droplet networks often employ a microfluidic system to generate a series of volume-controlled BZ droplets which are subsequently anchored in a spatial geometry with varied dimensions to study the effect of the oscillating networks [236].

1.7 Aims and Objectives

In this thesis, we will investigate the effect of external perturbations on the self-organisation and bio-mimicry of the Belousov Zhabotinsky reaction. Using the BZ reaction as a model to study the manner in which biological systems interact with one another and their environment will lead to a proxy enabling repeatable experiments, and provide further applications within physical chemistry and engineering. We aim to produce a physical model of common biological processes which we can replicate to study how the mechanism allows the phenomena to present. Understanding the interactions between nonlinear chemical reactions and spontaneous motion is crucial to understanding biological processes, as well as other complex and ordered structures in nature.

Aim 1: Investigate the effect of an external DC field application on BZ droplets at different powers alongside using different concentrations of the metal catalyst.

Objective 1: Determine the electrostatic effect the external DC field has on the droplet behaviour, and how the power applied affects the outcome. Using different concentrations of the metal catalyst Ferroin will help determine if the chemical concentrations play a role in any effects observed.

Aim 2: Investigate the elongation of the BZ droplet and if they can divide.

Objective 2: Determine the optimal combination of SDS concentration within the oil phase, in correlation to the polarity switching frequency of an external AC field to produce the greatest elongation of the BZ droplet. Along with increasing elongation, we will determine if the droplets can routinely divide in this experimental condition.

Aim 3: Investigate the hydrodynamic coupling of droplets separated at different distances.

Objective 3: Determine the mechanism behind the signal propagation of separated droplets using droplets confined at different distances to determine the nature of the inter-droplet signal propagation. The droplets will be anchored in place and recorded, to study their oscillating frequency as it changes through time. The perturbation onto one another will be traced through the oil phase using the presence of trace particles suspended in the oil phase.

Chapter 2

Materials and Methods

The Belousov Zhabotinsky (BZ) reaction is typically run as either a batch solution, in a beaker under continual stirring, or as a quasi 2D set-up, run in a petri dish. Both experiments give the characteristic colour change, but as the batch solution is an instantaneous global colour change, it is not plausible to utilise this phenomenon due to the nature of its simplicity, as the homogeneity will not lead to any gradients that we can utilise for driving motor coupled systems. So, the 2D system was chosen. We will be taking advantage of the fact that we can observe wave generation and pattern formation to understand the effect that applying an electric field has on the BZ reaction. We will be observing the reaction under normal conditions and whilst varying the strength of the electric field that is applied.

2.1 Solution Preparation

The protocol for the BZ reaction is as such:

A: 33.5ml H_2O + 1ml ccH_2SO_4 + 2.5g $NaBrO_3$

B: 10ml H_2O + 1g Malonic Acid

C: 10ml H_2O + 1g NaBr

D: Ferroin Solution

3 different concentrations of the Ferroin solution are used for the experiments, the measurements for such are:

1: 0.015M: 0.2085g $Fe_2SO_4x7H_2O$ and 0.4055g 1,10-Phenanthroline

2: 0.025M: 0.3438g $Fe_2SO_4x7H_2O$ and 0.6758g 1,10-Phenanthroline

3: 0.035M: 0.4813g $Fe_2SO_4x7H_2O$ and 0.9461g 1,10-Phenanthroline

Each of these sets of measurements were used to make 50cm^3 solutions of the Ferroin solution, which is only used on the day of preparation, as the solution denatures very quickly when stored at room temperature. Therefore fresh batches of the solution are prepared on the day to ensure reliability in the results gained. The chemicals were extra pure lab grade reagents and required no further purification, sourced from Sigma-Aldrich and Thermo-Fisher.

Preparing the excitable BZ solution was performed following the procedure reported by Arthur Winfree in "The geometry of biological time" [170]. Where 6ml of solution A is mixed with 1ml of solution B and 0.5ml of solution C and allowed to rest in a sealed container. During this time Bromine gas is produced and reabsorbed, this process turns the solution to a cloudy orange colour, then once the Bromine gas has been reabsorbed, the solution will have returned to a colourless state. At this point 1ml of the Ferroin solution can be added, which will turn the solution to a dark red colour, then under stirred conditions, an instantaneous bulk colour change to blue will occur, followed by a gradual return to the dark red colour.

In batch solutions, the chemical waves will originate from any location, and propagate through the entire solution until they annihilate with another wave, or reach the container boundary. In a stirred solution this colour change will be observed as an instantaneous colour change of the entire solution. When considering a cross-sectional plane, the propagation of the chemical wave will form the appearance of target patterns. This formation can be produced experimentally by reducing the volume of the batch solution such that it only covers the bottom of the container. This unstirred experiment can be considered a 'quasi-2D form of the batch solution experiment. For quasi-2D experiments, this volume of solution is then simply transferred to a standard 90mm diameter petri dish. For the experiments involving droplets of BZ solution, the oil phase is first created, by pouring 20ml of Oleic acid into the petri dish. The droplets are then pipetted onto the surface of the oil phase by hand. The droplets range in size from 50-100μl throughout the pilot studies, then settling on the use

of 50μl droplets for the systematic analysis of the electrotaxis behaviour of droplets, and the droplet-droplet synchronization study.

In the droplet-droplet synchronisation experiments, SDS was dissolved into the oleic acid to reduce the surface tension, and therefore the interfacial tension between the droplet and the oil phase. After experimentation, a concentration of 0.225g of SDS per litre of Oleic acid was chosen, with 0.9g SDS per litre of Oleic acid for the droplet division experiments. When preparing the solution in batch for the oil phase required for these experiments, it was paramount to routinely stir the solution to ensure the micelles remain in solution. After a waiting period, the SDS micelles would fall out of solution and settle at the bottom of the container storing the batch-prepared oil phase. This was not a problem during the experiments, due to the shallowness of the oil phase, and the presence of the aqueous droplet.

2.2 Electrode Design

The electrodes used for the pilot study were constructed from insulated wire, with no exposed wire submerged in the BZ solution. the submerged portion of the electrode measured 50mm in length and was affixed to the petri dish by bending the end to form an anchor, which was then secured to the dish with tape. Electrodes formed in a similar with exposed wire, measuring 10 mm, submerged within the BZ solutions were also used. The wires were placed with a separation of 70 mm tip to tip, within the solution. This, however, leads to an electrolysis reaction of the water used in the solutions, leading to the degradation and erosion of the wire along with the production of the unwanted substrate along with the production of gases and effervescent within the solution. Therefore, no further experiments were conducted in this manner.

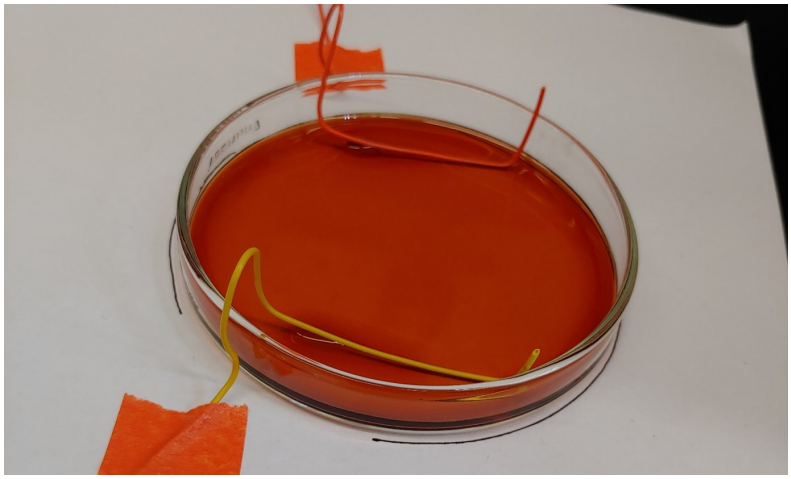

Figure 2.1: Construction of wire electrodes used in a pilot study on quasi-2D experimental design. The wire is insulated copper and is measured to the length of 30 mm of submerged wire. The submerged wire is supported by taping the wire down to the surface separate from the petri dish the reaction is performed within. The wires were inserted into the dish before adding the BZ solutions. As stated within the thesis, this design was adjusted to submerge the uninsulated tip within the solutions, with a length of 10 mm of wire. The wires were held at a separation of 70 mm, but these experiments were discontinued due to possible health hazards, as great amounts of substrate were formed within the solution, with large volumes of unknown gases being released from the reaction of the electrode with the BZ solutions.

For the systematic study, a pair of plate electrodes were constructed out of copper, with dimensions: 100 mm x 20 mm x 2 mm. The electrodes were connected to a Tenma 72-10505 lab bench power supply and were supported by 3D-printed braces to hold the plates in place throughout the duration of the experiment. The plate electrodes were positioned to be 90 mm apart, on either side of the petri dish. The decision to not submerge the electrodes was made to produce a more repeatable experiment with regard to the effect on breaking surface tension would have on the solution.

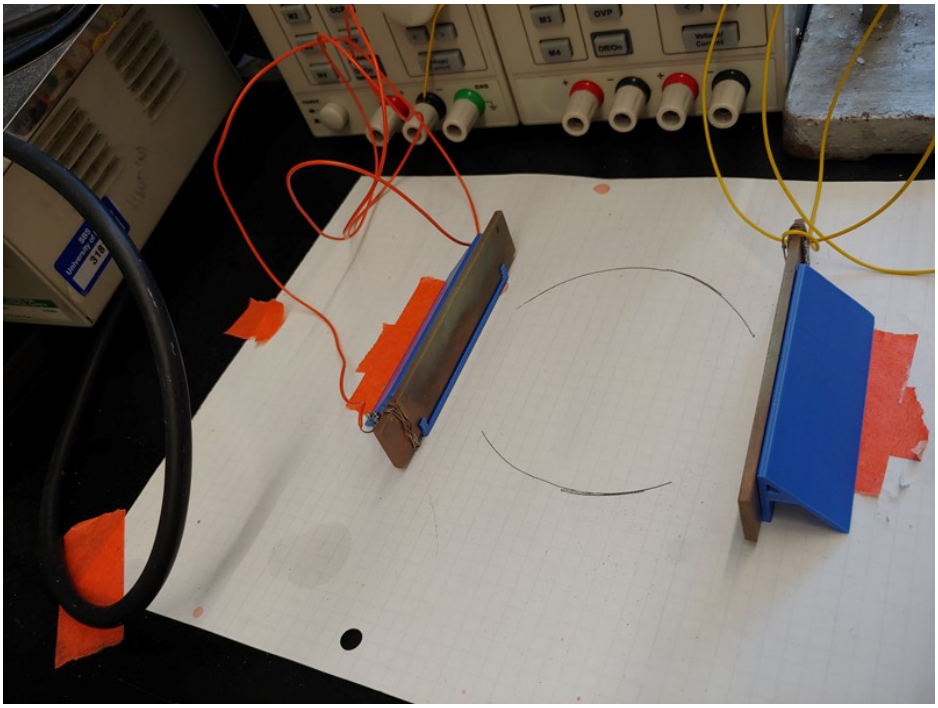

Figure 2.2: Plate electrodes fabricated from copper mounted external to the reaction vessel. Electrodes were fabricated from sheet copper with dimensions 100 mm x 20 mm x 2 mm. Copper wires were soldered to the plates to form a connection with the lab bench power supply (Tenma 72-10505). The electrodes were mounted using a 3D-printed bracket, which was subsequently supported to remain in position using tape.

For the pilot study, the voltage used ranged from 0V (no field applied) to 30V, with intervals of 5V. This corresponds to around 0.05V/mm, through to 0.3V/mm being applied across the petri dish.

2.3 Millifluidic Device

During the droplet-droplet synchronisation study, the droplets need to be anchored in place to maintain a constant distance of separation. To achieve this a millifluidic device was fabricated out of acrylic through a CNC process. The droplets' centre mass was anchored in place by a dimple in the array. Initially, 2 test devices were used to test the efficacy of the designs, 1 where the droplets centre of mass' are separated by 30mm, and the second has the same separation, with the addition of a 1mm deep channel between the 2 dimples. The device was able to be reused after experiments, as the acrylic can be cleaned easily.

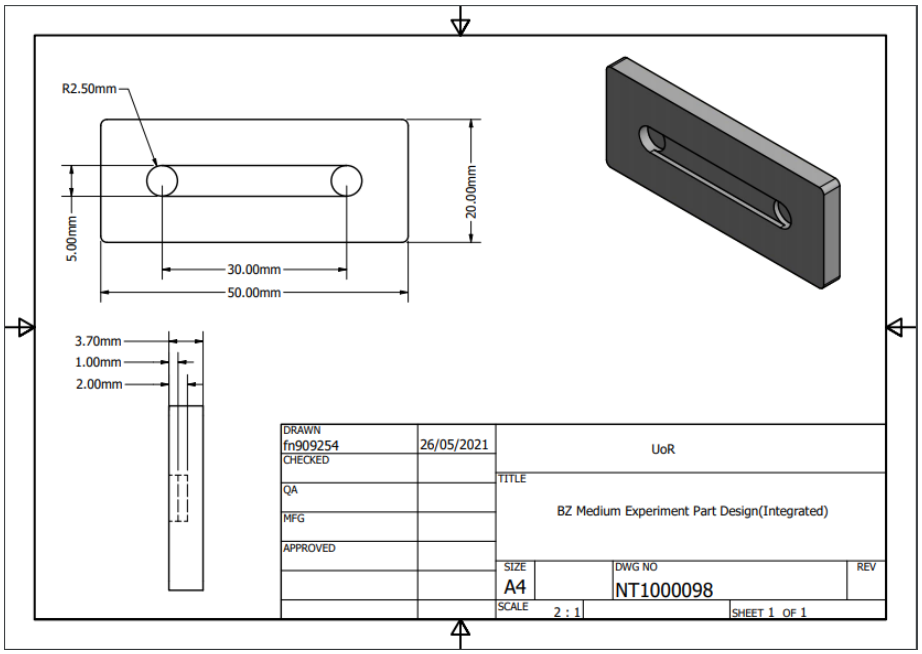

Figure 2.3: Schematic of millifluidic device showing the position and depth of channels and dimples used to anchor droplets in experiments studying droplet-to-droplet synchronization. The dimples had a diameter of 5 mm, and a depth of 2 mm. the channels measured a separation of 30 mm, with a depth of 20 mm. The device was fabricated using a machine CNC to mill the channels and dimples out of a sheet of acrylic plastic.

Fig.2.3 shows the schematic of the millifluidic device used to anchor the droplets. Shown in figure 2.3 is the device with the channel between the dimples.

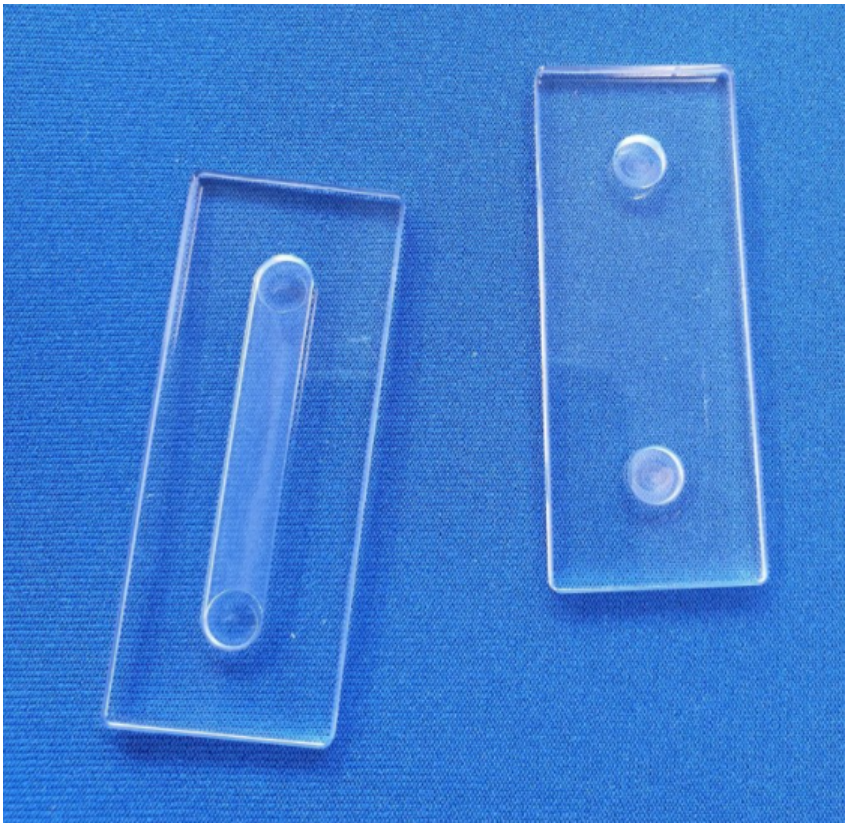

Figure 2.4: Millifluidic devices used in the pilot study of the droplet-to-droplet synchronization experiments. Shown within the figure is an example of the device with 2 dimples for the droplets to anchor to, along with the version containing a channel between the droplets. After repeated studies, it was found that the device with the channel would be used for systematic analysis of droplet communication. Subsequent devices were fabricated with the same length separation as initially tested, along with 10 mm, and 20 mm separation also.

2.4 Data Capture and Analysis

The chemical wave formation of the quasi-2D solution was captured using a Raspberry Pi computer module and a Raspberry Pi camera module. Time-lapse footage was created by capturing a still image every 10 seconds and stored on the computer's SD card.

The experiments concerning BZ droplets used a GoPro Hero 7 camera recording at 30 frames per second, then later a Nikon D7500 camera recording at 59.94 frames per second. The decision to start recording at a higher frame per second was made as it allowed the capture of the droplet's chemical wave dynamics to be captured in higher time resolution, along with the increase in pixel density and higher colour image quality allowing for more

accurate analysis of the wave formation to be completed. Recording with a higher number of frames per second also allows the translational motion and droplet deformation to also be more accurately captured and analysed.

To analyse the wave propagation speed in the quasi-2D study the time-lapse images are first read into the MATLAB programming environment. The location within the image where we observe the formation of a leading centre is obtained. The coordinates of this location are then programmed into a script which cycles through all of the images and stores the pixel value from the blue channel of the RGB image at the chosen location. This time series graph shows us the pixel intensity values through time and allows us to see the wave formation, as that location in the image changes from red(low blue pixel value) to blue(high blue pixel value). From here, we can calculate the time from peak to peak, to determine the oscillation period, and therefore the frequency of the wave generation.

Following on from this technique, using the same coordinate as before, we can take a 1x50 vector of pixels from the blue channel of the RGB of each frame of the image, then stitch them together to produce a type of space-time graph called a Kymograph [237]. The Kymograph gives us a visual representation of the wave formation through time and space.

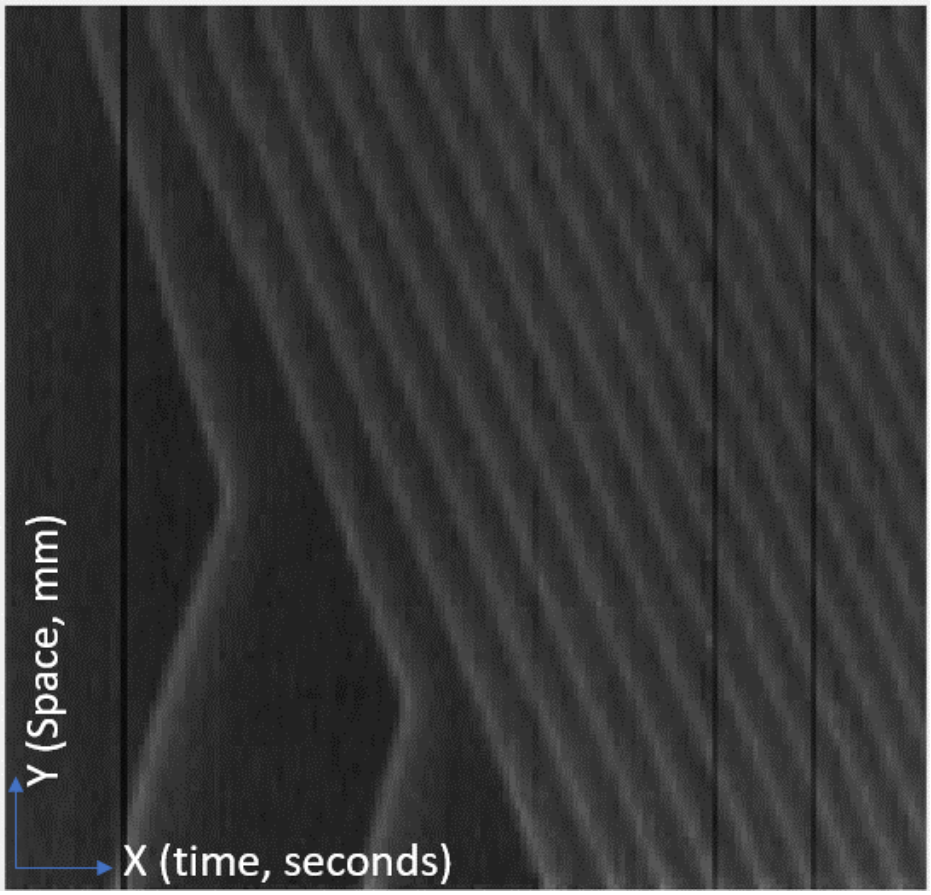

Figure 2.5: Kymograph showing wave formation as a function of time and space. The x-axis shows time, increasing from left to right, whilst the y-axis shows space, with the leading centre being located at the top of the image. It can be seen that another leading centre produces propagating waves, which are seen to annihilate upon contact with the waves from the first leading centre.

Fig.2.5 shows the wave generation through time and space. The wave speed can be calculated by finding the gradient of the line observed in the Kymograph. This process is repeated for each experiment, from each experimental condition. The results are then compared using box plots to easily see variation between experiments and the average wave speed observed.

To analyse the BZ droplets, the image is first segmented to only cover the region within the image where the droplet lies. This means only 1 droplet has to be analysed at a time which drastically lowers the big O notation of the software developed to analyse the images. It also reduces computational time as only a relatively small region of the image is required.

The next step involves a binarization of the image. The binarization process is dynamic

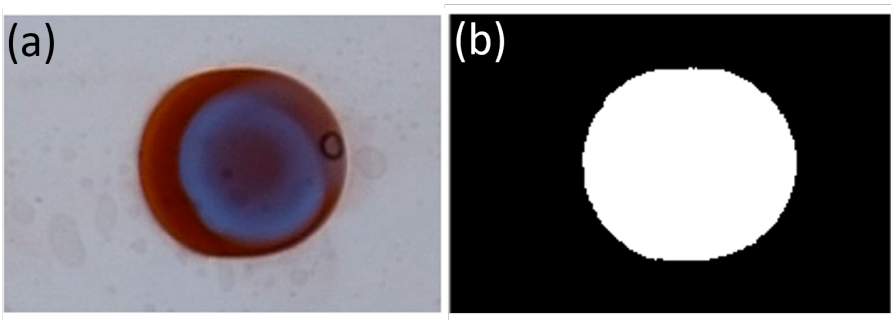

Figure 2.6: Presented within this figure is an example of the binarization of an image of a BZ droplet. the original image taken from a timelapse movie is shown in part (a), whereas the binarized image is shown in (b). The binarization process is carried out using thresholding of image values to determine the droplet, represented in white, and its background, represented in black. The process is performed sequentially across frames of a movie captured from the experiment. The source of constant back-lighting provides regular values for the background, allowing for the same thresholding values to be used throughout an entire experiment. The binarization gives information regarding the location within an image as to where the droplet is located, along with the size of its footprint, giving metrics about any shape deformation and elongation of the droplet.

throughout the course of the recording, as this allows for subtle changes in backlighting to be accounted for. To perform this the mean pixel value is found for the current frame, and then nested 'for' loops are used to perform a check on each pixel. If the value at this position is sufficiently lower than the mean value, the same position in a binary image is given the value '1', otherwise, the position remains a 0. The results from this process are shown in figure 2.6, where the segmented colour image is transformed into the binary image, showing the droplet in white, and the background in black.

Once the binarized image is obtained, the pixel locations in which the droplet lies can be found using the MATLAB command 'find', where the condition to be met is that the pixel value is equal to 1. The code to run this is written as such:

$$[y, x] = find(BinaryImage == 1);$$

This code will produce 2 vectors, one containing the y coordinates, and the other containing the x coordinates of the droplet's position within the image. The size of these arrays allows the study of droplet deformation, as the droplet does not undergo any volume changes, we can observe shape deformation form the minimum energy state by creating a time series

of the observed size through time. The coordinate list of the droplet's position in the image can be used to create a sub-image of the binarized droplet. This image can have the canny operator [238] applied to find the edge of the droplet. This information can then be used to calculate the perimeter length of the droplet, which can be used to study droplet deformation.

The vector lists of coordinates can also be used to generate the pixel locations of multiple droplets. The first coordinate pair is added to a new list, and then the program loops through the original list, adding any coordinate pair in which the Euclidean distance is less than or equal to $\sqrt{2}$. This coordinate pair is then added to the new list and removed from the original list. This process is repeated until a pass is made where no new coordinates are added. At this point the next unused coordinate is added to the beginning of a new list, to denote a new droplet's coordinates. This process is carried out until no new droplets are identified and the original coordinate list is empty.

The time series of the pixel intensity can be found by taking an average of a 5x5 grid of pixels from the droplet's centre mass. This point is found by finding the median values from the coordinate vectors. It can alternatively be programmed in at the start, where the point is manually selected. Through experimentation it is found that there is minimal difference in the data produced from sampling at either point, however for the analysis of time series data in the droplet-droplet synchronization experiments, the hard-coded value was used as it is a stable point to sample from. However, the centre mass calculation still found its use in tracking the droplets through space during the electrotaxis behaviour study.

Figure 2.7 shows the algorithm flowchart followed to track droplets through sequential imaging of the oscillating droplets. The colour image extracted from the video file is converted to grayscale using MATLAB's inbuilt function 'im2gray'. This will return a new binary image with the droplets isolated from the background, appearing as white circles on a black background. The pixel locations of the white pixels are then obtained using code: '[y, x] = find(BinaryImage == 1)', which returns an x, and y, array for the coordinates within the image where the droplets appear. The first coordinates are then added to a new profile list, which will contain all the coordinates of pixel locations displaying that droplet. The original

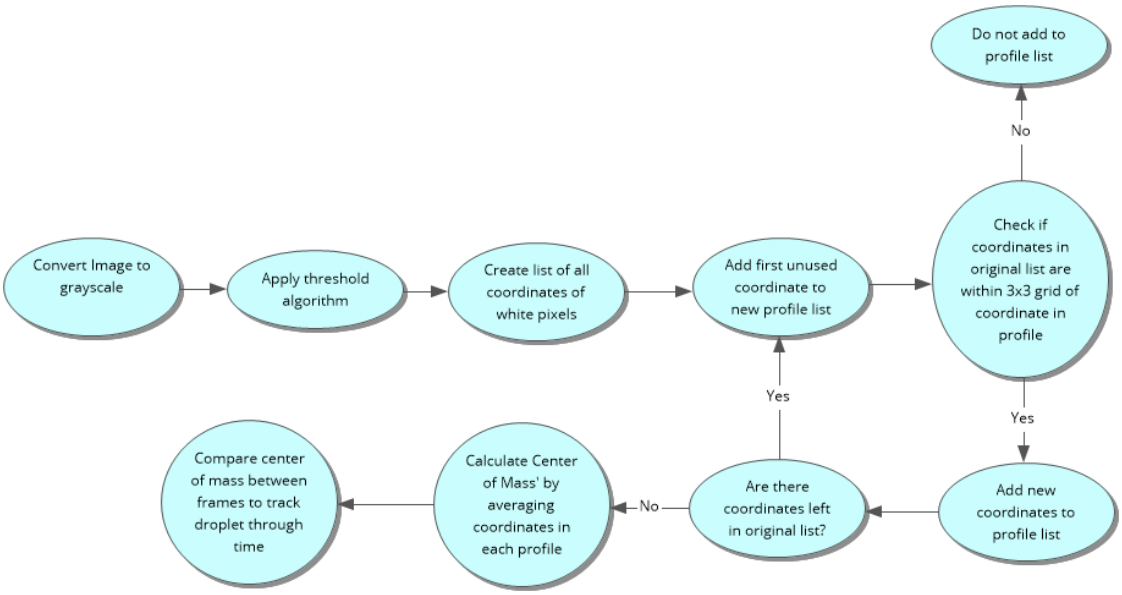

Figure 2.7: Flowchart depicting the algorithmic approach to extracting individual droplet locations, and centre of mass, from a time series image data set. The algorithm processes the colour image into a grayscale image before applying a pixel threshold to isolate the droplet from the background. This new image is then inspected and each white pixel location is added to a list. A new list is created with the first unused coordinates as the start point, called a profile list. Then, the original list is looped through, with each coordinate being compared to the current profile list, if the coordinate is within a 3x3 grid centred around a coordinate in the profile list, that set of coordinates is added to that profile. This process is repeated until no more coordinates are added to the profile, at which point the next unused coordinate from the original list is added to a new profile, and the previous loop is repeated. This is carried out until there are no unused coordinates within the original list. Once each droplet has been identified within the image, the centre of mass is calculated, by averaging the coordinates. This value is used in the tracking of droplets through time, as the subsequent frames will be subject to the same algorithm, and the centre of mass is used to align each droplet frame by frame.

list is looped through, comparing the distance to each coordinate in the profile list, if this distance is within a 3x3 grid centred around the coordinates within the list, the new list is updated to include this coordinate. The original list is then continued to be looped through until no new coordinates are added to the current profile, at which point the next unused coordinate is added to a new profile, where the previous cycle is repeated until there are no new coordinates to assign. Each profile is then averaged to determine the droplet centre of mass(CoM), which will then be compared to CoMs from the next frame, where the closely related CoMs will be matched up, to track the droplet's positions through time.

Chapter 3

Electrotaxis Behaviour of Droplets Composed of Aqueous Belousov-Zhabotinsky Solutions Suspended in Oil Phase

3.1 Abstract

Taxis is ubiquitous in biological and physical chemistry systems as a response to various external stimulations. We prepared aqueous droplets containing Belousov-Zhabotinsky (BZ) solutions suspended on an oleic acid oil phase subject to DC electric field and found that these BZ droplets undergo chemically driven translational motion towards the negative electrode under DC electric field. This electrotaxis phenomenon originates from the field-induced inhomogeneous distribution of reactants, in particular Br^- ions, and consequently the biased location of the leading centers towards the positive electrode. We define the 'Leading center' (LC), where the BZ chemical wave (target pattern) is initiated within a whole droplet at a specific location within the droplet. The chemical wave generated from the LC propagates passing the droplet center of mass and creates a gradient of interfacial tension when reaching the droplet-oil interface on the other side, resulting in a momentum exchange between the droplet and oil phases which drives the droplet motion in the direction of the electric field. A

greater electric field strength renders a more substantial electrotaxis effect.

3.2 Introduction

The study of taxis phenomena has attracted a lot of interest in the field of biology and physical chemistry, demonstrating the minimum or primitive form of intelligence. All living systems can sense external stimulations, process information, make an appropriate reaction, or show adaptive behavior.

Many biological systems exhibit taxis as a response to environmental changes [239, 240]. For example, organisms like *E. coli* have demonstrated chemotaxis phenomenon by changing their moving trajectories in response to a detectable chemical gradient[241]. Similarly, the chemotaxis mechanism was utilized to guide immune cells to reach infection sites, allowing wounds to heal [242]. Magnetotaxis and electrotaxis phenomena were also observed in various bacteria. Magnetotactic bacteria can align their cell orientations with the magnetic field of the planet Earth[243], while electric fields can induce curved growth of Enterobacter cloacae and Escherichia coli cells, which can rapidly curve towards the cathode in the post-division state, with a higher growth rate at the cell ends facing the anode than the ends facing the cathode[244]. The electrotaxis of Paramecium cells can be attributed to the depolarization of ionic species within the cell, leading to a torque orienting the body towards the cathode. A physical model was developed to describe their galvanotaxis by linking their microscopic ciliary motion with the macroscopic behavior [245].

On the other hand, chemotaxis has been studied in physical chemistry systems as they can give an insight into how an artificial system can be used to represent or understand complex biological behaviors [246]. For example, chemotaxis of chemotactic droplets containing an organic solvent and 2-hexyldecanoic acid has been used to solve a constructed maze, where the motion of the droplets was driven by a pH gradient within the maze[247]. In a related work, Čejková *et al.* found that a gradient in salt concentration could drive translational motion of alcohol droplets in an aqueous solution of sodium decanoate [248]. Manipulation of the motion of a mercury droplet submerged in a conductive liquid medium by using a direct electric field was studied by Hollo *et al.* [249]. The electric potential drop across the droplet

was found to generate Marangoni flow within the liquid which drives the droplet to move towards the cathode. The moving velocity of the droplet is proportional to the electric current density. They also showed that the droplet motion direction can be further manipulated by changing the conductivity of the liquid medium.

Kitahata *et al.* proposed a mechanism of hydrodynamics coupled with chemical reaction to explain the translational motion of water droplets in an alcohol phase where the Marangoni effect is responsible for the droplet drifting [250]. In another work, the collective behavior of artificial squirmers was investigated for understanding large scale biological pattern formation[251].

The Belousov-Zhabotinsky (BZ) reaction is a well-studied non-equilibrium reaction-diffusion process demonstrating unusual oscillatory properties[252, 169]. It involves the oxidation of malonic acid to carbon dioxide by bromate ions in the presence of transition metal catalyst, such as Ferroin solution. The BZ reaction can be described by the Field–Körös–Noyes (FKN) mechanism which consists of three competing processes and was theoretically described by the Oregonator model.[171, 253] Processes A and B form an inorganic subsystem of the BZ reaction and function as a so-called chemical clock. Process (A) acts as a long induction period that involves the consumption of Br^- ions by multiple reactions. In Process B, increased production of $HBrO_3$ occurs followed by the oxidation of the ferroin solution. This is followed by Process C, which acts as the reset for the chemical clock. This reset causes the reduction of ferroin and bromide ions produced in greater quantities again, which leads to the dominance of the reactions governing Process A. The type of process in which the solution alternates from the reduced state to the oxidized state is known as a redox reaction. The oxidation process can be visualized by the colour change of the metal catalyst from red (reduced) to blue (oxidized). The BZ reaction produces target wave patterns in quasi-2D systems [254, 255], which have long been studied for their nonlinear dynamics [256, 257]. For example, when an aqueous BZ solution is contained in a shallow dish, chemical waves are generated at locations called leading centers (LCs) which can be produced at any location within the droplet, and propagate towards the edge of the dish [258, 259]. The formation of the LCs and subsequent wave propagation are typically of an unpredictable nature, but can be manipulated by external interference, such as application of external electric field as studied

in the current work.

Previous experimental works have shown that adjusting the concentration of metal catalyst, e.g., Ferroin, can alter the propagating speed of the chemical wave through the BZ solution [193]. Such adjustment in catalyst concentration was also shown to impact the beating frequency, amplitude, and wave count, where the study of wave propagation along the arrays of contacted BZ droplets formed in oil phase was conducted [195]. On the other hand, Steinbock *et al.* found that the oscillatory dynamics of BZ droplets depends on the size of the droplets [260].

Studies on the effect of external electric or magnetic fields on chemical wave generation and propagation in quasi-2D BZ solutions, and BZ droplets suspended in an oil phase have led to the discovery of taxis of BZ droplets.

Agladze *et al.* showed that applying an electric field to gels containing BZ solutions can increase the propagation speed of the spiral waves within the gel. [200]. Blank *et al.* reported that low-frequency electromagnetic fields can accelerate the BZ reaction, and consequently the wave travelling speed [261, 262]. It was also found that modulation of externally applied electric potential could alter the dynamic state of BZ microbeads from global oscillation to travelling waves or vice versa [263]. Furthermore, Okano *et al.* showed that application of a static magnetic field can also increase the wave propagation speed in quasi-2D BZ solution [264].

Another interesting taxis phenomenon is the phototaxis of Ruthenium catalysed droplets containing BZ solutions in the presence a spatial gradient of light intensity [232, 265]. These droplets undergo translational motion due to the phototactic effect, but no local switchback was observed. They can be even fixed in place if being exposed to a light source right after the chemically driven translational motion [232]. The motion of the phototactic BZ droplets can guided by using computer vision software to track and applying spatial gradient of illumination to alter their moving direction. It was discovered that these droplets could follow a predetermined path guided by updating a control box each second [265].

In this study, we investigated the electrotaxis behavior of BZ droplets with varied Ferroin

concentrations suspended in an oil phase under the effect of electric fields of differing strength. We focus on analysing the field-induced inhomogeneous distribution of the leading center locations and the resulted translational motion of the droplets in parallel to the electric field. The magnitude of the electrotaxis effect was found to increase with the electric field strength. To the best of our knowledge, this is the first experimental demonstration of electrotaxis of BZ droplets. The physical mechanism of using electric field to manipulate the direction of motion of self-propelled BZ droplets is of fundamental difference from the photochemical mechanism underlying the photo illumination method used to control the motion of photosensitive BZ droplets [232, 265]. The electrotaxis of BZ droplets can find potential applications in biological environments and confined systems where a light source is hard to apply, and also call for new theoretical model descriptions.

3.3 Methods

The solutions were prepared by mixing 2 ml sulfuric acid(H_2SO_4) with 10 g sodium bromate ($NaBrO_3$) in 67 ml H_2O, to produce *Solution A*. 1 g malonic acid ($CH_2(COOH)_2$) was dissolved into 10 ml H_2O to produce *Solution B*. Then 1 g sodium bromide(NaBr) was dissolved in 10 ml H_2O to produce *Solution C*. All the lab-grade chemicals were bought from Sigma-Aldrich and Thermo-Fisher.

The reaction was initiated by mixing a solution containing 6 ml of *Solution A*, 1 ml of *Solution B* and 0.5 ml of *Solution C*. Upon mixing the three solutions, the mixture turned into a cloudy orange colour due to Bromine gas being released. This solution was then left for a period of up to 5 minutes to allow for the re-absorption of the Bromine. Once the solution returned to a colourless state, 1 ml of Ferroin solution was added.

A single BZ droplet of volume in the range of 25 to 100 μl was then pipetted onto the oil phase of oleic acid in a 90 mm diameter petri dish where its images and moving trajectories were recorded to investigate the chemically driven translational motion. We have studied the electrotaxis effects of droplets with volumes 25μl, 50μl, 75μl and 100μl, respectively. For each droplet size, a total number of 60-100 droplets were generated and tested. In droplets of larger sizes (75μl and 100μl), there are typically multiple leading centers co-existing within their bodies which are formed at different locations and different moments. The chemical

waves originated from these LCs are out of phase by different degrees and thus interfere with each other. The integrated driving forces acting on these relatively large droplets did not lead to translational displacements as significant as those observed in the droplets of 50μl size over the electric field strength range studied in this work. On the other hand, the dimensions of the 25μl droplets are comparable to the wavelength of the BZ waves, leaving little space for wave propagation. These small droplets are thus not suitable for observing electrotaxis effect. For these reasons, we have chosen to use the 50μl droplets in the current work. The diameter of the 50μl droplets was measured to be 5mm.

The motion of the BZ droplet was recorded, using a Nikon D7500 camera recording at 60 frames per second for 30 minutes. The images were analysed to track the droplet positions over time. A pixel grouping algorithm was applied to detect individual droplets and track their moving trajectories between consecutive images. The LC locations within the droplet were also recorded. As a reference experiment, the translational motion of the droplets in absence of electric stimulation was recorded. This allows comparison between droplets under electric field effect and droplets without electric field effect. As the droplets will continue to produce chemical waves from the same leading center, each data point collected is from a new droplet.

Initial experiments were conducted to determine the impact that the concentration of Ferroin has on the electrotaxis effect. These experiments were carried out by recording the chemically induced translational motion of droplets subjected to either a 30V electric field application, or no electric field application, with the concentration of Ferroin varying from 15 mM to 35 mM.

To apply the external electric field, a DC field (1.1 - 3.3 V/cm) was applied across the petri dish. The electric field was generated by placing a plate electrode at either end of the petri dish. Figure 3.1 shows the arrangement of the electrodes at each side of the reaction vessel, a petri dish with a diameter of 90 mm, with a voltage range of 10 V to 30 V and a current of 3 A applied by a Tenma 72-10505 lab bench power supply. The electrodes were made of copper and have dimensions of 100 mm x 20 mm x 2 mm. For both sets of experiments, the droplets within the experimental system were recorded for 30 minutes at room temperature.

The 3D droplets were recorded top-down using the camera to produce a 2D representation of the experiment to be analysed in MATLAB later. The visual images of the BZ droplets were taken to include the center of mass of the droplet, which was calculated using the image

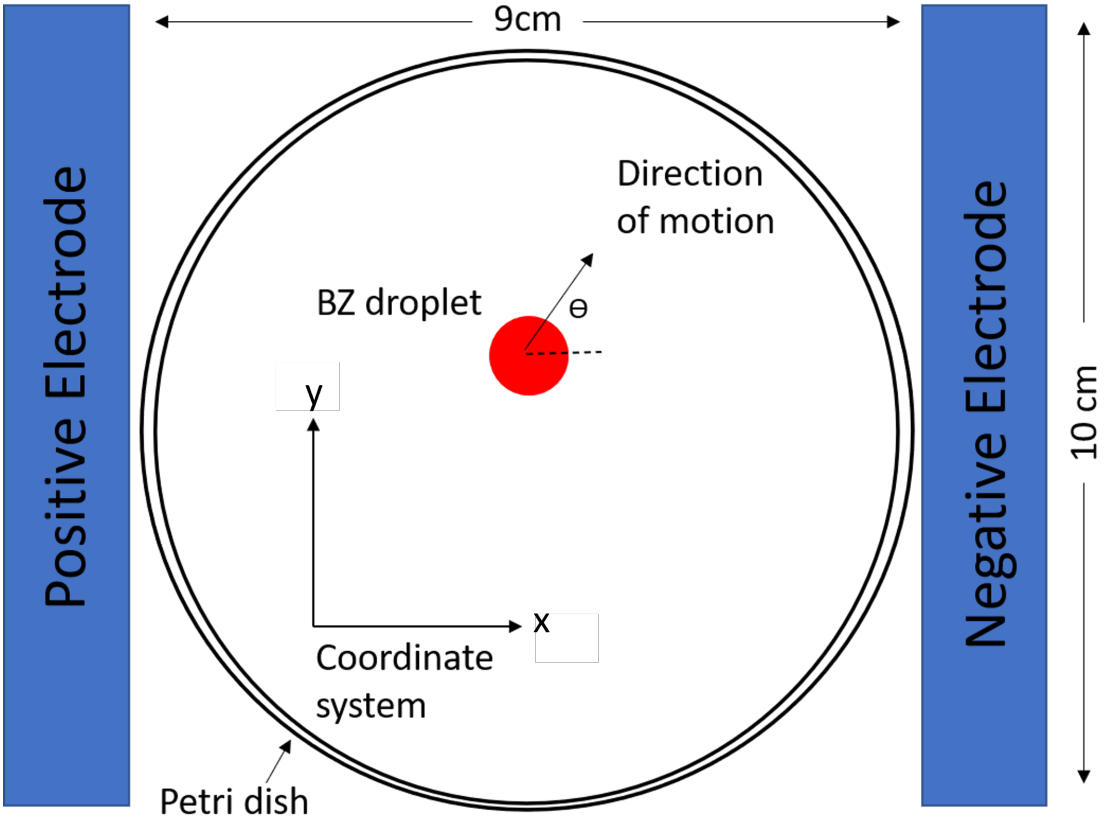

Figure 3.1: Schematics of the reaction vessel with plate electrodes from top down. The x-y coordinate frame is shown. The red circle represents a moving BZ droplet, with an arrow showing its direction of translational motion. The angle θ shows the angle to the coaxial of the electric field in which the droplet travels. The electric field was applied in strength range 1.1 - 3.3 V/cm from the left to the right

.

analysis tool developed by our team. The colour changes were analysed in the blue channel of an RGB image. To analyse the motion of the droplets, the x-y coordinate system was defined with the y-axis spanning the coaxial line of the electric field lines. The angle θ, which measures the direction of the self-propelled droplets with respect to the y-axis, was calculated from the recorded images. The decision to align the y-axis along the coaxial to the externally applied electric field was because we will have a distribution of angles around 0°, rather than 90°, or 270°.

The location of the LC formation within the droplets were extracted and projected onto a circle representing the droplet (see fig. 3.7) to show the distribution of the formations across multiple experiments.

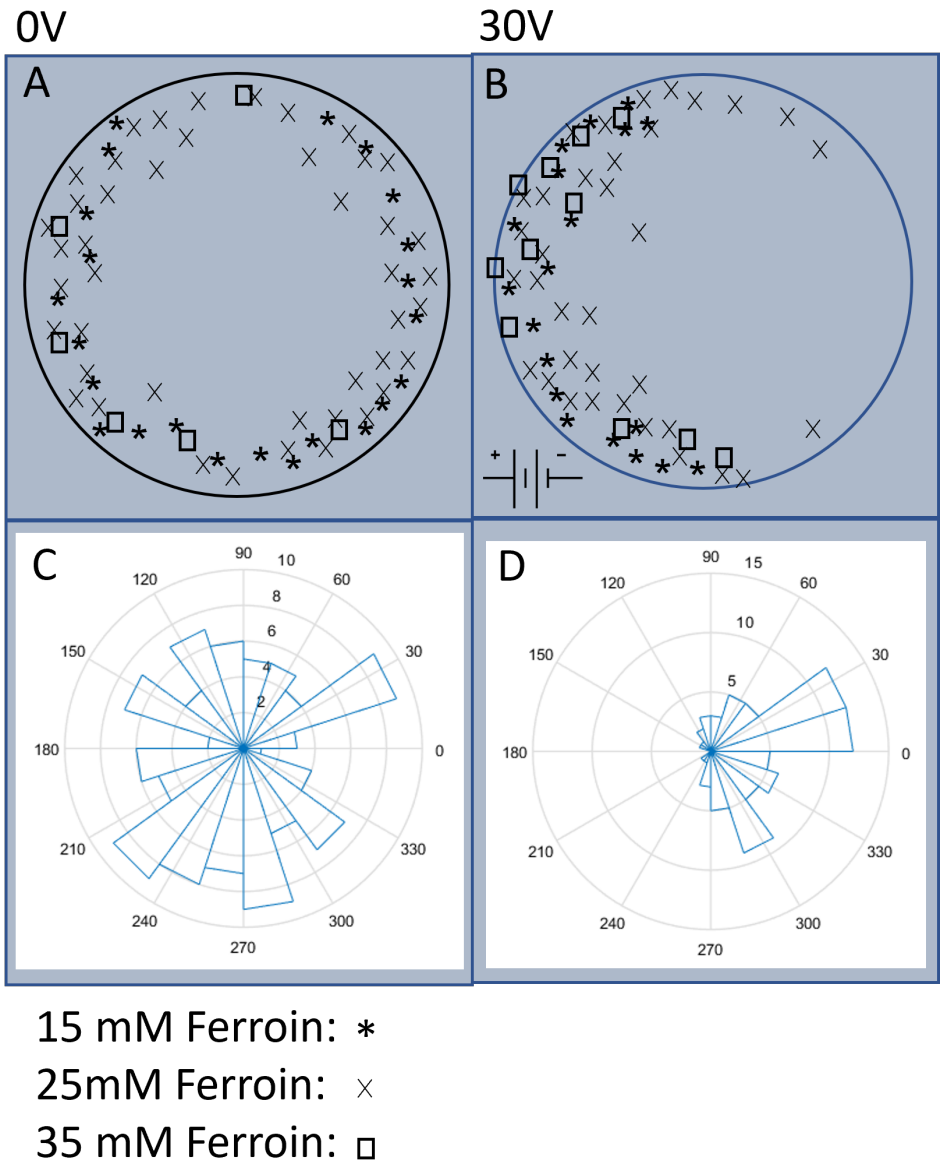

Figure 3.2: (A-B) Distribution of the leading centers within an aqueous droplet under the application of an external DC electric field with strength 3.3V/cm, applied from left to right, as denoted by the symbol in the lower left. (B), and for the control case with no external field applied (A). Experiment data obtained from droplets containing Ferroin concentrations of 15 mM, 25 mM and 35 mM are shown with asterisk (*), cross (x) and open square symbols, respectively. (C-D) Circular histogram of the traveling angle of chemically driven translational motion of BZ droplets. The electric field was applied with the positive electrode on the left, and the negative electrode on the right. The field-induced biased distribution of LC formation in favour of the positive electrode is prominent when comparing (B) with (A). The data also shows that the taxis effect is insensitive to the Ferroin concentration. Data points were collected from 147 different droplets.

Experiments have also been performed in a pilot study to examine if the concentration of Ferroin has an impact on the electrotaxis effect of the BZ droplets. Data sets obtained

using three different Ferroin concentrations (15, 25 and 35mM) are presented in Figure 3.2 which show no significant difference. We thus chose a Ferroin concentration of 25 mM for the remaining part of the study.

3.4 Results

As described in the Experimental Methods section, the BZ droplets we studied are submerged in the oil phase contained in a petri dish. We tracked their trajectories individually and quantified their moving directions as well as the locations of the leading centers formed within the droplets. The bottom of the petri dish has a convex shape with the middle slightly thicker than the edges. The droplets thus have a trend of slowly drifting towards the edge under gravity, see Supplementary Information. Such drifting behavior is interrupted by the electrotaxis effect when a chemical wave is generated from the leading center (LC) formed inside a droplet and propagates across its body, which induces a translational motion of the droplet along the electric field direction. Once the chemical wave ceases, the drifting motion due to gravity resumes. Our analysis of the electrotaxis effect is thus focused on the trajectories within the time window, where a chemical wave is generated and propagating across the body of the BZ droplet.

The drifting can be attributed to the liquid droplet sedimenting within the oil phase. The sedimentation velocity can be calculated using the Stokes formula based on gravity. The sedimentation velocity is calculated based on the droplet being subject to 3 forces: The gravitational force pointing downwards, the buoyant force pointing upwards, and the Stokes' drag force pointing upwards.

The gravitational force is calculated using:

$$F_g = mg$$

Where m is the mass of the droplet, and g is the acceleration due to gravity.

The buoyant force is calculated using:

$$F_b = \rho_a * V_d * g$$

The Stokes' drag force is calculated using:

$$F_d = 6\pi * \mu * R * v$$

Where ρ_d is the density of the BZ droplet equal to 1 g/ml, V_d is the volume of the droplet, R is the radius of the droplet, g is the acceleration due to gravity and is equal to $9.8m/s^2$, ρ_a is the density of the Oleic acid equal to 0.895 g/mL, μ is the dynamic viscosity of the Oleic acid equal to 40 mPas, and v is the sedimentation velocity.

When we neglect inertia, the force balance produces the following equation:

$$F_g = F_b + F_d$$

Which is equal to:

$$\rho_d V_d * g = \rho_a * V_d * g + 6\pi * \mu * R * v$$

This can be re-written in terms of the sedimentation velocity, v:

$$v = (\rho_d - \rho_a) * V_d * g / 6\pi * \mu * R$$

Which simplifies to:

$$v = (2/9) * (\rho_d - \rho_a) * R^2 * g/\mu$$

Which produces a sedimentation velocity of 0.0357 mm/s

One example moving trajectory of a BZ droplet under an external electric field is shown in Figure 3.3. The DC field is applied using plate electrodes external to the droplet, represented with a sketch in the top right corner of the figure. The coordinate of the center of mass

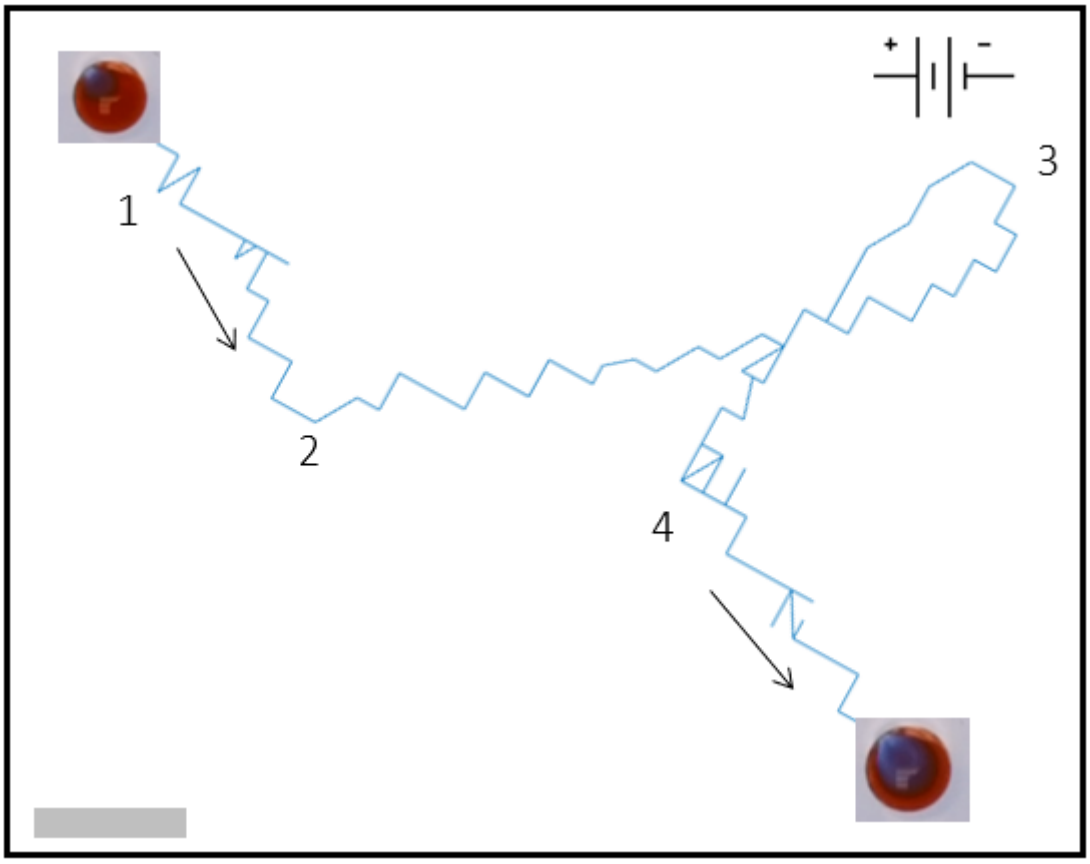

Figure 3.3: Trajectory of a BZ droplet moving under a DC electric field directed horizontally from left to right, see the setup sketched in the top right corner. The droplet initially drifts along a path diagonally across the figure, as indicated by the black arrow with Label 1, but undergoes a chemically-driven translational motion from Point 2 to Point 3 in accordance with the direction of the electric field and also chemical wave propagation across the droplet body. After that, its trajectory shows a partial reset with the droplet moving back from Point 3 towards Point 2, but does not reach there. Due to the cessation of the chemical wave propagation, the droplet resumes its original drifting in the direction marked by the arrow with Label 4. The video clip recording this trajectory can be found in the SI. The scale bar at the lower-left corner represents 1 mm of the droplet trajectory.

(CoM) of the droplet was extracted from the time-lapse images, as the droplet drifts across the oil phase. The initial drifting of the droplet in the circular petri dish with convex shaped bottom is roughly along the radial direction towards its edge. In Figure 3.3, for convenience of demonstration, the coordinates of the experimental system have been rotated so that the electric field is directed horizontally from left to right. The initial drifting direction of the droplet turns out to be roughly along the diagonal line of the figure, as shown by the arrow with Label 1, which is interrupted when the chemical wave generated from a LC propagates across the droplet. This leads to the chemically-driven translational motion of the droplet in the direction of the applied field, see the trajectory from Point 2 to Point 3. After that, the trajectory shows a local switchback by moving back towards the onset point of the translational motion but does not fully return to Point 2. Due to inertia and hydrodynamic effects, the back-turn of the droplet does not happen sharply but goes through a small looping path about Point 3. After the wave propagation ceases, the droplet resumes its drifting behavior along the initial direction, as indicated by the arrow marked with Label 4. We note that the trajectory contains some small discrepancies in the droplet's position due to subtle noise picked up when analysing the timelapse footage, which is represented by the aberrations away from pure vectorial motion.

Figure 3.4 (A) shows the temporal and spatial propagation of the chemical wave across a single droplet in the presence of an electric field. This space-time image, known as a kymograph, was created by taking thin diametric segments coaxial to the electric field from the droplet images recorded at a frequency of 5 Hz over a 100-second window and stacking them downwards along the ordinate axis. The redox process and associated chemical wave propagation can be visualized from the colour changes in the kymograph. The displacement of the droplet along the horizontal (electric field) direction can be deduced from the spatial location of the segment along the abscissa axis. Sampled images of the entire droplet taken 10 seconds apart are given in Figure 3.4 (B). The motion of the droplet before and after the chemical wave propagation (and corresponding chemically driven translational motion) was the slow drifting towards the edge of the petri dish. This drifting is overcome by the chemically induced translational motion which alters the moving direction and trajectory of the droplet until the chemical wave ceases.

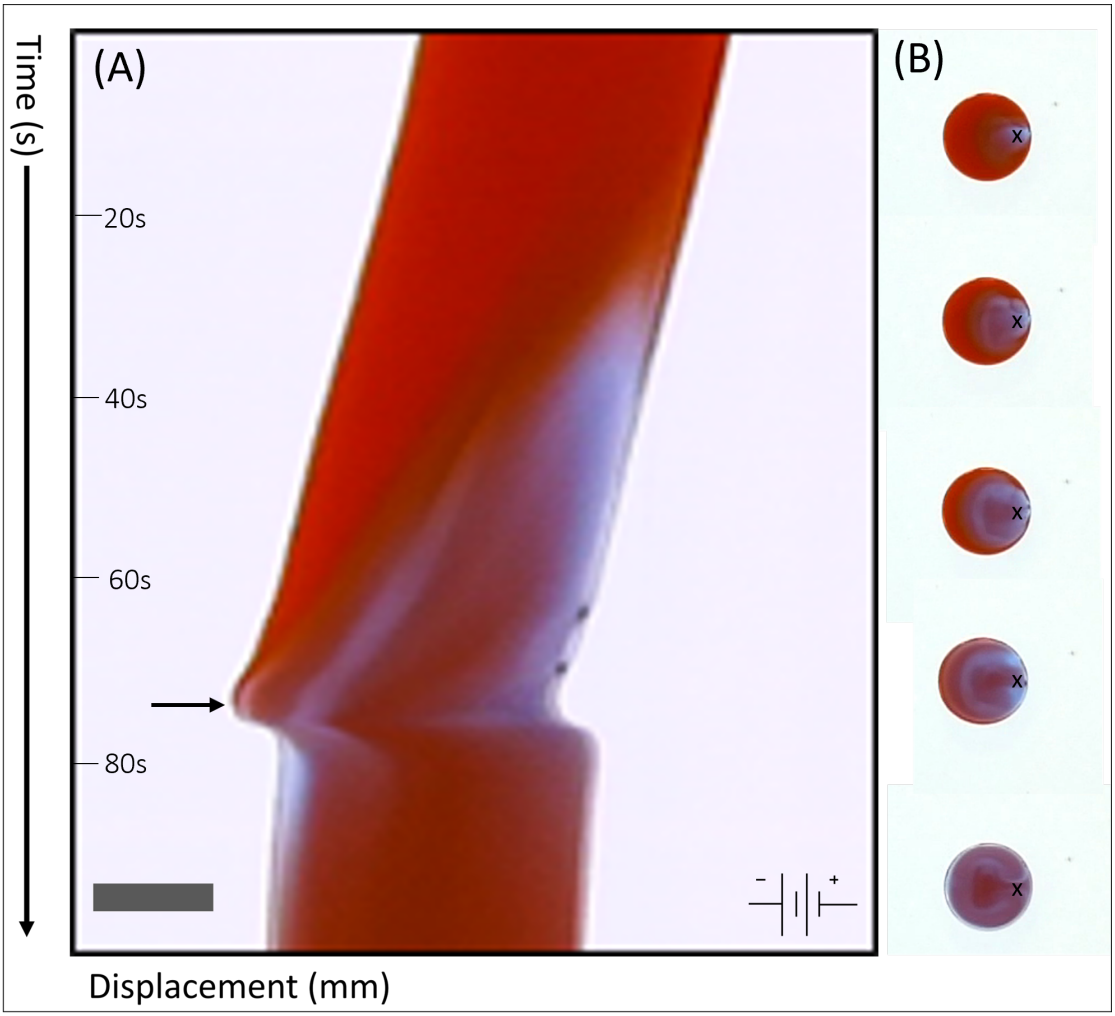

Figure 3.4: (A) Kymograph demonstrating the spatial and temporal pattern of chemical wave propagation in a BZ droplet in the presence of external electric field, see details in the main text. The electric field is in horizontal direction pointing to the left. The scale bar represents 2 mm. The total time duration was 100 seconds. The peak displacement of the droplet is marked with an arrow.
(B) Time-lapse images of the entire droplet taken 10 s apart. The location of the leading center is marked with an 'x'. The wave propagation can be seen from the colour changes in the images.

In connection with the droplet trajectory shown in Figure 3.3, we can also see in Figure 3.4 (A) that the color of the entire segment remains roughly homogeneous and unchanged during the initial drifting process until a leading center appears at its right-hand-side (rhs) side, see also the droplet image on the top of 3.4 (B). The preferred location of the LC under the external electric field will be discussed in more detail below. A wave of oxidized Ferroin is generated from the LC and propagates towards the other side of the droplet. When it approaches the droplet-oil interface, the droplet undergoes a fast translational motion, which is driven by the flow induced by the Marangoni stress generated by the gradient of interfacial tension between the two phases in response to the chemical wave.

In figures 3.4 and 3.5 the peak displacement of the droplet is marked with an arrow. The colour change in the droplet as it undergoes translational motion can be pictured in the Kymograph in figure 3.4 (A), and is supported by the graph of droplet displacement, and colour change in figure 3.5 (C) and (D).

To quantify the chemically induced translational motion of the droplets, we extracted the center of mass positions of the droplets using image processing within the MATLAB environment and stored them in time series data sets. Figure 3.5(A-C) show the average displacements of the droplets undergoing translational motion at DC field strengths 10 V, 20 V, and 30 V, respectively. In each case, the results were obtained by averaging over 10-15 independently measured data sets after shifting their peak positions to the same reference time point. The error bars reflect the standard deviations in the data sets calculated at 10 second intervals using statistical tests. For convenience of comparison, the locations of the displacement peaks in Panels (A-C) are also aligned with each other. With the increase of the electric field strength, both the growth and decay rates of the displacement curves around their peaks, corresponding to the average velocities of the droplets moving along and against the electric field direction, show increments. For example, the average velocity moving along the field direction increases from 0.14 mm/s at 10 V to 0.28 mm/s at 30 V, and the average velocity moving against the field direction changes from –0.23 mm/s at 10 V to –0.48 mm/s at 30V. The peak or maximum translational displacement also increases from 1.82 mm at 10

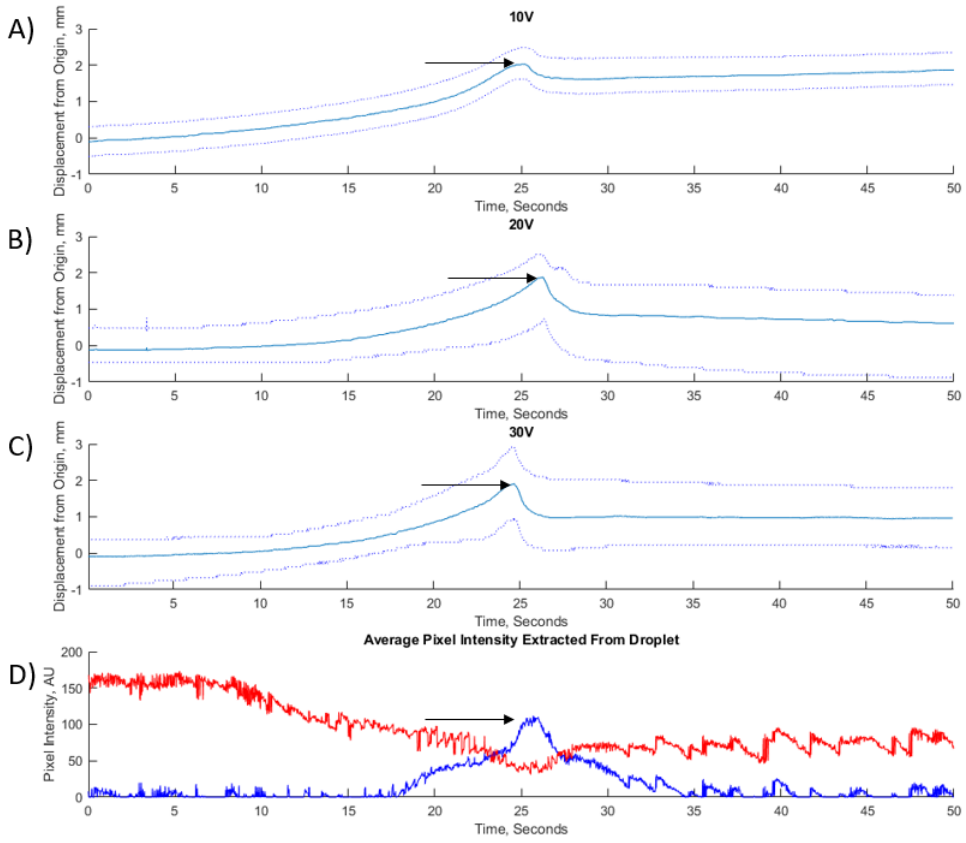

Figure 3.5: (A-C) Error envelopes showing average droplet displacement as a function of time from droplets subject to DC fields with strengths 10V, 20V and 30V, respectively. All curves were averaged over 10 - 15 sample data sets by shifting their peak displacements to the same reference time, and the error bars represent the standard deviations in the data sets. (D) Average pixel intensity values for the red and blue channels of the droplet RGB images. The chemical wave propagates across the droplet driving it to undergo translational motion under 30V DC field. The peak displacement of the droplet on each graph is marked with an arrow.

V to 2.1 mm at 30 V.

The decrease in the displacement value after the peak reflects the local switchback of the droplet position, which happens at a higher speed than the growth of the displacement. The non-zero plateau value at longer times indicates that the droplet does not fully return to its original position at the onset of the chemically-driven translational motion, in consistence with Figures 3.3 and 3.4. The magnitude of the switchback displacement also shows a larger amplitude at higher field strength. The enhanced translational and switchback motions with increasing field strength can be related to the closer proximity of the lead centers formed at higher field strength to the edge of the droplets, as will be discussed below. We should note that the field-strength dependent effects observed in Figure 3.5(A-C) are still within the statistical errors of our measurements. Further studies using a wider range of electric field strengths and larger number of samples are still needed to build up quantitative relationships between the velocity of translational motion as a function of the field strength.

A small sample of BZ solution undergoing homogeneous redox process will change its colour periodically from red (reduced state of Ferroin) to light blue (oxidized state of Ferroin). However, in the BZ droplet of millimeter size, the redox process and colour transition do not occur homogeneously or instantaneously across the entire droplet. Instead, the chemical wave is generated from a LC where the oxidation of Ferroin begins and propagation within the droplet, see Figure 3.4. The wave generation and propagation process can be quantified by the time-dependent red and blue pixel intensity values inside the droplets, as shown in Figure 3.5(D) for the droplets studied in Figure 3.5(C). These data were collected by defining a 9×9 grid centered around the CoM of each droplet and averaging the pixel intensity values from the red and blue channels of their RGB images over the same time window at in (C). The red pixel value decreases as the blue value increases, representing the oxidation process where the droplets color changes from red to blue. The maximum of the blue pixel intensity is reached when the chemical wave has propagated across the entire droplet and so the droplet is in the maximum oxidation state. The simultaneous occurrence of this oxidation peak value with the maximum droplet displacement shown in Figure 3.5(C) supports the physical picture that the electrotaxis of BZ droplet is driven by the chemical wave propagation and the resulted

gradient in the interfacial tension between the droplet and oil phases. The decay in the red values is found to occur prior to the growth in the blue values, and both the decay and growth processes of the red pixel values take much longer times to return to the pre-oscillation levels than the blue values. These results are consistent with the fast oxidation and slow reduction observed in BZ solutions. A lingering blue colour remains for a short time after the translational motion has ceased.

The switchback of the moving trajectory takes place when the oxidized chemical wave starts to cease after reaching the droplet-oil interface on the opposite side of the droplet and the Ferroin begins to return to the reduced state, see Fig.3.4. The changes in the wave propagation status and Ferroin redox state effectively reverse the gradient of the interfacial tension across the droplet, generating a momentum transfer in the opposite direction to the wave propagation direction and consequently a reversed moving direction of the droplet [230, 231].

In order to directly find the correlation between the location of the LCs and the direction of the chemically driven translation motion of the droplet, we calculated the travelling angle θ of the droplet in the 2D coordinate system defined in Fig. 3.6 (A) where the origin is at the CoM of the droplet and the x-axis is along the vector pointing from the CoM to the LC location, which is in the opposite direction of the wave propagation. Fig. 3.6 (B) presents the circular histogram of the angle θ between the translation motion direction and the x-axis in cases both with and without external field. The results show clearly that θ is centered around 180°, indicating that the direction of the chemically driven translational motion is indeed determined by the location of the LC and pointing from the LC to the CoM of the droplet. This is well consistent with Fig.3.7, i.e., the direction of translation motion is guided by the wave propagation from the LC.

Since the locations of the leading centers determine the chemical wave generation/propagation process and consequently translational motion of the droplets, we carried out a systematic study of the effect of electric field strength on the spatial distributions of the LCs. Fig.3.7(A-D) show the results collected from 163 independent experiments and superimposed

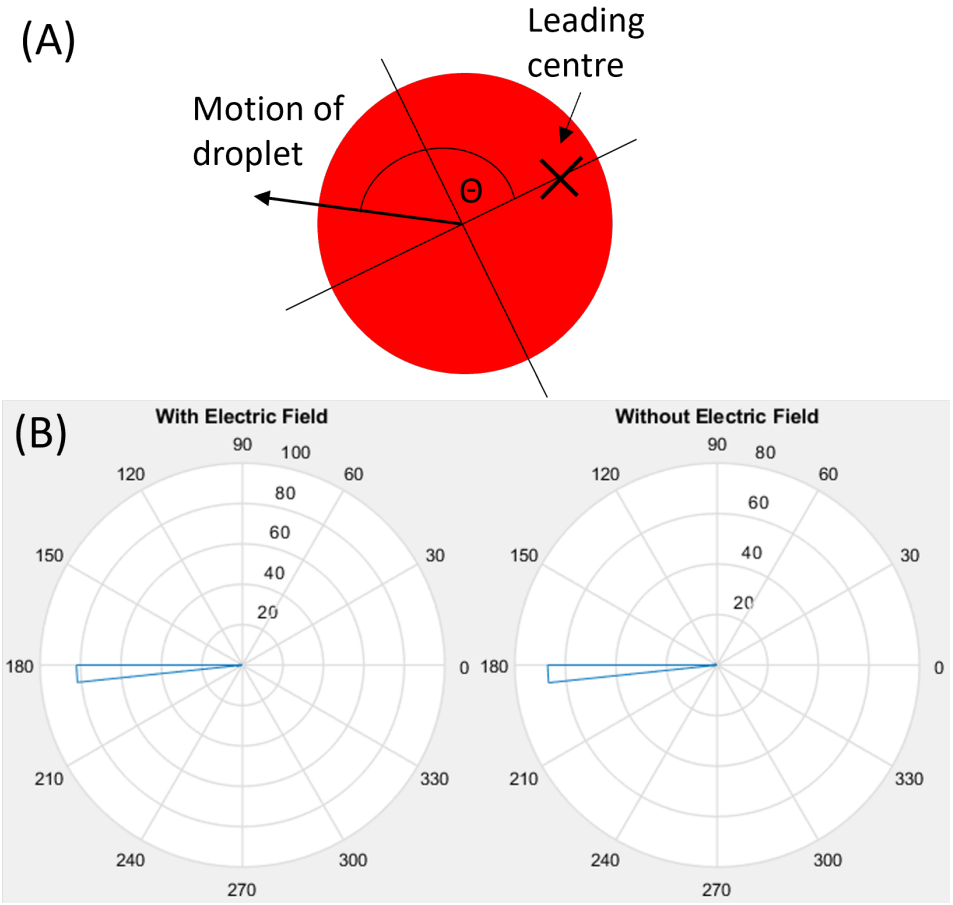

Figure 3.6: (A) Schematic of the 2D coordinate system defined on a droplet where the origin is at the CoM of the droplet and the x-axis pointing from the CoM to the location of the leading center. The angle θ is defined between the travelling direction of the droplet with respect to the x-axis. (B) Circular histogram of the travelling angle θ measured with and without external electric field.

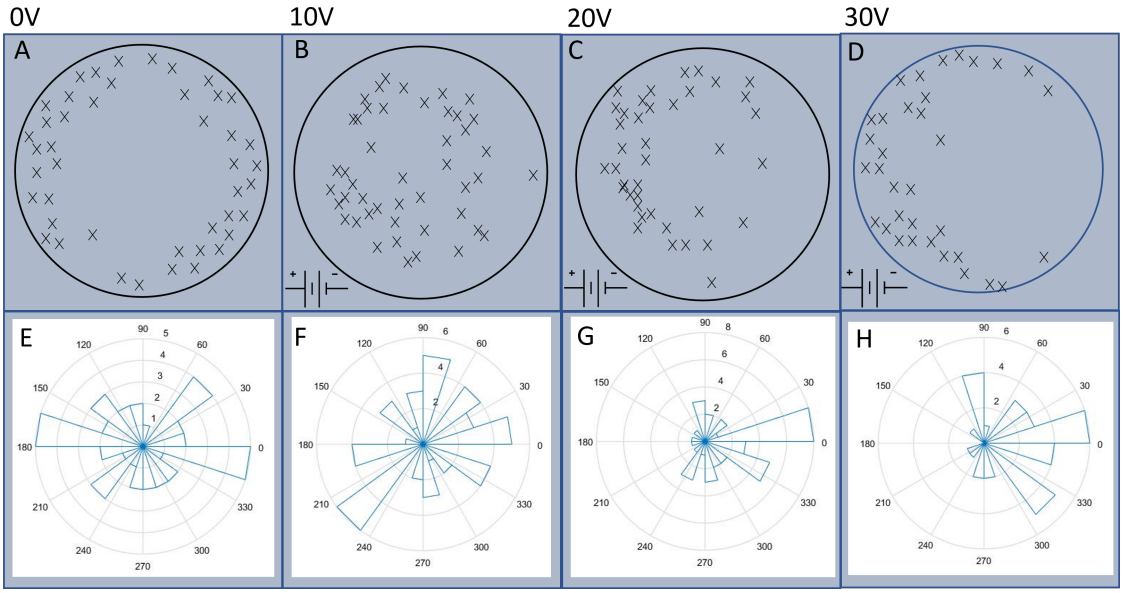

Figure 3.7: (A-D) Distributions of the leading center locations (marked with x) within a schematic BZ droplet at different external electric field strengths. (E-H) Circular histogram of the traveling angles of chemically driven translation motion of droplet. The electric field was applied with the positive electrode on the left, and the negative electrode on the right. The applied voltages across the petri dish are shown in the labels on the top row. Data points were collected from 163 different droplets.

onto a model droplet at four different electric field strength, i.e., $E = 0, 1.1, 2.2$ and 3.3 V/cm. In these experiments the concentration of Ferroin in the droplets is kept at 25 mM. In our testing experiments reported in the Experimental Method section (see Fig.3.2), a change of the Ferroin concentration from 15 to 35 mM makes no significant difference in the spatial distribution of the LCs both in absence or presence of external electric field. This implies that the electrotaxis of BZ droplets reported in this work is insensitive to the Ferroin concentration, as long as it is high enough to trigger the BZ reaction. So we will only present experimental results obtained at one Ferroin concentration (25 mM).

Figure 3.7 shows clearly that under zero or weak electric fields (A-B), the LCs are unbiasedly formed inside the droplet, but at higher field strengths (C-D), the LCs have a strong tendency to be formed closer to the positive electrode. Chemical waves are generated from these LCs and propagate across the droplet bodies until reaching droplet-oil interfaces on both sides. Waves generated from the LCs located close to the droplet-oil interface can travel relatively long distances by passing the CoM of the droplet and reaching the interface on

the opposite side. Such waves typically lead to larger translational displacement than those generated from the LCs close to the CoM of the droplets.

To quantify the effect of the electric field strength on the droplet motion direction, we use the coordinate system defined in Fig. 3.1 with the origin at the CoM of the droplet and the x-axis along the electric field direction. The traveling direction of the droplet translational motion can be conveniently defined by the tangential angle of the trajectory, $\tan^{-1}(y/x)$, at the origin. The experimental results on the travelling angles are collected from the recorded trajectories and presented in Fig.3.7(E-H). Under zero or weak electric fields (E-F), the angles are in general uniformly distributed over 0°-360°, as expected from the unbiased distribution of the LC locations. However, the distribution narrows down to the two right quadrants ($0°$-90° and $270°$-360°), because the LCs are dominantly formed on the left side of the droplet close to the positive electrode. These results clearly indicate that the chemically driven translational motion of the BZ droplets is in alignment with the electric field direction. Increasing the applied field strength will produce a greater taxis effect on the droplet.

For further information, we have also measured the chemical wave propagation speed within the BZ droplets travelling towards and against the electric field. Figure 3.8 shows that the average propagation speed is slightly higher when the wave travels along the electric field than travelling against it. This effect may need to be taken into account when developing theoretical models to describe the electrotaxis phenomenon of BZ droplets [261, 200].

We also note that droplets formed by solutions without Ferroin catalyst do not produce chemical wave patterns and show no chemically driven translational motion. Therefore no electrotaxis was observed in such systems. The presence of Ferroin is vital for triggering the BZ reaction and electrotaxis of the studied droplets, although the results are rather insensitive to the Ferroin concentration over the range we investigated (15-35mM).

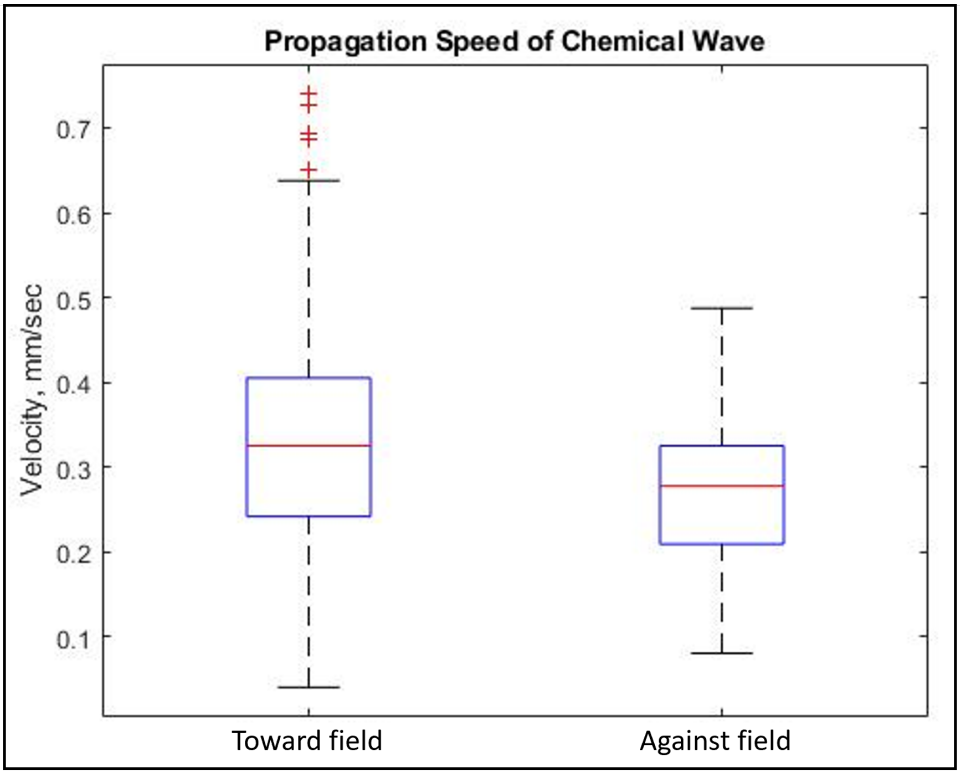

Figure 3.8: Boxplots showing propagation speeds of chemical waves travelling along and against the electric field direction. The median is shown with the red line, and the upper and lower quartiles are shown with the blue box. The black lines show the min and max values, and the red crosses show outliers.

3.5 Discussion

The spontaneous motion of BZ droplets floating on an oil phase has been previously studied by Kitahata *et al.* in the absence of electric field [230, 231, 266]. The propagation of the chemical wave was found to induce inhomogeneous interfacial tension, which in turn generates convective flow at the interface between the BZ solution and oil phases due to the Marangoni effect. The flow velocity differs in the fluids with different viscosities, leading to a momentum exchange between the two phases via interfacial friction. The droplet gains momentum, or propulsion force, in the opposite direction of the flow and undergoes spontaneous motion [230, 267, 231]. The translational motion of BZ droplets can be interpreted using the same mechanism as a result of chemo-mechanical energy transduction. The key finding of the current work is that the direction and magnitude of the chemically driven translational motion of BZ droplets can be controlled by applying an external electric field with different strengths, giving rise to the electrotaxis.

To understand the electrotaxis of BZ droplets, we recall the FKN mechanism which describes the BZ reaction as three periodically repeated processes [171, 253]. Process A acts as a long induction period that involves the consumption of Br^- ions by multiple reactions. Process B is the autocatalytic part with increased production of $HBrO_3$ and fast oxidation of metal ion (Ferroin in our case). This is followed by Process C, which acts as the reset for the chemical clock. This reset causes the reduction of Ferroin, and bromide ions are produced in greater quantities again which leads to the dominance of the reactions governing process A. The process in which the solution alternates from the reduced state to the oxidized state is known as a redox reaction. In the BZ reaction, the oxidation process is visually shown by the colour change of the metal catalyst (Ferroin) from red to blue. This event leads to the propagation of the chemical wave across the solution, as the reaction becomes oxidized at surrounding regions, followed by a slower reduction of the catalyst. The location where this occurs is the leading center (LC).

The LC can appear anywhere within the droplet when there is no external DC field applied. The direction of translational motion of the droplet will depend on the location within the droplet that the chemical wave forms. The closer to the centre that the wave is generated from, the smaller the resultant translational motion will be [177]. Therefore, the greatest translational motion, and therefore droplet velocity, will occur when the LC forms at the droplet boundary.

Figure 3.9 shows the schematic of a pair of BZ droplets undergoing chemically induced translational motion. The chemical wave is represented with a blue arc across the red body of the droplet, and the LC is represented with a black x in its location. The direction of the translational motion is shown with the blue arrows above the droplets. The left droplet is shown to be travelling further due to having the LC formation at the edge of the droplet.

Different from typical experiments on quasi-2D BZ solutions and BZ droplets without external field where the location of the wave formation is unpredictable [258, 259], the application of electric field leads to biased spatial formation of LCs towards the positive electrode. This bias can be attributed to the field-induced concentration gradient of Br^- ions across the

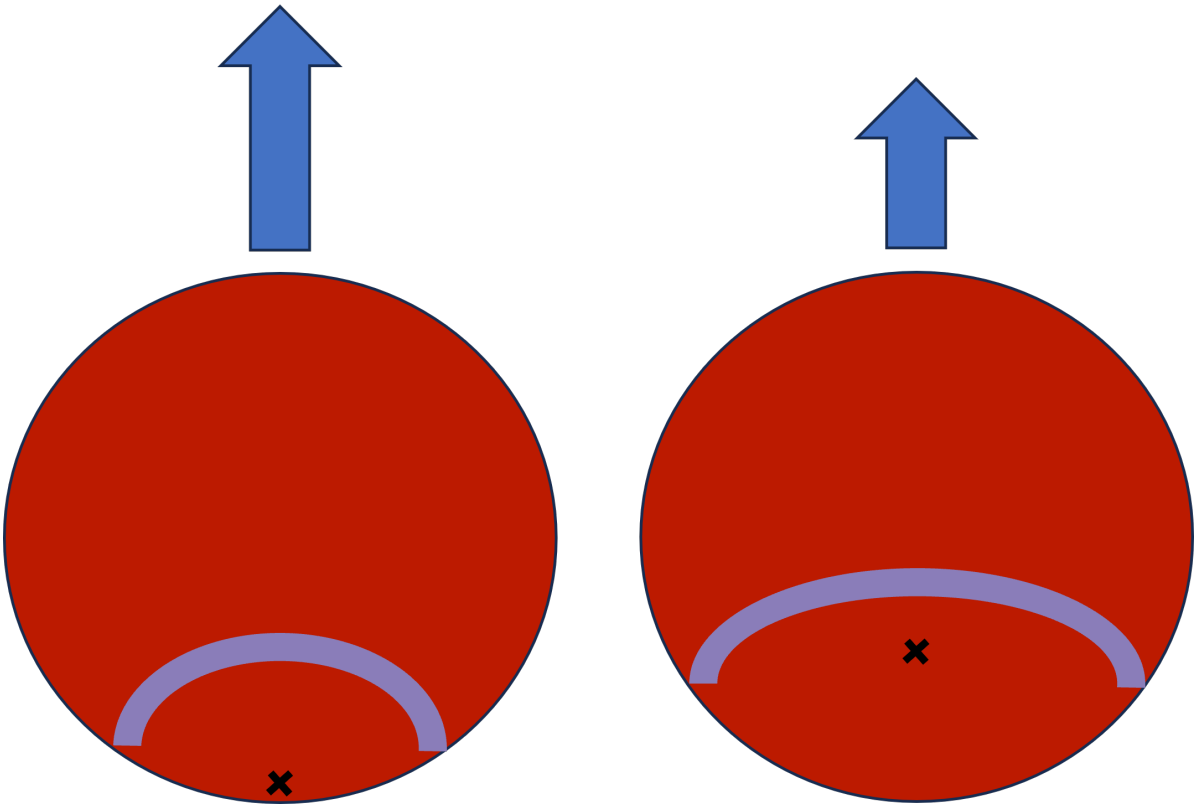

Figure 3.9: 2 examples of BZ droplets undergoing chemically driven translational motion. The droplet on the left will move further due to the LC formation being closer to the edge than that of the droplet on the right.

droplet which causes an instability of the chemical reaction [268, 269]. The increased density of Br^- in the proximity of the positive electrode allows for Process A to dominate the reaction process, leading to the oxidation of metal catalyst Ferroin in Process B. The chemical wave is then generated from a LC location biased towards the positive electrode [171]. Our experiments have revealed a strong correlation between the biased distribution of the LC locations and the direction of the chemically driven translation motion of the BZ droplets. A greater electric field strength was found to produce a greater control of the electrotaxis effect of the BZ droplets.

It was also observed that the BZ droplets underwent a reverse motion after reaching their maximum chemically driven displacement, but never fully returned to the original position at the onset of the translational motion, see Figure 3.5. This phenomenon, which we call the local switchback, can be explained by the longer time that the droplet spent in the oxidized state during the chemical wave propagation, where the translation displacement took place,

than that in the reduced state after the chemical wave ceased, where it moved backwards.

The wave propagation speed is shown in Figure 3.8 to be higher when the wave travels along the electric field direction than against it. This can presumably be explained by the fact that the oxidized Ferroin ion of 3+ valence experiences an electrostatic force pointing along the electric field lines, which favours its motion along the field direction and so speeds up the associated wave propagation.

The discovery of electrotaxis phenomena in BZ droplets has an interesting application in the role of self oscillating hydrogels, employing the use of BZ solutions, where electrotaxis can be utilised to break symmetry within the isotropic solution, causing the generation of a leading center [270]. This will act as a form of control for the origin of the BZ reaction within the gel. Therefore controlling the chemo-mechanical coupling of the gel will be in a future study of the BZ electrotaxis phenomena. This could allow for control of the motion in a more guided matter, allowing for advances in hydrogel based soft robotics. The electrotaxis effect of BZ droplets can also find potential applications in confined systems where it is possible to apply a light resource and for some photosensitive materials which may suffer light damage if using phototaxis effects [265].

3.6 Conclusion

We presented the electrotaxis of aqueous droplets of BZ solutions suspended on an oil phase. The application of an external DC electric field leads to a density gradient in the Br^- ions within the droplet, and consequently biased location of the leading centers in favour of the positive electrode. A chemical wave of oxidized metal catalyst Ferroin is generated from the LC and propagates across the droplet by passing it center of mass. When reaching the droplet-oil interface on the other side (close to the negative electrode), the chemical wave creates inhomogeneous interfacial tension between the two phases and in turn a convective flow. This results in a momentum exchange between the BZ solution in the droplet and the oil phase, effectively producing a force which moves the droplet translationally in the opposite direction of the electric field.

The droplet also undergoes a so-called local switchback by moving in the reverse direction after reaching the maximum translational displacement after the wave ceases and the droplet is in the reduced state. The electrotaxis effect increases with the increase of the electric field strength. This effect is however insensitive to the concentration of the metal catalyst Ferroin as long as it is high enough to trigger the BZ reaction.

Chapter 4

Reaction-Diffusion driven Elongation and Division of Aqueous Droplets Containing BZ Solutions

4.1 Abstract

Hydrodynamic principles of water droplets in oil have been studied previously. Extending our approach, we have observed a division of the Belousov Zhabotinsky (BZ) droplets under an alternating electric field applied externally to the droplet. The area of study has an attraction for the comparison between the division of aqueous droplets and the modelling of cell division. The study of a dividing active droplet can help to shed light on the role that reaction-diffusion along with hydrodynamics has within biological cell division, and can help to describe how early protocells were capable of proliferating. Reaction-diffusion systems are a commonly used physical-chemical model of biological mechanisms but have not yet been involved in the modelling of cell divisions. Therefore, understanding the hydrodynamics of the droplet division will allow for a greater understanding of biological cell division, where the water in oil systems can act as a physical model of the event. Through the study of the BZ-driven division of a water droplet in oil, we can gain an understanding of the forces the cell undergoes to be able to divide. We investigated aqueous droplets containing BZ solutions, which were suspended within a millifluidic channel filled with Oleic acid saturated with surfactant and exposed to

an AC electric field with a varying period, resulting in shape deformation and elongation of the BZ droplet. The combination of shape deformation and elongation of the droplet led to the water droplet-in-oil division. In this report, we present how the elongation and division of water in oil droplets were driven by the BZ reaction. The leading centre locations were analysed to reveal patterns that determine the initial conditions required for the division event to occur. Then the flow of the oxidised wave is characterised within the elongating droplet to determine the source of the hydrodynamic forces derived from within the droplet. The flow is characterised by performing particle image velocimetry analysis on the time series imaging of the droplets containing microbeads to allow the flow tracking to be conducted. The nature of the elongation is studied, as it was observed that inhomogeneous elongation took place across the dividing droplets. The role this plays in the division event is remarkably complex and crucial for the division of the droplet.

The inhomogeneous elongation of the droplet appears to be caused due to the nature of the development of the leading centre formations. The hydrodynamic forces induced by the chemical wave propagation starting from these LCs create novel phenomena where the water droplet containing BZ solutions is able to divide. The coupling between the oil phase and the aqueous phase leads to turbulent flow within the droplet, as colliding vortex flows from many leading centres impart a momentum transfer due to the incompressible nature of water. This turbulence plays a tremendous role in both the elongation and deformation of the droplet, which eventually leads to its division.

4.2 Introduction

Environmental stimulation plays a role in the manner in which cell division occurs. The use of static magnetic fields (MF) has been shown to direct the cleavage planes of frog eggs, and static electric fields (EF) have a profound effect on the cleavage plane in *C. Elegans* [271, 272]. The application of MF or EF of physiological strength is shown to cause the alignment of the cell to become parallel to the applied field. Other studies involving the application of an external EF to cells yielded results showing the orientation of human stem cells to be perpendicular to the applied field. Additionally, it was found that a 5-fold greater cell proliferation rate could be achieved, with no change to the pH levels, and no production

of Hydrogen Peroxide. This allows for the stem cells to self-regulate as though they were in normal environmental conditions, meaning normal biological function can be carried out with the advantage of the increased proliferation rate [273].

Other studies of cell membrane potential have led to the understanding of the role of such potentials in the context of cell division[274]. Endogenous voltage gradients have been shown to have a level of control over cell division and proliferation. Polarization across cells impacts ion flows relating to cell-cell communication and the use of voltage gradients acts as powerful modalities for the control of growth and form [275, 276]. Cell-to-cell signalling plays a tremendous role in the regulation of cell growth and division. The cell cycle regulation is important as the growth of an organism needs to be carefully controlled. An example of the requirement for control is wound healing, where an initial increase in the growth rate will allow the cell proliferation to heal said wound, which is followed by the down-regulation of the growth once the cell organisation has been restored. Cell growth dysregulation has been linked with health conditions like cancer, where there is no downregulation for unhealthy cells, which keep proliferating, and lead to tumour growth [277, 278]. It is apparent that the cell membrane potential regulation and signalling from other cells are crucial to the proper regulation and maintenance of cell function. In regular cell function, the external stimulus is largely only from neighbouring cells communicating. However, it has been shown that cells can detect and react to environmental stimulation, which is where the parallel to our study forms, where the water in oil, droplet division occurs due to the droplets' regulation of internal redox signalling in combination with the effects from an externally applied AC field. Similar to the biological system, the function of the droplet division seems to rely on the specificity of the environmental conditions.

The mechanism behind biological cell division was uncovered to be largely led by a network of proteins called actin. The actin proteins form filaments which are responsible for the regulation of the cytoskeleton of the cell which needs to undergo significant structural changes for processes like cell division, but also for cell growth and motility. The regulation of actin which forms its self-organisation is very sensitive and requires a precise morphology to achieve the biological function [279]. If there is a problem or a mutation on a gene which is responsible for the regulation of actin, problems like disorganisation of actin can occur, which can lead to pre-cursors to cancer [280, 281]. When a cell successfully undergoes a division event, a

contractile ring of actin-myosin forms, which acts as a cleavage furrow on the cell body and applies a sheer force which causes the cell to divide. Application of external EF to biological systems has shown changes in motility rates. The external application of electric fields to Actin filaments was found to accelerate, decelerate, and reverse the velocity depending on the direction of the applied field [282]. Quadrupole electrode arrangements have also been optimised to generate pattern formation of actin on myosin, where the manipulation and orientation of actin-myosin were achieved through the application of an external electric field [283]. The role of electrical signalling, along with an organism's ability to detect external electric fields plays a fundamental role in motility, and proliferation in biological systems. In particular, the actin-myosin system seems to be greatly affected by the external EFs. The role of the actin-myosin system in cell division has been studied to gain an understanding of the nature of both biological cell division, and the fission of constituent parts. Ultrastructure and dynamics of actin-myosin II cytoskeleton during mitochondrial fission was captured by Yang *et al.* via the employment of fluorescent microscopy, revealing a network of criss-cross actin filaments spanning the cell structure [284]. Electrotaxis of cells structure was found, where the application of an external EF, to the extent that the distribution of actin and myosin was asymmetrically distributed in the migrating cell. The gene PTEN was discovered to play a crucial role in such redistribution, showing that there is a biological mechanism to drive the scission of the cell body [285]. The electrotaxis phenomena of Actin, and its crucial role in the cell division cycle presents a clear link between environmental stimulation and cell division. The generation of the scission force around the body of the cell undergoing cytokinesis will generate hydrodynamic flows within the cell, which act as a mechanism for mass transit, but also for the maintenance of thermodynamic equilibrium. Hydrodynamic flows external to cells have been studied to determine their impact on the cell life cycle [286]. Hydrodynamic flow through the heart has been studied due to the importance of having blood flow to tissues throughout the body, which is studied by cardiologists using imaging techniques that observe the flow in and out of the heart [287]. Studying the flow of the heart has also led to the study of the shape of red blood cells, which must change shape depending on the narrowing or widening of the vessels of which they pass through when they travel throughout the body [288].

Modelling of biological processes has taken advantage of reaction-diffusion (RD) systems

due to their natural tendency to crop up in chemical and biological systems. They are a powerful tool for many reasons, for example, their ability to remain in a non-equilibrium state for long durations, and due to the ability to incorporate a time delay effect in the reaction term which allows for more accurate modelling of biological processes [289]. The use of a time delay in modelling systems can be used to incorporate complex spatio-temporal behaviour with standing waves, travelling waves, and inhomogeneous dynamics at non-equilibrium states required for spatial perturbations to form within the system. For this reason, RD systems have been used to model growth in systems such as virus evolution and cancer growth [290, 291, 292]. The rate of transmission of the Zika virus was modelled using RD systems to provide an optimized introduction of vaccination to decrease costs and prevent loss of life[293].

The study of biological pattern formation carries specific interest with scientists with a variety of scopes, including birth defects, the self-organization of bacteria, and the patterning of animal stripes [294, 295]. Reaction-diffusion systems have been used to model biological processes before, as it was discovered that RD mechanisms are responsible for biological pattern formation [107, 296]. Models of mechanisms of self-organisation which result in biological pattern formation have been studied for their use in generating synthetic self-organisation systems, which may lead to advancements in the development of synthetic tissues [297]. Research has shown that contact-dependent depolarization plays an influential role in the biological pattern formation of zebrafish skin, resulting in the striping pattern exhibited across the length of the body of the zebrafish. Small perturbations are responsible for cascading changes in small variables, which lead to the unique patterning observable in biology [298]. There exist 2 pigment cell types, melanophores, and xanthrophores. Upon contact with the xanthrophore dendrites, the melanophore membrane will depolarize transiently. Migration of the melanohpore cell is triggered by its depolarisation which causes a repulsive movement between cells, which leads to a dispersion of the depolarized cells throughout the organism, which leads to the patterning of stripes that form in the zebrafish skin. Small changes like thermal fluctuations or minute changes in the initial distribution of both pigment cells, or the ratio in the population of each of these cells produce drastically different results in the formation of the patterning in the fish. This is the principle behind chaotic systems and the pattern formation that forms in reaction-diffusion systems.

Attempts to produce mathematical models of cell division have been made, whereby a

series of differential and algebraic equations governing the cell cycle have been formulated with some success. The protein interactions involved in the cell cycle of yeast were studied and a model was produced [299]. These protein-protein interactions were studied for their role in the division of the yeast due to their interactions forming the structure and signalling which leads to the division event [300, 301]. In another study, the scission and branching free energies in a model of a charged miscille in the presence of inorganic and organic salts were calculated [302]. The general method behind the model is adaptable to other surfactant solutions and can be used to calculate scission and branching energies.

Experimentally studied water-in-oil droplets undergoing swimming motion were studied by de Blois *et al.* [303]. Glass capillaries of various geometries were filled with a continuous surfactant-oil phase, and a water droplet was introduced. The motion of the droplet was instigated by a combination of 2 factors, the first being: the system being far from physico-chemical thermodynamic equilibrium. The second effect is; that the resulting isotropic concentration field of inverse swollen micelles is unstable against the hydrodynamic flow, which can be induced by effects such as Marangoni stress. As the system uses surfactants in oil, a small gradient of micelles can form, which will cause Marangoni stress to induce an internal flow within the oil phase. This flow is enough to cause the swimming motion of said droplets. In some cases where the change in the capillary morphology is sufficient, spontaneous droplet division is observed, where the 2 sub-droplets that form will continue to act in the swimming motion previously observed, and in some cases, the sub-droplets themselves will undergo further divisions. Related works show how the flow fields around an active droplet can be visualised for analysis, allowing for more information regarding the fluid dynamics to be uncovered [304].

The role of hydrodynamic flows in the division of a droplet via the action of a chemical reaction has been simulated with success [305]. The motivation for the study of chemically induced droplet division was initiated by the comparison of living cells to water droplets, where the cellular systems are compartmentalised and form in order to organise on a biochemical level, where internal reactions govern the life cycle, where external forces collaborate to process the self-organization and structure of the cell. The formation of the cell shape is in part due to the genetics [306], along with the external forces such as hydrodynamic flow and the capillary effect [307, 308]. It was discovered that hydrodynamic flow helps to stabilise the droplet into

spherical shapes, but when a sufficiently large driving force is created by chemical reactions, the droplet is capable of dividing. The oil-in-water droplet was shown to elongate, creating a reduction in the width, as the mass transit stretches the droplet out prior to the division. This elongation and division were shown to involve mechanical work against the surface tension of the droplet, allowing them to deform out of the hydrodynamic equilibrium which forces the droplet to remain in a spherical shape. Another investigation into the mechanics behind the division of a proto-cell led to the experimental findings of shape changes and budding of giant vesicles [309]. A novel approach was demonstrated where the deformation of giant unilamellar vesicles was induced by purely physical stimuli. Hydrodynamic forces induced by osmotic pressure caused by the cross-membrane transfer of urea which initiated the urea-urase enzymatic reaction, which further caused the pH to increase, and so further deformed the shape. The vesicles did not fully separate in the state following the fast enzymatic reaction which induces the deformation, because the vesicles were connected by a long narrow neck, which could be broken when the budded vesicles were irradiated by a laser beam. The spontaneous deformation and fission of oil droplets have been further studied by Okada *et al.* [310].

In other related work, the droplet breakup modes were investigated, where a DC field was applied to droplets which were observed to elongate and divide [311]. The droplet breakup is found to be different depending on the mode [312]. The breakup modes often depend on the external stimuli applied to the droplet, but the internal flows will also play a role. Flow is best described by the Navier-Stokes equations [114]. The Navier-Stokes equations describe the flow of incompressible flows (liquids) and compressible flows (gases), where viscosity is involved. In the equations, viscosity accounts for friction, which is a much greater factor in liquids with greater viscosities. Chaos and turbulence are currently not well accounted for in the current work, as the 3-dimensional solutions to the Navier-Stokes equations are currently unavailable [313, 314] but simplifications can be made to incorporate the equations into a model of flow in a system. These simplifications largely involve a degree of averaging which is used to group 'similar' flows together to make the solution less computationally expensive.

Many RD systems are studied for their physico-chemical dynamics relating to biological processes. The Belousov Zhabotinsky (BZ) reaction is a well-studied physical chemistry re-

action involving the oxidation and reduction of a metal catalyst and is often used as a model for the citric acid cycle [179]. The oxidation of the metal catalyst results in a remarkable colour change from red to blue. This oxidation can be observed in non-stirred conditions as a blue wave propagates through the solution. Examples of the non-stirred conditions include a quasi-2D solution in a petri dish; the aqueous droplets of BZ solutions suspended in an oil phase. Droplets of BZ solutions have been shown to exhibit chemically induced translational motion when suspended on an oil phase. This motion is due to the oxidised state of the metal catalyst having a different charge than the reduced state. These different states have different interfacial tensions with the oil phase. So when the oxidised wave propagates across the body of the droplet, a gradient of the interfacial tension is generated. Marangoni stress is therefore induced in the two phases, generated by the gradient of interfacial tension, such stress induces surface flows in each phase. Due to the flow at the surface, a bulk flow within the body of the droplet occurs as a compensatory measure. This is remarked by a subtle shape change in the body of the droplet where an elongation in the direction of the flow of the oxidised wave will occur. Friction between the phases occurs due to the different viscosities of the phases, which results in a momentum transfer between the oil phase and the liquid phase of the droplet. This results in the translational motion of the droplet in the direction of the travelling chemical wave. The magnitude of the translational motion is greater than the elongation observed in the droplet. The group used the Navier-Stokes equations coupled with the originator model to study the flows inside the droplet, as well as the oil phase. This modelling confirms the experimental findings [315, 316].

A previous study determined a taxis effect of BZ droplets suspended in a pure oil phase where the report details an electrotaxis behaviour of aqueous droplets containing ferroin-catalysed BZ solutions when suspended in an oil phase. The application of an external DC field across the droplets caused the droplets to align their translational motion in line with the applied electric field [317]. The application of the field creates a dipole within the droplet and causes a flow within the droplets to form an inhomogeneous ion gradient, leading to inhomogeneous LC distribution within the droplet with a bias to the side of the droplet closest to the positive electrode. Blank *et al.* discovered that the wave propagation speed could be manipulated by the application of an external electromagnetic field, where the dynamics

of the BZ reaction can be altered by the application of external stimulus [318]. Similar studies involve the use of guided light sources with ruthenium-catalysed droplets to control the translational motion of the droplets where the light stimulation causes the oxidation of the catalyst, affecting the nature of the interfacial tension, allowing control of the guided droplet motion [232, 265]. Taxis effects are relevant for the study of the elongation and division of droplets due to the biological significance of translational motion relating to the motility of biological cells, and the elongation observed under chemically driven translational motion mimicking the elongation cells undergo prior to cell division.

In this chapter, we present the elongation and shape deformation mechanics of BZ droplets suspended in an oil phase as the result of applying an alternating stimulation regime. The optimization approach to obtain the maximal elongation of the droplet elongation was investigated, with the results represented in this work. We also present a physical chemistry model of cell division using the BZ droplet acting under the previously mentioned alternating stimulation regime. The employment of sodium dodecyl sulfate (SDS) within the oil phase acts to reduce the surface tension between the droplet and oil phase, allowing for chemically driven elongation to occur. The use of the AC field acts as EF stimulation of the droplet, inducing the tripole effect with regard to the LC formation across the body of the droplet. A tripole here refers to the state where the droplet has charges alternating from positive, to negative, then back to positive, or alternatively, negative, to positive, and back to negative. This allows for the maximal elongation to occur, and subsequently the division of the droplet. An explanation of the division is presented, using flow tracking and analysis of LC formation to determine the conditions for the division event to occur. We posit that the internal driving force behind water in oil droplet division can play a role in understanding the mechanistic view of early protocol division events as biological cell division is driven entirely by internal forces generated from the chemical stimulus.

4.3 Methods

4.3.1 Preparation of BZ solution

The Ferroin catalysed Belousov Zhabotinsky (BZ) reaction was performed according to the recipe written by Winfree [170] in their work "The geometry of biological time". 3 solutions were produced and mixed to produce a batch solution of BZ solutions, which was then mixed with Ferroin, the metal catalyst, which produces the vibrant colour change. This solution was then pipetted into the millifluidic channel and recorded for the duration of the experiment.

The solutions were prepared as such:
Solution A: 33.5ml H_2O + 1ml ccH_2SO_4 + 2.5g $NaBrO_3$
Solution B: 10ml H_2O + 1g Malonic Acid
Solution C: 10ml H_2O + 1g NaBr
Solution D: 25 mM Ferroin Solution

The 25mM Ferroin solution was produced by mixing 0.3438 g Fe_2SO_4x7H_2O and 0.6758 g 1,10-Phenanthroline. 6 ml of Sol.A was mixed with 1 ml of Sol.B and 0.5 ml of Sol.C and stirred until clear. Then 1 ml of Ferroin solution is mixed. All chemicals were of extra pure lab-grade quality and required no further purification and were sourced from Fisher Scientific. The water used was double distilled by a water purifier system.

4.3.2 Experimental setup

Figure 4.1 shows the millifluidic device housed within a petri dish [319]. The channel along with the petri dish was filled with a solution of Sodium dodecyl Sulfate (SDS) and Oleic acid. The initial concentration of SDS in the solution is 0.45g SDS per litre of Oleic acid. The electrodes were placed on either side of the petri dish as shown, which had dimensions of 1000 mm x 20 mm x 2 mm and were fabricated from copper.

The millifluidic channel was CNC milled from acrylic to produce a 20 mm long channel with a diameter of 5 mm. A dimple is milled into the ends to anchor the droplet in place. A droplet with a volume of 50 μl was pipetted onto the dimple within the millifluidic channel at the beginning of the experiment. 50 μl was chosen due to the volume being optimised for

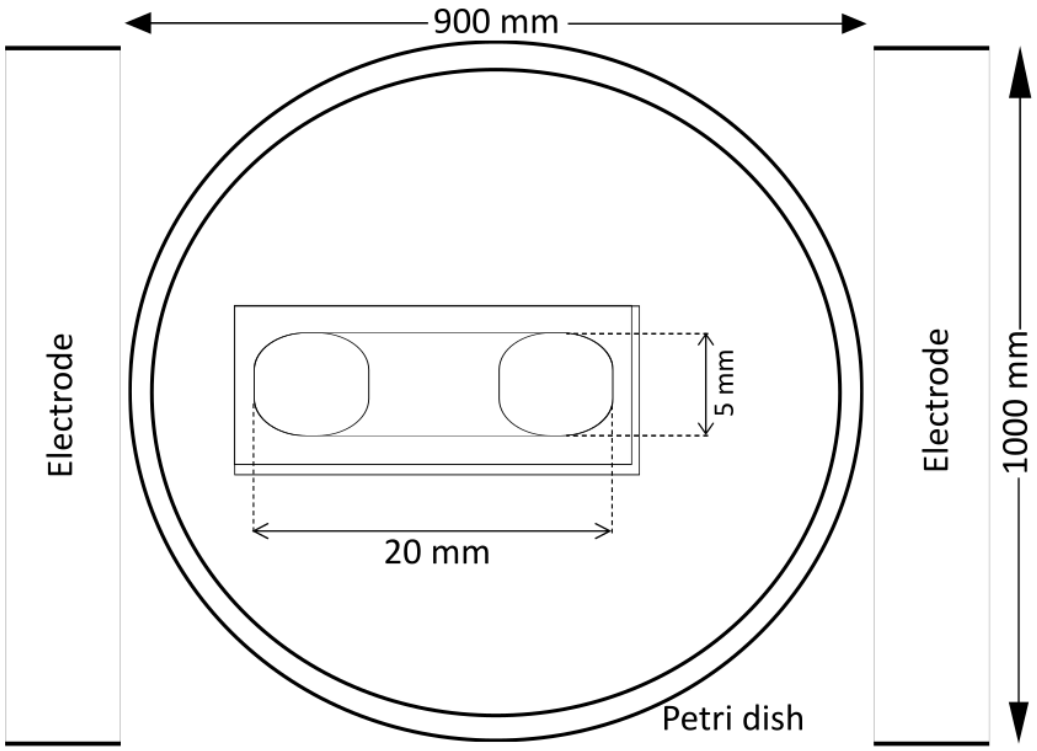

Figure 4.1: Schematic of Millifluidic device contained within a petri dish. The Millifluidic device was fabricated from CNC-milled acrylic and features a dimple at either end to anchor the droplet when it is initially pipetted onto the device. This acts to retain the initial position so the droplet's elongation and shape deformation can be measured. Electrodes used to generate the AC field are shown on either side of the dish and were fabricated from sheet copper with dimensions 100 mm x 20 mm x 2 mm. The petri dish is filled with Oleic acid saturated with Sodium dodecyl Sulfate.

the millifluidic chamber, whilst also being large enough that the visualisation of LC formation was plausible. The top of the millifluidic chamber was not enclosed, and the droplet was submerged in the oil phase. Once pipetted, the droplets are allowed to oscillate under natural conditions, with the addition of the AC field application. No other mechanical or chemical perturbations are applied.

4.3.3 Application of electric fields

The power supply used was a Tenma 72-10505 lab bench power supply operating at a voltage of 30 V corresponding to 3.3V/cm. To determine the operating frequency of the AC field that produced the greatest elongation, we repeated experiments with periods of 1 minute through to 5 minutes, with an interval of 1 minute. Then experiments were conducted with periods of

1 minute and 30 seconds, and 2 minutes and 30 seconds to confirm that the 2-minute period was the greatest source of external perturbation.

As a next step to determine the SDS concentration for droplet division, experiments were conducted with varying concentrations of SDS. SDS is highly soluble and will begin to form micelles above a concentration of 8.2mM. The concentrations of SDS used for the systematic study ranged from 0.113g to 0.9g of SDS per litre of Oleic acid. 0.9g of SDS per litre of Oleic acid was chosen as the maximum concentration, as the greater concentration of surfactant in the oil phase led to an increase in SDS micelles forming, which lead to bromine leaching from the droplet, causing the chemical oscillations to break down. The leaching occurs due to the SDS causing excitatory chemical species to leach from the aqueous droplet. Here, the excitatory species is bromate, which is why the complex formed has an orange hue (see appendix 8.37).

4.3.4 Recording and Visual analysis

Each experiment was recorded using a Nikon D7500 camera from the top down at 60 frames per second, and the images were analysed in MATLAB. Each experiment was recorded for 30 minutes, or until the droplet had reached the fully oxidised state. This time span was decided on due to technical limitations of camera recording equipment, but also due to the concentrations of Malonic acid, and Ferroin solution used in the droplets [195].

To aid in understanding the nature of the elongation and division of droplets, the use of Microbeads was employed to visualise hydrodynamic flows within the droplet. The Microbeads used were bought from Thermo Fisher and were fabricated from Polystyrene Crosslinked Divinylbenzene. The Microbeads were suspended within the aqueous droplet as to observe the internal flow within the droplet induced by the Marangoni stress created by the propagation of the chemical wave. Important care was placed to ensure the tracer particles would not impact the flow in any manner, therefore research was conducted to find appropriately sized particles which could be tracked, but the impact on the flow would be negligible [320]. The trace particles were then tracked using the inbuilt MATLAB image analysis toolbox as a way to visualize and analyse the flow.

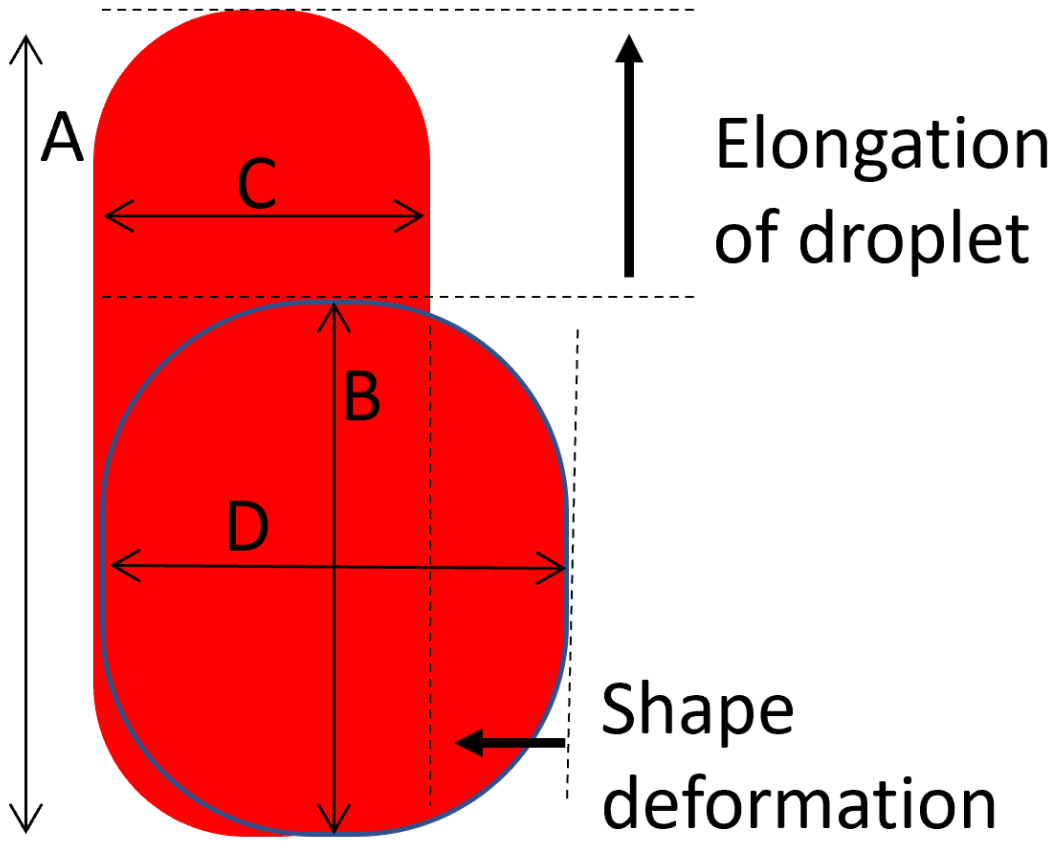

Figure 4.2: The elongation and shape deformation of the droplet is shown here. The length A represents the elongated droplet's length, with B being the original length. length C is the width of the elongated droplet, and length D is the original width of the droplet. The elongation is found by dividing the lengths, A/B, and the shape deformation is found by diving the widths, C/D. The use of the black directional arrows shows the elongation and shape deformation the droplet undergoes.

4.4 Results

4.4.1 Droplet Elongation

The BZ droplets were studied and analysed to gather data relating to their elongation and shape deformation. The starting length and width of the droplet are obtained from analysis in MATLAB. The initial length is compared to the max length the droplet reaches under oscillation, the width at this moment is then compared to the initial width of the droplet. The calculations for the relative elongation and shape deformation are visually represented in figure 4.2. Where the elongation is the elongated length A, divided by the initial length, B. The shape deformation is the new width C divided by the original width, D. The length is measured

from tip to tip of the droplet, whilst the width is recorded as the narrowest section along the body of the droplet. This series of measurements will be utilised for statistical analysis of the viability of the alternating stimulation regime, and SDS concentration as a measure of the ability to elongate the oscillating droplet.

The averages of these values are obtained over the course of repeat experiments and stored for statistical analysis. The AC field was applied as to generate a tripole within the droplet, as the polarity of the AC field switches, the internal flow of ions within the solution will change, allowing for an ion density gradient to be generated at opposing ends of the droplet. This alternation stimulation regime will generate the tripole, allowing for the LC formation at either end of the droplet. This will lead to the greatest elongation of the droplet, allowing the division event to occur, as hypothesised from our previous study.

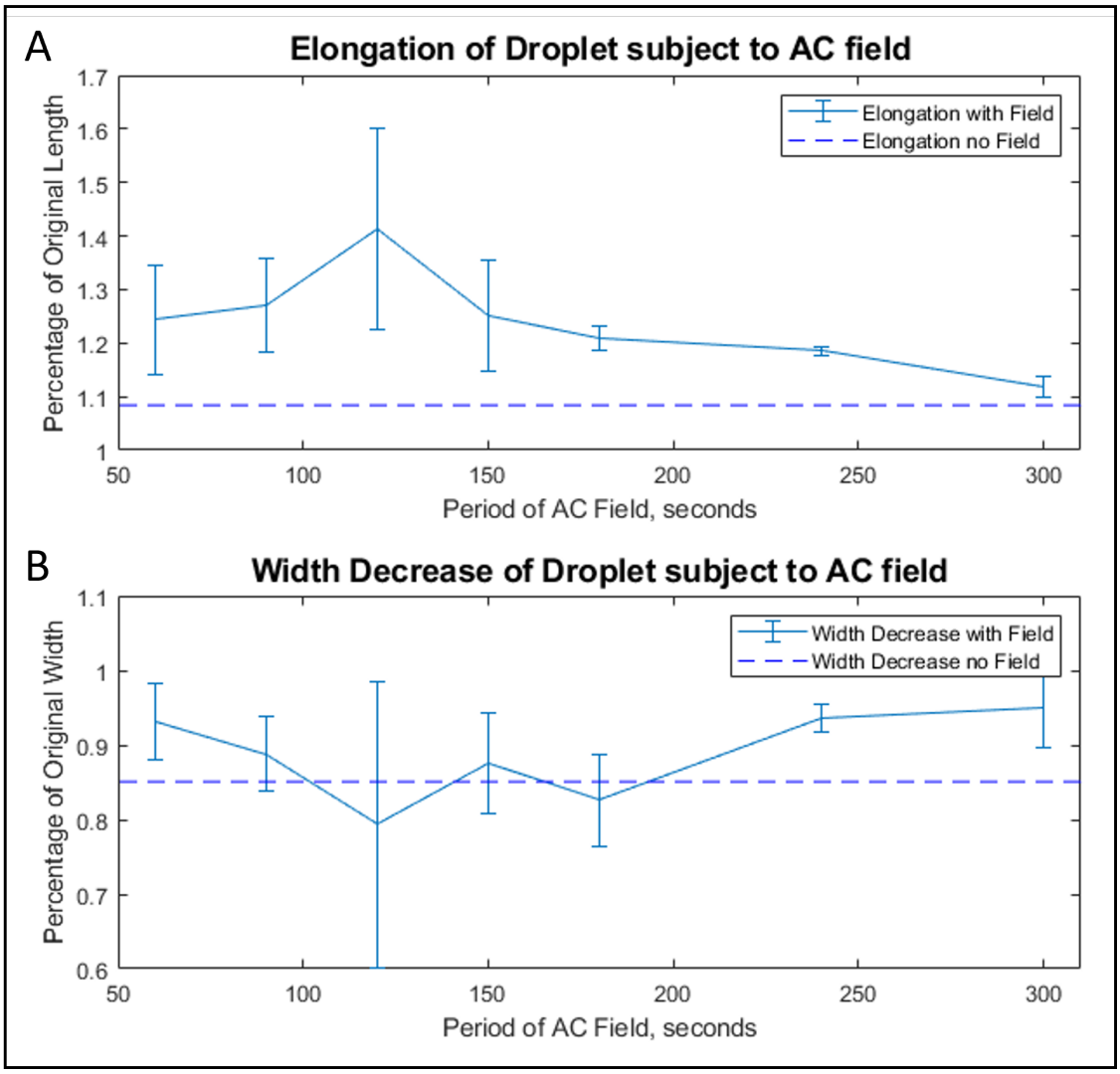

Figure 4.3: (A) Elongation of a droplet containing BZ solutions subject to an alternating stimulation regime. The solid line graph denotes the data where the period of polarity flipping of the AC field is changed, and the dotted line represents the control condition where no field is applied. The greatest elongation was observed where the period of the AC field is 2 minutes. In each scenario where an AC field is applied, the elongation is greater than the control condition. Emphasizing the electric field (EF) stimulation's effect on droplet elongation. (B) Width decrease of the non-dividing droplet is represented by the solid line. The EF stimulation that induced the greatest elongation also induced the greatest width decrease. However, the shape deformation was not of linear proportion, as the 3-minute period produced disproportionate shape deformation when compared to the elongation achieved by this period of the alternating stimulation regime. The error bars in both graphs represent the standard deviation.

Figure 4.3 (A) shows the elongation of the droplets as a function of the applied AC field polarity. The alternating stimulation regime was applied over a range of periods to determine the optimal period for generating the greatest elongation of the BZ droplet. The periods of the AC field used ranged from 1 minute, through to 5 minutes with an interval of 1 minute,

which was reduced to 30 seconds to isolate the period able to generate the greatest elongation. This period was found to be 2 minutes, with a linear decrease in elongation as the period increases past 2 minutes, and a linear increase as the period approaches the 2-minute mark. In all cases for the elongation of the droplet, having the application of an AC field causes a greater elongation than in the scenario of no external field being applied. (B) shows the width decrease as a function of the period of the AC field's polarity. Only non-dividing droplets are represented in the graph here, to study the decrease in width decrease where no divide-by-0 errors can occur. It is shown that the width decrease is not much different to the case where no external electric field has been applied. The case for the 2-minute period shows a greater decrease in width, but the greatest, and smallest period applied leads to a smaller decrease in width compared to the control scenario, of no application of the external electric field. It was discovered that the 2-minute period gave the largest elongation, along with the greatest width decrease of the droplet. There is a trend showing that the increase in elongation correlated with a larger decrease in width due to the incompressibility of the droplet. This trend holds true for all cases except the 3-minute period, where it is believed that the period of the alternating AC field is close to the resonant frequency of the BZ reaction, so whilst the elongation was not the greatest, the alternating stimulation regime created a great enough perturbation to the droplet that the shape deformation was still great in magnitude. An interesting observation lies in the finding that the decrease in width in the control group was greater than most experimental conditions with the application of the AC field. This could be explained by the presence of the field creating altered positions for the LC formations in the droplet, which lead to the elongation with altered deformation patterns in the non-dividing droplets. The AC field may also have increased the frequency of the LC formations which lead to greater surface flows in the droplet, causing a decrease in the thickness of the droplet, rather than its width. The surface flows would be accounted for with a bulk flow at the centre of mass of the droplet, which travels through the body of the droplet, not at the surface. This could be an aligning factor in the increased elongation of the droplet. An experiment to test for this could involve using a side-mounted camera to view any decrease in droplet thickness, which was not plausible in the current experimental setup due to the distortion caused by the curved petri dish. It was observed that the droplet subject to no externally applied AC field would still elongate and consequently show a reduction in width. This is in accordance with

prior research showing that the propagation of chemical waves reduces the interfacial tension between the droplet and oil phase, and causes elongation in the droplet [134, 231].

Application of the alternating field (AC)

The LC locations from multiple non-dividing droplets were collected and projected onto a model droplet in figure 4.4. The positions were identified within elongation droplets which did not divide and marked on a model droplet with an 'x'. The panels, A to G, represent the alternating stimulation regime, in the form of the application of an AC field externally, with the altered time period of the AC. The range of periods used was 60 seconds, 90 seconds, 120 seconds, 150 seconds, 180 seconds, 240 seconds, and 300 seconds.

A total of 39 LCs were extracted from the 60-second period experiments, 26 LCs from the 90-second period experiments, 30 LCs were extracted from the 120-second period experiments, 57 LCs were extracted from the 150-second period experiments, 52 LCs were extracted from the 240-second period experiments, and 46 LCs were extracted from the 300-second period experiments.

Very distinct segmentation of the LC locations can be observed in the box labelled 'C', which corresponds to the 120-second period of the AC field, and is the experimental condition which produced the greatest elongation of the BZ droplet. The conditions which produced the second greatest elongations are the 90, and 150-second periods, which also show a great degree of inhomogeneity in the LC distributions.

A potential reason for the inhomogeneity in the LC distributions is due to the AC field acting as a push-pull mechanism on the Br^- ions, creating sub-regions inside the droplet with more densely packed ion gradients, that result in the formation of LCs at these regions. The lower and higher periods which were applied to the droplets did not cause this effect, possibly due to operating out of the resonance frequency of the droplet. It is hypothesised that the specific locations where the LC will form throughout the droplet will contribute to the greater elongation effect observed in these conditions. Box A does not show any significant pattern formation which is likely due to the fact that the AC field is switching polarity too fast for

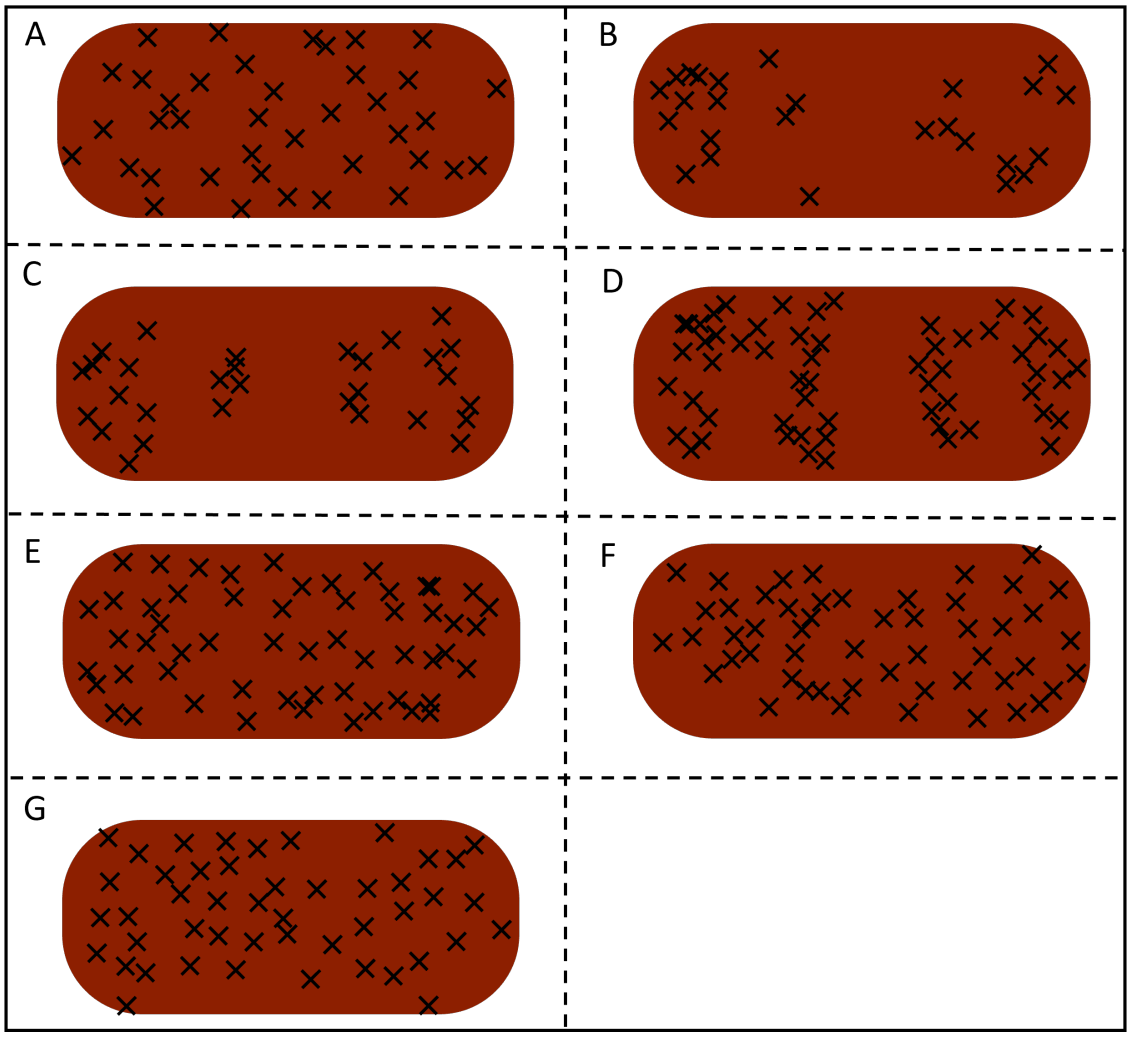

Figure 4.4: Leading centre (LC) locations within the non-dividing droplets subjected to varied alternating stimulation regimes were extracted and projected onto a model droplet with an 'x'. Boxes A through G show the LC formations within droplets subjected to an AC field with periods 60 seconds, 90 seconds, 120 seconds, 150 seconds, 180 seconds, 240 seconds, and 300 seconds, respectively. The locations within the droplets subjected to the 90-second, 120-second, and 150-second AC periods show less homogeneity in the LC formations when compared to the other stimulation regimes. A total of 310 independent LC formations were analysed.

there to be a bias in the LC formation, therefore resulting in a normal distribution across the droplet[317].

Boxes E, through to G also show a largely homogeneous distribution of LC formations across the droplet body, whilst these droplets were subject to a longer period AC field. The reason for the homogeneous LC distribution lies in the averaging effect that alternating the direction of the field has over time. Application of a long-period AC field is akin to applying a DC field in one direction, then switching the polarity to apply it in the opposing direction, leading to speculation about the resultant LC formation across the droplet subject to the long-period AC field.

The biased development of LC formation presented in chapter 3 occurs over a longer time scale, allowing the gradient in ion distribution to form in a manner that a single LC formation occurs nearest the positive electrode, whereas, in this system, the shorter time frame that the droplet is subject to does not have a strong enough impact on the formation of the distributed ion gradient to cause the biased distribution seen in the electrotaxis study. Droplets subjected to the 300-second period AC field showed the smallest elongation, which was not significantly greater than the control condition with no external field applied. Because of the findings that the 120-second period of the AC field gained the greatest elongation and the most prominent alteration to the LC formation within the droplet, this period was chosen to be used for further experiments where instead of altering the period of the AC field, the concentration of the SDS within the oil phase is manipulated.

t-test of elongation as a function of SDS concentration		
SDS concentration	h-value	p-value
0.113g/litre	1	0.0140
0.225g/litre	1	0.0470
0.338g/litre	1	0.0172
0.45g/litre	1	0.0211
0.563g/litre	1	0.0013
0.675g/litre	1	8.9993e-04
0.786g/litre	1	1.9171e-04
0.9g/litre	1	0.0026

Table 4.1: Results of T-test performed in the MATLAB computational environment, comparing the elongation of BZ droplets in the presence of an AC field, with varied SDS concentration present in the oil phase, to the control group, with no electric field stimulation. Statistically significant elongation was found in each concentration of SDS.

Statistical analysis was conducted and is displayed in table 8.1. It was found that the application of the alternating stimulation regime in the form of the AC field with a period of 120-second, was able to produce statistically significant elongation of the droplet, according to a t-test performed in the MATLAB computational environment, when compared to the control group. The greatest elongation in this group was the 0.9g per litre condition, which is expected as this would produce the greatest decrease in surface tension and allow the droplet to elongate the most.

Effect of the surface tension by changing the SDS concentration

Figure 4.5 shows the effect changing the concentration of SDS within the oleic acid has on the elongation (A) and shape deformation (B) of the droplet subject to an alternating stimulation regime, where an AC field is applied externally to the droplet. The AC field applied to the droplet operated with a period of 2 minutes, as this was found to produce the greatest elongation of the droplet regardless of the SDS concentration. The results shown depict the increase in SDS concentration resulting in an increase in the elongation of the droplet, corresponding also to the greatest decrease in the width of the droplet.

The application of the AC field is shown to induce a tripole effect within the droplet. The AC field acts as a push-pull mechanism on the ions distributed within the BZ droplet. The changing field externally applied to the droplet causes back-and-forth flow within the droplet, which creates distinct regions of ion density within the droplet when the field is applied at the correct frequency. The tripole affects the droplet where a distribution of the leading centre (LC) is found to form across the droplet. In comparison to the application of a DC field, where an inhomogeneous bias to LC distribution is found at the side of the droplet closest to the positive electrode [317], with the triple we can observe LC formations across the droplet, with a distinct pattern forming with the tripole in effect. The inhomogeneous distribution of LC formations occurs in a similar manner to the reason we observe the electrotaxis effect in the droplets subject to a DC field. There is an inhomogeneous distribution of the Br^- ions, which leads to the formation of an LC at this region.

The surfactant present in the oil phase creates an interesting effect, where the reduction of interfacial tension allows for the droplet to elongate, rather than driving translational mo-

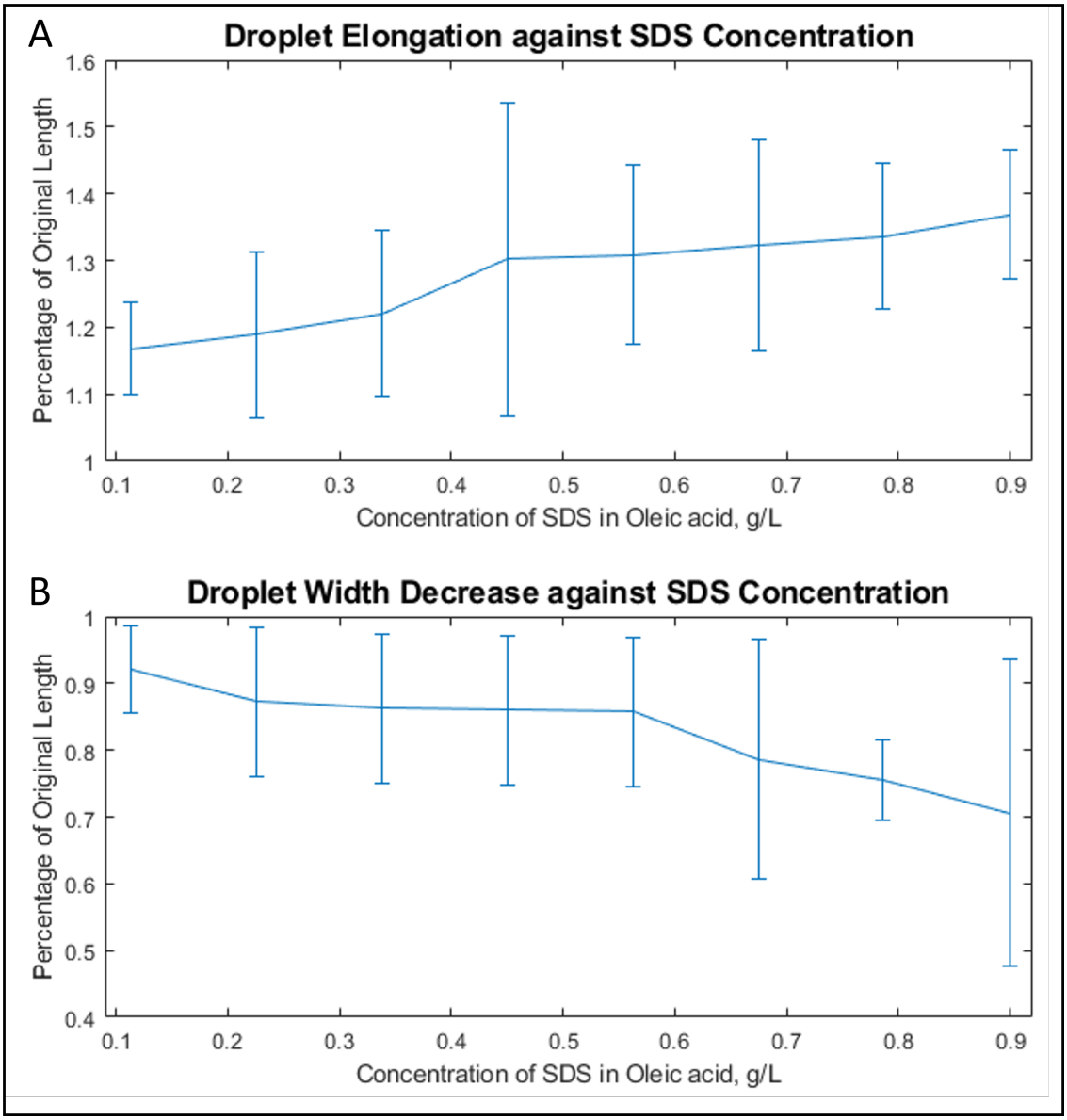

Figure 4.5: BZ droplets were subject to an alternating stimulation regime, in which an AC field with a polarity switching period of 2 minutes was applied across the droplet externally. (A) Elongation of Droplet as a function of Sodium dodecyl Sulfate (SDS) concentration in Oleic acid. A linear trend emerges, where the increase in SDS concentration corresponds with an increase in the elongation of the Droplet. (B) The width decrease as a function of the SDS concentration is shown, where the increase in concentration results in a greater reduction of the width of the droplet. This data is correlated with graph (A) showing the linear increase in elongation as a function of SDS concentration. The error bars in both graphs represent the standard deviation.

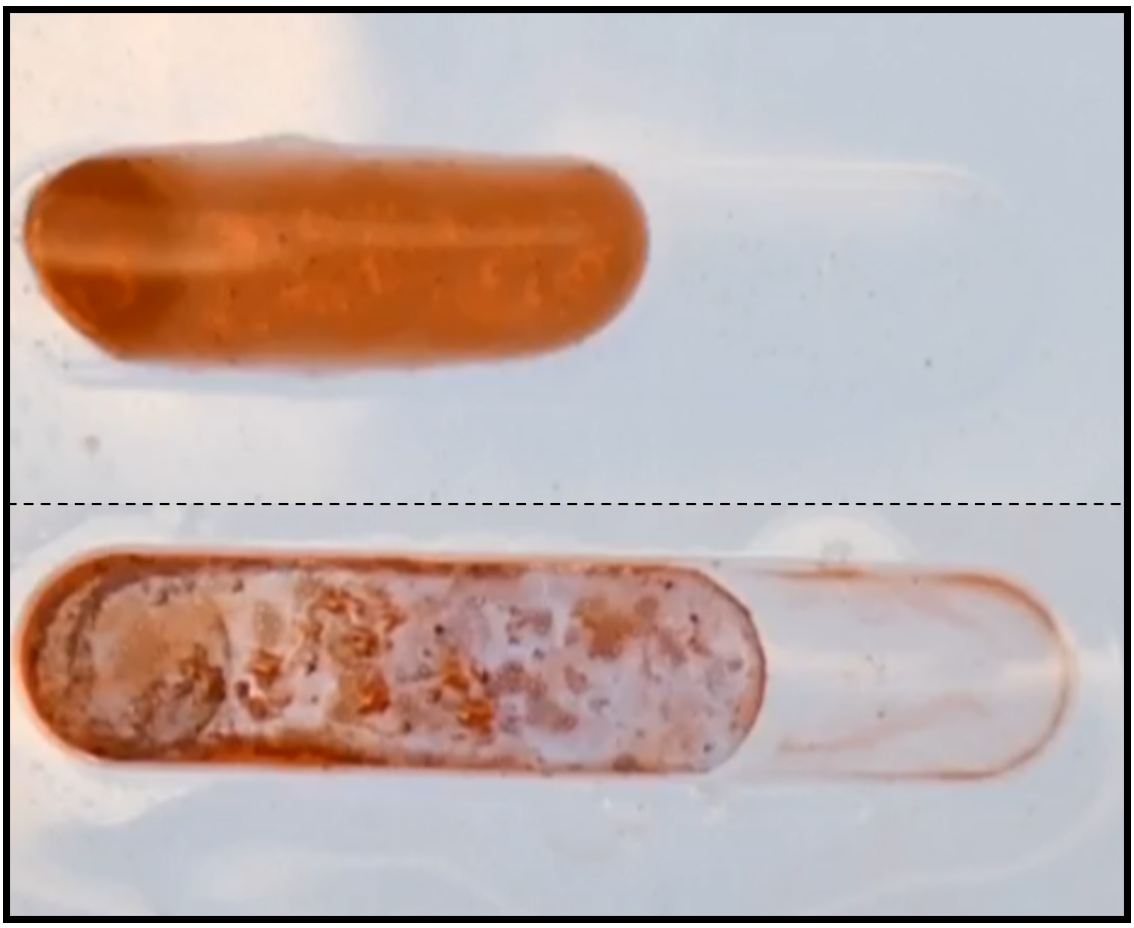

Figure 4.6: Elongation of non-dividing BZ droplet. The droplet cannot undergo further elongation due to the BZ reaction reaching thermodynamic equilibrium. Trace amounts of brominated-SDS can be observed in the reaction vessel.

tion[315, 316]. Along with the AC field inducing the tripole effect throughout the droplet, an increase in the elongation phenomena was observed in the droplet. The effects of which can be observed in figure 4.5, and table 8.1.

A significant note to make follows from the electrotaxis effect, where the magnitude of the chemically driven translational displacement was recorded to be around 2mm depending on the stimulus applied to said droplet [317]. Whereas in this scenario a much greater elongation was achieved. This is important to note, due to the occurrence of deformation in the elongating droplets. This deformation is due in part to the change in the interfacial tension between the droplet and the oil phase. However, due to the employment of surfactants at the interface between the oil phase and the aqueous droplets, this interfacial tension is reduced, which presents interesting phenomena where the elongation of the droplet far exceeds the original translationally motion observed in the travelling droplets.

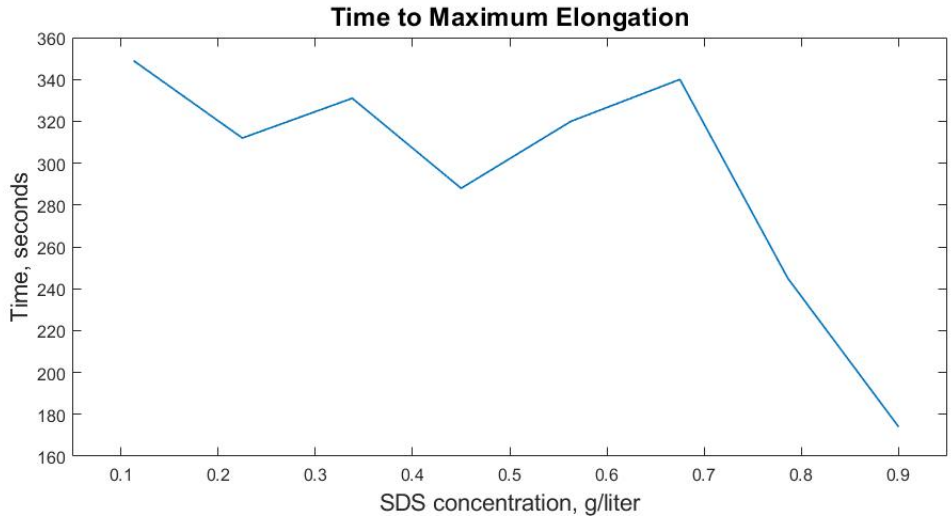

Figure 4.7: The time taken for BZ droplets to reach maximum elongation. BZ droplets were suspended in an oil phase with varied concentrations of the surfactant, SDS. The SDS concentration ranged from 0.113g, up to 0.9g per litre of oleic acid. At the lower range of concentrations, up to 0.675 per litre, the time until the maximum elongation is reached is around 5 minutes, however, this rapidly decreases as the concentration is increased to 0.786g and 0.9g per litre.

Figure 4.6 shows the elongation of a non-dividing droplet. No further elongation will be possible due to the BZ reaction reaching thermodynamic equilibrium, where the wave generation ceases due to the inability to generate subsequent LCs. With the maximum SDS concentration, it takes the droplets between 20 and 25 minutes to reach thermodynamic equilibrium. At this point, the droplet will appear to be homogeneously blue, with no Ferroin in the reduced state. The lack of deformation is noticeable as well, as there is no mechanical work being performed to drive this phenomenon. There is a trace amount of brominated-SDS visible in the reaction vessel, due to the SDS leaching excitatory chemical species out of the droplet, which pushes the BZ reaction further towards thermodynamic equilibrium, inhibiting the reaction from continuing and shortening its lifecycle. SDS is known to catalyse the bromination process [321, 322]. The SDS resides at the interface between the oil phase and the aqueous phase of the droplet, due to its structure containing a hydrophobic end, and a hydrophilic end. The SDS in contact with the excitatory chemical species in the droplet (bromate) will cause the bromination to occur, which will result in the bromine leaching from the droplet and into the oil phase as brominated-SDS. This effect is visible as an orange hue forming a sort of halo around the droplet, shown in the appendix figure 8.37.

Figure 4.7 shows the average time taken for the BZ droplets to elongate to the maximum

length they reached. This elongation was achieved without the division event taking place. There is a slow trend of decreasing time as the concentration of the SDS within the oil phase is increased from 0.113g to 0.675g per litre. The time rapidly decreases when the concentrations are set to 0.786g, and 0.9g per litre. The result of increasing the surfactant concentration is an accelerated elongation. In combination with the results presented in figure 4.5, the effect of increasing the surfactant is a greater elongation, in a shorter time period. The decrease in the time it takes for the oscillating BZ droplet to reach its maximum elongated length can be attributed to 2 main factors. The first is the reduction in surface tension making it easier for the aqueous phase to slide across the oil phase. The surfactant acts to reduce the interfacial tension, which means a smaller friction will occur between the phases resulting in less resistance to the elongation. The second factor for the increased acceleration of the elongation could occur from the perturbation on the droplet from the surfactant binding with the water of the droplet. This perturbation would cause the formation of the LCs to occur faster, which would result in quicker elongation due to the nature of the LC forming earlier. This would mean the conversion of chemical energy into mechanical work would simply occur earlier, therefore leading to a faster acceleration of the elongation.

4.4.2 Droplet Division Event

The optimization of the AC field stimulation regime to beget the greatest elongation was found to utilise a 0.9g per litre of SDS in oleic acid, whilst applying an AC field with a period of 2 minutes. These two conditions of the AC field and SDS concentration were utilised in further experiments to study the division of the BZ droplet.

Throughout the course of running experiments on individual droplets, only around 10% of the sample produced dividing droplets. A major factor in this low conversion rate is the specificity of the requirements which will lead to a division event occurring, but on top of this, the mechanical work required for the division event to occur is derived from the chemical reaction inside the droplet, which only has a specific time period it can be active for. More so, the lifespan of the droplet is inhibited by the surfactant present in the oil phase, which is required to create the specific conditions for the division event to be possible, whilst also acting as a limiting factor for the BZ reaction.

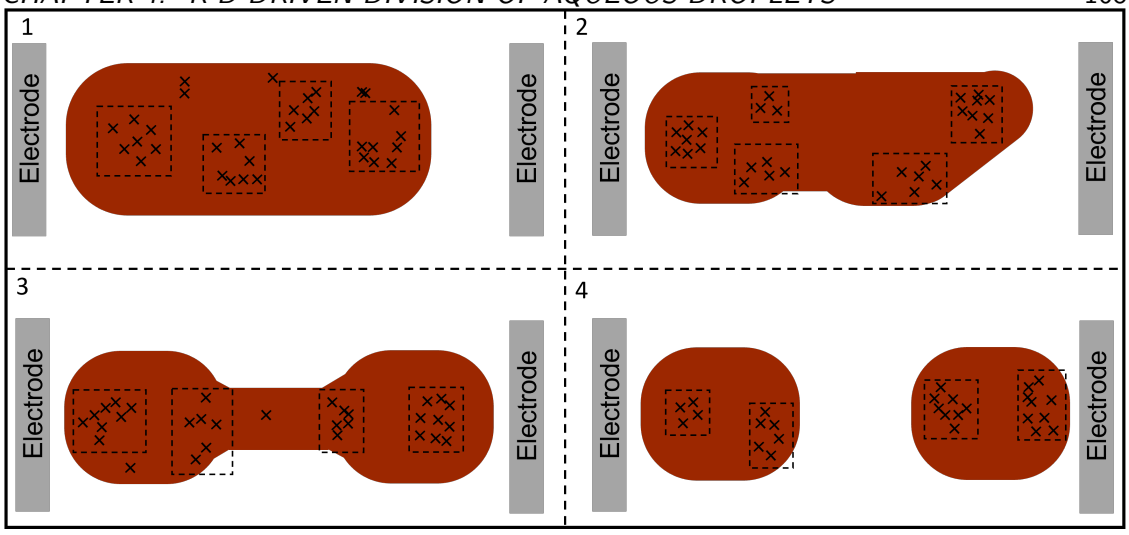

Figure 4.8: Diagram of LC distribution projected onto model droplets. The droplet shapes were extrapolated from observing a series of independent droplet division events and discerning a pattern in the shape deformation and elongation observed of the droplets. 4 shapes were observed within each division event. Panel 1 shows the initial shape where the initial LC formation takes place, prior to any deformation or elongation. Panel 2 represents the deformation stage, where the droplet begins to deform and elongate. Panel 3 represents an elongated stage where the deformation on the elongating end of the droplet has been reduced, and the width of the droplet then drastically decreases. lastly, panel 4 shows the stage where the droplets have divided into 2 sub droplets. The locations of LC formation within droplets undergoing division events were extracted and projected onto the model droplet for each stage in the division process. The 'x' within the droplet represents a location where an LC forms and the dotted box shows the segmentation of the groupings.

Observations were taken of elongating droplets which did not divide, showing that the chemical energy is converted into hydrodynamic forces within the droplet, corresponding to the elongation and deformation of the droplet, resulting in an increased surface area. The energy released through the BZ reaction is conserved as it is converted into the free energy from the increased surface area. This free energy is released upon the kinetic relaxation of the droplet as it returns to its original shape as the droplet minimises its surface area. The relaxation is kinetic due to the retroactive motion of the once elongated droplet, as the surface area is minimised so that the droplet has the optimal surface area to volume ratio. The kinetics of the relaxation does not involve the BZ reaction, as the motion is not chemically driven, it is simply entropic and enthalpic contributions leading to this motion. 96 total experiments were performed, observing droplets undergoing shape deformation and elongation. In total, 16 division events were observed, with 3 including microspheres to track flow within the droplets.

Figure 4.8 shows the distribution of LC formation projected within a model droplet rep-

resenting each stage in the division event. The shapes of the droplet at each stage in the division event were extracted from observing pattern formation within division events across independent experiments. The results of such analysis produced a series of 4 stages each droplet follows when undergoing a division event. The electrodes are shown for reference.

- Panel 1 shows the initial stage, where the droplet begins to form LCs distributed across the body of the droplet. This is because of the tripole effect generated by the AC field. As the electric field applied externally to the droplet is not static, and changes through time, there is a push-pull mechanism on the ions in solution within the droplet. This leads to an inhomogeneous density gradient of the ions, where some regions will have substantially more Br^- than others which results in a distribution of LC formations across the droplet, compared to a singular instance seen in Chapter 3. At this stage, there has been no shape deformation or elongation. However, due to the LC formation at the specified locations, there will be elongation generated by the flow directed towards the end of the droplet.

- Panel 2 represents the stage where the droplet has begun to elongate and is subject to deformation around the droplet centre of mass (CoM), and at the elongating end of the droplet. There is an inhomogeneous elongation towards the end of the droplet where the turbulent flow creates a pressure wave inside the droplet due to the liquid's incompressible nature. This is reflected in the figure where the top edge of the droplet protrudes greater than the bottom edge as shown in the pictures and diagrams. This deformation is not only found on the lower edge but also mirrored and found on the top edge. This was clarified to reduce the environmental impacts produced by the experimental setup.

- Panel 3 represents the next stage in the division process, where the deformation around the elongating end of the droplet has decreased in conjunction with the deformation on the CoM increasing and causing a drastic decrease in the width of the droplet. This stage shows the formation of the stalk structure, where the droplet has elongated, and so to preserve the conservation of volume, the width at the CoM has decreased.

- Finally, panel 4 represents the post-division stage, where the 2 sub-droplets have formed

following the division. The shapes the sub-droplets have assumed are due to the minimisation of the surface tension, resulting in two spherical droplets due to the surface area to volume ratio being optimised.

The LC formation within each dividing droplet through the series of experiments is extracted and projected onto the model droplets to show how the formations of LCs are distributed for each stage in the division event. A grouping algorithm is applied to segment the LCs into groups which is used to find their average position in the droplet.

Representative example of a single droplet

A representative example of a single droplet undergoing a division event is presented in figure 4.9, where an aqueous droplet containing BZ solutions was suspended in an oil phase saturated with surfactant sodium dodecyl sulfate (SDS) with a concentration of 0.9g/litre. The droplet was subject to an alternating stimulation regime where an AC field was applied with a 2-minute period, meaning the polarity switches every 60 seconds. The rhythmic formation of the LC distributed throughout the body of the droplet created the required conditions for the elongation and division of the droplet to occur.

The initial state of the droplet is shown in the top panel, where the minimum free energy state of the droplet was realised, and no LC formation has begun. The second panel shows the initial state in the division event process, where no elongation of shape deformation has begun to occur, but the initial formation of LC throughout the body of the droplet has begun. The LC formation occurs around the locations where the average positions of LC were found as shown in panel 1 of figure 4.8. The average positions were taken from the clusters of LCs forming within the droplets, shown with the dotted boxes. At this stage, LCs begin to form and induce flows due to the generation of Marangoni stress. The droplet will start to undergo shape deformation. The shape deformation is shown in the third panel, where the width decrease is beginning to occur, and the elongation has occurred in an inhomogeneous manner, where a leading edge forms, which extends through the oil phase, whilst the alternate edge appears to reduce in length. The deformation is driven by the friction between the oil phase and the droplet as the Marangoni flow induces motion in both phases. The motion

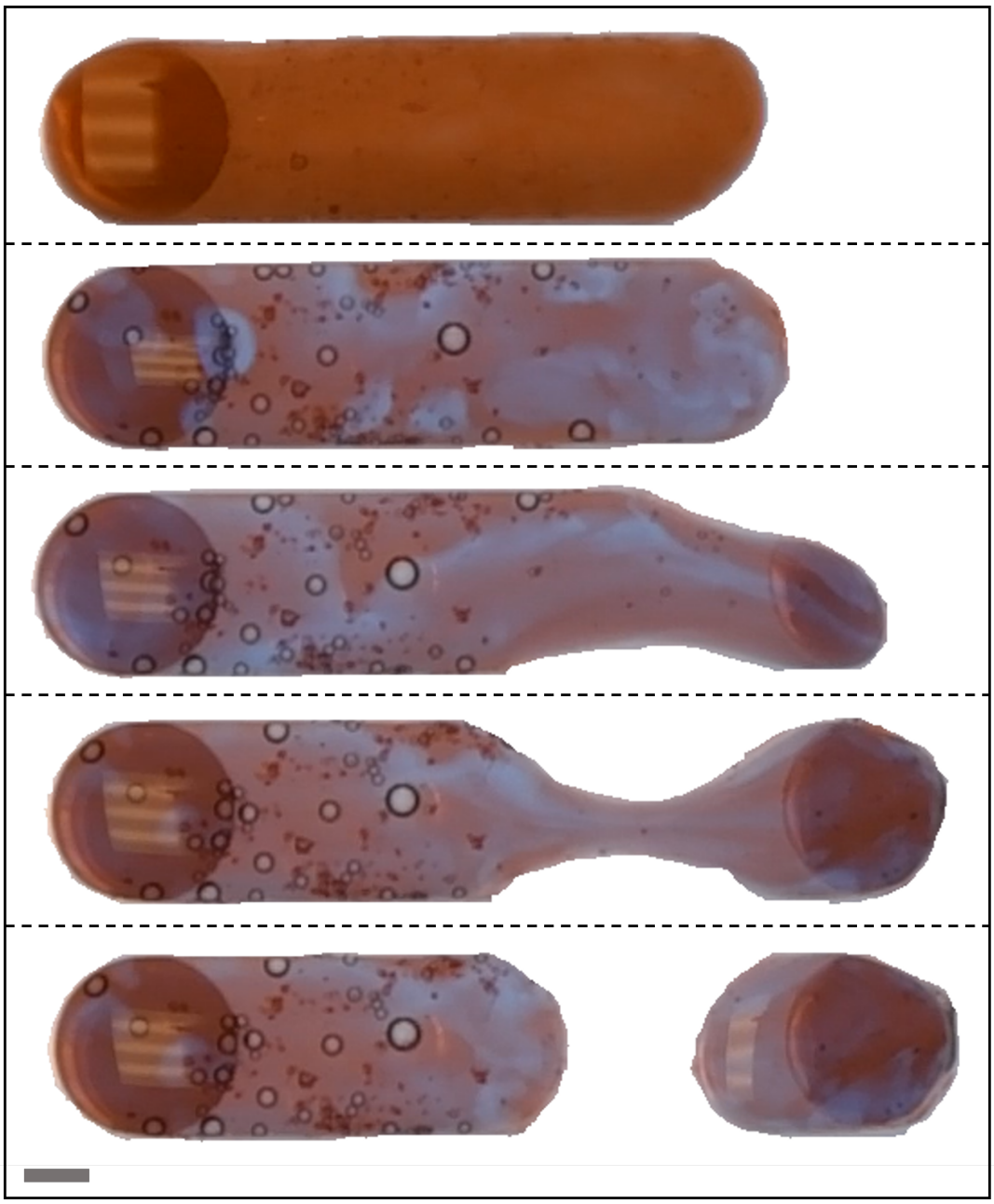

Figure 4.9: Successive images isolated from a timelapse movie to demonstrate each state the droplet undergoes from the natural resting state, through to division. The generation of leading centres (LC) across the body of the droplet can be clearly identified, and fit the representation displayed in the model of droplet division. The initial stage of droplet deformation can be found in the third panel down, where the elongation and width decrease is clearly shown in correlation to the LC formation throughout the body of the droplet. The deformation on the elongating end is due to the resistive forces acting as a mechanical perturbation on the droplet, from the surrounding oil phase. The next stage, shown in the 4th panel, shows the elongated droplet, as the elongated end of the droplet has normalised to the minimum energy state shape, with the resulting decrease in width, as the turbulent bulk flow within the droplet increases. The final panel shows the divided droplets, as they have returned to the minimum free energy state. The LC formation within these sub-droplets can be seen at each end of the droplet pair. The visible bubbles are CO_2 forming as a by-product of the BZ reaction. The scale bar represents 2mm.

is induced from the flow induced by the Marangonis stress between the 2 liquid phases, generated by the many gradients of interfacial tension, as multiple LCs produce propagating waves through the droplet. In combination with the increased SDS concentration in the oil phase (see 4.7), this results in the rapid elongation of the droplet. However, the resistance from the oil phase is much greater, due to the speed at which the droplet is elongating. The elongation occurs in a much shorter time span when compared to an unperturbed droplet in an oil phase containing no surfactant. Therefore, a greater force must be overcome by the elongating droplet, which results in shape deformation of the elongating end of the droplet. The viscosity of the oil phase acts as a limiting factor to the rate of elongation but does not inhibit elongation, rather it deforms the droplet. Once the droplet has reached its elongated state and holds the position for long enough, a mass transit flow can be generated from the droplet CoM, to compensate for the deformation at the ends of the droplet. The flow will allow the volume at the end of the droplet to increase and form a spherical shape to reduce the free energy by reducing the ratio of volume to the surface area. This effect will decrease the width at the CoM, as the volume of the droplet at that region will be decreased.

This elongating motion of the droplet in the oil phase drives hydrodynamic flow which acts as mechanical perturbation and causes the droplet to retract on the opposite side to the elongating end, exacerbating the effect of deformation on the droplet, and driving more turbulent flow through the body of the droplet (see fig.4.10). The retraction is also induced by the surface tension minimising the surface area, and acts as a contributing factor here. The whole process resembles the cell membrane budding which is driven by free energy minimisation [323, 324], including surface free energy. In this example, some external factors drive its elongation, and internal flows compensate for the mass transit of the droplet, whereas in the droplet division, we find that the internal flows play a crucial role in the division event starting (see fig.4.9).

After a brief amount of time, varying between experiments, but usually, in the order of 10s of seconds, the forces acting on the elongated end of the droplet will equalise, causing the end to return to the minimum energy state where the spherical shape shown in the fourth panel of figure 4.8. The equalisation of forces between the viscosity of the oil phase and the surface free energy of the droplet follows the minimisation of the free energy as the droplet resumes a spherical shape to optimise the surface area to volume ratio, as the droplet performs

mechanical work as a conversion from the chemical energy to hydrodynamic forces through the BZ reaction to overcome the resistance from the viscosity of the oil phase. Without the BZ reaction, the droplet would form a spherical shape as a minimisation of the surface area. However, this would only occur through the kinetic relaxation of the droplet, as opposed to this example, where the kinetic relaxation does not occur. This is due to the mechanical work being performed as a result of the conversion of chemical energy from the BZ reaction causing the elongation to be sustained. This spherical shape formation is met with the mass transit from the CoM to compensate for the droplet volume.

This further increases the turbulent flow acting in the CoM of the droplet, as another source of flow away from the droplet CoM is introduced. Consequentially, the width decrease is further exacerbated and a pinching-like action is observed at the centre of the body of the droplet. The equalisation of forces on the elongated end of the droplet where the positive curvature forms due to the minimisation of free energy balances out the deformation from the viscosity of the oil phase applying resistance on the elongating droplet. The turbulent flow at the centre of the droplet leads to the division, as the width decrease becomes so great that the droplet will separate into two sub-droplets, shown in the bottom panel. These droplets quickly reach the minimum free energy state where a pair of spherical droplets form, still with active LC formation distributed across the body of the droplet.

PIV analysis for hydrodynamic flows

The next step is to study the internal hydrodynamic flow of the droplet during a division event, microspheres were suspended within the droplet and tracked visually. The suspension of spheres reveals how the flow through the droplet affects the elongation and shape deformation during the division event.

The PIV analysis performed in figure 4.10 shows that complex vortex-like flow is present throughout the droplet, particularly at the elongating end of the droplet shown in panel a. The streamlines and colour map of the particle speeds have been generated by analysing timelapse video footage of the dividing droplet containing tracking particles.

Panel a in Fig. 4.10 shows the droplet in the first deformed stage prior to the division where the LC formation has induced a complex chaotic motion within the droplet, and the

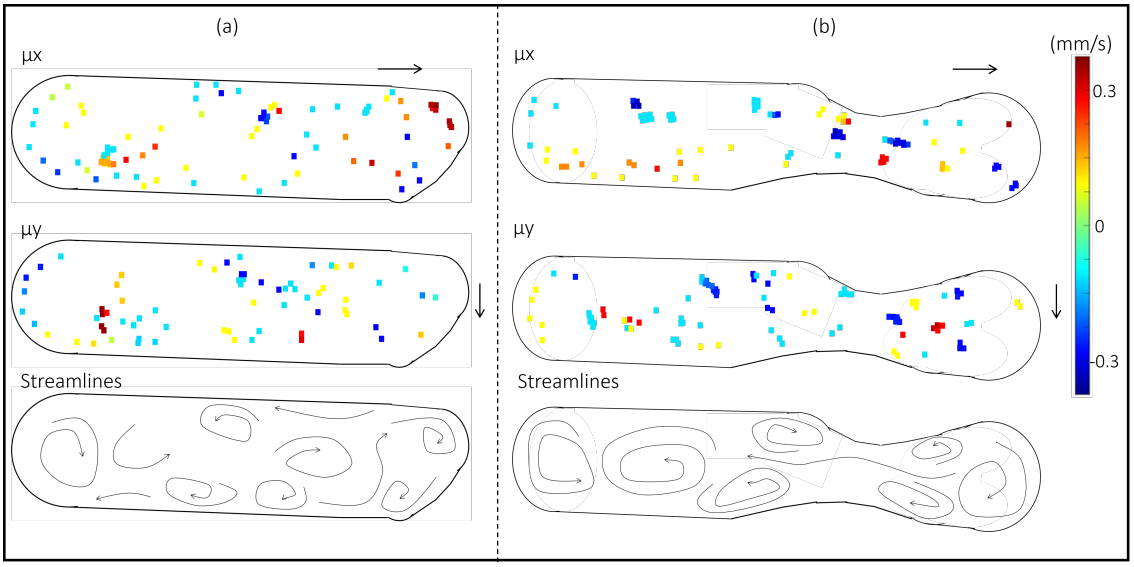

Figure 4.10: PIV analysis of a dividing droplet. (a) displays the state of droplet deformation, where the LC formation has begun to cause the droplet to elongate and become deformed, and (b) shows the elongated state prior to division, where the shape deformation has caused a reduced width of the droplet. μx shows the speed of particles travelling in the x direction, across the droplet from left to right, and μy shows the speed of trace particles travelling down in the y direction. The directions are marked with black arrows. The bottom row shows the streamlines generated from tracking multiple particles suspended within the droplet whilst it divides.

inhomogeneous elongation has begun to occur. The turbulent flow is generated by the collisions of the waves propagating from the multiple LC formations. The oxidised chemical wave annihilates as the waves collide, but the surface flows do not. Instead, they act as compressive forces on one another and cause the body of the droplet to deform, as the conservation of droplet volume is maintained, and the mass transit of BZ droplet is observed due to a compensatory bulk flow from another region within the droplet. This bulk flow adds to the coherent structure within the droplet, as other flow regimes are disturbed. The clockwise and anticlockwise vortex rings can be observed within the flow figure. The streamlines are shown to be colliding, whilst flowing in an antagonistic regime. If both flows were following the same trajectory, then the effect would be to increase the velocity, as one region absorbs the other. However, as we observe alternate directions for the flows, the compressive forces act on the flows, which leads to droplet elongation, as there is a momentum transfer between the flows. To compensate for this elongation, there is a bulk flow inside the droplet, and a corresponding width decrease which presents as negative curvature on the body of the droplet. Panel b shows the phase where the resolution of the deformed elongated end has occurred, where the

resistance from the oil phase causing deformation on the elongating end of the droplet has normalised due to the minimisation of free energy to preserve the optimal ratio of surface area to volume. A great width decrease at the droplet CoM has occurred, where the conservation of droplet volume requires a diminishment of width to compensate for the bulk flow towards the elongating end of the droplet. The vortex flow around the CoM of the droplet where the width decrease occurs supports the previous findings in figure 4.8, where the LC locations were found in the same locations. The turbulent flow observed visually during the division events can be attributed to the accelerated flow within the droplet at the locations where elongation and shape deformation are observed.

These fast flows will act to elongate the droplet at a much more accelerated rate than the standard conditions, which leads to the deformed elongation as a result of the droplet's requirement to overcome the inertia of the much more viscous oil phase it resides within.

Along with the vortex flow regime generating complex chaotic motion leading to compensatory bulk flows at the centre of the droplet due to the conservation of droplet volume causing a drastic deformation. A bulk flow is a mass transit at the centre of the droplet, as opposed to the droplet edge, which typically acts as a compensatory measure for a surface flow induced by the Marangoni effect, or in response to droplet elongation. The width decrease at the droplet CoM is remarked by the vortex flows away from the CoM, leading to less of the droplet volume in this location, and more at either end which eventually leads to the droplet division.

Further analysis can be found in the appendix (see figures 8.2 - 8.7), where a less coarse-grained approach to the time-segmenting is taken to help explain the flow-induced deformation and elongation of the BZ droplet.

The flow at the pinch point created by the formation of the stalk structure has increased in velocity, which is expected due to the continuity equation in hydrodynamics:

$$A_1\nu_1 = A_2\nu_2 \tag{A}$$

Where A refers to the cross-sectional area, and ν refers to the velocity of the flow in that region; as the cross-sectional area of the droplet decreases, the flow velocity within

the droplet at that region will increase. Therefore, as the stalk structure forms within the droplet, any flows generated by an LC formation will be accelerated through this region due to the contraction of the droplet width. A flow with a greater velocity will logically carry a greater momentum, which will have the impact of further elongation when directed against the end of the droplet. As the droplet acts as a continuum with no defined fixed points, the accelerated flow will create a disturbance on the elongating end of the droplet and alter its shape and dynamics.

This will have an impact on the internal forces derived from the surface tension as the morphology of the droplet changes, but also in the other flows derived from subsequent LC formations as the decrease in width due to the elongation will cause an acceleration on the flows due to the continuity equation.

Whilst the deformation is the most easily visible impact this flow regime has on the droplet, the increased velocity also acts as a disturbance to other flows in other regions. This increased velocity acts as a contributing factor to the turbulent flow regime, which can be visualised by the PIV diagram. The regime of turbulent flow will contribute further to the deformation of the droplet, which will lead to even further elongation, as the droplet will conserve its volume under the deformation it undergoes. This acts as a mechanism of a positive feedback loop of more elongation, leading to more deformation, and more deformation leads to further elongation.

4.4.3 Droplet Division Requirements

Figure 4.11 outlines the required conditions which need to be met for the division event to occur. The locations for LC formations within the droplet appear to be significant due to the importance of the chaotic flow in creating the droplet's elongation and deformation.

It was found that an AC field with an operating period of 2 minutes was capable of perturbating the droplets in such a fashion that the push-pull effect of the changing electric field created distinct regions within the droplet where LC formations would occur. This arrangement in LC formation is believed to be responsible for the optimal formation to generate the chaotic flow regime within the droplet.

The BZ reaction's lifecycle is another crucial factor in the division event occurring, as the

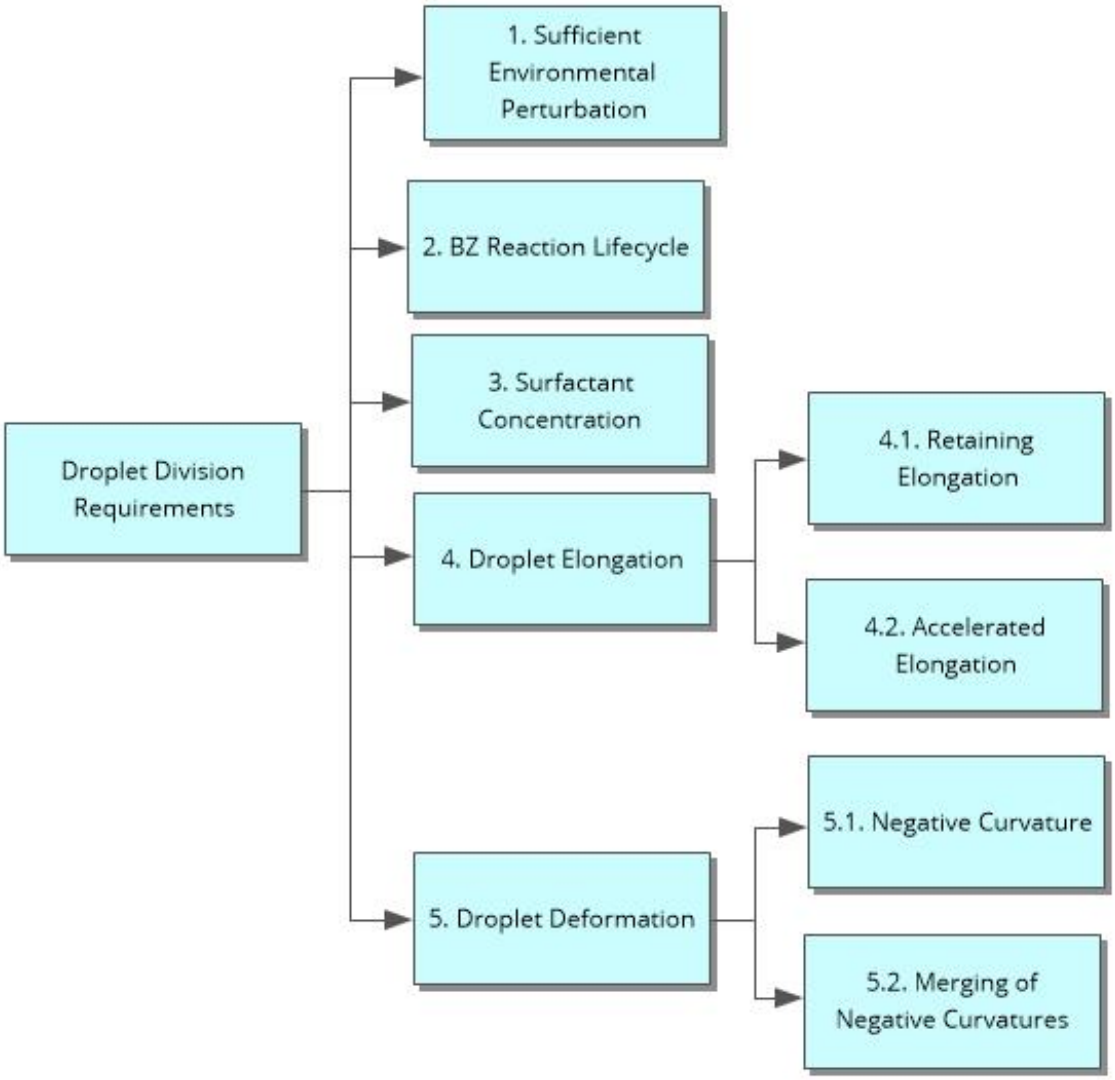

Figure 4.11: Requirements for the division of the BZ droplet to occur. The requirements involve sufficient environmental perturbation, in this study, we present the application of an external AC field for this. The BZ reaction lifecycle is a crucial requirement, as it is the energy that fuels the mechanical work to elongate the droplet. The surfactant concentration needs to be chosen carefully, as too low will not decrease the surface tension enough, but too high will lead to the breaching of excitatory chemical compounds from the BZ droplet which will decrease the BZ lifecycle. The droplet elongation requirement is coupled with the deformation stage, as neither can happen individually. The importance of the droplet's elongation and deformation cannot be understated, as the morphological changes are crucial for the division event to proceed.

chemical reaction is the fuel for the mechanical work to be performed. No further deformation or elongation will be driven without the oscillating BZ reaction. The lifecycle however can be diminished by the surfactant concentration, so a balance of enough SDS to produce a high enough decrease in surface tension, yet not being so high as to deplete the droplets' ability to produce LCs must be found.

Some diminishment of the lifecycle can be afforded, so long as it does not decrease the droplets' capacity to perform mechanical work prior to the division event taking place. Through the course of our pilot study and comprehensive experimentation, we discovered that the maximum concentration we could utilise was 0.9g of SDS per litre of oleic acid. Increasing the surfactant concentration further led to a leaching of the excitatory chemical species and degraded the BZ reaction to the point of no LC formations.

Upon increasing the surfactant concentration above the maximum stated concentration a formation of brominated-SDS appears around the border of the droplet in a halo formation. This is observable in appendix 8.8, where the red colour in the oil phase is the brominated-SDS. An example of a droplet which reached thermodynamic equilibrium prior to a division event occurring is available in figure 4.6. The BZ reaction was inhibited by the leaching of excitatory chemical species by the surfactant in the oil phase. A trace amount of brominated-SDS is present in the oil phase having leached from the droplet.

Point 3 proposes the surfactant concentration in the oil phase. In this study, we found that 0.9g of SDS per litre of oleic acid was sufficient to allow the surface tension to be adequately decreased, without the surfactant leaching excitatory chemicals from the BZ droplet. The extent of the leaching effect is viewable in the appendix 8.8, where the leaching of excitatory chemicals is visualised by a red hue surrounding the border of the droplet. This chemical complex would slowly diffuse through the oil phase, but with the interruption of the longitudinal wave generated from pressure derived from the deforming droplet. This pressure was visualised by the red chemical in the clear oil phase and promoted the use of plastic microsuspensions as trace particles within the droplet to visualise the internal flow. Upon altering the surfactant concentration in the oil phase, we discovered a linear increase in the elongation of the droplets as the concentration was increased. Therefore, to maximise the droplet elongation, and therefore the division, the greatest surfactant concentration which does not inhibit the BZ lifecycle should be employed.

Points 4 and 5 are coupled, as the elongation cannot occur without any deformation occurring due to the conservation of volume. As the surface area increases, the morphology has to change to account for the volume remaining constant. The droplet needs to elongate sufficiently to allow for the deformation to cause the division event to occur. The accelerated elongation appears to be a factor in the division, due to the correlation between this event,

and the increase in deformation observed. It is also plausible to suggest that the accelerated elongation is due in part to the acceleration of the complex chaotic motion within the droplet increasing the momentum of the BZ solution travelling toward the elongating end of the droplet, which only furthers its elongation. The acceleration of the elongation is presented in figure 4.7, where the surfactant impacted the elongation such that increasing its concentration caused such a reduction of the interfacial tension between the oil phase and the aqueous droplet, that the reduction in the friction allowed the droplet to elongate at a much greater rate. Another attribute the SDS contributes is the effect of perturbating the droplet into producing LCs at a greater rate, leading to the elongation occurring sooner than in experiments with a lesser concentration. The deformation can be presented as so-called 'negative curvature', where the decrease in the width of the droplet appears to follow the opposite morphology of the curvature realised when surface tension alone acts on the droplet. This type of curvature is apparent at either end of the droplet prior to wave formation or any deformation. When the width of the droplet decreases, the flow within the droplet is accelerated, and therefore carries more momentum. This will heighten the chaotic flow regime, and also act to further elongate the droplet. The greater the droplet deformation, the greater the reduction in its width, which logically would suggest that the deformation is the most prominent aspect of the division event. Merging of two areas of negative curvature can induce the division of the droplet, where two regions of negative curvature are occurring on the same side of the droplet, and converge, leaving one much greater negative curvature, which leads to the division event. Alternatively, if there are two negative curvatures on alternate sides of the droplet, the act of the deformation sites merging is a division in itself. Each of the five points listed acts in a feedback system where interplays between separate phenomena impact the droplet on different scales and timeframes, ultimately resulting in its division. When the elongation takes place, the end of the droplet extruding further into the oil phase will encounter resistance from the viscosity of the oil phase. This will result in a deformation of the droplet. If the mechanical work can be maintained for a great enough duration, then the equalisation of the forces, where the minimisation of the free energy at the end of the droplet can take place, acting to reduce the surface area to volume ratio. The resolution of these forces will result in a compensatory flow from the CoM towards the elongated end, to conserve the droplet volume. This will further reduce the width around the centre of mass, where the

regions of negative curvature will be increased, which will lead to even further deformation and elongation due to the acceleration of the flow through this stalk structure due to the continuity equation.

The culmination of the 5 main requirements for the BZ droplet division will correspond with fast elongation and deformation, with an active BZ droplet causing time-dependent laminar flow within the droplet, causing complex behaviours which lead a feedback loop for greater elongation and more severe deformation. If the time requirements are fulfilled, where the BZ reaction has not been diminished by the surfactant present in the oil phase, and the forces causing the droplet to elongate can resolve, then the division will be possible. This can either be instigated by two regions of negative curvature on the same side of the droplet, merging. This creates a much greater negative curvature region, which will cause the stalk structure to form in the droplet. The stalk structure, or neck, will create a choke point within the droplet, which acts to accelerate the flow due to the continuity equation in hydrodynamics. This only further elongates the droplet and contributes to the regime of complex, chaotic motion within the droplet. Alternatively, two regions of negative curvature on alternate sides of the droplet will line up to create said stalk structure, having the same effect as the singular, large, negative curvature. If the reaction can continue to generate mechanical work then a division event is imminent.

Following our previous study of droplet elongation, the model of droplet elongation has been extended to model the division of droplets. Figure 4.12 shows the mechanism detailing the process of a droplet undergoing division, where the behavioural characteristics of repeated droplet division events have been characterised onto a model droplet. Following the analysis in figure 4.8, where the LC positions were extracted and projected onto the model droplets, the average positions of the LCs were calculated and projected onto the model droplets here, as shown with the blue empty circle. The flow within the droplet as a result of Marangoni stress between the droplet and the oil phase is depicted with the black curved arrow within the droplet. Finally, the straight black arrows external to the droplet represent the shape deformation and elongation of the droplet and show the direction this motion occurs in. Panel 1 shows a single droplet with the formation of many LC inhomogeneously throughout the droplet. These LCs form a chemical wave which propagates across the body of the droplet. The flow induced by Marangoni stress[315, 316] between the droplet and the oil phase it resides

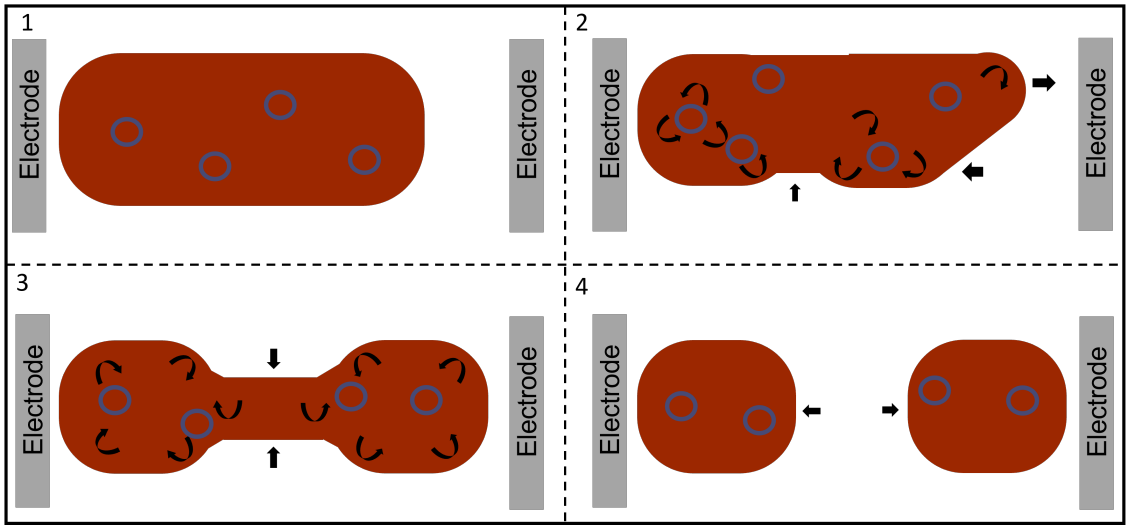

Figure 4.12: Schematic model of droplet division. Independent droplet division events were categorised to produce a schematic model of the droplet division, the shape deformation of the droplet was tracked between divisions and a corresponding pattern is formed. The distributed LC formation is subject to a grouping algorithm to determine the average LC location corresponding to the division event occurring. The diagram visually depicts how the flows interact and create hydrodynamic forces that lead to the deformation and division of the droplet. The black curved arrows represent the flow internal to the droplet, and the straight black arrows represent the deformation of the droplet. The blue circles represent the LC locations within the droplets. The flow and leading centre location within the droplets are indicative of typical division events and were taken as an average across independent divisions. Panel 1 shows the droplet at rest, prior to shape deformation. In this state the droplet shape lies at thermodynamic equilibrium and the beginning of the leading centre formation is due to occur. Panel 2 represents the initial deformation stage, where the rapid elongation causes an inhomogeneous shape deformation on the body of the droplet. As the droplet elongates, there is a large frictional force to overcome from the oil phase, which results in the deformed elongation of the droplet. Vortex flows within the droplet create a regime of complex motion within the CoM which creates a decrease in the width of the droplet, as the shape of the droplet compensates for the spiral flows around each end of the droplet. The deformation of the droplet can be observed as a negative curvature along the surface tension. Panel 3 represents the elongation stage and shows the state where the droplet has elongated and decreased in width. Flow vortices occur at each end of the droplet, travelling in alternate directions. At the same time, there exists flow at the centre, the deformed portion, of the droplet, which results in greater bulk flow within the droplet as a compensatory measure for the now greater distribution in the droplet volume across a wider space. This further accentuates the elongation and width decrease that is observed. Panel 4 shows when the droplet has divided into 2 sub-droplets, the remaining leading centres are represented within the sub-droplets.

in.

Panel 2 represents the deformation stage of the division event, and is the stage within the division event where the droplet has undergone shape deformation due to the internal flows. The black arrows represent the deformation that occurs, the width begins to decrease from one side, as the right-hand end extends at one portion, and decreases in length at the other. The width decrease is believed to be caused by a tremendous bulk flow caused by chaotic motion inside the droplet as it conserves its volume whilst becoming distributed over a wider area. This occurs within the droplet CoM, where competing flows create a vortex-like complex motion at the centre, causing the volume to decrease as the flow rapidly leaves that area. This deformation is marked with a black arrow showing the width decrease around the CoM of the droplet. The rapid elongation is caused by the flow of oxidised wave of ferroin propagating across the droplet creating a gradient of interfacial tension, but due to the decrease in surface tension created by the addition of the surfactant. Rather than the typical translational motion which occurs in the absence of surfactants[315], we observe an elongation instead. Deformation of the end of the droplet is observed and is represented by the arrows showing the motion of the deformation at the end of the droplet. This is due to the droplet overcoming the frictional force exhibited by the oil in front of the elongating droplet. As the droplet is elongating much faster than a typical example of droplet elongation, the resistive force imparted by the oil phase is much greater, and such deformation occurs due to a flow being induced within the oil phase, allowing one side of the droplet to elongate, whilst the other undergoes a mechanical perturbation. A compounding reason for this deformation coupled with the elongation could be due to the propagating angle of the wave generation from the LC. As mentioned before, when the wave propagation is parallel to the millifluidic channel, there is an elongation, and whilst the propagation is perpendicular to the channel, a deformation is observed. Therefore, it is possible that when the propagating angle of the wave is at 45° to the chamber, then an inhomogeneous elongation is observed, due to the momentum transfer from surface flows across the droplet causing a bulk flow disproportionately across the end of the droplet. This causes the droplet to elongate inhomogeneously, rather than merely extending forward through the oil phase. After a short period of inhomogeneous elongation, it seems forces within the droplet, and in the oil phase, externally, will equalise, and the droplet will form a normal curved end, as shown in panel 3. Panel 3 represents the elongation stage

of the division and is the moment where the forces on the elongating end of the droplet have equalised, and the end of the droplet resumes the normal spherical condition, usually observed in a droplet at rest. However, due to the elongation, a great width decrease has occurred at both sides of the droplet around the CoM, represented by the black arrows pointing inwards about the droplet body. The position of the LC (taken from successive averages) is shown to create coherent structures at the CoM as a result of the flow from the vortex rings within the droplet. The natural resting state for the droplet is to minimise free energy and form a spherical shape, but as the droplet lies in a state above the minimum free energy, there are forces at play which act to minimise this energy state and cause the droplet to return to a thermodynamic minimum state of resting energy. As such, this will cause the droplet to keep elongating until two sub-droplets are formed, and the middle section connecting the two no longer exists. Panel 4 shows this post-division state, where 2 sub-droplets have formed from the original droplet after division. The black arrows show the retraction of the previous connecting point between the 2 sub-droplets. The LC locations are visualised with empty circles.

4.5 Discussion

It was uncovered that an alternating electric field applied to aqueous droplets containing Belousov Zhabotinsky (BZ) solutions was able to influence the extent to which the droplet could elongate. The alternating field was applied to the droplet to induce a tripole effect within the droplet to influence leading centre (LC) formation across the droplet's body. The position of the LCs is believed to impact the droplet's ability to elongate. It was found that the greater the frequency of switching in polarity of the AC field, the greater the elongation was observed in the droplet up to a certain extent. This was coupled with a greater shape deformation of the body of the droplet, where the greater the elongation, the smaller the resulting width of the droplet would be. However, at certain lower frequencies, even when the droplet was shown to elongate further than the control group with no AC field, the width decrease was no greater. This is believed to be due to the altered position of LCs in the droplet affecting how the flows form inside the droplet. A leading centre will cause the propagation

of an oxidised chemical wave through the droplet, which in turn develops Marangoni stress due to the gradient of interfacial tension [315, 316]. The Marangoni stress induces surface flows which impart a momentum transfer between the oil phase, and the aqueous phase of the droplet. This momentum transfer is what is responsible for the translational motion in regular droplets, but when a surfactant is present, it results in the elongation we present in this study. However, when a surface flow is present, a bulk flow is induced to compensate for the flow at the droplet surface. This bulk flow would react differently within the droplet as a different arrangement of LC formation becomes present. This could be due to the positioning, or the frequency with that they appear, but in the droplets subjected to the low-frequency AC field, it is believed that the bulk flow causes deformation in droplet thickness, rather than the width decrease, which compensates for the increased elongation, without the decrease in width. Another possibility for the decrease in the width, is the lower frequency interferes with the droplet's natural deformation which occurs under the constraints, but also when the AC field is applied at a closer frequency to the natural resonance frequency of the droplet. We expect the greatest shape deformation of the BZ droplet to occur at the period that induces the greatest elongation, and whilst the data did reflect this, the greatest deformation was observed within the period of 2 minutes, which did induce the greatest elongation. However, it was observed that the second greatest deformation was observed at the 3-minute period, rather than the expected 90-second, or 150-second period, which were the closest periods to producing the maximum elongation shown in the 2-minute period experiments. Along with this, it was found that generally the greater the period, the lesser the effect that the AC field had on the shape deformation of the droplet. This is believed to be due to the tripole having a smaller impact on the internal dynamics of the droplet, as its effect is diminished due to the slower alternation between polarities, meaning the droplet behaves more closely to the un-perturbed state, shown with the dotted line in the graphs of elongation and shape deformation. The position of the LCs within the droplet where the division was possible was presented in figure 4.8, where the clusters of LC formations were averaged to produce the mechanistic description shown in figure 4.12. The positions where the wave propagates from are important, but what is more important is the distance between the multiple LCs which form. When the chemical waves of oxidised ferroin meet, they will annihilate, however, the flows generated by the Marangoni stress will not. Instead, these flows will compress and exert

resistive forces onto one another to avoid compression. This will compose the turbulent flow regime and will cause elongation and deformation of the droplet. The continuation of the LC formations throughout the droplet will contribute to the turbulent flow and the increase of the negative curvatures which form around the droplet edge as it elongates. More turbulent flows will impact the region of the droplet where the negative curvatures lie, which can lead to multiple regions on the same side merging, or 2 regions on alternate sides creating a stalk structure. The stalk structure will constrict the flow, and cause accelerations on any flow passing through, due to the continuity equation in hydrodynamics. This is supported by figure 4.10, where the flow at the stalk structure is shown to be of a much greater velocity than in other regions. Once a sufficiently large region of negative curvature has formed, or where 2 regions of negative curvature on alternate sides of the droplet line up, the division of the droplet is inevitable. Here the reduction of the surface area to minimise the free energy will occur when the elongated droplet divides into 2 smaller sub-droplets. The mechanism of droplet elongation follows the basic principle of the translational motion found in Kitahata's paper detailing how the gradient of interfacial tension drives Marangoni stress, which induces surface flows in both phases, imparting a momentum transfer on one another, leading to the translational motion [230, 316]. The mechanism detailed in the articles published by Kitahata explains how the elongation was initiated. The presence of multiple LCs causes the deformation that we observe in the droplets. A push-pull mechanism can be developed inside the droplet as a pair of LCs form and produce waveforms anti-sync from one another. The dynamics of the interfacial tension produced in this schema would make for an interesting follow-up study, where the anti-phase nature of the chemical wave production could be controlled by utilising silver wire as a technique for generating a chemical oscillation. The push-pull mechanism would create prominent complex chaotic motion which could be attributed to the successive division events that occur following the generation of the regions of negative curvature, which occur following LC-generated vortex flow inside the droplet.

The elongation of the droplet is caused by the momentum transfer between the oil phase, and the aqueous phase of the droplet creating shear stress along the interface between the droplet and the oil phase, but due to the surfactant, rather than undergoing translational motion, instead, the droplet stretches, presenting the elongation we are studying here. The same mechanism is responsible for the deformation in these droplets, as the droplet lies in

the millifluidic channel, an LC forms which creates the gradient in interfacial tension, driving Marangoni stress, and therefore inducing the surface flows that apply the momentum transfer observed in the droplets undergoing translational motion [317]. In the same manner, the momentum transfer causes elongation when the shear stress is along the plane of the millifluidic channel. When it is perpendicular, the droplet cannot elongate, or move translationally, so deformation is observed. There will be a bulk flow to compensate for this deformation and surface flow, which will act further to elongate the droplet. For the elongation of the droplet to be possible, the stretching force must overcome the forces from the surface tension. The formation of LCs within the droplet generates mechanical work which causes the stretching and elongates the droplet. It is remarked that the elongation observed in the droplets is greater than the magnitude of the translational motion observed in the travelling droplets studied in chapter 3. The median droplet in the class of droplets which were found to elongate and divide the most would elongate up to 1.4 times the original length of the droplet, which is a remarkable increase over the 2mm distance the droplets were found to travel in the electrotaxis study. This effect is caused by the fact the presence of the surfactant in the oil phase reduces the interfacial tension between the droplet and the oil phase. It was discovered that the process of the droplet undergoing chemically induced translational motion will cause minor shape changes in the droplet body, where a gradual elongation will be observed through the course of its motion. This is reflected yet amplified in the droplet elongation in our study, where the tremendous increase in elongation contributes to the division event occurring.

The distribution of LC formations is described in figure 4.4, and presented a clear pattern in the distribution of LCs when the period of the AC field was around 120 seconds. The formation of the LCs within the droplet produces a distinct pattern where 4 segmentable regions with densely packed LCs form, with open areas with minimal to no LC formations within. This formation is believed to be responsible for the increase in elongation we observe in the droplets subjected to an AC field, and especially in those subjected to the 90, 120, and 150 second period of AC field, where the elongation is shown to be increased over the other conditions, and the control group with no field application. The LC formations were studied further in the dividing droplet where the average positions of the LC formations which lead to the division state were categorised by collecting the LC locations from multiple experiments

and projecting them onto a model droplet where they were segmented into groups. The average position of each group was used to determine the LC position in the mechanistic view of the division events. It is believed that the position these groups fall into has a corresponding effect on the internal dynamics of the droplet stability. The source of the internal turbulence that causes deformation lies in the LC formation, and subsequently where the LC forms will have a demonstrable effect on the elongation and deformation prior to division. In order to quantify the effect the turbulent flow inside the droplet has on the internal dynamics, the flow was observed and analysed. Particle image velocimetry (PIV) analysis was undertaken to observe the nature of the internal flows within the droplet, and how the coupling between the chemical activity and hydrodynamic flow came about. The flow trajectories within the droplet were then projected onto the model droplet to help explain the primary cause of the deformation, which aided in the understanding of how the deformed elongation took place. The PIV analysis produced gainful results which validated the mechanism of division shown in figure 4.12. The flow of microspheres was tracked between successive frames to show the flow trajectory internal to the droplet. This helped to explain the inhomogeneous deformation and elongation of the body of the droplet, which led to the division event occurring.

Studying the flow within the droplet revealed that many sources of vortex-like flow are responsible for the elongation and shape deformation of the droplet. A pair of vortex flows will act as a compressive force on one another, which in turn imparts a momentum transfer due to the nature of liquids being incompressible. The momentum transfer mainly acts to elongate the droplet, but a secondary effect of shape deformation also results due to 2 factors. The first is the mass transit of a volume of the droplet away from the CoM towards the elongating end. This reduces the droplet width due to the conservation of mass, as the droplet elongates there needs to be a reduction in width to account for the volume decrease at this region. The second factor in the width reduction lies in the bulk flow generated by turbulent interactions of antagonistic flows within the droplet. This negative curvature which is created when a pair of antagonistic vortices collide creates an emphasis on further elongation and deformation occurring. This generation of the pressure induced by this interaction will often create a sink for the volume of the droplet which causes a flow inside the droplet great enough to overcome the surface tension of the droplet. Once the surface tension has been sufficiently overcome,

the droplet will be able to elongate to a length at which a division occurring incurs a smaller energy cost than the droplet returning to its original size will. More information regarding the study of the flow presented in particle image velocimetry analysis can be found in the appendix (see figures 8.2 - 8.7). The flow diagrams helped to uncover the nature of the division as a response to the internal flows creating an elongation and deformation, which causes an increase in surface tension, where the minimisation of which can be achieved through the division of the droplet, as this presents a lower energy cost compared to the droplet returning to its original shape.

Statistical analysis of elongation was carried out, and it was determined that the externally applied AC field, combined with the employment of the surfactant, produced statistically significant elongation of the BZ droplet suspended in the oil phase. The refinement of the perturbation applied by the experimental set-up produced the optimal conditions to produce the greatest elongation of the droplet. These conditions are to apply the AC field externally to the droplet with an operating period of 60 seconds, whilst the droplet is suspended within an oil phase of oleic acid, with sodium dodecyl sulfate (SDS) with a concentration of 0.9g/litre.

A descriptive mechanism for droplet division was uncovered and is described in figure 4.12. In the initial stages, an inhomogeneous distribution of the LC formation generates shape deformation about the body of the droplet and at one end. The decrease in width is caused by the generation of leading centres generating convective flow which causes a turbulent flow within the droplet centre of mass (CoM), which creates a turbulent flow effect through the droplet. This occurs in conjunction with the development of an LC at either end of the droplet, which under normal conditions would simply lead to the elongation of the droplet, but due to the internal turbulence, the flow causes an elongation on one side of the droplet, but not the other. The elongation occurs in such a manner, as the elongation occurs faster than a typical elongation, and as such, the oil phase applies a resistive force onto the droplet as there is friction between the phases. This causes the non-linear elongation of the droplet.

After a short period, the equalisation of internal and external forces occurs, due to the reaction-diffusion system driving the droplet out of thermodynamic equilibrium, where the

elongated end of the droplet will form a normalised shape, whilst remaining elongated. As the equalisation occurs within the elongated end of the droplet, the turbulence generated by the bulk flow as a compensatory measure in response to the uneven distribution of the droplet volume at the CoM still occurs but is only amplified by the flow from the CoM towards the elongated end of the droplet. This acts only to further increase the width decrease observed. This then eventually leads to the division, where the elongated state is held as the internal turbulence continues to be generated from the inhomogeneous distribution of the LC formation. Once the droplet has divided, the 2 sub-droplets return to the minimum energy state where they form into 2 spherical droplets.

Another major contributing factor is the merging of negative curvature along the body of the droplet. This occurs when 2 regions along the edge of the droplet are undergoing deformation where the width begins to decrease. The negative curvature refers to work being done against the surface tension, leading to an inwards curve into the body of the droplet, as opposed to the positive curvature that we see at either end of the droplet caused by capillary action. When 2 regions of negative curvature form along the same edge of the droplet, it is possible for these regions to merge to produce a single region of negative curvature, with much greater curvature. This region of deformation has a much greater impact on the droplet as it causes a far greater decrease in width than a singular region is capable of producing and greatly accelerates the division event. The merging of 2 regions with negative curvature creates a stalk structure, or neck, around the droplet CoM. At this point, the division event has a greater probability of occurring than the droplet returning to its original structure, so in order to minimise the surface tension the division event takes place.

Another form that can occur is when negative curvature regions form on opposite edges of the droplet, but meet in the middle, creating the stalk structure within the droplet that eventually leads to division. This is a more stereotypical depiction of a droplet division, but in fact, was a less frequent occurrence in the experimental procedure followed in this work. A possible explanation for this is due to the inhomogeneous LC distribution creating the turbulent flows that caused inhomogeneous elongation and deformation through the droplet, which lead to the negative curvature being offset from the droplet CoM.

The division has to happen within a limited timeframe due to the accelerated degradation of the BZ reaction due to the surfactant present in the oil phase. It is observed that at

sufficiently high surfactant concentrations the excitatory BZ species will leach out of the droplet and form brominated-SDS in the oil phase. This has a red appearance and forms around the droplet like a halo. This effect will diminish the lifecycle of the droplet and cease to produce LCs. Given the high surfactant concentration that was deployed, the lifecycle of the BZ reaction within the droplet was diminished, but not to the extent where the division event could be inhibited. In experiments where droplets failed to divide, it was often observed that the elongation and division were very similar to that observed in the dividing droplets, the difference was, that the droplet did not reach critical stages in the division event life cycle fast enough for the BZ reaction to have not been degraded enough by the SDS, that it was still capable to producing the mechanical work required to cause the division to occur.

The requirements for the division to be possible are described in figure 4.11, where the conditions within the droplet, and externally are laid out. The five requirements laid out are:

1. Sufficient Environmental Stimulation
2. BZ Reaction Lifecycle
3. Surfactant Concentration
4. Droplet Elongation
    (a) Retaining Elongation
    (b) Acceleration Elongation
5. Droplet Deformation
    (a) Negative Curvature
    (b) Merging of Negative Curvatures

The environmental stimulation has strict requirements, as you cannot simply apply an AC field to the droplets, the period needs to be modulated to a required frequency to allow for the push-pull mechanism to develop within the droplet, causing specific LC locations to form, allowing for the turbulent flow to generate the accelerated elongation and deformation (see fig 4.7). The BZ reaction lifecycle is crucial also, as there needs to be fuel for the mechanical work to be maintained. Using an increased surfactant concentration can degrade the

BZ reaction, and will inhibit LC formations, therefore limiting the lifecycle. The concentration of surfactant is crucial, as too little will result in interfacial friction which inhibits the droplet's ability to elongate sufficiently, whilst too much will degrade the BZ droplets' ability to produce LC formations. Droplet elongation and deformation are coupled, as neither exists without the other. The accelerated elongation will result in droplet deformation in the form of a negative curvature along the body of the droplet. If two of these regions on the same side merge, or if two regions on alternate sides line up, the width decrease will be so great that the flow at the CoM will be restricted. The decrease in the area will accelerate the flow due to the continuity equation from hydrodynamics, and will only further the rapid elongation and deformation, as a result of the momentum transfer and turbulent flow regime which is created.

The study of non-dividing droplets presented the results of the conversion of chemical energy into mechanical work causing the deformation and elongation of the droplet. This elongated droplet would eventually return to its original shape via the kinetic relaxation of the droplet due to the minimisation of its surface area to volume ratio. This presents a mechanism for converting chemical energy and mechanical work into potential energy. In the dividing droplets, this potential energy is not ignored, it is simply transformed into the kinetic relaxation of the pair of sub-droplets which form after the division, as they are shown to form the minimum surface area, post division. The non-dividing droplets subjected to the proposed optimal conditions shed light on time being a major factor in the division process. If the droplet does not divide in a certain time, then it is unlikely to undergo the division event due to the degradation of the BZ reaction through approaching thermodynamic equilibrium, but also from having key excitatory reactants leached from the aqueous droplet into the oil phase as brominated-SDS. This leads to the conclusion that the division event occurring is a balance between the conversion of chemical energy into mechanical work and the kinetic relaxation of the droplet. If the chemical energy lasts long enough the kinetic relaxation and forces from the surface tension can be overcome, and the elongation can be maximised leading to a division. If the chemical energy is depleted too fast, and cannot perform more mechanical work, then the forces from the surface tension will take over and kinetic relaxation will occur. A possible way to maximise this further would be a further refinement of the BZ recipe, where a decrease in the Ferroin and Malonic acid concentration, with an increase in sulfuric acid and

sodium bromate would increase the BZ lifetime, which could extend the droplet's ability to exert mechanical work, leading to greater numbers of division events.

4.6 Conclusion

In this chapter, we have presented the elongation and shape deformation of an aqueous droplet containing Belousov Zhabotinsky (BZ) solutions as a function of Sodium dodecyl Sulfate (SDS) concentration within the oil phase, and by the period of AC polarity switching. By carrying out sensitivity testing, we found that the alternating stimulation regime could be optimised to give the greatest elongation of the droplet when suspended in oil phase saturation with SDS. It was discovered that the 2-minute period of the AC field applied to the droplet produced the greatest elongation and shape deformation of the droplet and it was shown that there is a linear increase in elongation and shape deformation of the droplet as the concentration of SDS within the oil phase increases. Also presented within the paper, is the graphical representation illustrating the mechanism of elongation and deformation of the droplet, as it undergoes division.

The droplet division event occurs due to a multitude of variables, from the hydrodynamic flow within the droplet to resistive forces from the oil phase acting as a source of mechanical perturbation. The average leading centre (LC) location was determined and was found to play a role in the shape deformation which plays a crucial role in the division. It was learned that the internal flows within the droplet were responsible for initiating the shape deformation of the droplet. The flows were induced by Marangoni stress, which was generated by the propagation of the travelling chemical wave containing oxidised Ferroin solution. The flows cause turbulence due to bulk flow and antagonistic flows within the droplet, leading to a decrease in the width. This in combination with leading centres distributed to the ends of the droplets causes the rapid elongation of the droplet, but due to resistance caused by the oil phase surrounding the droplet, the elongation is inhomogeneous, causing deformation in the elongation. After this deformation normalises, and the droplet returns to the minimum energy state shape, the turbulent flow is then amplified around the centre of the droplet, leading to a greater width decrease, which eventually leads to the division of the droplet. The resulting sub-droplets are

quick to form the minimum energy state where 2 spherical droplets subside in the oil phase. A major factor in the division event occurring is the merging of the negative curvature regions. These regions are brought about by the turbulent flow within the droplet creating a compensatory bulk flow, along with the droplet volume being conserved whilst undergoing elongation. These negative curvatures work against surface tension, unlike the positive curvature, which we observe at the ends of the droplet due to capillary action before any deformation has altered the shape of the droplet. The negative curvatures act to decrease the droplet's width, so when 2 regions of negative curvature merge, a far greater decrease in width is produced. The regions can merge on the same edge of the droplet, which creates a stalk structure in the droplet CoM, or they can form on alternate sides of the droplet, which creates the stalk structure before they merge, which causes the droplet to divide. When the regions on the same edge merge, the increase in surface tension is so great, that it takes less energy for the droplet to divide, than to return to its original shape as a method for surface tension reduction.

The chemo-hydrodynamic coupling was realised as another major driving mechanism for the water in the oil droplet division. The propagation of a chemical wave through the body of the droplet induces the hydrodynamic flow within the water droplet and oil phase. This flow is what drives the elongation of the droplet, as friction between the 2 phases exists. This causes a momentum transfer between the phases which normally leads to translational motion, but in this case, due to the surfactant, results in an elongation of the droplet. Because there is a distribution of LC formation throughout the droplet, induced by the tripole effect created by the application of the externally applied AC field. The result of the distributed LC formation, rather than just a single LC, creates a much greater flow towards the end of the droplet and results in a faster elongation through the oil phase. Due to the viscosity of the oil phase, the droplet has a lot of inertia to overcome when elongating. This results in an inhomogeneous elongation where deformation occurs on the droplet's end. After some time this deformation will equalise and will result in a flow of BZ solution to the end of the droplet as it returns to a normal droplet shape. This then leads to a decrease in volume around the droplet CoM and results in a far decreased width of the droplet. The flow towards the end of the droplet also carries some momentum, which acts as a contributing factor to the division event. The momentum transfer can be mathematically explained by using the Navier-Stokes

equations, whilst the manifestation of this flow was created by the chemical wave, which can be modelled by the Oregonator model. The conversion of chemical energy into mechanical work was modelled using the modified Oregonator and Navier-Stokes model by Kitahata *et al.* in their work [315] involving the initial explanation of the spontaneous droplet motion. This modelling can help to explain and model the flows inside the droplet which cause the deformation and elongation of the droplet. The turbulent flows that we observe can be explained by the collisions of multiple waves propagating from independent LCs at different locations within the droplet creating non-linear gradients of interfacial tension. This has the effect of causing turbulent flow within the droplet and deforming the droplet edge at the interface with the oil phase.

The internal flow of the droplet was represented in the particle image velocimetry (PIV) analysis shown in figure 4.10. This flow was analysed and compared to the hypothetical flows projected onto the model droplets within the division mechanism (see fig. 4.12), which was produced by analysing a series of droplet division events, to determine a pattern in the elongation and deformation of the droplet for each case. The pattern was determined to involve an initial period where the leading centres' form within the droplet, within specific regions to create the internal turbulence to cause the inhomogeneous elongation and shape deformation, which is the second stage shown in the mechanism. The third stage during the division event is the elongation stage, where the inhomogeneous elongation of the droplet undergoes equalisation to the minimum energy state for the end of the droplet, which causes another flow within the droplet, as the turbulent flow about the droplet CoM is amplified, causing the width to decrease further. This leads to the final stage, where the droplet will divide into 2 sub-droplets. The turbulent flow created by interfering LC formation, in conjunction with the momentum of the flow within the droplet caused by the deformed end equalising in shape causes the droplet to divide into the sub-droplets. The volumes of the sub-droplets are not necessarily equal and depend on the location within the droplet where the width decrease occurs. The factors that determine this are currently unknown and further experimentation is needed to determine this. The elongation of the droplet is produced by the chemical reaction producing mechanical work, which corresponds to the deformation and lengthening of the droplet. This is a condition which must be considered, due to the time period the BZ reaction

must remain active for the division to be possible. As the BZ reaction must produce the required conditions for division before the life cycle of the reaction ends, there is a minimum duration which the solutions must remain outside of thermodynamic equilibrium for. This lifespan is majorly inhibited by the large quantity of surfactant utilised in the study to aid the required conditions being met, which is a contributing factor to the explanation for the low percentage of experiments which produced a dividing droplet.

Also presented within this study is the statistical analysis of the elongation of droplets under the experimental conditions of altering SDS concentration within the oil phase. The same analysis was performed to determine if the application of the AC field would produce statistically significant elongation of the droplet, the results of which can be found in the supplementary information. The control group for the statistical tests were recorded by observing a chemically active droplet under 'normal conditions'. Which involved no application of an external electric field, neither DC nor AC was applied, and the oil phase was surfactant free. The results from these experiments can be observed in figure 4.3, where the control group is represented by the dotted line within the graphs. The work carried out in this study found an optimization to produce the greatest elongation of the BZ droplets, where a concentration of 0.9g/litre of SDS dissolved in the oil phase, and an AC polarity period of 2 minutes was determined to produce the greatest elongation of the droplets.

Time is a crucial factor, as the division has to occur whilst the BZ reaction can still generate leading centres. The wave propagation from the LCs is how the droplet generates the mechanical work used to elongate and deform the droplet, without the LC formation, no mechanical work can be performed. The surfactant concentration is also a determining factor for the division, as the concentration must be great enough for the interfacial tension between the droplet and oil phase to be decreased sufficiently enough for the elongation to be possible, but must not be too great as to diminish the BZ lifecycle. A great enough concentration of SDS will lead to excitatory chemical species being leached from the droplet and forming brominated-SDS within the oil phase. This will push the BZ reaction further towards thermodynamic equilibrium and the reaction will cease. The environmental perturbation is another important factor, as it was shown that a too-low or too-high frequency of the changing of polarity in

the AC field which was applied externally to the droplet would not allow for the required conditions to be met for the droplet division to occur. The manner in which the deformation occurs is also crucial for the division event. When two regions of negative curvature merge on one side of the droplet, or when these regions on alternate sides align, the cross-sectional area will be decreased such that any flow travelling through this so-called 'stalk structure' will be accelerated, which increases the elongation due to the momentum transfer the accelerated flow has, and also contributes to the turbulent flow regime within the droplet. The deformation is coupled with the elongation of the droplet, as the elongation of the droplet causes some deformation, as the increase in the surface area occurs, with the conservation of the droplet volume. As the droplet elongates, more deformation is observed, and as the deformation is increased due to the turbulent flow regime, more elongation is induced. The culmination of all of these factors lining up results in the elongation and deformation of the BZ droplet which generates an instability, which is resolved with the division of the droplet. This instability breaks symmetry along the BZ droplet and allows the non-linear elongation and deformation to perpetuate the dynamics of the shape deformation for the remainder of the experiment.

Another crucial factor is the distance between the LCs producing the chemical waves which propagate across the droplet. It is well understood that converging chemical waves of oxidised ferroin will annihilate upon convergence. However, the flows generated by such waves do not. If the LC formations are too close there will not be enough time for the propagation of the chemical wave to generate the surface flows along the droplet surface. But when they are positioned sufficiently far away, then the propagation can take place, and the gradient of interfacial tension can be established, which will induce the surface flows. The flows generated by the propagation of the oxidised ferroin solution form in a vortex flow shape. Therefore, when the 2 wavefronts meet, the vortices will not merge, instead, they will apply compression onto one another which will repel the two regions of flow from one another. This will create turbulence within the droplet that will deform and elongate the droplet depending on its position. The repulsion of the converging flows will also then affect other flow regimes, which will contribute to the turbulent regime inside the droplet. If the BZ reaction can sustain this behaviour for a great enough period, the elongation and deformation will continue long enough for the division event to occur.

More experimental work could be carried out to increase the rate of division within experiments. This could be carried out by including a second set of electrodes, to apply an AC field at an angle of approximately 45° from the original set of electrodes. This would act to create the tripole effect within the droplet at an angle to generate the leading centre formation responsible for the division event to occur at a more frequent rate. Other future work includes experimentation to lead to a second set of divisions occurring from the sub-droplets generated from the initial division. The authors posit that this model of reaction-diffusion-driven division of an aqueous droplet containing BZ solutions can be used as a model to discover new knowledge about the biological process of cell division. Other experimental work would involve refining the BZ recipe to increase the time before the droplet reaches thermodynamic equilibrium so that the droplet can continue to apply mechanical work for a greater length of time, which would drastically increase the rate of successful experiments. An alternate way to increase the lifecycle would be to employ a different surfactant which does not cause the excitatory chemicals to leach from the dropped and into the oil phase. Understanding the symmetry breaking around the y-axis of the electric field would provide insight into the LC location dependence on the division event occurring. From the analysis of the dividing droplets, it is apparent that a break in symmetry is partially responsible for the division. The spacing of the distributed LCs has apparent importance, due to the requirement for the chemical waves to generate the Marangoni stress by propagating across the droplet. Having propagated and induced the flow upturns generated by the Marangoni stress, the pressure can develop which deforms and elongates the droplet. If the LC formations were too close, this would not happen because the chemical waves would annihilate before the gradient of interfacial tension could induce Marangoni stress. The breaking of symmetry across the y-axis allows for the greatest distance between the regions of LC formation, allowing for the convective flows to interact and repel each other. Further studies involving this symmetry breaking could increase the percentage yield of dividing droplets now that the optimal conditions for elongation and division have been found.

Chapter 5

Synchronization Through Entrainment in Spatially Distributed Droplets Containing Belousov Zhabotinsky Solutions

5.1 Abstract

Synchronisation is an important field of study in physics and biology, as it concerns the nature of clocks and biological rhythms. Synchronisation comes at the cost of free energy, and thus introduces entropy to a system. Compartmentalized droplets containing Ferroin-catalyzed Belousov Zhabotinsky (BZ) solutions were constructed with the aim of studying droplet-droplet signal transmission and synchronisation. Understanding the mechanisms at play will allow for greater a understanding of non-linear BZ droplet dynamics and to construct the inter-droplet signal propagation that has been studied for years, along with the energy dissipation observed in biochemical oscillators. There is currently little to no understanding of the mechanism allowing signal propagation between droplets in a network. Hypothetical explanations involve either diffusion of excitable chemical species across the lipid bilayer or hydrodynamic deformation between droplets, causing the signal propagation to occur. In this study, CNC-milled acrylic was used to fabricate a milli-fluidic structure to anchor droplets

submerged in SDS-saturated Oleic acid. The droplets were confined at defined distances apart to study the effect of mechanical perturbation diffusing through an oil phase on the droplets' ability to transmit signals and produce sync. The hydrodynamic flow was observed through the channel between the droplets in the milli-fluidic structure which caused an entrainment effect on the oscillating droplets due to the hydrodynamic flow between the droplet pair. The flow was observed as a longitudinal wave travelling perpendicular to the imaginary connecting line between the droplets. The flow was also observed to cause shape deformation of the droplet, which is believed to be involved in the entrainment of spatially separated droplets. The deformation causes the droplet to be removed from its minimum free energy state, which causes energy dissipation, increasing the entropy of the system. The formation of the spherical droplet occurs in the form of kinetic relaxation. Upon its return to the minimum energy state, the droplet resumes a spherical orientation with the minimisation of free surface energy. The deformation acts as a mechanical perturbation on the droplet and possibly induces some micro-stirring within the BZ solution. This induces leading centre formation in the droplet, which causes the propagation of a new wave in the secondary droplet. Also presented is a sync model using the FHN model modified with the Kuramoto oscillator to depict the sync, anti-sync, and non-synchronous signalling that can occur between the separated droplets.

5.2 Introduction

Synchronisation is the phenomenon where the coordination of events or signals within a system, or between multiple systems, operate in unison. When two signals are measured and are determined to be synchronised, they are said to be synchronous. An example of synchronous signals in the real world is the coupling that exists between a pair of pendulums fixed to the same supporting architecture. In the 17th century, Huygens experimented with pendulums in such a manner to develop a clock mechanism. the synchronized oscillators were coupled due to the transmission of signals between the oscillators, through the heavy beam they were attached to. This phenomenon was revisited and experimentally and computationally validated independently by different research teams [325, 326]. Applications of synchronised pendulums include the prior mentioned clocks, but also metronomes, earthquake seismometers, and furthering knowledge and understanding of areas of physics like motion, gravity and

inertia. Synchronization remains an issue in non-linear systems, where the exchange of weak interactions can adjust the internal rhythms to provide sync between the oscillators [327]. Theoretical modelling of the oscillators allowed for synchronisation regimes that Hygens did not observe in the 17th century when he first experimented with coupled oscillators [328]. These observations are categorised as: Quenching, beating death, partial synchronisation, and modulated behaviour. The quenching motion refers to the state where both pendulums stop 'working', where irregular motion occurs in a chaotic manner. The quenching behaviour is presented with a decrease in amplitude over time. Beating death refers to the state where one or both of the pendulums cease to function. Partial synchronisation shows the synchronous behaviour between the pendulums but over irregular intervals. This behaviour does not look like a synchronous signal over a long time period, where there is 0 phase difference in the pair of oscillators, in this scenario, there are periods where synchrony occurs, but the phase difference will be changing. This means the oscillators will fall out of synchrony, and back into synchronous behaviour randomly. The intermittent behaviour, or modulating behaviour, presents where the cross-sectional area of the connecting beams is decreased. here, the periodic amplitude modulation is observed, and the escapement mechanism periodically works. The emergence of sync in physics has led to observations of synchrony within many other types of systems. Neuroscience, biology, and social sciences [329]. Once 'in sync', there is no need for the physical characteristics of coupled oscillators to be considered. Whether the oscillators are a pair of spiking neurons, fireflies emitting a flash of light, or pendulum clocks swinging in sync, the only measurements that matter are the frequency of oscillation and the phase difference between the pair. As mentioned in their work, Nakao describes the importance of phase reduction in relation to coupled systems using non-linear oscillators [330]. Non-linear systems becoming synchronous follows a lot of the physics laid out in the synergetics theory by Herman Haken [71, 72]. Synergetics is the interdisciplinary science determining the pattern formation and self-organisation occurring in systems residing outside of thermodynamic equilibrium. In synergetics, macroscopic order is achieved through microscopic interactions in the system, where a reduction in entropy is presented as pattern formation. Synchronisation and self-organisation are related in Synergetics and thermodynamics in general as both show an organisational process by which entropy in a system is reduced via the mutual interactions which lead to global order in the system on the macro-scale [331].

Synchrony and self-organisation are also paramount within biological systems [55]. The nature of communication between organisms can be reduced to simply the reduction of phase differences in synchronous signals. Henceforth, research has been conducted into the nature of signal propagation within living systems, to both understand the mechanism of action for how it functions, and to gain an insight into its biological significance [332, 333]. The study of ion channels has led to the understanding of how bacterial colonies can communicate with bacteria within said colony [294]. The signal transmission within a type of densely populated colonies of bacteria, known as bio-films, was studied where it was found that this signalling was used to coordinate the collective behaviour of the bio-film [334]. Signal propagation has been found in a variety of circumstances for uses ranging from communication about nutrient gradients within a bacterial biofilm, to sharing carbon within trees in a forest[294, 335]. Similarly, chemical distress signals were learnt to be used in mycorrhizal networks [336]. Other examples of plant-plant communication networks have been discovered, which not only detail the use of chemical distress signals, but involve communication about nutrient gradients within soils, and have even been described as exhibiting cognition, or forming a form of 'social network' [337, 338, 339].

The counterpart to studying biological systems to understand their mechanisms is the study of physical systems capable of replicating biological phenomena. These models support and aid in growing an understanding of biological systems by simplifying the approach and removing redundant variables. Such models are developed to make studying mechanistic models of the interactions of an organism with its environments simpler to understand due to the reduction of surplus variables. Along with confirming experimental findings, the use of these models can allow us to learn new information that would be otherwise inaccessible without their development.

Self-propelled motion is a phenomenon observed often in systems of a droplet suspended in a liquid phase. In their work, Tanabe *et al.* modelled the mechanism responsible for the spontaneous droplet motion of an oil or aqueous droplet suspended in a liquid phase where a surfactant is present. The team made improvements to a model where an interfacial chem-

ical reaction between the droplet and surfactant produced Br_2 which altered the interfacial tension, creating Marangoni stress inducing spontaneous motion[141]. The work is based on a similar model, where convective flow is generated by reaction-diffusion and energy loss between 2 immiscible fluids, resulting in the formation of Marangoni patterns presenting[340]. The Marangoni effect in conjunction with chemical kinetics of the Belousov Zhabotinsky (BZ) reaction in nano-catalysed droplets, where the electrical conductivity of the nanocomposites was positively correlated with the increased in the speed of the self-propelled droplet[341]. Environmental perturbation has a variety of responses depending on the system involved. These responses can range from a colour change[342, 343], to translational motion[247, 344]. Translational motion as a response to changes in environmental conditions has been studied extensively, where typically a droplet of oil or water, is suspended in a liquid phase, often with a gradient in chemical concentration. Different systems with different sensitivities are exposed to a gradient in conditions, pH or salt concentration for example, which causes a gradient in surface tension within the liquid phase. At the phase transition between the droplet and liquid phase, it resides in, a gradient in interfacial tension is created due to the gradient in chemical concentration at that region. Marangoni stress at this interface induces flow within both phases, which imparts a momentum transfer onto each other due to friction, which leads to the translational motion of the droplet[345]. This translational motion has been employed by a maze-solving droplet driven by the Marangoni stress induced by a gradient in pH[346]. Similar results were gained from systems using salt concentration and even temperature[248].

The study of active matter has led to the development of Janus particles, named after the roman god of all beginnings, time, and duality, depicted with 2 faces, Janus is the perfect name-sake for this type of active particle. A Janus particle is a type of nanoparticle whose surfaces have 2 or more distinct physical and chemical properties, leading to interesting biphasic reactions governed by the side facing the stimulus. The derivation of a Janus particle comes from the modification of isotropic particles where one surface is exposed to a modifier, whilst the other, or others, are not [347, 348]. This leads to the particle having multiple types of coating on its surface which can lead to the complex behaviour demanded from its application. Janus particles are often incredibly small, sometimes only nanometers in diameter, but can range up to a few micrometres [349]. They are small enough to be affected by thermal fluctu-

ations, yet large enough to be observed by traditional optical microscopy. Due to the nature of their minuscule size, they are affected by Brownian motion, which acts as an external stimulus to their motion. Janus particles have shown a great emergence in biomedical research due to their applications [350]. Uses of Janus particles in biomedical applications include optics and catalysts in biomedicine due to their diverse and tunable compositions, structures, and features. Janus particles present the possibility of use in therapeutic environments where the technology can be used for drug delivery, sensing, or imaging within patients [351].

The Belousov Zhabotinsky (BZ) reaction is an example of a reaction-diffusion style redox reaction. Networks of BZ droplets[194] have been used to study to flow of information as excitatory waves propagate from droplet to droplet within such networks. The proposed mechanism by which excitatory signals propagate from droplet to droplet involves either the diffusion of excitatory chemicals between droplets or hydrodynamic flow causing deformation, which leads to an excitation within the BZ solutions in the following droplet, leading to the propagation of a chemical wave across the droplet, continuing the wave throughout the network. Milli-fluidic devices have been employed to generate networks of droplets[352], whilst other efforts have been made to fabricate milli-fluidic structures[353, 354, 319] to house chemical droplets submerged in oil during experiments as to control the morphology of the arrangement of the droplets in the network. Research into the droplet-droplet networks succeeded in producing signal propagation in a network of droplets separated by a lipid bilayer. Such droplets were introduced to a millifluidic device through the use of a microfluidic system to achieve consistent droplet volumes as they are introduced into the chamber device. As the droplets are submerged within an oil phase, they form cylindrical shapes due to the surface tension and capillary action. This shape is however maintained when in contact with neighbouring droplets, with the lipid bilayer preventing the droplets from merging. The team experimented with different concentrations of chemicals the BZ reaction requires to function, and remarked on their observations. A key point was that changing the concentration of malonic acid altered the lifespan of the reaction, where an increase in concentration, decreased the operating time of the excitable solution. Specific regions in the oscillatory output were categorised by the team, where the time the reaction stays in each category could be manipulated using the malonic acid concentration. The team also investigated pattern formation in a set of droplets,

where a spiral wave was initiated, and how this has an impact on the surrounding droplets. In a similar manner, networks of droplets composed of different chemical concentrations were also investigated, as this draws a parallel to the networks of neurons in a brain.

Other bifunctional chemical systems have been utilised for the study of signal propagation[195, 196]. Where the aim is to build a functional network of droplets, capable of performing basic computational tasks akin to an electronic computer. Synchronization in oscillatory systems is often studied as a measure of entrainment between independent systems[355, 356, 357, 358].

In related work, chemical computing studies have been carried out, where the reactions within chemical automata have been used to transcribe sequences of symbols that form languages according to Chomsky hierarchy [198]. 3 reactant non-linear chemical oscillators were involved, where an input string is a chemically transcribed input to the "one-pot-reactor", where the output is determined as a colour change as to whether the input was accepted or rejected. A limitation of the study due to inefficiency in the optimisation of the chemical recipes leaves a maximum word length of 20 letters as an input for the chemical Turing machine.

Another accept-reject criterion type Turing machine was investigated where the time delay was an important factor in its performance [359]. Analysis of variance in the response the ruthenium-catalysed BZ reaction has to aliquots being introduced as letter inputs to a Turing machine was conducted. The input, processing step, and output of the Turing machine if materialised through the employment of a bimolecular chemical reaction. An automatic pipetting robot was used to control the placement and droplet volume of the aliquots deployed in the study. They discovered that the greater the value of the time delay, the greater the results for the computation of language inputs of the chemical oscillator, however, care should be made for ensuring the time delay stays within the lifespan of the chemical reaction so that the reaction stays within the oscillatory regime. In a further study, a research group used chemical computing in a time evolution step of an AI system trained to detect schizophrenia in healthy patients [360]. Ruthenium-catalysed BZ reaction is used due to its photosensitive nature. Different geometries of oscillator networks were experimented with to determine the optimal formation for the chemical oscillators. The BZ reaction is contained within a disk

which allows the reaction to flow through to other disks, acting as an information exchange between sub-reactions. Different EEG nodes were experimented with before 2 were selected to be used. The originator model was used to simulate the BZ reaction, but the authors believe that the newer, more realistic model produced by Vanag and Epstein [361] would yield similar results. The 2 selected EEG channels were sampled for 1 minute at 128Hz, which were then averaged, and the potentials were then normalised using a function. 2 prediction values, P1 and P2, were generated from this term and used as input for a clustering classification. The chemical oscillators played a role in information processing gathered from recording EEG signals from the participant's scalp, where the prediction value was fed as input to the respective chemical oscillator. Using this method, the team were able to achieve 82% accuracy in schizophrenia detection on a training data set.

Hydrodynamic effects have been studied in chemical systems where a wave is shown to propagate and deform[362]. Instabilities in low Reynolds number liquids have prompted research into the study of the hydrodynamic flow of bromine species in the oil[363, 364, 365, 366]. Commonly in systems involving BZ droplets, a surfactant is used to reduce the interfacial tension between the aqueous phase and the oil phase. This is due to the chemical wave propagating across the body of the droplet, causing a gradient of the interfacial tension to be formed between the phases, which causes Marangoni stress. The Marangoni stress leads to translational motion due to the phases having differing viscosities, meaning that friction occurs between the phase, resulting in a momentum transfer which leads to spontaneous motion [266, 134, 231]. It was later shown that coupling between the chemical wave and the speed of the translational motion is found in the oscillating droplets [367]. It was found that the use of such surfactants [368, 369] could allow droplet-droplet contact without merging which can lead to synchronization between the droplets. The use of surfactants in droplet-in-oil experiments also has the effect of reducing the interfacial tension between the aqueous droplet and oil phase, resulting in no translational motion when the droplet undergoes chemical oscillation. Deformation of BZ droplets was involved in the model of spontaneous motion discussed by Kitahata *et al.* [134, 231]. Where the propagation of the travelling chemical wave leads to shape deformation due to the change in interfacial tension between the droplet and the oil phase. This propagation also drives Marangoni flows within both phases, which impart a momentum transfer onto one another due to the friction between them. This leads to the

translational motion of the BZ droplet.

It was suggested previously that the signal propagation between successive droplets was in part due to diffusable excitatory chemical species propagating through individual droplet solutions, causing leading centre (LC) formation in the following droplet, which then leads to the propagation of chemical wave across that droplet. This propagation travels across this droplet and leads into the following droplet where the excitatory chemical species then diffuses through onto the next droplet. Hypothesis for which chemical species within the BZ family of reactions suggested that BrO_2 and $HBrO_2$ were responsible for the propagation of chemical wave from droplet to droplet due to their diffusability in oil and crucial role in the BZ reaction. It was understood that a possible mechanism for the diffusion of the excitatory chemicals is due to the surfactant within the oil phase acting as a Br_2 scavenger. The Br_2 scavenger would act both as a mechanism for the diffusion of the excitatory chemical species, but also as a mechanism to limit inhibitory signalling, allowing for the propagation of a chemical wave between successive droplets .

An alternate hypothesis for the coupling involves no chemical transfer between droplets in a network, but rather the mechanism for signal propagation involves hydrodynamic flow between droplets acting as a signal carrier, due to the generation of a new LC through a mechanism of droplet deformation. The deformation of the droplet would increase the free energy principle of the droplet and also act as mechanical perturbation [370, 371, 372].

Developed in 1961, the Fitz-Hugh Nagumo (FHN) model extended the Van Der Pol equations of oscillators as a simplification of the 4-variable Hodgkin-Huxley model of squid axon, to create a simplified 2-variable model of neuronal spiking [188, 184, 181]. The FHN model consists of tunable parameters which produce a varied response in the oscillatory period and amplitude, which can be used for modelling biological processes [373]. The introduction of the Kuramoto oscillator can introduce feedback between a pair of oscillators that can result in entrainment and synchronization [374, 375, 376, 377, 378]. An adaptation of the FHN model was implemented with the memristor, which is a nonvolatile resistance tunable device, with the intention of validating binary adder structures capable of performing the AND, OR, and NOT functions. The FHN model was adapted with a nonlinear memristor to construct the memristive FHN model (MFHN) of a spiking neuron. When only a singular input is activated,

or no inputs are active, the total input is below the threshold, which means the MFHN model is at its resting state. The model was proposed as a potential building block for large-scale logic circuits when it experimentally validated the successful functionality of AND, OR, and NOT functions [379]. Synchronization of signals generated by the employment of the FHN model was utilised for modelling neurons in a manner applicable to the research of Parkinson's disease (PD). In PD, synchronicity in neuronal firing is observed, so the syn between FHN neurons was studied. The FHN modal can be equipped with noise and time delays to simulate the neuronal firing conditions found in biology. In absence of noise, the neuronal firing follows a coupled schema, where the coupling strength increases with the absence of noise. Additive noise was incorporated to simulate thermal fluctuations in a biological system and random external disturbances. The initial state of the two-neuron system was found to change from asynchronous, to synchronous for different coupling states [380].

Engelbrecht *et al.* used a mathematical model with the intention of describing the generation of an 'ensemble of waves' akin to that in a nerve fibre [381]. Modelling of external perturbations onto neuronal networks was conducted by Liu *et al.* where a photosensitive neuron is presented, to estimate the nonlinear encoding and output response of neurons driven by optical input signalling [189]. The model utilises a photocell as input for the activation of an FHN neuron for the simulation of signal transduction in a neural network. The FHN neuron can capture and encode external signals similar to that of an artificial eye. The bifurcation analysis was presented where the mode transition of the firing pattern selection of neuronal electrical activities was conducted. The sampled time series reproduced the main characteristics of bio-neurons under an activated regime, by activating the photocell with an optical input. Research to understand the natural functions of neuronal signalling has led to the development of an optimised fuzzy controller for the synchronisation of neuron models using the FHN model [382].

Hydrodynamics is a branch of physics concerned with the study of flows. Best described by the Navier-Stokes equations, the liquid flow has been studied for a multitude of reasons, from motion within a droplet [230, 316], to the flow of blood within the heart [383]. Heat transfer was studied in droplets by Megaridis *et al.* in rotating droplets, where a hydrophobic surface provided heat transfer to water droplets with surfactant [384]. The internal flow and

rate of heat transfer as impacted by the droplet's size. The change in the thermal gradient was found to affect the droplet's properties like surface tension and viscosity, which can lead to a further irregularity with the convection pattern internal to the droplet. The flow rate inside the droplet was measured with microscopic particle tracking techniques to corroborate the numerical model developed of practical experimentation.

Particle image velocimetry (PIV) was developed as a technique for obtaining instantaneous velocity measurements in fluids [385, 386, 387]. the fluid is seeded with particles used to trace the motion of the current. The particles are sufficiently small enough to be carried with the flow, without changing the liquid's properties. The particles are suspended within the fluid and their path is traced through time to give direction and magnitude of the flow [388]. High-speed confocal cameras have been deployed to track the internal flow of a moving droplet using micro-PIV [389]. To track the acceleration of mixing, or chemical reactions inside a droplet, a lab-on-a-chip device was produced so that the flow inside a droplet could be traced in 3 dimensions. The 3d volumetric velocity distribution was created by eliminating out-of-focus light, to obtain ultra-high contrast particle images within a thin cross-sectional plane of the droplet, which were subsequently stacked, to produce the 3D image of the velocity profiles of moving trace particles. Further developments in PIV techniques have been developed to both improve accuracy, whilst decreasing costs. Fan *et al.* developed a method for using laser-induced incandescence to measure single-shot velocity fields, whilst retaining spatial information [390]. Tungsten carbide (WC) particles were used to seed the fluid, which offers a far cheaper alternative to the plastic micro-suspensions typically employed for such a study. The black tracers were heated to several thousand degrees kelvin, without increasing the temperature of the surrounding area to a noticeable amount. The group found that the sub-micron WC particles can accurately follow the gas flow, and provide accurate velocity fields once the cross-correlation is applied. A comparison between laser-induced fluorescence and traditional PIV imaging was captured by Volkov *et al.* when they prepared a solution of Al_2O_3, and TiO_2 tracers to observe heating and evaporation of water droplets [391, 392]. The concentration of tracers was deployed as they did not degrade the accuracy of the temperature measurement of the planar laser, for the fluorescence imaging. Non-contact techniques were employed to perform temperature readings of the droplets under heating and evaporation, as to obtain the key characteristics of the droplet undergoing phase transformations. Using this

technique, they were able to perform velocity and temperature readings using non-contact techniques simultaneously. Practical applications of PIV analysis have been demonstrated by Tung *et al.* where the chaotic mixing and hydrodynamics were analysed within a droplet moving through a planar serpentine micromixer [393]. Rapid mixing is of great importance in droplet microfluidic applications, and so the observations in this paper are crucial to the understanding of the phenomena at a base level. The experimental findings of the flow within the droplet, along with the droplet shape changes were supported with numerical simulations, to determine the chaotic mixing and hydrodynamic effects observed in the droplet microfluidic system. Another application of particle tracing in a study of droplets was conducted by Kitahata, where they suspended microbeads in aqueous droplets containing BZ solutions whilst suspended on an oil phase [230, 231]. The flow within the oil phase and inside the droplet was mapped as the convective flow induced by the propagation of the BZ chemical wave. The research concluded that the propagation of the chemical wave induced Marangoni flow in both liquid phases, where the friction between the phases was responsible for the droplet motion.

As the droplets in this study are chemically active, the generation of a chemical wave emerges from the LC and propagates across the body of the droplet. Due to the employment of the surfactant within the oil phase, and the use of the anchoring via the millifluidic device, the droplet is unable to move translationally across the oil phase [134, 231, 319, 195]. This leads to the elongation of the droplet body in the direction of the paired droplet within the millifluidic device. The elongation of the droplet causes a small compression of the oil phase, leading to the development of greater pressure in that region, which leads to the propagation of hydrodynamic flow in the form of longitudinal waves through the oil phase. This wave is able to reach the secondary droplet and acts as mechanical perturbation onto the droplet. This perturbation causes compression resulting in shape deformation of the droplet, which creates an instability with the free energy the droplet is subject to. This instability leads to the generation of an LC within the secondary droplet, which in turn leads to the propagation of a chemical wave, and therefore droplet elongation. This in turn acts to create hydrodynamic flow back in the opposite direction, toward the initial droplet, creating a positive feedback loop of mechanical perturbation between droplets. Such a system can be described

as a chemical-mechanical-chemical coupling. The basis of this is dependent on the degree of separation at which the droplets lie, as the greater the separation, the larger the distance the hydrodynamic flow has to travel, and therefore the weaker the effect will be.

Presented in this study, we show the use of CNC-fabricated milli-fluidic structures containing dimples and connective channel used to anchor ferroin-catalyzed BZ droplets under oscillation. the dimples anchor the droplets suspended in the oil phase and allow hydrodynamic flow between the droplets. We have found entrainment in signalling activity between 2 separated aqueous droplets containing BZ solutions suspended in an oil phase. We present the findings involving varying degrees of separation on the entrainment of the droplet and found that the hydrodynamic flow between droplets is responsible for signal transduction. We present this argument as the cause for entrainment and signal propagation between 2 coupled droplets, rather than the previously published argument which involves the flow of excitatory chemical species carrying the excitation signal from droplet to droplet.

In this work, we have produced a model of synchronization between 2 coupled oscillators using the FHN model adapted with a modified Kuramoto oscillator. The model variables can be adapted to produce weaker or slower entrainment to simulate the change in distance between the BZ droplets.

5.3 Methods

The preparation of the excitable BZ solution was performed by following the procedure reported by Arthur Winfrey[170] in his book, "The geometry of biological time". The protocol involves the preparation of 4 solutions, A, B, C, and D, which when mixed produce the excitable BZ solution.

Solution A is produced by mixing 5g $NaBrO_3$ with 2ml of H_2SO_4, and 67ml of H_2O. Solution B is comprised of 1g of Malonic Acid and 10 ml of H_2O. Solution C consists of 1g NaBr and 10ml H_2O. Solution D is a 25mM concentration Ferroin solution and is produced by mixing stoichiometric amounts of 1,10-phenanthroline and ferrous sulfate, producing an aqueous solution of ferroin(tris (1,10-phenanthroline) iron (II) sulfate). The chemicals used

were extra pure lab-grade reagents, sourced from Sigma-Aldrich and Thermo-Fisher, and required no additional purification. The water used was filtered and double-distilled.

To initiate the reaction, 6ml of Solution A, 1ml of Solution B, and 0.5ml of Solution C are mixed in a sealed container, as the combination of the 3 solutions produces bromine gas. This solution is then left in the sealed container until the bromine is re-absorbed into the solution. At this point, 1ml of Solution D is introduced causing an initial colour change from red (reduced state of ferroin) to blue (ferriin oxidised state). After a moment the solution will return to the red (reduced) state and the solution is ready to be pipetted onto the millifluidic device.

The milli-fluidic structure[353, 354, 319] was fabricated through the use of CNC-guided engraving of acrylic to produce 2 dimples to anchor the BZ droplets in place, with a channel connecting the droplets to allow hydrodynamic flow to be directed between the droplets. The structure measures 50mm in length, 20mm in width, and 3.7mm thick. The diameter of the dimples measures 5mm with a depth of 2mm. The dimples are placed 30mm, 20mm, and 10mm apart, measured from the centre.

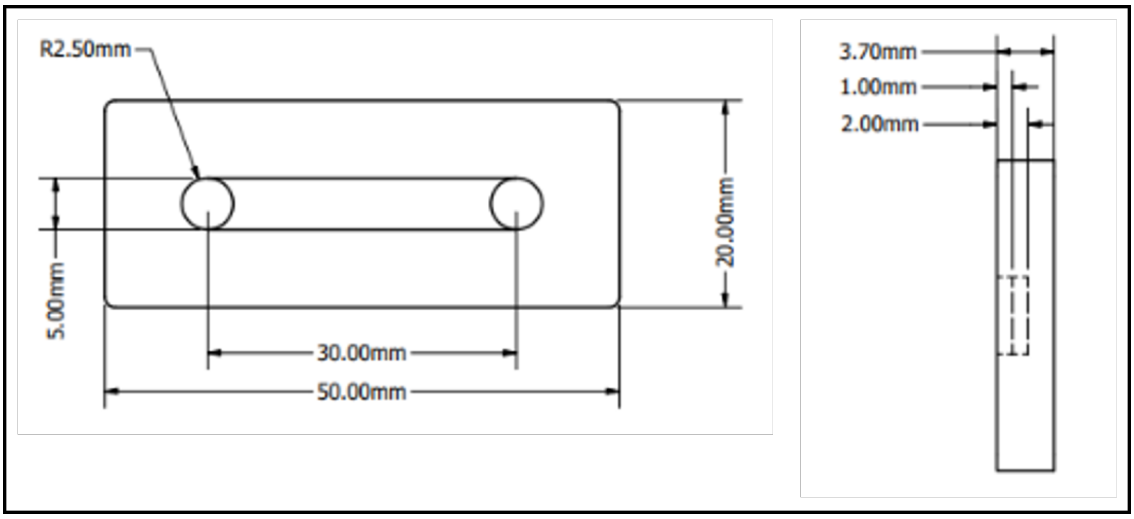

Figure 5.1: Schematic of milli-fluidic structure used to anchor droplets at a distance. The device was CNC-milled from acrylic, and the schematic shows droplets anchored with a spatial distribution of 30mm, with other devices, fabricated using a spatial distribution of 10mm and 20mm. The dimple created to anchor the droplets are 5mm in diameter, and 2mm in depth. The channel running between the pair is 1mm deep.

The milli-fluidic structure shown in Fig.5.1 is placed in a standard petri dish and submerged

in surfactant-saturated oleic acid. The surfactant used was sodium dodecyl sulfate (SDS), where 0.45g was dissolved into 1 litre of Oleic acid. A previous study found that increasing the concentration of SDS beyond 0.9g per litre of oleic acid had the effect of leeching oil diffusable excitatory species from the BZ droplet, having the effect of drastically decreasing the droplet lifespan. This was due to the SDS acting as a bromine scavenger once a critical mass of micelle formation is reached in the oil phase. Therefore the employment of 0.45g of SDS per litre was utilised as it obtained the desired effect of decreasing the surface tension, but allowed for the droplet to maintain chemical composition so as to continue to oscillate over the normal time span. The 50μl droplet of BZ solutions was then manually pipetted onto the dimple in the milli-fluidic structure and allowed to oscillate for 10 minutes prior to the introduction of the second droplet to allow for a baseline reading of the droplet activity. The 50μl volume of BZ solutions was utilised as the volume is large enough for thermal effects to be diminished, allowing for easy visualization of the propagating waves, whilst also being small enough that the droplet shape is easily maintained under the minimum free energy principle. Other droplet volumes were considered due to the relationship between oscillation frequency and droplet radius[260], but these factors were able to be ignored once pilot studies were conducted in addition to a previous[317] study where it was discovered that the oscillation frequency of the 50μl droplet volume oscillated at a high enough frequency to be studied effectively. The droplets were recorded top down using a Nikon D7500 camera recording at 60 frames per second from the time of the first droplet being pipetted until 20 minutes after the introduction of the second droplet. The droplets were illuminated through the use of a diffuse LED backlight. The images were analysed using software written in the MATLAB programming environment. Analysis of the droplets consisted of recording pixel intensity values to create a time series data set of the oscillations observed in the BZ medium, along with obtaining the volume of the droplet in each frame to study the deformation in correlation with the chemical activity of the oscillating droplet.

Particle image velocimetry (PIV) is utilised as a tool for the visualisation of hydrodynamic flow within the oil phase and was studied by suspending Microbeads within the oil phase between the oscillating droplets. The Microbeads used were Thermo Scientific™ 7000 Series Copolymer Microsphere Suspensions, fabricated from Polystyrene Crosslinked Divinylbenzene,

and were sourced from Thermo Fisher. The employment of the Microbeads allows for tracking of motion within the otherwise clear oil phase to be detected. The trace particles were detected in MATLAB using image analysis techniques, the motion was then visualised as a function of time to observe how the flow in the oil phase changes through time. This technique was used to map the motion between droplets as they oscillated and created hydrodynamic flow within the oil phase that acted as a mechanical perturbation for the droplets to become entrained. The flow between the droplets was visualised as the droplets cycle between the active and passive phases.

Analysis of the RGB images captured through the video recording was performed within the MATLAB programming environment. Images of the droplets were converted to time series information using the algorithm shown in figure 2.7, to identify the region within the image in that the droplets are contained. This information was then used to extract a 3x3 grid of pixels. The data from the blue channel of the RGB image was stored from the 3x3 locations and averaged to depict the periodicity of the BZ reaction within that droplet. The PSD and normalised cross-correlation function was calculated using MATLAB's inbuilt functions, along with all the other plots generated.

5.4 Results

5.4.1 Droplet Entrainment

Recordings of the droplets were made over the course of the experimentation. The first droplet, droplet A, is pipetted into the millifluidic device first and allowed to oscillate for 10 minutes prior to the introduction of the second droplet, droplet B. Droplet A is recorded without the presence of droplet B to gather baseline readings about the periodicity of chemical wave formation from LCs which form as the chemical reaction undertakes. Droplet B is pipetted from the same preparation of BZ solutions as droplet A is, and is introduced at a later time period to allow for the baseline readings of droplet A to be collected. In the case of droplet pairing exhibiting synchronisation, there is a lag period initially as the droplets become entrained, where a phase difference appears between the peaks of the pixel value

reading obtained from the RGB images created by the time-series photography. After a period of entrainment, the phase difference is reduced to 0 radians and the droplets have become coupled. This will be reflected in plotting the normalised cross-correlation function, where the synchronous behaviour can be determined by a peak in the graph at the τ=0 region.

The droplets become entrained through a process of forming a positive feedback loop, where each droplet has an effect on the other, and causes the feedback loop to be sustained. The loop is developed through the elongation of the droplets as the chemical wave propagates across its body. The elongation is generated by the Marangoni stress. This induces flow within the droplet and the oil phase. Friction between the flows causes a momentum transfer which acts as a stretching force on the droplet, causing it to elongate. The elongation creates a periodic velocity field inside the oil phase, which generates a longitudinal wave towards the paired droplet. This periodic velocity field compresses the other droplet slightly and causes a break in symmetry. The droplet will subsequently return to its original shape through kinetic relaxation to minimise the surface free energy. This will act with a small stirring effect on the droplet, causing a flow of the internal solutions. This stirring, in combination with the break in symmetry, will cause the formation of a new LC. This LC will subsequently cause a new chemical wave to propagate, which likewise, will generate the same elongation and longitudinal periodic velocity field, that originally led to the creation of the LC. This system will perpetuate between the droplets until they reach thermodynamic equilibrium and the reaction ceases. The effect of the longitudinal wave is diminished as a function of the distance between the droplets.

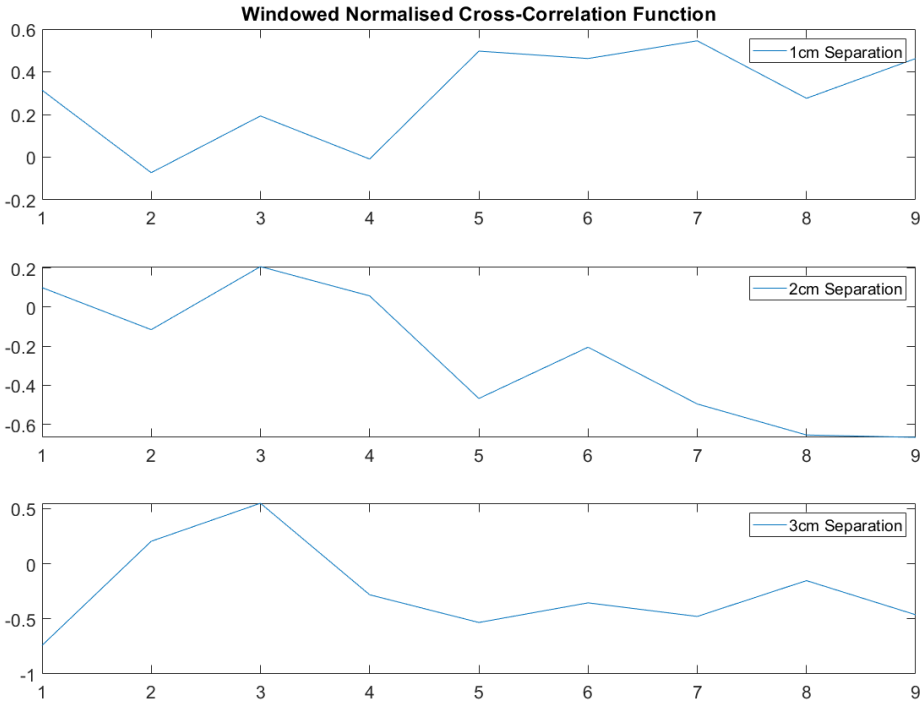

Figure 5.2: The time windowed normalised cross-correlation function was computed on samples to show the synchrony and entrainment in droplets separated by 1cm, 2cm, and 3cm. The sliding time window was applied across the data set with a window size equating to 2 minutes. The 3 representative examples show how the synchrony changes through time. The 1cm separated droplets are shown to produce sync around midway through the series, and then remain in sync until the end of the recording. The 2cm separated droplets follow a similar suit, with the main difference being that anti-sync was achieved rather than sync, and over a longer time period. The 3cm separated droplets are shown to follow no real pattern of synchrony. There is an emergence of sync at the start, but as this dies down, it can be concluded that this was a random similarity, that did not hold.

Studying synchrony between signals can be determined using the normalised cross-correlation function with a sliding time window. This was applied to the droplet pairings using a 2-minute sampling window, applied across the entirety of the dataset gathered post-droplet B introduction. Figure 5.2 shows the outcome, where the value extracted from the τ=0 region was stored and plotted in a time series data set for comparison between the different distances. The 1cm separated droplets were found to produce synchrony much faster than in the cases of the droplets being separated by 2cm, and 3cm. The tendency was also shown to find positive sync, as opposed to anti-sync. In the representative example of the 2cm separated droplets, anti-sync is found and emerges much later than the positive sync found in the 1cm separation was found. The example shown of the 3cm separated droplets initially shows a

degree of synchrony between the signalling, which decreases, and no synchrony is found after the droplet establish their rhythm. This initial synchronous behaviour can be attributed to purely random similarities, which did not appear through the remaining time series, as no entrainment was found between the pair of droplets. The emergence of sync in the 1cm and 2cm separated droplets can be attributed to the formation of the positive feedback loop which couples the droplets and shows entrainment. This phenomenon will be explained later in the chapter. More examples of the time windowed normalised cross-correlation function can be found in the appendices from figures 8.25 - 8.36.

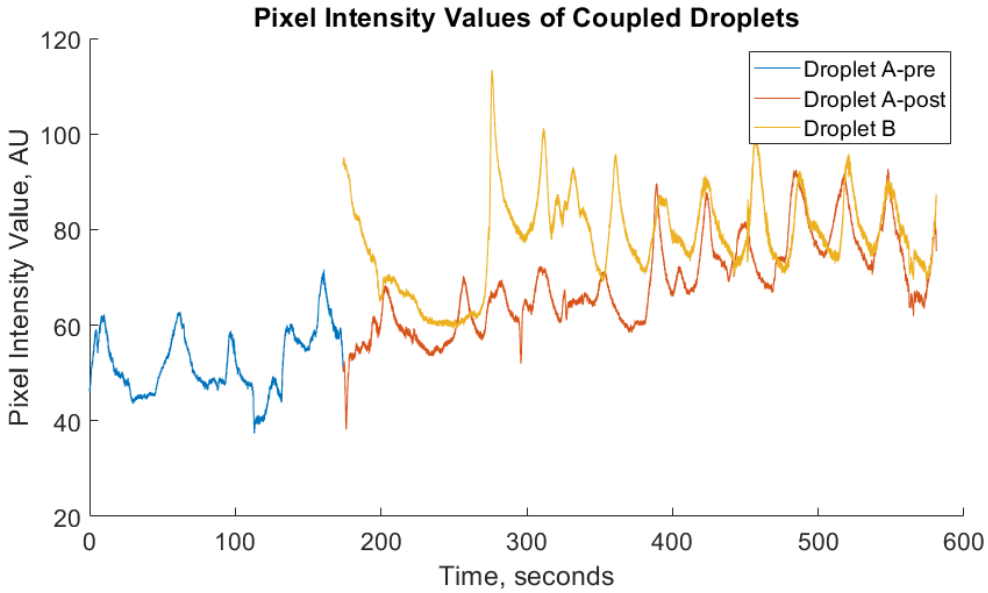

Figure 5.3: Time series pixel intensity values of entrained droplets. The pixel intensity values were extracted and averaged from the blue channel of the RGB image so that they describe the periodicity of the chemical wave formation, which is represented by the colour shift of ferroin changing from red to blue. The blue graph shows the pixel values extracted from droplet A, prior to the introduction of droplet B. The orange graph shows Droplet A, post-introduction of droplet B, and the yellow graph shows droplet B. The data is extracted from a 10-minute recording.

Figure 5.3 shows the emergence of synchronisation between a pair of oscillating droplets. The droplets were suspended in the millifluidic device employing a degree of 20mm spatial separation. The droplets initially show no signs of synchrony, but over time the wave generation becomes synchronised and the periodicity between the droplets aligns the peaks and troughs of the extracted data. The droplets become entrained, as the hydrodynamic flow generated by the oscillating droplets causes mechanical perturbation onto the coupled droplet, which

leads to the emergence of synchronisation. As the oscillations generated by each droplet convert to a synchronisation regime through the chemo-mechanical coupling which is aided by the hydrodynamic flow through the oil phase within the channel that the droplets are compartmentalized within. The change in periodicity observed in droplet A occurs following the introduction of droplet B, which begins to generate wave formations after its introduction to the millifluidic device. This is then remarked by the aligning of the generation of wave formations, presented with the peaks in the pixel intensity graph lining up over a time period of 4 minutes at the end of the recording. The phase synchrony converges closer towards 0° as the coupled droplet pair become more entrained. This behaviour is modelled in eq.(A) and eq.(C) in section 5.4.3, by increasing the entrainment term, K, from -0.23, through to 0.5.

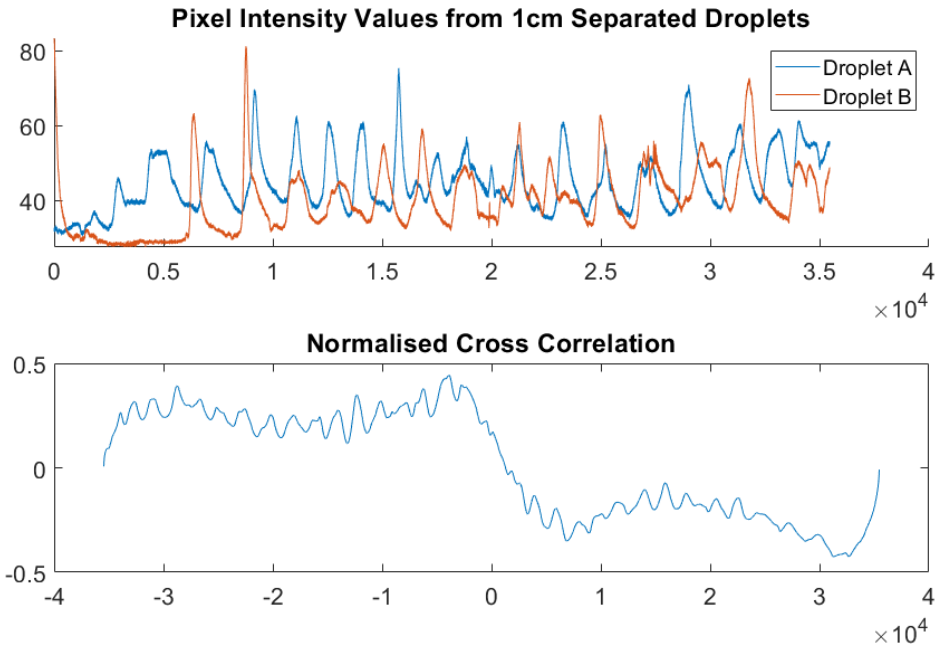

Figure 5.4: Pixel intensity values were extracted from entrained droplets. The x-axis refers to the sample number, where 60 samples were collected per second, and the y-axis is in arbitrary units, referring to the magnitude of the RGB value processed from the image. The synchronisation is shown in the normalised cross-correlation graph below, where τ=0 refers to 0 offset between the signals. The data displayed in this graph was gathered over a 10-minute period, after introducing the second droplet.

The pixel intensity values extracted from the oscillating droplets can depict the process of entertainment through the progression of synchronisation between the pair. Plotting the time series graphs together can reveal this phenomenon to the naked eye. A mathematical process

which can uncover the nature of the synchrony in a graphical format was utilised. This process is called the normalised cross-correlation function and is a measure of synchronisation through time, where the further away from τ=0, the greater the time difference in the synchrony. If the peak of the graph is closely related to the τ=0 position, it refers to a very high degree of correlation. Whilst a shift in τ does not mean there is no correlation, simply a shift in the phase difference, we are interested in when the peak is close to τ=0, as this refers to synchrony which occurs in phase. If there is no peak, it relates to the very minimal synchrony between the 2 signals, which suggests there is no coupling or entertainment. A peak with a great offset from the τ=0 position reveals a time delay in the synchronisation between the 2 signals. Figure 5.4 shows the strong correlation between a pair of droplets with a 1cm separation. There is a minimal offset between the τ=0, which demonstrates the high degree of synchrony observed between the pair of droplets. The shape of the normalised cross-correlation graph is very similar to that shown in a pair of sinusoids which are in synchrony. This shows the power of the correlation between the signals in this experimental condition.

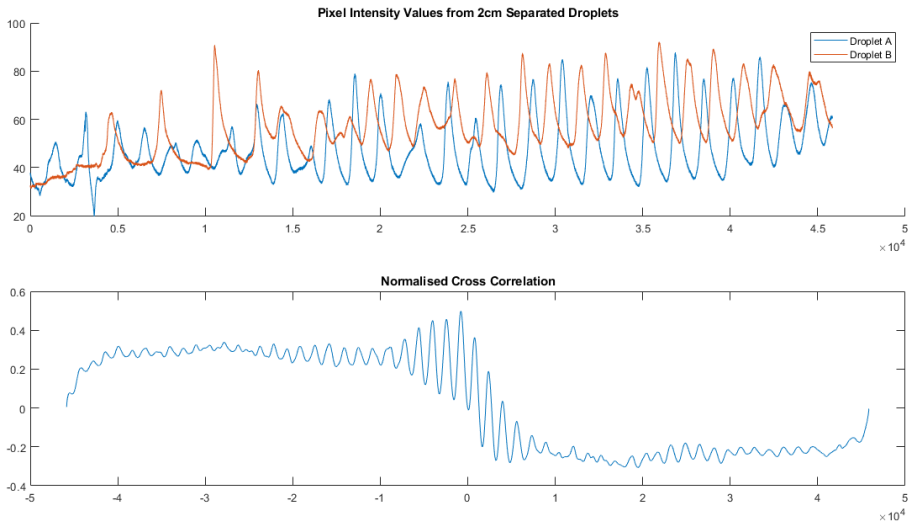

Figure 5.5: Pixel intensity values and normalised cross-correlation values of oscillating droplets separated by 2cm.

Figure 5.5 represents a representative example of a pair of droplets oscillating together, slightly out of synchrony. This is represented in the graph of pixel intensity values where the peaks in the pair of signals do not perfectly line up due to a mismatched frequency regime. In the graph of the normalised cross-correlation, the peak is slightly offset from τ=0, showing

that whilst the graphs are not entirely coupled, there still is a great degree of similarity between the graphs. Like in figure 5.4, there is a very similar output in the correlation graph to that shown in a pair of sinusoids. This lends itself towards a high degree of synchrony being observed between this pair of droplets, just to a lesser degree than that shown in the 1cm separation case.

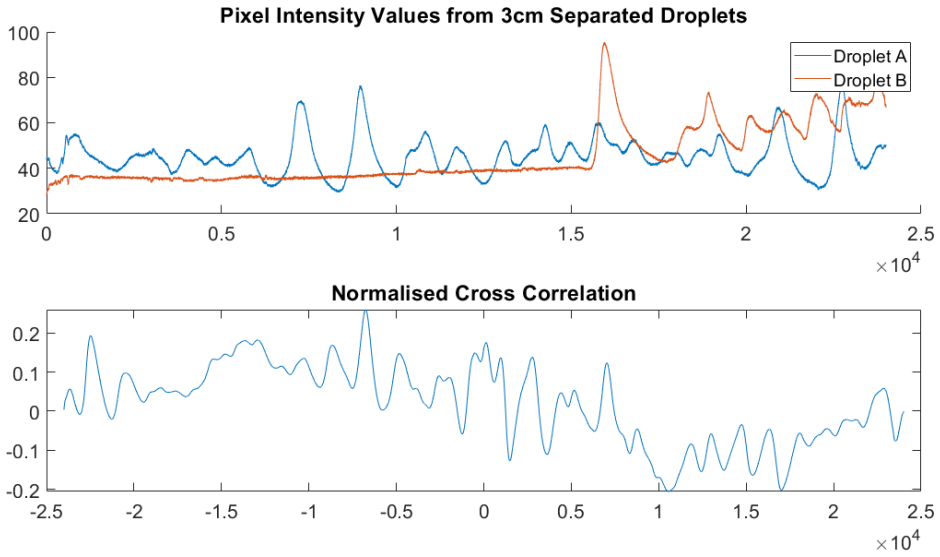

Figure 5.6: Pixel intensity values and normalised cross-correlation values of oscillating droplets separated by 3cm.

In figure 5.6, it is obvious that the separation between the droplets has decreased the entrainment power, one has on the other, as there is no visually noticeable synchrony in the graph of pixel intensity values, along with the graph of the normalised cross-correlation values, where the peak has a great offset away from the τ=0. In comparison to figure 5.4 where the peak is much closer to the τ=0 region, and the synchrony is visually more obvious, this shows the effect of increasing the distance between the pair of BZ droplets. Another comparison to be made is the far lesser number of waves present in the time series data. Figures 5.4, and 5.5, representing 1cm and 2cm droplet separations show much greater numbers of waves in the same time period. This can be explained by the closer droplets acting as a source of mechanical perturbation on one another, leading to an increased frequency in wave generation.

The higher the correlation between the 2 signals, the closer the normalised cross-correlation graph appears. This is validated by checking the graphs against the output of performing the normalised cross-correlation on a pair of sinusoids. Figure 8.24 can be found in the appendix

for the comparison.

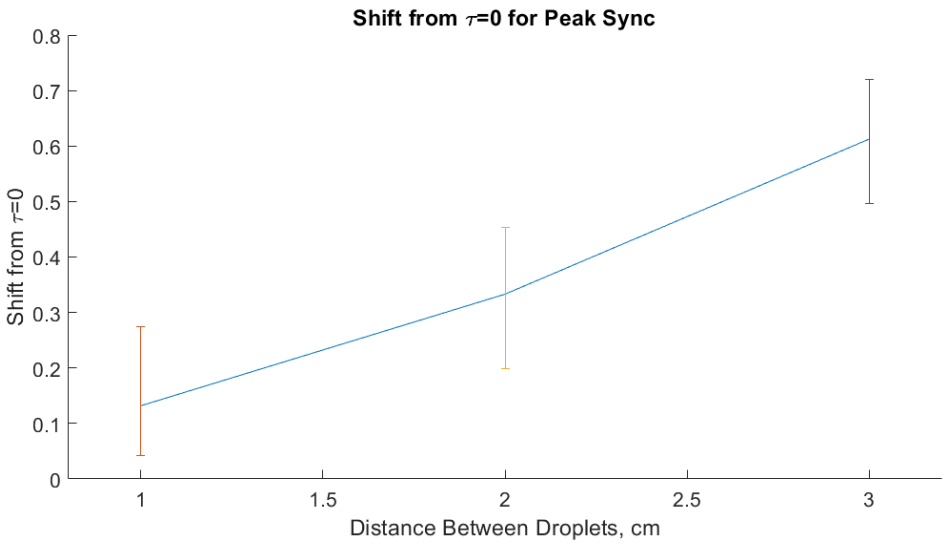

Figure 5.7: Shift in τ where the peak correlation values are found as a function of the distance between the droplets. The normalised cross-correlation function was applied to the signals, droplet A-post, and droplet B, and the peak correlation value was extracted. The shift in the τ position where this value was found was then computed as a percentage of the original dataset length. These values were stored and averaged, to be plotted as a function of droplet separation. The error bars show the minimum and maximum values extracted from the data, over 34 samples.

Figure 5.7 shows the decrease in signal correlation as a function of the distance between the droplets. The signals extracted from droplet A, post introduction of droplet B, were correlated against the subsequent droplet B signal using MATLAB's inbuilt normalised cross-correlation function. The peak correlation value was extracted, and the displacement from τ was converted into a percentage of the original dataset length so all the values could be averaged. This was then plotted against the droplet separation and reveals the exponential increase in displacement from τ=0 that the peak correlation exists at.

The plot shows how the correlation in the activity of the droplets decreases exponentially as the distance increases. This is due to the fact that the diffusion of the aforementioned longitudinal wave propagating between the droplets decreases in power the further it has to travel through the oil phase. This is an example of the inverse power law, where the further apart 2 sources are, the less they impact one another. It is difficult to notice in the coarse-grained approach to the correlation as a function of distance study, but the gradient of the curve between 2cm and 3cm, is steeper than the gradient between 1cm and 2cm. This begins

to highlight the effect the inverse power law has in our system. The further away the droplets are from one another, the lesser the impact they have towards the other. The change in the mean correlation shift from τ=0 as a function of distance is supported by figure 5.9, where the greater the distance, the less similar the frequencies in the PSD are.

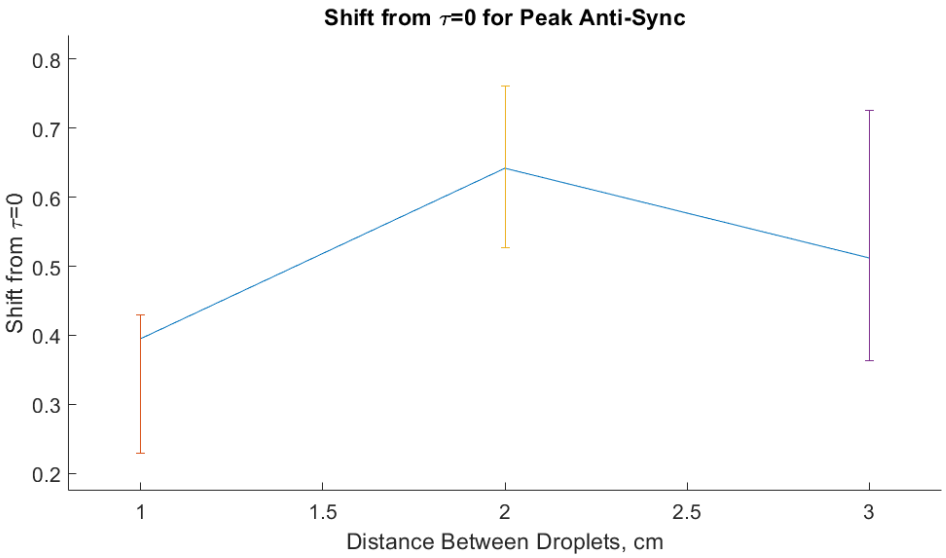

Figure 5.8: The shift from τ=0 where the maximum value of the anti-sync correlation occurs in the graph of the normalised cross-correlation function for droplets separated by 1cm, 2cm, and 3cm. Data was extracted from a series of 34 experiments.

Figure 5.8 shows the shift from τ=0 as a proportion of the dataset, that the most significant peak in anti-sync occurs in the normalised cross-correlation function, applied to droplets separated by 1cm, 2cm, and 3cmm. Averages were taken from a series of experiments. The 1cm separated droplets produce anti-sync at a greater shift from the τ=0 point. This is an interesting remark, as it shows the nature of the nonlinearity in the BZ reaction and how this plays out in practical experiments with external factors. Whilst figure 5.8 doesn't follow the same pattern as figure 5.7 does, it does reveal that the 3cm separated droplets show a greater anti-sync regime than the 2cm separation. This could be an artefact in the analysis, but could also show some form of coupling between the droplets at 3cm, which does not appear in the analysis when looking for positive correlation sync in the graph of the normalised cross-correlation function.

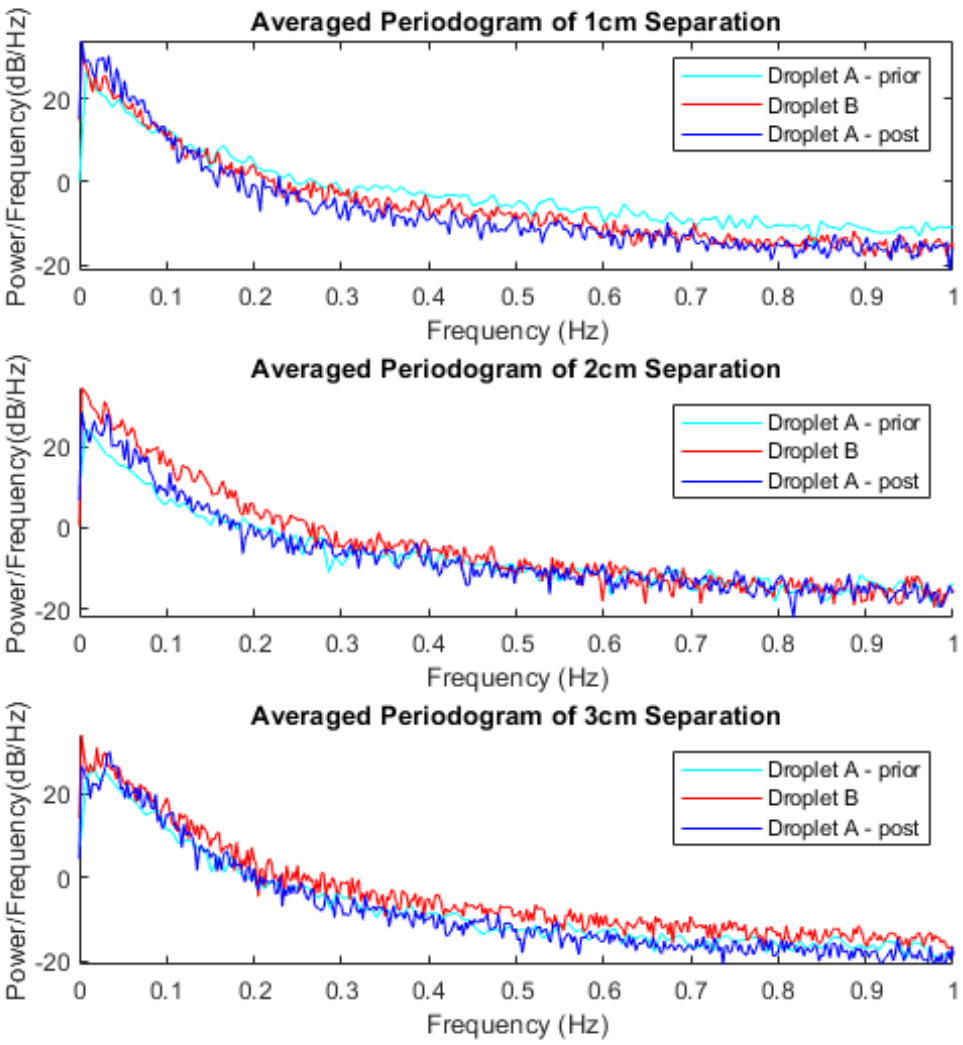

Figure 5.9: Averaged periodograms of droplet time series data captured from time-lapse imaging. the frequency range spans from 0-1Hz due to the nature of the BZ periodicity having a long period. The different droplet separations are plotted independently, with the graphs showing droplet A prior to the addition of droplet B, droplet B, and droplet A post-introduction of droplet B. It is shown that the frequency response of Droplet A changes to more closely match droplet B in the 1 cm separation graph, showing that there is an entrainment response of the droplet once a new droplet is introduced. As the droplets are moved further and further away the entrainment decreases. Graphs are averaged from 45 independent time series data sets.

Figure 5.9 shows the averaged periodogram of droplets within the millifluidic devices with droplet separations of 1cm, 2cm, and 3 cm. The frequency range of focus is related to the physiological frequencies that can be observed in the BZ reaction. The normal frequency of chemical wave generation is low due to the LC formations occurring in the order of 10s of

seconds, to minutes per wave. Therefore, only the extremely low frequencies are considered from the PSD. The data was collected regarding the periodicity of the oxidation of the metal catalyst, represented visually by the colour change from red to blue. The pixel intensity values of the oscillating droplet were collected by applying a 3x3 spatial filter to the droplet and averaging the values. The time-series data for droplet A was segmented to define the time period prior to the introduction of the second droplet, droplet B, and droplet A post-droplet B introduction. The data sets are therefore named and referred to as, Droplet A - prior, Droplet A - post, and Droplet B. The averaged values were stored in a time series dataset where the frequency information was extracted in the MATLAB programming environment, using predefined procedures in the signal processing toolbox. The graphs shown were produced by averaging 45 independent power spectral density calculations taken from the extracted time series data. We see that the shorter the distance between the oscillating droplets, the closer the frequency profiles line up, and therefore, the greater the entrainment effect is. In each graph, the cyan plot represents droplet A prior to the addition of droplet B, the blue plot represents droplet A post-introduction of droplet B, and droplet B is represented with the red plot. It is observed in the initial plot that droplet A becomes entrained with droplet B, as shown by the frequency graphs synchronising. Interestingly, it is more apparent at the higher end of the frequency range, but apparent all the same. This effect is also apparent in the graph representing the 2cm separation of droplets, but with a much greater diminished effect. The graphs of droplet A-prior and droplet A-post are more similar to one another at the low frequencies, but at the higher end of the frequency spectrum become more similar to droplet B. This could be an explanation for the high correlation in activity, but the addition of some phase difference in figures 5.7 and 5.8. The last plot, showing the periodogram of the droplets separated by 3cm shows no entrainment effect (see fig.5.9), where the frequency profile of droplet A prior to, and post-introduction of droplet B are largely the same, showing no tendency to align with the frequency behaviour of droplet B. The profiles of droplet A-prior and droplet A-post are almost identical, with very minor deviations. They show no similarities with the graph of droplet B, implying that there is no correlation in the activity, meaning the droplets did not become entrained in the 3cm separation experimental condition.

The PSD data reflects the coupling observed experimentally, where a system of active-passive switching occurs between the coupled droplets. This switching is responsible for the

feedback loop that forms with the pair of oscillating droplets which become entrained(see fig.5.10 for more).

5.4.2 Mechanical Perturbation via Droplet Elongation

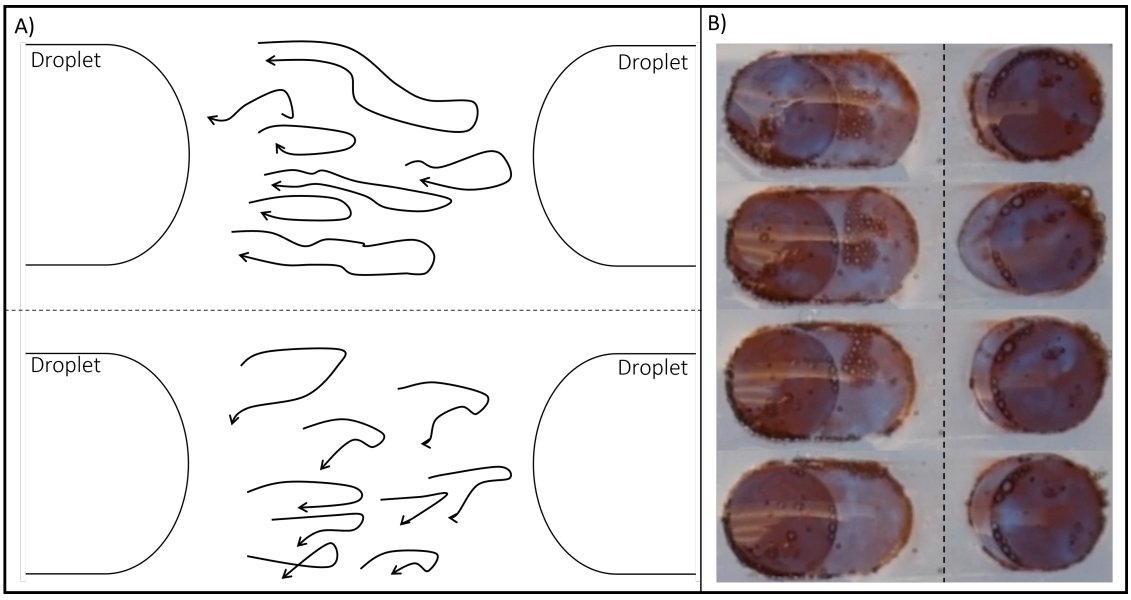

Figure 5.10: (A) ASreamlines of flow field between a pair of coupled droplets with separation of 2cm. Time series imaging of coupled droplets with hydrodynamic flow visualised by tracking Microbeads suspended within the oil phase separating the droplet pair. The flow within the Oil phase is visualised as the droplets switch between active and passive, in an alternate fashion. The flow observed between the droplets is responsible for driving the entrainment of the spatially separated pair of droplets containing Belousov-Zhabotinsky solutions. Each frame shows an active and passive cycle for each droplet, with the leftmost droplet starting as active, and the right droplet starting as passive in each frame. (B) Time-lapse photography of the coupled droplets. The dotted line represents the space separating the pair. The shape deformation is observable as the droplets switch between active and passive classification. The streamlines of the flow field here are shown to be gradually misaligned with the virtual connecting line of the 2 droplets.

The flow between a pair of coupled droplets is visualised through the use of particle image velocimetry in figure 5.10. presented in panel A is a schematic view of a pair of droplets is shown with flow trajectories mapped between the pair. During the course of the recordings, each droplet switches phases from active to passive. The leftmost droplet switches from active to passive in both diagrams, whilst the rightmost droplet switches from passive to active. A droplet in the active phase has the effect to create a hydrodynamic flow between the pair of droplets through the mechanism of chemo-mechanical induced elongation of the droplet. the

hydrodynamic flow occurs in the form of a longitudinal periodic velocity field through the oil phase. The elongation of the droplet creates a positive pressure barrier in front of the droplet which creates the hydrodynamic flow through the oil phase towards the passive droplet. This flow acts as a mechanical perturbation on the inactive droplet causing a slight deformation of the droplet. The deformation causes the free surface energy of the droplet to increase, which drives the generation of flow to return the droplet to the initial non-deformed state, where the surface area is minimised. This release of energy drives the creation of new LC in the droplet, which causes the phase transition from inactive, to active. The generation of the new LCs and causes the propagation of a chemical wave across the body of the droplet. This drives the elongation of the droplet, resulting in hydrodynamic flow in the opposite direction to the original flow. This flow acts as a mechanical perturbation on the original active droplet, now in the passive state, and causes LC formation in this droplet for the same reasons previously stated. This forms a positive feedback loop where both droplets are chemo-mechanically coupled. The effect of this coupling diminishes with distance, as the power of the flow decreases exponentially as the spatial distribution of the droplets increases. Panel B shows a timelapse of the droplets as they alternate from active to passive throughout the course of the coupling. The shape deformation is visible at the connecting ends of the droplet, and the dotted line is employed to show the separation of the droplets. The wave formation from the LCs can be visualised in this manner, as the flow throughout the droplets can be observed in this time interval. The shape changes of the droplet through time are indicative of the shape deformation observed when a liquid droplet is perturbated by a hydrodynamic flow at the liquid-liquid barrier. Due to the incompressible nature of the aqueous droplet, the volume cannot change, which is reflected by the slight flattening of the edge in the compressed droplet. The droplet will try to minimise its free energy by reducing the ratio of volume to the surface area, which when deformed, is increased. The droplet will return to its original shape formation where the ends of the droplet are formed due to capillary action, minimising the surface area. This change in shape is one manner in which hydrodynamic flow will be induced within the oil phase separating the pair of droplets. The other is the elongation caused by the propagation of chemical wave across the body of the droplet. This wave will cause a shape change in the droplet due to the gradient of interfacial tension at the phase separation. In both scenarios, there is a generation of pressure that builds up as the droplet extends back

into the millifluidic channel, and creates hydrodynamic flow back towards the paired droplet.

The generation of the LC in response to the mechanical perturbation is generated due to the micro-stirring effect caused by the hydrodynamic perturbation, along with the symmetry breaking under the compressive force of the mechanical perturbation from the hydrodynamic flow. As the droplet is compressed and changes shape due to the hydrodynamic flow, there will be a bulk flow to compensate. This causes a mass transit within the droplet. The mirroring of this mass transit occurs when the droplet normalises to its original shape to minimise the surface area, causing another stirring effect due to the mass transit. This stirring effect will lead to an acceleration of the BZ reaction and will instantiate an LC formation within the droplet. This will subsequently cause the elongation of the droplet, applying a mechanical perturbation on the original droplet in the form of hydrodynamic flow and repeating the cycle. In the arrangement with droplet pairing positioned closer together, the mechanical perturbation will be increased and deform the droplet to an even greater extent. This will have a positive impact on the nature of the coupling, whereas droplets at a greater distance will have a diminished coupling effect due to the decrease in effect that the hydrodynamic flow will have as a source of mechanical perturbation due to its diffusion through the oil phase over a longer distance.

Figure 5.11 shows an indicative response of the droplet to elongate under the chemical wave propagation. The droplet has extended towards the left, following the channel in the millifluidic device due to the hydrodynamic flow of the oil phase acting as a mechanical perturbation to the CoM of the droplet. The dotted lines are used to indicate the droplet elongation under the chemical activity and show that the length of the droplet increases as the LC forms spiral waves over the 90-second period. The mechanism for the elongation is the same as shown in figure 4.9, from section 4. The elongation is driven by the rapid increase in the LC formation generated by the mechanical perturbation from the SDS micelles present in the oil phase. There is deformation along the edge of the droplet as it elongates through the millifluidic chamber. Many LC formations can be observed, which create flows induced by the Marangoni stress from the many gradients of interfacial tension, due to multiple sites of LCs forming. As the flows converge, there is a compressive force, as the vortices repel one another. This creates a regime of turbulent flow inside the droplet which corresponds to

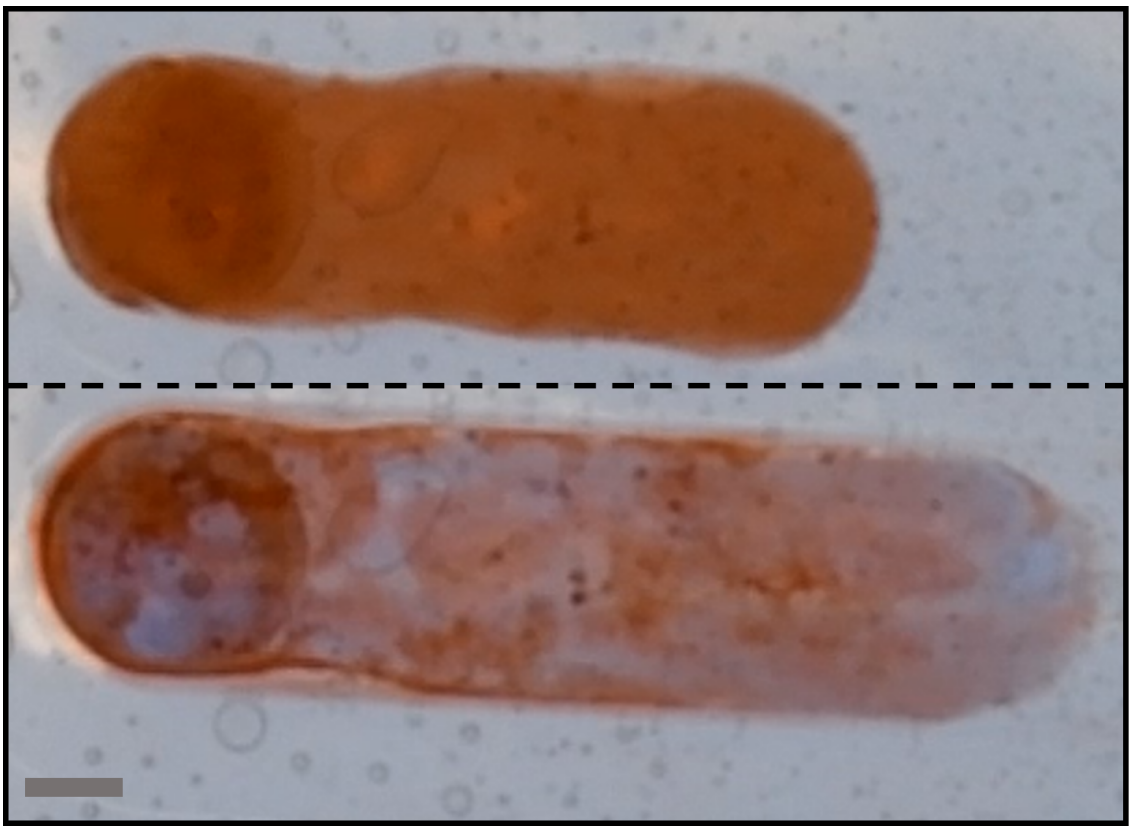

Figure 5.11: Chemically driven droplet elongation observed over a 60-second interval. Leading centre formation at each end of the droplet results in the elongation of the droplet. The elongation appears to play an important role in the coupling of the droplet pairs. Scale bar represents 2mm.

deformation and greater elongation that is normally observed in the oscillating droplets. This elongation is the mechanism for the generation of the longitudinal wave propagation observed in the oil phase between the droplets that become entrained. A potential limiting factor to the generation of the positive feedback loop which entrains the droplets is the deformation of the end of the elongating droplet (see fig.4.10 and 4.12). If this end elongates too fast and undergoes the deformation associated with overcoming the viscosity of the oil phase, it may result in the longitudinal wave being produced at an angle to the line connecting the droplets, rather than travelling parallel. When the wave travels parallel to the connecting line, the wave will extend from one droplet, directly onto the droplet it is paired with. However, if the wave travels at an angle, it will have a reduced impact on the droplet, or may not even compress the second droplet. This would lead to a depleted mechanical perturbation which may result in the droplets not becoming entrained. This effect would compound with the distance as there will already be a dissipative effect due to the inverse power law. The

longitudinal wave being misaligned is visible slightly in figure 5.10, where the returning flow from droplet B is not parallel to the virtual connecting line. The effect here is minimal, due to the confined separation of the droplets, but is likely to be a major contributing factor to the droplets becoming unpaired in a matter of minutes after showing highly correlated activity. The deformation is hard to notice, but apparent when looking at the ends of the droplets closest to one another. When the misaligned longitudinal flow through the oil phase makes contact with the paired droplet. the mechanical perturbation will not be as effective, as the force vector is not straight through the droplet, instead it is angled in such a manner that it will have a decreased impact on the stirring effect.

Figure 5.12 describes the mechanism of which the hydrodynamic flow between a pair of coupled droplets causes the entrainment of droplets. Panel A represents the moment where the chemically active begins to elongate, shown by the blue arrow. The elongation is induced by the formation of an LC in the droplet, causing an oxidised wave of ferroin to propagate across the droplet body. As this chemical wave has a different charge ($3+$) compared to the reduced state ($2+$), a gradient of the interfacial tension is created between the aqueous phase of the droplet, and the oil phase it is suspended within. Maranongi flow is induced in the phases due to such gradient and imparts a momentum transfer due to friction between each phase, due to the phases having a different viscosity. Due to the surfactant, and the anchoring of the droplet by the millifluidic device, instead of undergoing self-propelled translational motion, the droplet will elongate into the channel separating the droplets in the millifluidic device. The elongation causes compression of the oil phase, which builds up positive pressure, causing a longitudinal wave of hydrodynamic flow towards the other droplet which dissipates over distance and is represented by the black arrow between the droplets. In the scenario where there is a small degree of separation between the droplets, the hydrodynamic flow is not diminished enough to have limited impact and instead acts as a form of mechanical perturbation onto the second droplet. In the scenario where droplets lie closer to one another, the hydrodynamic flow is able to apply mechanical perturbation onto the second droplet, which causes a small build-up of pressure and causes shape deformation on the droplet. The shape deformation of the droplet is represented in panel B, and is shown by the blue arrow. This deformation of the droplet causes an increase in free energy of the droplet, which will be minimised by decreasing the

deformation which will create a flow within the droplet. The release of energy as the droplet returns to the minimum energy state causes LC formation within the droplet, which leads to the propagation of an oxidised chemical wave across the body of the droplet. This process is displayed within panel C, where the droplet has returned to its initial shape, shown with the blue arrow, and shows the chemical wave propagating across the body of the droplet, shown in light blue. This chemical wave propagation leads to the same elongation and hydrodynamic flow shown within panel A and will cause shape deformation onto the initial active droplet, which is currently in the inactive state. This system of mechanical perturbation between droplets leads to a positive feedback loop, where the droplets become entrained with each other. The entrainment can be observed as the droplet becomes synchronised over time.

5.4.3 Modelling entrainment

The coupling of the droplets was modelled using the FHN model modified with the Kuramoto oscillator. The FHN model has routine periodic oscillations which can become entrained with the addition of the Kuramoto oscillator. The modified FHN model with the adapted Kuramoto oscillator can be represented by the following pair of coupled equations:

$$\frac{\partial \upsilon_1}{\partial t} = \upsilon_1 - \upsilon_1^3 - \omega_1 + K(\upsilon_2 - \upsilon_1) \tag{A}$$

$$\frac{\partial \omega_1}{\partial t} = \alpha(\beta \upsilon_1 - \omega_1) \tag{B}$$

$$\frac{\partial \upsilon_2}{\partial t} = \upsilon_2 - \upsilon_2^3 - \omega_2 + K(\upsilon_1 - \upsilon_2) \tag{C}$$

$$\frac{\partial \omega_2}{\partial t} = \alpha(\beta \upsilon_2 - \omega_2) \tag{D}$$

υ_1 and υ_2 represent the voltage, and ω_1 and ω_2 represent the reset variables. Here, K refers to the entrainment variable as part of the modified Kuramoto oscillator term. To model the real system, the variable k represents the inverse of the distance between the 2 droplets. Sensitivity testing was conducted on the model with the aim to produce a pair of entrained signals to simulate the correlated activity shown in the experimental results. The entrainment

term K was used to simulate the inverse of the spatial separation the droplets are subjected to in the experimental system. Values for α, β, and ω, were optimised to produce stable regions for anti-phase, and phase synchrony, through the repeated sensitivity testing that was conducted. Analysis of the signal output in the time and phase domains ensured the entrainment of the signals would occur whilst maintaining stability in the system.

Fig.5.13 (a) shows anti-phase signals, produces by modifying the entrainment term K to be equal to -0.025. The system is shown to be stable in the phase portrait of each signal shown in part (b). When a system produces mechanical work, which we observe in the BZ droplet, the pathway in the phase space will follow a cyclical pathway. This is observed in the simulation of the coupling between the pair of droplets, as the initial position in the phase space is outside of the stability region, which is quickly convolved as the synchronised signals become entrained, and the cyclic pathway is formed in the phase space. Through sensitivity testing, it was discerned that 3 independent states can occur. These states are: The instability region; The anti-phase region; and, The synchrony region. The instability region was discovered to exist when K is set equal to, or less than -0.23. The anti-phase region was found to lie between values of K set to -0.22 to 0.02. Then the signals were found to synchronise through entrainment when the value of K is set to 0.03 or greater. The entrainment term, K, can be used to represent the degree of separation between the droplets. Where the greater the value of K, the closer the droplets are, and therefore, the greater the entrainment factor is.

K Value	Mean Phase Difference
-0.23	π
-0.22	π
0	0.72368
0.03	0.00584
0.5	0

Table 5.1: Phase differences as the entrainment term, K, is adjusted to represent the instability region (K = -0.23), no entrainment (K = 0), anti-phase signalling (K = -0.22), and in-phase signalling (K = 0.03, and K = 0.5).

Table.5.1 shows the phase difference for different values of the entrainment term, K. It is shown that once the entertainment term reaches the value of 0.03 that the signals become entrained and produce a synchronized behaviour, with 0 phase difference. These signals

are then determined to be coupled, as any changes in either signal will directly affect the corresponding signal.

5.5 Discussion

Presented in this chapter is the mechanism of hydrodynamic coupling between water droplets containing Belousov Zhabotinsky solutions. The coupling of spatially distributed droplets was found to occur at a distance of 1cm, and weakly at a distance of 2cm. No entrainment was found when the distance between the droplets was 3cm. The mechanism presented could explain the signal proliferation observed in networks of BZ droplets [319]. The current hypothesis from the authors involves the diffusion of excitatory chemical compounds between the droplets. Whereas we have shown the proliferation of signals where the diffusion of excitatory chemical species would be impossible. The absence of chemical species diffusing through the oil phase lends itself to the argument that the cause of the signal propagation between droplets is due to the chemo-hydrodynamic coupling, rather than an excitatory species diffusing through a lipid-bilayer from droplet to droplet. The concentration of the surfactant employed was kept too low for the saturation of micelles to build up enough for it to act as a bromine scavenger, which would have allowed for the diffusion of excitatory chemical species between the droplets. Instead, the use of 0.45g of sodium dodecyl sulfate (SDS) per litre of oleic acid allowed for the desired effect of reducing the interfacial tension between the aqueous droplet and the oil phase but did not allow for the diffusion of excitatory reactive species of bromine between the droplets. To study the hydrodynamic flow between the droplets, the use of microspheres was deployed within the oil phase, which were tracked through the timelapse footage of the oscillating droplets and show flow from the active droplet, towards the passive droplet, which then becomes deformed due to the hydrodynamic flow acting as mechanical perturbation onto the droplet. The deformed droplet is pushed out of its minimum free energy state and thus has to release energy to return to its minimum energy state. This release of energy creates the formation of new LC within the droplet, which leads to the propagation of an oxidised chemical wave across the body of the droplet. The oxidised chemical wave has a 3+ charge, compared to the 2+ charge of the reduced state. Due to the difference in charge, a gradient of the interfacial tension is generated between the droplet and the oil

phase, which induces Marangoni flow in both phases. Due to the difference in viscosity of the phases, friction occurs when the flow is induced, which imparts a momentum transfer onto both phases. This momentum transfer goes largely unrealised within the oil phase but causes translational motion in the aqueous phase. In a system where no surfactant is present within the oil phase, this translational motion is realised as a shift in position in the whole droplet, but when the surfactant is present, instead, the droplet will be shown to elongate. This elongation of the droplet causes positive pressure to build up in the oil phase, which is subsided with the induction of hydrodynamic flow in the direction of the alternate droplet. This flow then has the same impact on the original droplet, leading to a positive feedback loop between the droplets. when the droplets are sufficiently close to one another, which was determined to be a maximum of 2cm, the coupling can occur, where the loop will persevere until the reactive species has died out due to the droplet reaching thermodynamic equilibrium, and the chemical reaction ceases. In the case where the droplets are at a larger distribution, 3cm, the diffusion of the hydrodynamic flow is too great to act as mechanical perturbation onto the second droplet, which causes a lack of entrainment to occur in the system.

A crucial factor was uncovered, where the deformation of the droplet could be responsible both for the droplets becoming coupled, and also failing to couple. The mechanism for the entrainment lies in the hydrodynamic flow occurring as a longitudinal wave through the oil phase. When the droplet deforms and elongates, this periodic velocity field is sent parallel to the virtual connecting line between the pair of droplets. It acts as a source of mechanical perturbation on the next droplet, which will cause LC formation, and the subsequent mechanical perturbation onto the original droplet. However, when the deformation on the elongating end of the droplet is not homogeneous and occurs at one edge more than the other, the longitudinal wave will not travel parallel to the connecting line, instead, it will travel at an angle. In the confined droplets, this will not be a great problem, as the wave is likely to still have a direct 'hit' onto the other droplet, and produce the mechanical perturbation required to maintain the feedback loop. But in the cases where there is a greater difference between the droplets, the periodic velocity field will not have a direct impact on the droplet or may miss it entirely, at this stage the feedback loop is not maintained and the droplets will fall out of synchronisation. This would explain the signal propagation in the study performed

by Chang *et al.* [195], as their network of droplets were in close contact with one another, only separated by a lipid bilayer to prevent merging. This close proximity would allow for the periodic velocity field to have a maximal impact on the following droplet, to allow the signal propagation to occur successfully. We also present a finding that the closer droplets produce chemical waves at a greater frequency than the droplets separated further apart, this will also act as a factor in the entrainment, where the greater frequency of the wave generation will act as a more frequency mechanical perturbation onto the second droplet, which will subsequently cause that droplet to produce waves more frequently. This will help to increase the positive feedback loop which will keep the droplets entrained in such a manner.

Entrainment between a pair of droplets was modelled using the FHN model modified with a Kuramoto oscillator. The k term in the entrainment model is the inverse of distance, as the greater the term k, the less entrained the modelled signals become. Increasing the k term through the values presented causes the phase difference of the coupled oscillators to change from π radians, through to 0 radians, showing that the signals have become entrained. This aligns with the plot showing the correlation shift as a function of the distance between the droplets, where the closer the droplets are, the smaller the shift from τ=0 is shown to be. The distance between the droplets can be modelled with the inverse of the entrainment term, k.

Previous studies of signal propagation in networks on BZ droplets have been conducted, where droplets are in physical contact, but separated via a lipid bilayer which stops the droplets from merging[195]. The immediate proximity of the following droplet would cause considerable distortion forces between the droplets, causing the whole system of droplets to be out of a state of minimum energy whilst undergoing chemical propagation. The authors posited that the propagation of the chemical wave was due to the diffusable excitatory chemical species travelling from droplet to droplet via diffusion through the droplet membrane, into the next droplet. This subsequently causes the next droplet in the array to form an LC which causes wave propagation across that droplet, which will propagate onto the subsequent droplet again. This explanation seems logical, and the propagation of oil-diffusable excitatory species is possible from droplet to oil phase, however, the excitatory species diffusing back into the droplet, or into a subsequent droplet would have very different chemical properties to the excitatory

species remaining within the droplet. Brominated-SDS will appear to 'leech' from the droplet and appear as a flow light red chemical from the droplet when surfactant concentration is sufficiently high. This chemical compound however will not behave the same as the bromine species will due to the changed properties when it reacted with the SDS. In our study, the droplets were not in physical proximity to one another but were within an impactful range due to the hydrodynamic flow at the 1cm and 2cm separation, however, at the 3cm range, the effect was diminished due to the decay of the flow at the increased distance. The concentration of the SDS within the oil phase was also kept sufficiently low so as to not allow for great enough micelle formation to allow for the bromination of SDS, which leaches the excitatory signalling molecules out of the droplet. This was confirmed visually as there was no trace of the brominated SDS within the oil phase, along with no decrease in the active lifespan of the BZ droplet. This showed us that the deforming forces occurring between the droplets were causing the signal propagation, as opposed to the diffusion of chemical species between the droplets. We posit that this finding can help to develop greater computational networks of BZ droplets, along with building an understanding of how droplet-droplet networks can be developed in the future.

5.6 Conclusion

Distance-dependent entrainment of aqueous droplets containing Belousov Zhabotinsky (BZ) solutions was found to occur due to hydrodynamic flow-induced deformation forming a positive feedback loop between a pair of coupled droplets. The formation of a leading centre (LC) within one droplet, will cause its elongation, which in turn results in a positive periodic velocity field which is generated at the front of the droplet and causes the hydrodynamic flow to project towards the second droplet. This flow will disperse within the oil phase as a function of distance, but where the droplets are sufficiently close together, the flow will act as a mechanical perturbation on the second droplet. This will result in shape deformation on the droplet, which removes it from its minimum free energy state. As the droplet returns to the minimum energy state, there is a release of energy which causes LC formation to occur in the droplet, which then leads to the propagation of the chemical wave, and subsequent elongation

which in turn causes hydrodynamic flow back into the direction of the original droplet. This positive feedback loop results in the synchronisation of the droplet, as the beating frequency becomes aligned between the coupled pair of droplets. Due to the absence of oil-diffusable excitatory chemical species present in the oil phase, the authors posit that this mechanism of chemo-hydrodynamic coupling is an explanation for the signal propagation in larger-scale networks of droplets previously reported in the literature. The coupling observed in the droplets was modelled using a modified FHN model to include the Kuramoto oscillator. The model uses the variable k as the inverse of the distance between the 2 droplets and displays the phase difference reducing from π radians to 0 radians as the entrainment occurs.

In this work, we present the coupling between a chemical reaction and mechanical work, for both single droplets, and droplet-to-droplet. The chemical wave propagating across the droplet performs mechanical work which involves elongating the droplet within the experimental apparatus, which causes a longitudinal wave to form within the oil phase, which acts as a mechanical perturbation onto the secondary droplet, causing a deformation. This mechanical work acts as an instigator for the chemical wave to form within the receiving droplet due to the small stirring effect the deformation has on the droplet. The LC produces from this stimulus creates the same mechanical work that we observed in the initial droplet and causes the same flow within the oil phase as before, closing the loop for the chemical to mechanical, to mechanical, to chemical coupling. This closed-loop system creates a cycle of active-passive droplets switching roles to continue the effect until the mechanical work decreases with the life span of the BZ reaction. The droplets separated at a shorter distance also were found to produce a greater number of chemical waves in the same time frame when compared to those held at a greater distance.

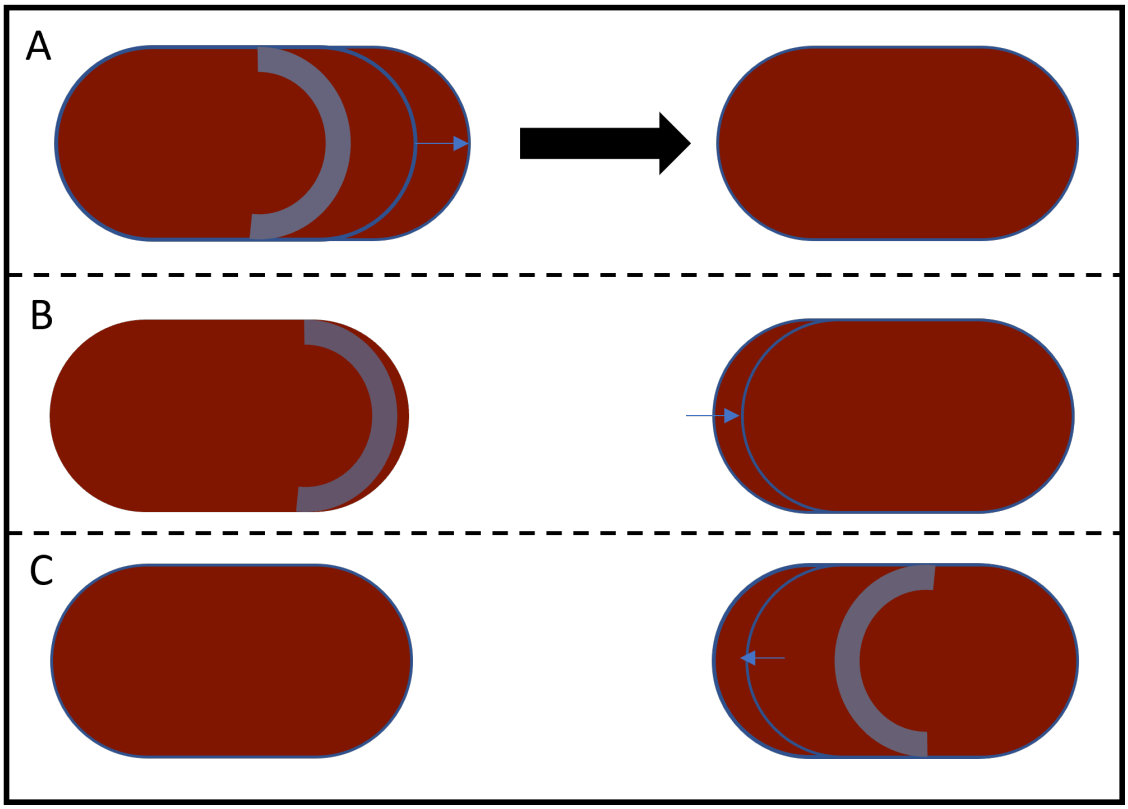

Figure 5.12: Simplified diagram of hydrodynamic flow generation acting to couple droplets spatially separated suspended in an oil phase. In panel A, the left droplet is shown to undergo elongation, represented by the blue arrow, due to the propagation of chemical wave across the body of the droplet. This elongation acts to compress the oil in front of the droplet. The compression of the oil creates pressure within the phase, which leads to a flow across the oil phase directed towards the second droplet, shown with the black arrow between the droplets. This flow causes mechanical perturbation on the secondary droplet. This flow acts to compress the droplet, shown in panel B via the blue arrow. This compression causes instability of the free energy of the droplet, which leads to internal stress of the droplet which creates a leading centre within the body of the droplet. Panel C shows the formation of the leading centre, and the droplet beginning to return to the initial size before the mechanical perturbation. The chemical wave formed at the leading centre will propagate across the body of the droplet, and lead to the hydrodynamic flow described previously, creating a positive feedback loop of mechanical perturbation from droplet to droplet, which results in droplet entrainment.

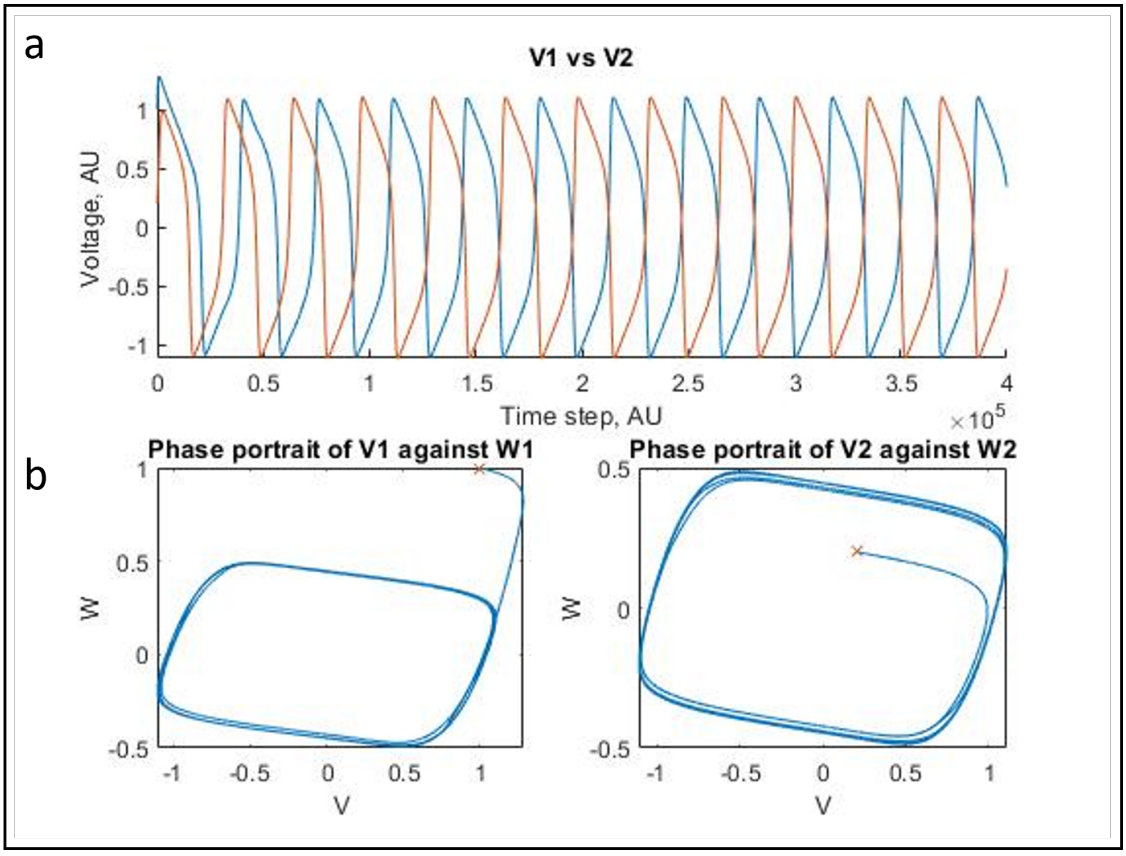

Figure 5.13: (a) Time series data of anti-phase entrained signals generated by a modified FHN model with Kuramoto oscillator. V1 is shown in blue, with V2 is shown in red. Whilst the coupled oscillators are functioning in an anti-phase regime, this does show synchronisation, only with a time variable causing the offset in the peaks. (b) Phase portrait of the voltage and reset signals. The start of the pathway through the phase space is remarked by an 'x' within the plots. Parameters used: $\alpha = 0.1$, $\beta = -1$, K=-0.025, Initial conditions: $\upsilon_1 = \omega_1 = 1$, $\upsilon_2 = \omega_2 = 0.2$

Chapter 6

General Discussion and Conclusion

In this chapter, we will compile the concluding arguments of each chapter together to tell a cohesive story about the connections each research project makes with one another. The first chapter involves the discovery of the BZ droplet electrotraxis phenomena. An externally applied electric field was able to produce directed translational motion of the oscillating BZ droplet, due to generating an inhomogeneous distribution of LC formations due to an ion density gradient forming as a result of the DC field. The second chapter details the process of the elongating, deformation, and division of an aqueous BZ droplet suspended in an SDS-saturated oil phase. The division was only possible due to the environmental perturbations, which were optimised over the course of the experimental process. The final results chapter shows the synchronization of a pair of BZ droplets as they become entrained. The droplets are compartmentalised and held at a distance. This research project was designed to determine if the inter-droplet chemical wave propagation was due to the diffusion of excitable chemical species travelling through the lipid bilayer in previous studies, or if it was hydrodynamic forces acting on the droplets and causing them to produce a chemical wave. Due to the distance between the droplets, we were able to deduce that the chemical wave propagation was due to the hydrodynamic forces acting on the secondary droplet, as opposed to the diffusion of the excitatory chemical species.

6.0.1 General Discussion

To aid in the understanding, a graphical representation of the entire research conducted for this thesis has been compiled in figure 6.1. The Electrotaxis behaviour of the BZ droplet found in section 3 is depicted in the top left where the DC field is shown being applied externally to an oscillating BZ droplet, which is travelling along the direction of the EF. This is followed by the graphic in the lower left, which depicts the elongation and division of a droplet subjected to an AC field. The final graphic, presented on the right-hand side of the image, details the entrainment of a pair of oscillating BZ droplets. The graphic depicts the oscillating causing elongation of the BZ droplet, in the direction of the alternate droplet. This process is heavily involved in the synchronisation of their activity, which is shown in the lower portion of the graphic.

The discovery that the BZ droplets were not impervious to the effect of an externally applied DC field, and subsequently the impact the tripole effect has on the elongation of a droplet, relays the connection between biological motility, and cell division. Fundamentally, the process which governs the electrotaxis behaviour of the droplet is the same mechanism which produces the elongation that causes the division event to occur. When the droplets have subsequently divided, the elongation causes a periodic velocity field to present mechanical perturbation onto the paired droplet. This is akin to the cell-cell communication observed in bacteria, where the daughter cells will oscillate in synchronisation after the division event occurs.

6.0.2 BZ Droplet Electrotaxis

To understand the electrotaxis of BZ droplets, we recall the FKN mechanism which describes the BZ reaction as three periodically repeated processes. This description has been the backbone of the BZ understanding, and the core of many mathematical models. The periodicity of the reaction is depicted by the peaks and troughs in the graphical output of the 3 variables in the Oregonator, or by colour changes in 3D simulations of the reaction. In the BZ reaction, the oxidation process is visualised by the colour change of the metal catalyst (Ferroin) from red (reduced - 2+) to blue (oxidised 3+), with other colour changes in BZ reactions with different

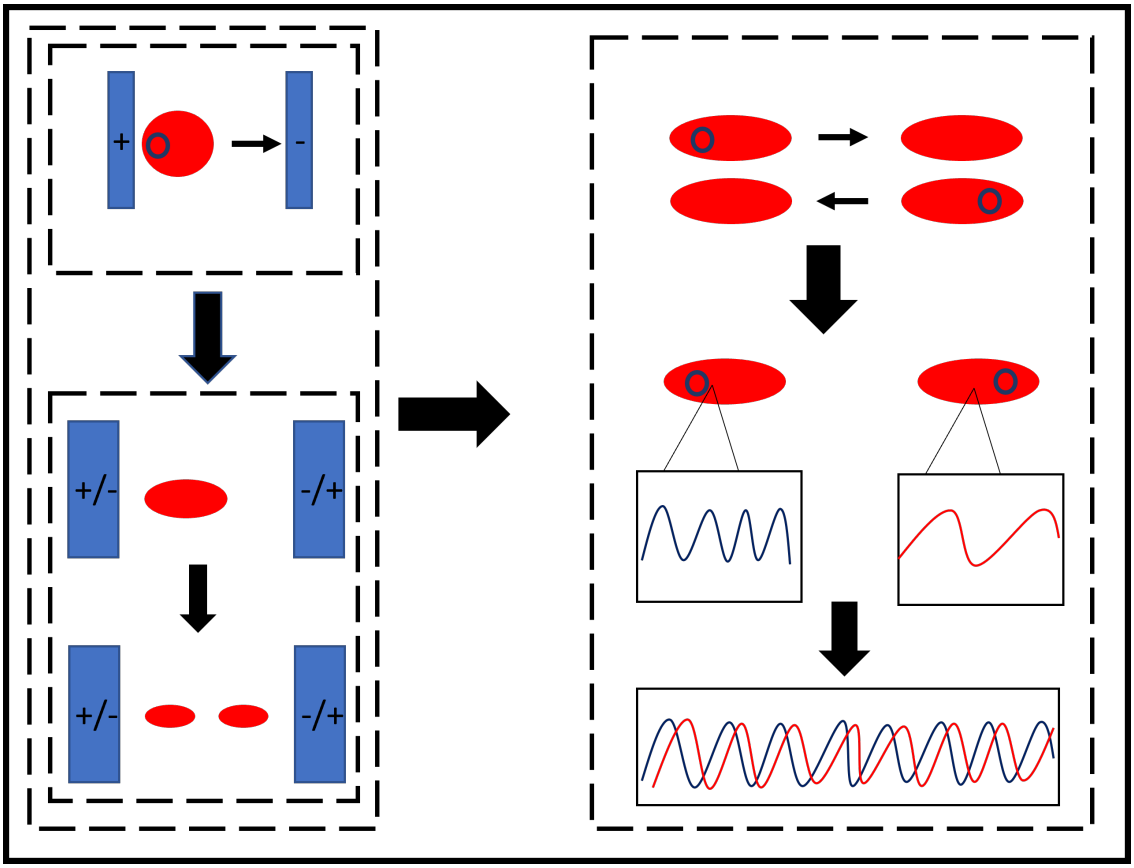

Figure 6.1: Graphical representation of the 3 results chapters and how they relate. The electrotaxis of the BZ droplet is shown, where the DC field is perturbating the droplet in such a manner that it controls the translational motion of the oscillating droplet. The Droplet division is then shown, where the AC field contributes to the elongation of the droplet, which eventually divides. This is then relayed into the final results chapter, where the pair of droplets show influence on one another, where the propagation of a chemical wave produces an elongation of the droplet, creating a periodic velocity field aimed toward the paired droplet. This mechanical perturbation produces a positive feedback loop which couples the droplets' oscillatory behaviour.

recipes. The electrotaxis behaviour of the aqueous BZ droplets was discovered, where a DC electric field (EF) was applied externally to the suspended in an oil phase. With the application of an EF, the location of the wave formation is biased towards the positive electrode. This is in contrast to typical experiments using quasi-2D BZ solutions and BZ droplets without an external field, where the formation of the LC occurs homogeneously across the entire reaction in an unpredictable manner. Our experiments have revealed a strong correlation between the biased distribution of the LC locations and the direction of the chemically driven translation motion of the BZ droplets. This was represented in figure 3.6, where it was proved that the translational motion follows the vector of the wave propagation. The static EF applied to the

droplet caused an inhomogeneous distribution of ions within the droplet. The field attracted negatively charged ions to the positive electrode, and positively charged ions to the negative electrode. This caused a flow of ions within the droplet, potentially acting as a low-power stirring of the ions in solution, but mainly in generating a gradient of ions within the droplet. When the Br- ions accumulate, process A in the FKN mechanism can easily dominate. After some time the consumption of the Br- ions will cause the concentration to drop below the threshold required for process A to dominate. Then, process B will begin to take over as the dominant chemical process, which leads to the autocatalytic oxidation of the ferroin solution by BrO2, producing HBrO2 in the process. This will form the leading centre, as the ferroin solution is oxidised from its 2+ reduced state to the oxidised 3+ state. This LC will be formed near the positive electrode due to the increased concentration of Br- ions at this location due to the attractive force from the electrode. The propagation of this chemical wave will lead to the translational motion from the positive electrode towards the negative, displaying the electrotaxis effect.

Where previous taxis studies have been performed on the BZ reaction, our study differs due to the experimental conditions and BZ recipe utilised. Previous electrotaxis studies have only been performed on quasi-2D BZ reactions contained inside hydrogels to study the change in angle and speed of rotating spiral waves, whereas we have used BZ droplets to show a change in directed motion. In addition, other taxis studies involving BZ droplets, used alternate environmental perturbations, such as light, whereas we used an electric field. These studies also used the photosensitive ruthenium catalyst, whereas we employed ferroin solution as ours. The use of the static EF means that the application of the perturbation can be less direct, and the droplet can be housed inside other apparatus where a light source would not be able to be used. When the BZ droplet is contained within apparatus which we cannot be accessed so easily, we can still apply the electric field with the same power, by simply having the electrodes further apart, with a much greater voltage applied, so that the voltage per millimetre remains the same as displayed in our study.

An important note to make regarding the symmetry breaking across the droplet which leads to the LC formations, is the symmetry breaking that occurs along the y-axis of the applied AC field. We observe the push-pull effect the AC field has on generating LCs at the

distinct regions outlined in fig.4.8. However, there was no perturbation to cause the y-axis symmetry breaking, which was important in the division event occurring. This is crucial, as the distance between the LCs is required for the chemical wave to be formed, and to propagate which causes the gradient of interfacial tension to be formed, inducing the Marangoni stress which leads to the elongation and deformation in the droplet. If the LCs form too close to one another, the chemical waves will annihilate too early, and the deformation and elongation will be limited. Therefore, the LC formations are of paramount importance, and breaking the y-axis symmetry is the next step to increase the percentage yield of dividing droplets in the experimental process.

Microfluidics, drug delivery, and chemical mixing could benefit from the research findings on droplets moving in an electric field. By controlling the movement of droplets, we could create efficient and precise methods for mixing and delivering chemicals or drugs by incorporating the BZ solution into hydrogels. Furthermore, the findings may also pave the way for further development in fields such as soft robotics, in which the movement of droplets can be used to create soft and flexible devices, where the actuation is derived from the electrotaxis phenomena observed in the BZ droplets.

6.0.3 Droplet Division

Where the control of the LC formation could be established using a static EF, the application of an AC field was introduced as a source of environmental perturbation onto compartmentalised droplets to act as a 'push-pull' system on the ions within the solution. The push-pull system meant that no gradient over the droplet as a whole was generated, but on a microscopic scale the gradient of ion distribution did exist. The effect of the application of the AC field applied externally to the individual droplet, was a series of LC formations across the body of the droplet. The AC field in effect generates a tripole over the droplet, whereas a static DC field would create a bipolar droplet, having the source of the field periodically switching polarity means no inhomogeneous LC formation exists, like in the electrotaxis study. Whilst the distribution occurs on a much smaller scale than that in the electrotaxis study, it still does exist, and as such there are many sites where we observe LC formation when the frequency

of the AC field is applied correctly. It was found that when the frequency was too low, or too high, a homogeneous distribution was found in the LC formation. But at the correct frequency range, the formations would form in segments, distributed across the droplet. This contributed to the elongation of the droplet which is observed when the chemical waves propagate across the body of the droplet. As the droplet is anchored in the millifluidic chamber, any wave generation acts to elongate the droplet. This is as opposed to inducing translational motion, observed in the droplets suspended in the oil phase. The elongation is increased drastically when the frequency aligns with the natural frequency of the BZ droplet and can act as a push-pull mechanism on the droplet. The space between the LC formations allows for the propagation of waves to build up and then collide, rather than immediately annihilate. The fact that the waves can collide means that there will be a compression of the vortex flows generated by the Marangoni stress as a result of the gradient of interfacial tension. This will create turbulence within the droplet that will cause deformation and elongation.

The mechanism of droplet elongation follows the basic principle of the translational motion found in Kitahata's paper detailing how the gradient of interfacial tension drives Marangoni stress, which induces surface flows in both phases, imparting a momentum transfer on one another, leading to the translational motion. The same mechanism is responsible for the deformation in these droplets, as the droplet lies in the millifluidic channel, an LC forms which creates the gradient in interfacial tension, driving Marangoni stress, and inducing the surface flows that apply the momentum transfer which was observed in the droplets undergoing translational motion. When the droplet is found to sustain the elongation, the division of said droplet becomes increasingly more likely. Factors were uncovered which produced a greater likelihood of the division event occurring. These factors are:

1. Sufficient Environmental Stimulation
2. BZ Reaction Lifecycle
3. Surfactant Concentration
4. Droplet Elongation
    (a) Retaining Elongation
    (b) Acceleration Elongation

5. Droplet Deformation

    (a) Negative Curvature

    (b) Merging of Negative Curvatures

The environmental stimulation has strict requirements, as you cannot simply apply an AC field to the droplets, the period needs to be modulated to a required frequency to allow for the push-pull mechanism to develop within the droplet, causing specific LC locations to form, allowing for the turbulent flow to generate the accelerated elongation and deformation. This is where bullet point 1 becomes prominent, the AC field application needs to be applied at the frequency which lines up with the natural frequency of the BZ droplet. In the same vein, the surfactant concentration is crucial, as too little will limit the elongation due to the friction between the phases reducing the elongation. With too great of a concentration acting as an inhibiting factor as the micelles will leech excitatory chemical species from inside the droplet, into the oil phase. This will diminish the lifecycle of the BZ droplet, and it will reach thermodynamic equilibrium much faster. This will stop the division event from occurring, as there is no longer chemical energy to be converted into mechanical work.

For the droplet to elongate, there must be a reduction in width at some region along the edge(s) of the droplet. This region of width contraction is referred to as a negative curvature, as the curvature works against the normal forces created by the surface tension. When the droplet elongates enough, the region of negative curvature will reach a critical size, where the pinch point created at the CoM of the droplet causes acceleration on the flows travelling through this point. These flows will add to the regime of turbulent flow inside the droplet, which will lead to further elongation and subsequent deformation. There are 2 other manners in which the droplet should elongate enough to divide. Both of which involve a pair of negative curvature regions. Example one is when both of the regions are contained on the same edge of the droplet. Over time, the turbulence between the regions, and at either end of the droplet will cause the merging of the regions of negative curvature. This will produce a much larger region, which will have the same effect on the flows as the previous example, where the pinch point accelerates the flows due to the continuity equation from hydrodynamics, eventually leading to the division of the droplet. The last arrangement is when the regions of negative

curvature are on opposite sides of the droplet. Here, when the regions reach a critical size and merge, instead of one large region, this is the instance where the droplet will simply divide. Multiple regions of negative curvature can form on a single droplet. In one experiment it was observed that 2 regions had formed on one edge, with one on another. The cause of the division was due to the 2 on one edge merging, leaving a bizarrely shaped droplet, where a pinch point of great width reduction had formed, leading into another region of negative curvature. After the initial merging of the regions on the same side, the division occurred very soon after.

To help describe the nature of the division event, microspheres were utilised to track the flows inside the droplet. The flow diagrams helped to uncover the nature of the division as a response to the internal flows creating an elongation and deformation, which causes an increase in surface tension, where the minimisation of which can be achieved through the division of the droplet, as this presents a lower energy cost compared to the droplet returning to its original shape. Experimentally, there have been no studies of a droplet division, driven by an internal chemical reaction reported in the literature. Whilst there have been studies using an electric field, or a high-frequency speaker to cause droplet breakup, there have never been studies conducted prior, where the mechanism of division is driven by reaction-diffusion. A similarity involves the use of an EF in our study, but this is a system of environmental perturbation onto the BZ reaction, rather than a mechanism for droplet division.

6.0.4 Droplet-Droplet Synchronization

The post-division state of the divided droplet is remarkably similar to the droplet-droplet synchronisation experiments upon the introduction of droplet B. The only significant difference is the environmental perturbation. In the synchronisation study, the droplets are un-perturbed via an external EF, and the surfactant concentration is maintained at 0.45g per litre throughout the entire study, whereas the surfactant concentration was altered as part of the droplet division study. The pair of droplets were studied to uncover the nature of signal propagation in BZ droplets suspended in an oil phase. If the propagation of the excitable chemical wave is possible when the droplets are held at a distance, then it proves that hydrodynamic forces are

responsible for the propagation of information between droplets, as opposed to the hypothesised flow of excitatory chemical species through the lipid bi-layer preventing droplets from merging in the study performed by Chang *et al.*

The study of non-dividing droplets presented the results of the conversion of chemical energy into mechanical work causing the deformation and elongation of the droplet. This allowed us to visualise the generation of the longitudinal periodic velocity field through the oil phase, as the droplets would periodically elongate, and then relax to the original shape. Because the droplets were not dividing, there was an accurate study of the impact one droplet had on the other, whilst maintaining the separation.

The droplets were suspended in a millifluidic device, to anchor their positions, maintaining a constant distance throughout the course of the experiment. When the pair of droplets were anchored with only a 1cm distance, the behaviour of the pair would become entrained, where their oscillating frequencies would align, and the periodicity of the chemical waves would synchronise. As the distance increased, the tendency for the frequencies to align would decrease, along with the synchronisation. The cause for this effect is believed to be due to the inverse power law, where the further apart the droplets are, the less they can influence one another. To determine a baseline reading, the initial experimental condition only involves a singular droplet, which was recorded alone to gather a baseline reading regarding its periodicity. The introduction of the second droplet (droplet B) at a later point means the change in droplet A's behaviour can be quantified. To track the impact each droplet had on the other, a plastic micro-suspension was incorporated into the oil phase in the region between the pair of droplets. The microbeads were then tracked using image analysis software built in the MATLAB programming environment so the flows could be traced.

This elongation of the droplet causes positive pressure to build up in the oil phase, which is subsided with the induction of hydrodynamic flow in the direction of the alternate droplet. The hydrodynamic flow towards the alternate droplet would act as a mechanical perturbation. This mechanical stimulus would act as a compressive force, which upon relaxation presents a compression and stretching of the droplet. This motion would manipulate the droplet akin to stirring, which is believed to be the source of the generation of an LC within the droplet. This LC then produces the target pattern, responsible for the elongation of this droplet, which

in turn builds up a periodic velocity field through the oil phase, which acts on the original droplet. This pattern, when maintained, forms a self-sustained positive feedback loop which will keep the droplets in a synchronised regime.

Some of the major factors which can reduce the entrainment of the droplets are the distance between the pair, as this will reduce the power of the longitudinal periodic velocity field due to its diffusion through the oil phase. Another factor is the shape deformation of the droplet as it elongates, as this can produce a periodic velocity field which does not travel parallel to the imaginary connecting line between the two droplets. In the case where the droplets are not separated by a great distance, this may not be an issue, as the periodic velocity field can still have a direct hit onto the paired droplet, but with a greater separation, this angled periodic velocity field may miss the droplet, or have a far reduced impact, which would lead to no entrainment in the pair.

6.0.5 Conclusion

We can conclude by saying that BZ droplets are a viable candidate for studying self-organisation and bio-mimicry. The range of different BZ recipes makes the droplets a viable option for studying various sources of environmental perturbation. The relation between the BZ reaction and the study of the Krebs cycle draws a strong connection between real biology and using the BZ reaction as a replication of the redox signalling we observe in nature. Together, the three results chapters demonstrate that the use of BZ droplets can aid in the understanding of biological processes, from taxis effects, and cell division, to cell-to-cell communication. Further research is required to confirm the mechanisms presented in this thesis. A computational study, whilst complex, could detail the precise nature of individual variables presented in this work.

6.0.6 Strengths of the Study

According to the literature regarding the wider field of research, no studies have previously demonstrated the electrotaxis phenomena, nor the division of BZ droplets. We also present

the first known study to demonstrate BZ signal propagation between separated droplets and propose a mechanism to explain the phenomenon.

6.0.7 Limitations of the Study

The primary limitation of our study is the absence of ultra-high-quality imaging apparatus for viewing microsuspensions within the BZ droplet. This would allow greater resolution of the streamlines depicting the flow inside the droplet. This would allow a greater quality data set, and therefore more reliable results concerning the flow inside the droplet, and within the oil phase, when studying the droplet division, and the droplet-droplet synchronization. Another limitation of this study is the cost of the microsuspensions, a very conservative approach was required to ensure future experiments requiring the visualisation of the flows could be performed. One method to combat this, involved the use of turmeric powder during pilot studies, as it is known to not dissolve in oleic acid, or the water droplet containing BZ solutions, so could be used to study the flows before committing to using the more expensive microsuspensions. Higher frame rate recording would add additional authentication to the results reported, as greater scrutiny can be applied when analysing the flow streamlines.

Another limitation of the study was the degree of randomness observed within the droplet division experiments. There are some factors outside of our control at this current time, meaning that the precise locations within the droplet were subject to random chance, which meant that a much lower percentage repeatability of division events occurring was observed. This could be combated if a new system was devised that used the presented push-pull system using the AC field as a perturbation, which was able to manipulate more finely the precise location within the droplet that the LCs would form. This could be achieved through probing with a silver wire, but this introduces another layer of uncertainty that we wish to avoid, by only utilising a fully repeatable methodology, either by our group, or an external team aiming to replicate our study. Lastly, a limitation in the power of EF which could be applied was present due to the technical limitations of the available lab bench power supply. It is possible to use higher voltage power supplies to provide the EF, but an unnecessary degree of danger within the lab would be introduced, along with additional cost.

Chapter 7

Further Work

7.0.1 Further Work On The Electrotaxis Phenomenon

Upon receiving reviewer feedback relating to the study detailed in Chapter 3, where the question as to whether the application of an electric field has any impact on the magnitude of the chemically induced translational motion prompted an experiment to be devised, where the BZ droplets are suspended within microtubes fabricated from acrylic. These tubes would be mounted at specific angles to the applied external electric field so that when the LC formation occurs, it will be at an angle to the DC field which is equal to the mounted angle and induces translational motion. The speed and magnitude of the motion can be measured to quantify a correlation between the growth and decay rates of the translational motion as a function of the angle to the electric field. This would allow us to study if the direction of the applied field has any bearing on the magnitude of the motion, along with controlling the direction of the motion as well. An issue presented with performing this study would be frictional forces applied onto the droplet from the millifluidic device. This could be reduced but allowing a greater radius of the chamber but would rely heavily on the precise LC formation, which would largely negate the reason to have the 'guide rails' which would be the purpose of using the millifluidic chamber in the first place. The device could be fabricated in the same manner as the millifluidic device shown in chapter 4 figure 4.1, and chapter 5 figure 2.3. A further quantitative study of the change in growth and decay rate of the translational motion as subject to varied strength electric fields would be a conclusive end to the study of the BZ droplet electrotaxis phenomena. This would simply involve a greater magnitude of data collection

specific to the currently tested electric field strengths, but also with finer intervals, as well as over a wider voltage range which was not possible given the current circumstances. From the same study, it would be pertinent to test the electrotaxis behaviour of BZ solutions within a hydrogel. Said hydrogel would be capable of self-oscillation and would undergo periodic swelling and deswelling due to the interaction with the BZ gel. Subsequently, control of the LC formation within the BZ solution within the gel would yield control over the swelling and deswelling cycles. This would have an application in the study of chemo-mechanical coupling in hydrogels which have applications within the drug delivery research field.

7.0.2 Further Experimentation Regarding Droplet Divisions

Refining the BZ recipe further would be beneficial for increasing the percentage yield of divided droplets in our experiments. The work done by Zauner *et al.* highlights a possible way to extend the BZ lifespan by increasing concentrations of Malonic acid, whilst decreasing the concentration of Ferroin solution, Sodium Bromate, and Sulfuric acid. The optimisation would involve the balance between retaining a high frequency of LC reformation whilst extending the droplet lifespan, as the decrease in Sodium Bromate and Sulfuric acid will decrease the frequency of the reaction [195]. It was found that decreasing the Ferroin solution would increase the frequency, so this may be a way to compensate for the drop.

It is clear that the droplet division presents exciting possibilities for future work. An interesting direction the project could be taken to involves the use of a ruthenium metal catalyst instead of the Ferroin solution, such that the phototaxis phenomena as shown by Kitawaka *et al.* and Jamaluddin *et al.* where the control of the BZ reaction is manipulated by the deployment of light control [232, 265]. Instead of deploying an AC field to induce the tripole effect within the droplet, the light control box will be employed to perturbate the droplet via the mechanism of oxidising the metal catalyst via the phototaxis mechanism to generate the tripole. This method for the application of external perturbation of the droplet is interesting, as it provokes the idea for perturbation at very specific regions within the droplet, which could significantly increase the number of divisions. An alternative source of perturbation which would induce the LC formation is the employment of perturbation via silver wire. This has

been shown to generate the LC formation within BZ solutions and would be a method of generating the required conditions to increase the percentage yield of dividing droplets. Using the data gathered in figure 4.8 to decide where on the droplet the perturbation from the wire should be applied, it would be possible to instantiate LC formations at precise locations on the droplet, to test the symmetry breaking across the y-axis as a mechanism to create greater deformation and elongation on the droplet, subsequently leading to its division. Machine vision to detect the droplet in real-time would be employed, and could be developed built off of the droplet detection software developed already for this project. This would then be used with a model of a virtual droplet to map the perturbation onto real coordinates, where a linear actuator with a silver wire end effector would perturbate the droplet. PID and lag compensators would be used to ensure that the droplet is not greatly disturbed by this action.

7.0.3 Multiple Droplet Divisions

Multiple divisions from the same droplet could also be studied, whereby a larger initial droplet size is calibrated, and a second set of electrodes are employed, to be perpendicular to the droplet, rather than parallel. This would allow for greater experimental variability, as the polarity switching frequency of either pair can be altered to study the effects, or alternatively, setting one pair of electrodes to apply a DC voltage, whilst the other applies AC. Pulsing the applied fields would be beneficial, as it would stop interference between the fields, and would allow the push-pull mechanism to be properly instantiated within the droplet, to allow the symmetry to be broken across the x-axis, and y-axis simultaneously. Sensitivity testing would be required to determine the optimal experimental protocol to follow to allow for subsequent divisions to occur. Especially with concern to the angle that the second field is applied in relation to the original. The concentration of Ferroin may not need to be adjusted due to our previous experimentation where it was discovered that the concentration plays no role in the electrotaxis effect of the droplet. However, it may be of benefit to adjust the malonic acid concentration to provide a longer life cycle of the droplet, which would be pertinent to garner a second division event, especially considering the optimal concentrations currently utilise such a high concentration of surfactant which is known to inhibit the BZ reaction in the long

run [195]. As the subsequent divisions may add a lot more time to the experiment, the SDS concentration could also be a variable to consider. It was discovered that the greater SDS concentration in oleic acid (0.9g/litre oleic acid) produced the greatest elongation and allowed for division events to occur. However, with a greater concentration of surfactant within an oil phase, the greater the miscille concentration will be. The increased concentration of surfactant will induce the formation of a colloidal suspension which can cause bromine leaching via the production of brominated SDS. This was not a problem for the division experiments, however decreasing the malonic acid concentration to provide a longer droplet life cycle would allow for a greater time the droplet is exposed to the surfactant saturated oil phase, which could lead to greater leaching of bromine, which would prematurely end the experiment due to the BZ solutions reaching thermodynamic equilibrium, and the generation of LC formations would cease. The droplets would also require new millifluidic devices to be fabricated, which whilst the complexity of which would not be difficult for the device to be produced, as the 3D printing or CNC milling of acrylic would be more than suitable, the precise dimensions and mechanism of such devices would require many rounds of design and testing to optimise for the second division to take place, due to the unpredictability of its action. It was found in the experiments that the droplet division was not perfect even across both sub-droplets. This would mean that the initial set of sub-droplets would have different volumes which would present an issue. It is unlikely for a droplet with a smaller volume to be capable of undergoing a division event, as the mechanical work generated from the RD system would not be great enough to overcome the surface energy or to deform the droplet great enough that it is able to divide.

Repeating the experiments from chapter 4, where a source of mechanical perturbation was applied instead of the application of an external AC field would be an interesting scenario. It is known from the literature that the stimulation of the BZ reaction using silver wire will instantiate the formation of an LC. Therefore, using the silver wire to generate the LC locations found in figure 4.12 to increase the repeatability of the droplet divisions, but also to experiment with optimal timing and order of such formation of LCs so that optimal internal turbulence can be generated, which would lead to a greater deformation, and increase the existence of negative curvature regions along the droplet edge, which would increase the

percentage yield of dividing droplets..

7.0.4 Mathematical Modelling

Mathematical modelling of the division event or the water in oil system would allow for a greater understanding of the hydrodynamics relating to both the droplet division, along with biological cell division. This scenario presents an interesting and difficult problem in the field of hydrodynamics, as little progress has been made in the literature involving the modelling of water in oil division. Modelling of the division via the mechanism of an externally applied AC field, along with modelling of the previous experiment where a silver wire is used to perturbate the solution would be of interest, as understanding the effect the internal flow of ions has on the division event is worth understanding. A series of calculations involving the Reynolds instability would be pertinent to solving hydrodynamics problems related to the mathematical modelling and simulation of this work.

7.0.5 Droplet-Droplet Synchrony

Continuing with the droplet-droplet synchronisation experiments, an interesting factor would involve extending the network to include successive droplets after the initial 2. This method could be used to study long-range signal propagation, as the droplet at the beginning could be perturbed using silver wire to initiate the reaction at the leading centre, where the droplet was perturbed by the wire. This would then initiate the coupling process between that droplet and its neighbour, but in the arrangement with an increased number of droplets, the flow generated by the second droplet, would not only travel back to couple with the initial droplet but also down toward the end droplet. This would be an interesting study to perform, as the distances between the droplet pairs could be manipulated to generate a stronger coupling between specific pairs, but not others, to study how the arrangement affects long-range signal propagation, akin to that in a biological neural network. Different arrangements of the multiple droplet network could also be employed, as it would be a greater simulation of the arrangement of neurons in a biological system. Starting with small-scale experiments adding

1 more droplet at a time could allow for an understanding of the dynamics at play in a larger-scale droplet network, which would then lead to modelling information processing seen in logic gates such as XOR and NAND gates.

Simulating computational logic gates with droplets provokes the question of using the wave generation itself to compute simple logic. Micro chamber capillaries could be employed as a method to segregate chemical wave propagation from other waves, allowing for propagation without annihilation upon convergence. The physical barrier could be employed to direct the propagation of the chemical signal until it is required. Understanding the dynamics of such a system could allow to computational logic to be performed, possibly even Chomsky hierarchical grammar.

To gain a better understanding of the deformation of the droplets subjected to an AC field, a different experimental set-up should be employed, where a droplet is housed within a square dish so that the curvature does not impede the ability of a camera to record the decrease in thickness of the droplet as it elongates. This would prove the hypothesis that the droplets are decreasing in thickness as well as undergoing width decrease in the experiments where an AC field is applied, causing a great elongation of the droplet, yet no greater decrease in width in the non-dividing droplets. Another method for determining the extent of the deformation would be to deploy a high-speed camera with a macro lens to zoom in on the droplet and retain the high-quality imaging, whilst capturing many hundreds of frames per second to allow the studying of the micro-changes to the surface tension of the droplet with perfect precision. The technical limitations of this solution would involve the great cost to acquire such apparatus, along with the storage solutions for the incredibly large file sizes it would generate.

Chapter 8

Appendices

8.1 Code For Analysis

8.1.1 Image Analysis

The code file shown below contains many subroutines that were frequently utilised for analysing the droplet videos generated throughout the course of experimentation.

```
%% view specific image


v = VideoReader('exp 1 p3.MOV');

frame = read(v,40*60);

imshow(frame);

%% show segmented image

% v = VideoReader('exp 1 p2.MOV');

frame = read(v,100*60);

```

```
16 xseg = [1159 1276];
17 yseg = [787 905];
18
19 seg = frame(yseg(1):yseg(2),xseg(1):xseg(2),:);
20
21 imshow(seg);
22
23 %% loop through frames
24
25 % v = VideoReader('exp 1 p1.MOV');
26
27 % xseg = [1140 1264];
28 % yseg = [150 280];
29
30
31 Startpoint = 40*60;
32 Endpoint = 100*60;
33
34
35
36 position = 0;
37
38
39 for count = Startpoint:1:Endpoint
40
41     modf = mod(count,100);
42     if  modf==0
43         disp(count);
44     end
45
```

```
46      position = position + 1;
47
48      frame = read(v,count);
49
50      seg = frame(yseg(1):yseg(2),xseg(1):xseg(2),:);
51
52      gray = rgb2gray(seg);
53
54      med = median(median(gray));
55
56      temp = zeros(yseg(2)-yseg(1),xseg(2)-xseg(1));
57
58      for i = 1:yseg(2)-yseg(1)
59          for j = 1:xseg(2)-xseg(1)
60
61              if gray(i,j)<med/2
62
63                  temp(i,j) = 1;
64
65
66              end
67
68          end
69      end
70
71
72      [ypos,xpos] = find(temp==1);
73
74      ystore(position) = median(ypos);
75      xstore(position) = median(xpos);
```

```
76
77 %      ed = temp;
78 %      proftest8;
79
80 end
81
82 figure, plot(xstore,ystore);
83
84 %% diff
85 pos = 0;
86 for i = 2:length(xstore)
87     pos = pos + 1;
88     displace(pos) = xstore(i)-xstore(1);
89
90 end
91
92 % figure,plot(displace);
93 plot(displace);
94
95 %% plot RGB values
96
97 pos = 0;
98
99 % xseg = [1140 1264];
100 % yseg = [150 280];
101
102
103
104 for i = Startpoint:1:Endpoint
105
```

```
106     modf = mod(i,100);
107     if  modf==0
108         disp(i);
109     end
110
111
112     pos = pos + 1;
113
114     frame = read(v,i);
115     seg = frame(yseg(1):yseg(2),xseg(1):xseg(2),:);
116
117     BVal(pos) = seg(round(ystore(pos)),round(xstore(pos)),3);
118     RVal(pos) = seg(round(ystore(pos)),round(xstore(pos)),1);
119
120 end
121
122 figure, hold on, plot(BVal),plot(RVal);
123
124
125
126 %% every 10 seconds
127
128 v = VideoReader('exp 1 p1.MOV');
129
130 % pos = 0;
131 for count = Startpoint:600:Endpoint
132
133     pos = pos + 1;
134
135     frame = read(v,count);
```

```
136     imshow(frame);
137
138 %     FS{pos} = frame;
139
140 end
141
142 %% output hydrodynamic flor visualization
143
144
145 for i = 1:97
146
147
148     x1 = coords(i,1);
149     y1 = coords(i,2);
150     x2 = coords(i,3);
151     y2 = coords(i,4);
152
153     plot([x1 x2],[y1 y2],'k');
154 %     plot(x2,y2,'kx');
155
156
157
158 end
159
160 %% generate quiver data
161
162 for i = 1:132
163
164     X(i) = coords(i,1);
165     Y(i) = coords(i,2);
```

```
166     U(i) = coords(i,3)-coords(i,1);
167     V(i) = coords(i,4)-coords(i,2);
168
169 end
170
171 figure, hold on, quiver(X,Y,U,V,'k');
172
173 %% output hydrodynamic flor visualization using quiver
174
175
176 for i = 1:97
177
178
179     x1 = coords(i,1);
180     y1 = coords(i,2);
181     x2 = coords(i,3);
182     y2 = coords(i,4);
183
184     quiver([x1 x2],[y1 y2]);
185 %      plot(x2,y2,'kx');
186
187
188
189 end
```

This is the second series of subroutines often used for the analysis and data extraction of the time-lapse videos generated throughout the experiments.

```
%% Load in first set of images

disp('Reading First Image...');

vid = VideoReader('GH010222.mp4');

vidWidth = vid.Width;
vidHeight = vid.Height;

disp('Movie struct created');

mov = struct('cdata',zeros(vidHeight,vidWidth,3,'uint8'),'
    colormap',[]);

vid.CurrentTime = 15*60;

k = 1;

disp('Starting');

while vid.CurrentTime <17*60+24

    mov(k).cdata = readFrame(vid);

    k = k+1;

    if mod(k,500)==0

```

```
28          disp('Still Working...');
29
30      end
31
32  end
33
34  disp('Finished Reading First Images');
35
36  %% disp start and end
37  StartFrame = 1;
38  EndFrame = 4320;
39  tslen = EndFrame+1-StartFrame;
40
41  imshow(mov(StartFrame).cdata);
42  tit = ['Frame: ', num2str(StartFrame)];
43  set(gcf, 'Name', tit)
44
45  figure,imshow(mov(EndFrame).cdata);
46  tit = ['Frame: ', num2str(EndFrame)];
47  set(gcf, 'Name', tit)
48
49  %% view vid
50
51  for i = 1:20:5400
52      im = mov(i).cdata;
53      imshow(im);
54  % imshow(imSeg1{i});
55
56  end
57  disp('fin');
```

```
58
59 %% image segmentation
60 ii = 0;
61 for i = 1:4320
62     ii = ii+1;
63     temp = mov(i).cdata;
64     imSeg1{ii}(:,:,1) = temp(685:787,803:945,1);
65     imSeg1{ii}(:,:,2) = temp(685:787,803:945,2);
66     imSeg1{ii}(:,:,3) = temp(685:787,803:945,3);
67     imSeg2{ii}(:,:,1) = temp(685:787,1171:1319,1);
68     imSeg2{ii}(:,:,2) = temp(685:787,1171:1319,2);
69     imSeg2{ii}(:,:,3) = temp(685:787,1171:1319,3);
70
71
72 %     imshow(imSeg{i});
73 end
74
75 disp('Segmentation complete');
76
77 %  pull data
78 ii=0;
79 for i = 1:5:5400
80    ii = ii+1;
81     imCollage1(ii,:,1) = imSeg1{i}(62,:,1)';
82 %     imCollage2(ii,:,1) = imSeg2{i}(137,:,1)';
83     imCollage1(ii,:,2) = imSeg1{i}(62,:,2)';
84 %     imCollage2(ii,:,2) = imSeg2{i}(137,:,2)';
85     imCollage1(ii,:,3) = imSeg1{i}(62,:,3)';
86 %     imCollage2(ii,:,3) = imSeg2{i}(137,:,3)';
87 end
```

```
88 imshow(imCollage1);
89 % figure, imshow(imCollage2);
90
91 %% halo data
92 ii = 0;
93
94 for i = 1:5:4320
95     im = mov(i).cdata;
96     ii = ii+1;
97     halo(ii,:,1) = im(733,857:1255,1)';
98     halo(ii,:,2) = im(733,857:1255,2)';
99     halo(ii,:,3) = im(733,857:1255,3)';
100
101    halo2(:,ii,1) = im(733,857:1255,1);
102    halo2(:,ii,2) = im(733,857:1255,2);
103    halo2(:,ii,3) = im(733,857:1255,3);
104
105
106 end
107 imshow(halo);
108
109 %% segment then profile droplets
110 position = 0;
111
112 for ct = StartFrame:EndFrame
113
114     position = position +1;
115
116     frame = mov(ct).cdata;
117
```

```
118     seg1x = [857,1093];
119     seg1y = [381,625];
120
121     seg2x = [881,1165];
122     seg2y = [746,949];
123
124     seg1 = frame(seg1y(1):seg1y(2),seg1x(1):seg1x(2),1); %
    plug these values into the offset for reading image data
125     seg2 = frame(seg2y(1):seg2y(2),seg2x(1):seg2x(2),1);
126
127     d1mov{position} = seg1;
128     d2mov{position} = seg2;
129
130     [y,x] = size(seg1);
131
132     temp = zeros(y,x);
133     meanval = mean(mean(seg1));
134
135     for i = 1:y
136        for j = 1:x
137
138           if seg1(i,j) <meanval-15
139              temp(i,j) = 1;
140           end
141
142        end
143     end
144     is1{position} = temp;
145
146     [y,x] = size(seg2);
```

```
147
148     temp = zeros(y,x);
149     meanval = mean(mean(seg2));
150
151     for i = 1:y
152        for j = 1:x
153
154            if seg2(i,j) <meanval-15
155               temp(i,j) = 1;
156            end
157
158        end
159     end
160     is2{position} = temp;
161 end
162
163 disp('finished generating set');
164
165
166 %% image checker
167 close all;
168 % pause(1);
169 for i = 1:10
170    imshow(is1{i});
171 end
172 for i = tslen-10:tslen
173     imshow(is1{i});
174 end
175 for i = 1:10
176    imshow(is2{i});
```

```
177 end
178 for i = tslen-10:tslen
179     imshow(is2{i});
180 end
181
182 %% playback droplet movie
183
184 for i = 1:10:tslen
185    subplot(1,2,1), imshow(d1mov{i});
186    subplot(1,2,2), imshow(is1{i});
187    pause(0.1);
188 end
189 disp('finished playback');
190
191 %% find values
192
193 for i = 1:length(is1)
194
195     [xlist1,ylist1] = find(is1{i}==1);
196     [xlist2,ylist2] = find(is2{i}==1);
197
198     d1coords{i,1} = xlist1;
199     d1coords{i,2} = ylist1;
200
201     d2coords{i,1} = xlist2;
202     d2coords{i,2} = ylist2;
203
204     drop1x(i) = seg1x(1)+mean(xlist1);
205     drop1y(i) = seg1y(1)+mean(ylist1);
206     drop2x(i) = seg2x(1)+mean(xlist2);
```

```
207     drop2y(i) = seg2y(1)+mean(ylist2);
208 end
209
210 disp('fin');
211
212 %% find values for edges
213
214 for i = 1:length(is1)
215
216     [xlist1,ylist1] = find(is1{i}==1);
217     [xlist2,ylist2] = find(is2{i}==1);
218
219     d1coords{i,1} = xlist1;
220     d1coords{i,2} = ylist1;
221
222     d2coords{i,1} = xlist2;
223     d2coords{i,2} = ylist2;
224
225     drop1x(i) = seg1x(1)+mean(xlist1);
226     drop1y(i) = seg1y(1)+max(ylist1);
227     drop2x(i) = seg2x(1)+mean(xlist2);
228     drop2y(i) = seg2y(1)+min(ylist2);
229
230
231
232 %     drop1x(i) = seg1x(1)+mean(xlist1);
233 %     drop1y(i) = seg1y(1)+mean(ylist1);
234 %     drop2x(i) = seg2x(1)+mean(xlist2);
235 %     drop2y(i) = seg2y(1)+mean(ylist2);
236 end
```

```
237
238 tempy1 = max(drop1y);
239 tempy2 = min(drop2y);
240 ymidpoint = round((tempy1+tempy2)/2);
241 xmidpoint = round(median([drop1x,drop2x]));
242
243 disp('fin');
244
245
246 %% find droplet edges
247
248 for i = 1:(EndFrame-StartFrame)+1
249
250     temp = edge(is1{i},'canny');
251
252     [yposs,xposs] = find(temp == 1);
253
254     drop1x(i) = seg1y(1)+ max(yposs);
255
256     bot = max(xposs);
257
258     vals = find(is1{1}(:,bot(1))==1);
259
260     drop1y(i) = seg1x(1)+round(mean(vals));
261
262
263
264     temp = edge(is2{i},'canny');
265
266     [yposs,xposs] = find(temp == 1);
```

```
267
268     drop2x(i) = seg2y(1)+ min(yposs);
269
270     top = min(yposs);
271
272     vals = find(is2{1}(:,top)==1);
273
274     drop2y(i) = seg2x(1)+round(mean(vals));
275
276 end
277
278 disp('fin');
279
280 %% use xy coords to pull data
281
282 endpos = length(is1);
283 maxdist = sqrt((drop1x(endpos)-drop2x(endpos))^2+(drop1y(
       endpos)-drop2y(endpos))^2);
284 position = 0;
285 for i = StartFrame:EndFrame
286
287     position = position +1;
288
289     if drop1x(position)<drop2x(position)
290        Lx = drop1x(position);
291        Hx = drop2x(position);
292     else
293         Lx = drop2x(position);
294         Hx = drop1x(position);
295     end
```

```
296
297     if drop1y(position)<drop2y(position)
298        Ly = drop1y(position);
299        Hy = drop2y(position);
300     else
301         Ly = drop2y(position);
302         Hy = drop1y(position);
303     end
304
305     Dx = abs(drop1x(position)-drop2x(position));
306     Dy = abs(drop1y(position)-drop2y(position));
307
308     xRange = round(Lx:Dx/maxdist:Hx);
309     yRange = round(Ly:Dy/maxdist:Hy);
310
311     if length(xRange)>0
312        tempx = xRange;
313     end
314
315     if isempty(xRange)
316        xRange = tempx;
317     end
318
319     if mod(position,50)==0
320
321         disp('Still Processing');
322
323     end
324
325     frame = mov(i).cdata;
```

```
326
327     for j = 1:length(xRange)
328
329
330
331         mid(j,position) = frame(yRange(j),xRange(j)); %from
    midpoint to midpoint
332         midm25(j,position) = frame(yRange(j)-25,xRange(j),1);
     %25 then 50 offset to the negative
333         midm50(j,position) = frame(yRange(j)-50,xRange(j),1);
334         midp25(j,position) = frame(yRange(j)+25,xRange(j),1);
     %25 and 50 offset to the positive
335         midp50(j,position) = frame(yRange(j)+50,xRange(j),1);
336
337
338 %         testmid(j,position) = frame(yRange(j),xRange(j));
339
340     end
341
342     % calculate the median alue for each stream
343     midmean(position) = mean(mid(:,position));
344     midm25mean(position) = mean(midm25(:,position));
345     midm50mean(position) = mean(midm50(:,position));
346     midp25mean(position) = mean(midp25(:,position));
347     midp50mean(position) = mean(midp50(:,position));
348
349     localdata(position) = frame(ymidpoint,xmidpoint);
350
351
352 end
```

```
353
354 disp('Finished')
355
356 subplot(6,1,1),plot(midm50mean);
357 title('Offset: -50');
358
359 subplot(6,1,2),plot(midm25mean);
360 title('Offset: -25');
361
362 subplot(6,1,3),plot(midmean);
363 title('Mid-Point');
364
365 subplot(6,1,4),plot(midp25mean);
366 title('Offset: +25');
367
368 subplot(6,1,5),plot(midp50mean);
369 title('Offset: +50');
370
371 subplot(6,1,6),plot(localdata);
372 title('Mid point between droplets');
373
374 %% LC information retreival
375
376 for i = 1:tslen
377
378     clear list;
379
380    xlist = d1coords{i,1};
381    ylist = d1coords{i,2};
382
```

```
383     for j = 1:length(xlist)
384 
385         list(j) = d1mov{i}(xlist(j),ylist(j));
386 
387     end
388 
389     d1dat(i) = mean(list);
390     d1localdat(i) = d1mov{i}(round(median(xlist)),round(median
        (ylist)));
391 
392     clear list;
393 
394     xlist = d2coords{i,1};
395     ylist = d2coords{i,2};
396 
397     for j = 1:length(xlist)
398 
399         list(j) = d2mov{i}(xlist(j),ylist(j));
400 
401     end
402 
403     d2dat(i) = mean(list);
404     d2localdat(i) = d2mov{i}(round(median(xlist)),round(median
        (ylist)));
405 
406 end
407 
408 figure;
409 hold on;
410 plot(d1dat);
```

```
411 plot(d2dat);
412 plot(d1localdat,'.');
413 plot(d2localdat,'.');
414 legend('Median Data Droplet 1','Median Data Droplet 2','
       Droplet 1 Local Probe','Droplet 2 Local Probe');
415 title('Red value of RGB image, averaged for each droplet');
416 ylabel('Average Pixel Value');
417 xlabel('Sample Number, 30/sec');
418
419 figure;
420 plot(normxcorr2(d1dat,d2dat));
421 title('Cross Correlation of droplet pixel values');
422 t = (normxcorr2(d1dat,d2dat));
423 dif = find(t==max(t))-(0.5*length(t));
424 disp(dif);
425 tit = ['difference: ', num2str(dif)];
426 set(gcf, 'Name', tit)
427
428 figure;
429 plot(normxcorr2(d2dat,d1dat));
430 title('Cross Correlation of droplet pixel values');
431 t = (normxcorr2(d2dat,d1dat));
432 dif = find(t==max(t))-(0.5*length(t));
433 disp(dif);
434 tit = ['difference: ', num2str(dif)];
435 set(gcf, 'Name', tit)
436
437 figure;
438 plot(normxcorr2(d1localdat,d2localdat));
439 title('Cross Correlation of local droplet pixel values');
```

```
440 t = (normxcorr2(d1localdat,d2localdat));
441 dif = find(t==max(t))-(0.5*length(t));
442 disp(dif);
443 tit = ['difference: ', num2str(dif)];
444 set(gcf, 'Name', tit)
445
446 figure;
447 plot(normxcorr2(d2localdat,d1localdat));
448 title('Cross Correlation of local droplet pixel values');
449 t = (normxcorr2(d2localdat,d1localdat));
450 dif = find(t==max(t))-(0.5*length(t));
451 disp(dif);
452 tit = ['difference: ', num2str(dif)];
453 set(gcf, 'Name', tit)
454
455
456
457
458
459
460 figure, plot(d1localdat), figure, plot(d2localdat);
461
462
463
464
465
466
467 %% trace pull from non-drifter
468
469 % StartFrame = 290;
```

```
% EndFrame = 1130;

    D1x = 1059;
    D1y = 405;

    D2x = 1025;
    D2y = 795;

    Dx = abs(D1x - D2x);
    Dy = abs(D1y - D2y);

    DxDy = sqrt((Dx*Dx)+(Dy*Dy));

    xRange = round(D2x:Dx/DxDy:D1x);
    yRange = round(D1y:Dy/DxDy:D2y);
position = 0;
for counter = StartFrame:EndFrame
    position = position +1;
    if mod(counter,50)==0

        disp('Still Processing');

    end
    frame = mov(counter).cdata;

    for i = 1:length(xRange)



        mid(i,position) = frame(yRange(i),xRange(i)); %from
```

```
   midpoint to midpoint
500         midm25(i,position) = frame(yRange(i)-25,xRange(i),1);
    %25 then 50 offset to the negative
501         midm50(i,position) = frame(yRange(i)-50,xRange(i),1);
502         midp25(i,position) = frame(yRange(i)+25,xRange(i),1);
    %25 and 50 offset to the positive
503         midp50(i,position) = frame(yRange(i)+50,xRange(i),1);
504
505
506
507     end
508
509     % calculate the median alue for each stream
510     midmean(position) = mean(mid(:,position));
511     midm25mean(position) = mean(midm25(:,position));
512     midm50mean(position) = mean(midm50(:,position));
513     midp25mean(position) = mean(midp25(:,position));
514     midp50mean(position) = mean(midp50(:,position));
515
516 end
517
518 disp('Finished')
519
520 subplot(5,1,1),plot(midm50mean);
521 title('Offset: -50');
522
523 subplot(5,1,2),plot(midm25mean);
524 title('Offset: -25');
525
526 subplot(5,1,3),plot(midmean);
```

```
527 title('Mid-Point');
528
529 subplot(5,1,4),plot(midp25mean);
530 title('Offset: +25');
531
532 subplot(5,1,5),plot(midp50mean);
533 title('Offset: +50');
534
535 %% 10 images at once
536
537 position = 0;
538
539 for i = 3900:3903
540    position = position +1;
541
542
543     subplot(2,2,position), imshow(mov(i).cdata);
544
545 end
546 %% read specific frames
547 vid = VideoReader('GH010128.mp4');
548
549 vidWidth = vid.Width;
550 vidHeight = vid.Height;
551
552 mov = struct('cdata',zeros(vidHeight,vidWidth,3,'uint8'),'
       colormap',[]);
553
554 frames = readFrame(vid,[1 2500]);
555 disp('Finished Reading Images');
```

```
556
557 %% pull data from mid point of mid image
558
559 [y,x] = size(mid);
560
561 dynamiclocal = mid(round(y/2),:);
562
563 plot(dynamiclocal);
564 save('D:\PhD\BZ data\Photos with ring light\SDS signal
       propagation\data\channel\midpoint\Droplet0063dynamic.mat',
       'dynamiclocal')
565
566 %% correlation between channel data
567
568 for i = 1:21
569     for j = 1:21
570
571         t1 = size(DynamicCell{i});
572         t2 = size(DynamicCell{j});
573
574         if t1(2) < t2(2)
575             lower = DynamicCell{i};
576             higher = DynamicCell{j};
577         else
578             lower = DynamicCell{j};
579             higher = DynamicCell{i};
580         end
581
582         t = normxcorr2(lower,higher);
583         tmax = max(t);
```

```
584
585         maxpoint = find(t==tmax);
586         delta = abs(maxpoint - ((length(t)+1)/2));
587
588         DynamicAdj(i,j) = delta;
589         DmaxAdj(i,j) = tmax;
590
591     end
592 end
593
594
595 %% generate windowed data
596 %
597 % for i =1:21
598 %
599 %     t1 = size(DynamicCell{i});
600 %         t2 = size(DynamicCell{j});
601 %
602 %         if t1(2) < t2(2)
603 %             lower = DynamicCell{i};
604 %             higher = DynamicCell{j};
605 %         else
606 %             lower = DynamicCell{j};
607 %             higher = DynamicCell{i};
608 %         end
609 %
610 %
611 %
612 % end
613
```

```
614 t1 = size(DynamicCell{i});
615 t2 = size(DynamicCell{j});
616
617 if t1(2) < t2(2)
618     lower = DynamicCell{i};
619     higher = DynamicCell{j};
620 else
621     lower = DynamicCell{j};
622     higher = DynamicCell{i};
623 end
624
625 t = normxcorr2(lower,higher);
626 tmax = max(t);
627
628 maxpoint = find(t==tmax);
629 delta = (maxpoint - ((length(t)+1)/2));
630
631 len = length(higher);
632
633 if delta>1
634
635    win1 = higher(1:1348);
636    win2 = lower(length(lower)-1347:length(lower));
637    disp('trigger');
638
639 else
640     win1 = higher(1+1348:len);
641     win2 = lower(1:length(win1));
642 end
643
```

```
644 plot(normxcorr2(win1,win2));
645 t = normxcorr2(win1,win2);
646 disp(max(t));
647
648
649
650
651
652 %% generate windows from data
653
654 for i = 1:21
655    for j = 1:21
656
657
658        t1 = size(DynamicCell{i});
659        t2 = size(DynamicCell{j});
660
661        if t1(2) < t2(2)
662           lower = DynamicCell{i};
663           higher = DynamicCell{j};
664        else
665           lower = DynamicCell{j};
666           higher = DynamicCell{i};
667        end
668
669        t = normxcorr2(lower,higher);
670        tmax = max(t);
671
672        maxpoint = find(t==tmax);
673        delta = (maxpoint - ((length(t)+1)/2));
```

```
674         len = length(higher);
675         nel = length(lower);
676 
677         if delta>1
678 
679             if DynamicAdj(i,j) > length(lower)
680                 win2 = lower;
681                 win1 = higher(1:length(win2));
682             else
683                  win1 = higher(1:(DynamicAdj(i,j)));
684                  win2 = lower(length(lower)-(DynamicAdj(i,j)-1)
    :length(lower));
685             end
686 
687         else
688             win1 = higher(2+DynamicAdj(i,j)+round((len-nel)/2)
    :len);
689 
690             if length(win1)> nel
691                 dif = length(win1)-nel;
692                 stpt = 2+DynamicAdj(i,j)+round((len-nel)/2) +
    dif;
693                 win1 = higher(stpt:len);
694             end
695             win2 = lower(1:length(win1));
696         end
697 
698         Normalised{i,j}(1,:)= win1;
699         Normalised{i,j}(2,:)= win2;
700         clear win1;
```

```
701         clear win2;
702
703     end
704 end
705
706
707 %% comput PLV
708 clear i;
709 for k = 1:21
710     for j = 1:21
711
712         phi1 = angle(hilbert(Normalised{k,j}(1,:)));
713         phi2 = angle(hilbert(Normalised{k,j}(2,:)));
714
715         PLV(k,j) = abs(sum(exp(1i*(phi1-phi2))))/length(phi1);
716         PLVstat{k,j} = abs(exp(1i*(phi1-phi2)));
717
718
719     end
720 end
721
722
723 %% single data PLV
724
725
726 phi1 = angle(hilbert(d1localdat));
727 phi2 = angle(hilbert(d2localdat));
728
729 PLVsum = abs(sum(exp(1i*(phi1-phi2))))/length(phi1);
730 PLVts = (exp(1i*(phi1-phi2)));
```

```
731
732 disp(PLVsum);
733 figure, hold on;
734 plot(real(PLVts));
735 plot(imag(PLVts));
736 title('PLV');
737 legend('Real Part','Imaginary Part');
738
739 figure;
740
741 plot(normxcorr2(d1localdat,d2localdat));
742 title('Normalised Cross Correlation');
743
744 imax = max(imag(PLVts));
745 t = find(imag(PLVts) == imax);
746 disp(t);
747
748 %% segment the data
749
750 pos1 = 1213;
751 pos2 = 2200;
752
753 LC2LC{1} = d1localdat(pos1:pos2);
754 LC2LC{2} = d2localdat(pos1:pos2);
755
756 LCtoend{1} = d1localdat(pos1:length(d1localdat));
757 LCtoend{2} = d2localdat(pos1:length(d2localdat));
758
759 LCprior{1,1} = d1localdat(pos1-900:pos1);
760 LCprior{1,2} = d1localdat(pos2-900:pos2);
```

```
761 LCprior{2,1} = d2localdat(pos1-900:pos1);
762 LCprior{2,2} = d2localdat(pos2-900:pos2);
763
764 LCpost{1,1} = d1localdat(pos1:pos1+900);
765 LCpost{1,2} = d1localdat(pos2:pos2+900);
766 LCpost{2,1} = d2localdat(pos1:pos1+900);
767 LCpost{2,2} = d2localdat(pos2:pos2+900);
768
769 LC2toend{1} = d1localdat(pos2:length(d1localdat));
770 LC2toend{2} = d2localdat(pos2:length(d2localdat));
771
772 t = normxcorr2(LC2LC{1},LC2LC{2});
773 lent = length(t);
774 l = (length(t)-1)/-2;
775 u = (length(t)-1)/2;
776 figure, plot([l:u],t);
777 title('Leading Center to Leading Center');
778
779 t = normxcorr2(LCtoend{1},LCtoend{2});
780 lent = length(t);
781 l = (length(t)-1)/-2;
782 u = (length(t)-1)/2;
783 figure, plot([l:u],t);
784 % figure, plot(normxcorr2(LCtoend{1},LCtoend{2}));
785 title('First Leading Center to End');
786
787 t = normxcorr2(LC2toend{1},LC2toend{2});
788 lent = length(t);
789 l = (length(t)-1)/-2;
790 u = (length(t)-1)/2;
```

```
figure, plot([l:u],t);
% figure, plot(normxcorr2(LC2toend{1},LC2toend{2}));
title('Second Leading Center to End');

t = normxcorr2(LCprior{1,1},LCprior{2,1});
lent = length(t);
l = (length(t)-1)/-2;
u = (length(t)-1)/2;
figure, plot([l:u],t);
% figure, plot(normxcorr2(LCprior{1,1},LCprior{2,1}));
title('30 seconds prior to LC1(D1) x 30 seconds prior to LC1(
   D2)');

t = normxcorr2(LCprior{1,1},LCprior{2,2});
lent = length(t);
l = (length(t)-1)/-2;
u = (length(t)-1)/2;
figure, plot([l:u],t);
% figure, plot(normxcorr2(LCprior{1,1},LCprior{2,2}));
title('30 seconds prior to LC1(D1) x 30 seconds prior to LC2(
   D2)');

t = normxcorr2(LCprior{2,1},LCprior{1,1});
lent = length(t);
l = (length(t)-1)/-2;
u = (length(t)-1)/2;
figure, plot([l:u],t);
% figure, plot(normxcorr2(LCprior{2,1},LCprior{1,1}));
title('30 seconds prior to LC1(D2) x 30 seconds prior to LC1(
   D1)');
```

```
818
819 t = normxcorr2(LCprior{2,1},LCprior{1,2});
820 lent = length(t);
821 l = (length(t)-1)/-2;
822 u = (length(t)-1)/2;
823 figure, plot([l:u],t);
824 % figure, plot(normxcorr2(LCprior{2,1},LCprior{1,2}));
825 title('30 seconds prior to LC1(D2) x 30 seconds prior to LC2(
       D1)');
826
827 t = normxcorr2(LCpost{1,1},LCpost{2,1});
828 lent = length(t);
829 l = (length(t)-1)/-2;
830 u = (length(t)-1)/2;
831 figure, plot([l:u],t);
832 % figure, plot(normxcorr2(LCpost{1,1},LCpost{2,1}));
833 title('30 seconds post LC1(D1) x 30 seconds post LC1(D2)');
834
835 t = normxcorr2(LCpost{1,1},LCpost{2,2});
836 lent = length(t);
837 l = (length(t)-1)/-2;
838 u = (length(t)-1)/2;
839 figure, plot([l:u],t);
840 % figure, plot(normxcorr2(LCpost{1,1},LCpost{2,2}));
841 title('30 seconds post LC1(D1) x 30 seconds post LC2(D2)');
842
843 t = normxcorr2(LCpost{2,1},LCpost{1,1});
844 lent = length(t);
845 l = (length(t)-1)/-2;
846 u = (length(t)-1)/2;
```

```
847 figure, plot([l:u],t);
848 % figure, plot(normxcorr2(LCpost{2,1},LCpost{1,1}));
849 title('30 seconds post LC1(D2) x 30 seconds post LC1(D1)');
850
851 t = normxcorr2(LCpost{2,1},LCpost{1,2});
852 lent = length(t);
853 l = (length(t)-1)/-2;
854 u = (length(t)-1)/2;
855 figure, plot([l:u],t);
856 % figure, plot(normxcorr2(LCpost{2,1},LCpost{1,2}));
857 title('30 seconds post LC1(D2) x 30 seconds post LC2(D1)');
858
859 t = normxcorr2(LC2toend{2},LC2toend{2});
860 lent = length(t);
861 l = (length(t)-1)/-2;
862 u = (length(t)-1)/2;
863 figure, plot([l:u],t);
864 % figure, plot(normxcorr2(LC2toend{2},LC2toend{2}));
865 title('leading center 2 to end');
866
867 close all;
868
869 %% sect
870
871 figure; hold on;
872
873 t = normxcorr2(LC2LC{1},LC2LC{2});
874 subplot(7,1,1); plot(t);
875 title('Leading Center to Leading Center');
876
```

```
877 subplot(7,1,2); plot(normxcorr2(LCtoend{1},LCtoend{2}));
878 title('First Leading Center to End');
879
880 subplot(7,1,3); plot(normxcorr2(LC2toend{1},LC2toend{2}));
881 title('Second Leading Center to End');
882
883 subplot(7,1,4); plot(normxcorr2(LCprior{1,1},LCprior{2,1}));
884 title('30 seconds prior to LC1(D1) x 30 seconds prior to LC1(
       D2)');
885
886 subplot(7,1,5); plot(normxcorr2(LCprior{1,1},LCprior{2,2}));
887 title('30 seconds prior to LC1(D1) x 30 seconds prior to LC2(
       D2)');
888
889 subplot(7,1,6); plot(normxcorr2(LCprior{2,1},LCprior{1,1}));
890 title('30 seconds prior to LC1(D2) x 30 seconds prior to LC1(
       D1)');
891
892 subplot(7,1,7); plot(normxcorr2(LCprior{2,1},LCprior{1,2}));
893 title('30 seconds prior to LC1(D2) x 30 seconds prior to LC2(
       D1)');
```

8.1.2 Profile Generator

The code shown here was used to develop the droplet tracking software, in which a profile is generated containing droplet positions in the image fed into the program.

```
% find all locations of droplets, returns them into a list

%ed = edgedStore{1500,1};
pos = 1;

[y,x] = size(ed);

for i = 1:y
   for j = 1:x

       if ed(i,j)==1
           store(pos,1) = i;
           store(pos,2) = j;
           pos = pos+1;
       end

   end
end
pos = pos-1;
%disp('finished');

% find position for each cord
used = zeros(pos,1);
cellcount = zeros(4,1);
clear profile;
profile{1,1}(1,1) = store(1,1);
profile{1,1}(1,2) = store(1,2);
```

```
28 cellcount(1,1) = 1;
29 used(1,1) = 1;
30 numcell = 1;
31
32
33 while(sum(used)<pos)
34 %     disp(sum(used));
35     %for t = 1:numcell %cycle through each profile
36         t = numcell;
37         z = cellcount(numcell,1);
38         flag = flag + 1;
39          for i = 1:z %cycle through each cell in each profile
40
41              for j = 1:pos %cycle through each cell in the
    list
42
43                  dx = abs(profile{t,1}(i,1)-store(j,1));
44                  dy = abs(profile{t,1}(i,2)-store(j,2));
45
46                  dydx = sqrt((dx*dx)+(dy*dy));
47
48                  if dydx <2 && used(j,1)==0
49                      z = z+1;
50                      cellcount(numcell,1) = cellcount(numcell)
    +1;
51                      profile{t,1}(z,1) = store(j,1);
52                      profile{t,1}(z,2) = store(j,2);
53                      used(j,1) = 1;
54
55                      flag = 0;
```

```
56                  end
57
58
59              end
60
61              if flag==10
62                  numcell = numcell+1;
63                  cellcount(numcell,1) = 1;
64                  [a] = find(used(:,1)==0);
65                  temp = a(1);
66                  profile{numcell,1}(1,1) = store(temp,1);
67                  profile{numcell,1}(1,2) = store(temp,2);
68                  used(temp,1) = 1;
69                  flag = 0;
70              end
71          end
72
73      %end
74
75  end
```

8.1.3 FFT Analysis

Presented in this subsection are the Fourier analysis tools developed using MATLAB's in-built functions, to analyse the frequency spectrum of the data extracted from the time-series videos of the droplet experiments.

```
%% fft on whole signal

t = APre{2,i};%-mean(tep);%-mean(cell2);

t = t-mean(t);

Fs = 0.1;

N = length(t);


X = fftshift(fft(t));
dt = 1/Fs;
dF = Fs/N;
f = -Fs/2:dF:Fs/2-dF;
% figure;
% subplot(2,1,1),
plot(f,abs(X)/N);
% fftstore(i,:)=abs(X)/N;
i = i+1;
xlabel('Frequency (in hertz)');
title('Average Magnitude Response of Membrane Potential of
   All Children', 'fontsize', 14);
% subplot(2,1,2),plot(Elongation{2,6});
% title('Length of Cell Through Time');
% ylabel('Cell Length, Pixels');
```

```
26
27 %% detrend data
28 figure, hold on;
29 x = DBData2';
30
31 offset = x - mean(x);
32 xx = 1:10:length(offset)*10;
33
34 plot(x)
35 plot(offset);
36
37 P = polyfit(xx',offset,1);
38 yfit = P(1)*xx+P(2);
39
40
41 plot(yfit);
42
43 detrended = offset - yfit';
44
45 % plot(xx,detrended);
46 plot(detrended);
47 % {1,i} = detrended;
48 i = i+1;
49 close all;
50
51 %% bulk out for winter
52
53 x = DApreData2';
54
55 offset = x - mean(x);
```

```
56 xx = 1:10:length(offset)*10;
57
58
59 P = polyfit(xx',offset,1);
60 yfit = P(1)*xx+P(2);
61
62
63 detrended = offset - yfit';
64
65
66 APre{1,i} = detrended;
67
68
69 x = DApostData2';
70
71 offset = x - mean(x);
72 xx = 1:10:length(offset)*10;
73
74
75 P = polyfit(xx',offset,1);
76 yfit = P(1)*xx+P(2);
77
78
79 detrended = offset - yfit';
80
81
82 APost{1,i} = detrended;
83
84
85
```

```
86 x = DBData2';
87
88 offset = x - mean(x);
89 xx = 1:10:length(offset)*10;
90
91
92 P = polyfit(xx',offset,1);
93 yfit = P(1)*xx+P(2);
94
95
96 detrended = offset - yfit';
97
98
99 AB{1,i} = detrended;
100 i = i+1;
101
102 %% low pass filter
103 x = APre{1,i};
104 filtered = lowpass(x,1,59.94);
105
106 APre{2,i} = filtered;
107
108 x = APost{1,i};
109 filtered = lowpass(x,1,59.94);
110
111 APost{2,i} = filtered;
112
113 x = AB{1,i};
114 filtered = lowpass(x,1,59.94);
115
```

```
116 AB{2,i} = filtered;
117 i = i+1;
118 %% bandpass detrended
119
120 bfilt = bandpass(APre{1,1},[0.01 0.04],0.1);
121
122 % Dtest=bfilt;
123
124 plot(bfilt)
125 % i = i+1;
126
127 %% Harry Plotter
128
129 len = length(DApreData2)+length(DApostData2);
130 ts = 1/59.94:1/59.94:len/59.94;
131 figure, hold on;
132 plot(ts(1:length(DApreData2)),DApreData2);
133 plot(ts(length(DApreData2)+1:length(DApreData2)+length(
       DApostData2)),DApostData2);
134 plot(ts(length(DApreData2)+1:length(DApreData2)+length(
       DApostData2)),DBData2);
135 legend('Droplet A pre','Droplet A post','Droplet B');
136 ylabel('Intensity, AU');
137 xlabel('Time, seconds');
138 title('3cm delta experiment 1');
139
140 figure;
141 subplot(3,1,1),plot(DAprevolume),title('Droplet A pre volume'
       );
142 subplot(3,1,2),plot(DApostvolume),title('Droplet A post
```

```
    volume');
143 subplot(3,1,3),plot(DBvolume),title('Droplet B volume');
144
145
146 %% PSD
147
148 Fs = 59.94;
149 x = APre{2,i}(1:7921);
150 % x = x(length(x)-7920:length(x));
151 % x = x-mean(x);
152
153 N = length(x);
154 xdft = fft(x);
155 xdft = xdft(1:N/2+1);
156 psdx = (1/(Fs*N)) * abs(xdft).^2;
157 psdx(2:end-1) = 2*psdx(2:end-1);
158 freq = 0:Fs/length(x):Fs/2;
159
160 plen = length(psdx);
161 flen= length(freq);
162
163 PSD{i} = 10*log10(psdx);
164 % aPSDE1334(i,:) = 10*log10(psdx);
165 i = i+1;
166
167 plot(freq(2:flen),10*log10(psdx(2:plen)),'b')
168 grid on
169 title('Periodogram Using FFT')
170 xlabel('Frequency (Hz)')
171 ylabel('Power/Frequency (dB/Hz)')
```

```
172
173 %% sampler
174 ii = 0;
175 % ct = 1;
176
177 len = length(PSD{ct});
178
179 for i = 1:len/3961:len
180     ii = ii+1;
181
182     avg(ct,ii) = PSD{ct}(round(i));
183
184
185
186 end
187 ct = ct+1;
188
189 %% cross cor with x axis
190 figure;
191 dat1 = DApostData2;
192 dat2 = DBData2;
193
194 if length(dat1)<length(dat2)
195     lt = normxcorr2(dat1,dat2);
196     len = (length(lt)-1)/2;
197     plot(-len:len,normxcorr2(dat1,dat2));
198
199 else
200     lt = normxcorr2(dat2,dat1);
201     len = (length(lt)-1)/2;
```

```
202     plot(-len:len,normxcorr2(dat2,dat1));
203
204 end
205
206 hold on, plot([0,0],[-1,1],':');
207 ylabel('Correlation');
208 xlabel('Tau Offset');
209 title('Droplet A post x Droplet B');
210
211 % mxlt = max(lt);
212
213 % delt = find(lt == mxlt);
214
215 % offset(ii) = mod(delt,len/2);
216
217 % mid = (length(dat1)+length(dat2)/2);
218
219 % tau0(ii) = lt(round(length(lt)/2));
220
221 % ii= ii+1;
222
223 %% cross cor with x axis
224 figure;
225 dat1 = DApreData2;
226 dat2 = DBData2;
227
228 if length(dat1)<length(dat2)
229     lt = normxcorr2(dat1,dat2);
230     len = (length(lt)-1)/2;
231     plot(-len:len,normxcorr2(dat1,dat2));
```

```
232
233 else
234     lt = normxcorr2(dat2,dat1);
235     len = (length(lt)-1)/2;
236     plot(-len:len,normxcorr2(dat2,dat1));
237
238 end
239
240 hold on, plot([0,0],[-1,1],':');
241 ylabel('Correlation');
242 xlabel('Tau Offset');
243 title('Droplet A pre x Droplet B');
244
245 %% cross cor with x axis
246 figure;
247 dat1 = DApostData2;
248 dat2 = DApreData2;
249
250 if length(dat1)<length(dat2)
251     lt = normxcorr2(dat1,dat2);
252     len = (length(lt)-1)/2;
253     plot(-len:len,normxcorr2(dat1,dat2));
254
255 else
256     lt = normxcorr2(dat2,dat1);
257     len = (length(lt)-1)/2;
258     plot(-len:len,normxcorr2(dat2,dat1));
259
260 end
261
```

```
262 hold on, plot([0,0],[-1,1],':');
263 ylabel('Correlation');
264 xlabel('Tau Offset');
265 title('Droplet A pre x Droplet A post');
266
267 %% cross correlation table
268 x = 0;
269 for i =1:2
270    for ii = 1:2
271        x = x + 1;
272
273        if length(dat{i})<length(dat{ii})
274           subplot(2,2,x), plot(normxcorr2(dat{i},dat{ii}));
275        else
276            subplot(2,2,x), plot(normxcorr2(dat{ii},dat{i}));
277        end
278
279
280    end
281 end
282
283 %% test
284
285 xxx = input('test');
286 disp(xxx);
287 %% frequency change through time
288 t = D1;
289 t = t-mean(t);
290 Fs = 0.1;
291 N = length(t);
```

```
X = fftshift(fft(t));
dt = 1/Fs;
dF = Fs/N;
f = -Fs/2:dF:Fs/2-dF;
figure;
subplot(3,1,1),plot(f,abs(X)/N);
title('Magnitude of Frequency of n0 for Cell D1');

t = D1(1:55);
t = t-mean(t);
Fs = 0.1;
N = length(t);
X = fftshift(fft(t));
dt = 1/Fs;
dF = Fs/N;
f = -Fs/2:dF:Fs/2-dF;
subplot(3,1,2),plot(f,abs(X)/N);
title('Magnitude of Frequency of first 50% of Cell D1');

t = D1(56:110);
t = t-mean(t);
Fs = 0.1;
N = length(t);
X = fftshift(fft(t));
dt = 1/Fs;
dF = Fs/N;
f = -Fs/2:dF:Fs/2-dF;
subplot(3,1,3),plot(f,abs(X)/N);
title('Magnitude of Frequency of last 50% of Cell D1');

```

```
322 %% bandpass and plot
323
324 sig = double(M2D2D2LB05);
325
326 bpass = bandpass(sig,[0.015 0.025], 0.1);
327
328 plot(bpass);
329 title('0.5%LB M2D2D2 2mHz Bandpass Response','fontsize',32);
330
331 %% plot multiple fft
332 figure;
333 hold on;
334 for i = 1:6
335
336     t = Elongation{2,i};
337     N = length(t);
338     X = ElonFFT{i};
339     dt = 1/Fs;
340     dF = Fs/N;
341     f = -Fs/2:dF:Fs/2-dF;
342
343     plot(f,abs(X)/N);
344
345 end
346
347 %% hilbert plotting
348
349 y = hilbert(ifft(ifftshift(Pre{3,1})));
350 figure, hold on
351 plot(real(y))
```

```
352 plot(imag(y))
353 legend('Real Part','Imaginary Part')
354 title('Phase of Pre n0 signal')
355 figure, hold on
356 plot(angle(y))
357 title('Phase Angle of Pre n0 Signal')
358
359 y = hilbert(ifft(ifftshift(Pre{3,2})));
360 figure, hold on
361 plot(real(y))
362 plot(imag(y))
363 legend('Real Part','Imaginary Part')
364 title('Phase of Pre n25 signal')
365 figure, hold on
366 plot(angle(y))
367 title('Phase Angle of Pre n25 Signal')
368
369 y = hilbert(ifft(ifftshift(Pre{3,3})));
370 figure, hold on
371 plot(real(y))
372 plot(imag(y))
373 legend('Real Part','Imaginary Part')
374 title('Phase of Pre n50 signal')
375 figure, hold on
376 plot(angle(y))
377 title('Phase Angle of Pre n50 Signal')
378
379 y = hilbert(ifft(ifftshift(Pre{3,4})));
380 figure, hold on
381 plot(real(y))
```

```
382 plot(imag(y))
383 legend('Real Part','Imaginary Part')
384 title('Phase of Pre n75 signal')
385 figure, hold on
386 plot(angle(y))
387 title('Phase Angle of Pre n75 Signal')
388
389 %% Bandpass and extract phase
390
391 sig = nP4C1;
392
393 fre1 = bandpass(sig,[0.001 0.002], 0.1);
394 fre2 = bandpass(sig,[0.002 0.003], 0.1);
395 fre3 = bandpass(sig,[0.003 0.004], 0.1);
396 fre4 = bandpass(sig,[0.004 0.005], 0.1);
397 fre5 = bandpass(sig,[0.005 0.006], 0.1);
398
399 y = hilbert(fre1);
400 % figure, hold on;
401 subplot(5,1,1),plot(angle(y));
402 title('1mHz Phase Extracted from bandpassed data from P4C1');
403
404 % plot(real(y))
405 % plot(imag(y))
406 % plot(abs(y))
407 % legend('Real Part','Imaginary Part','Absolute Value')
408 % title('Phase extracted from 1mHz signal of P2C2')
409
410 y = hilbert(fre2);
411 subplot(5,1,2),plot(angle(y));
```

```
412 title('2mHz Phase Extracted from bandpassed data from P4C1');
413
414 % figure, hold on
415 % plot(real(y))
416 % plot(imag(y))
417 % plot(abs(y))
418 % legend('Real Part','Imaginary Part','Absolute Value')
419 % title('Phase extracted from 2mHz signal of P2C2')
420
421 y = hilbert(fre3);
422 subplot(5,1,3),plot(angle(y));
423 title('3mHz Phase Extracted from bandpassed data from P4C1');
424
425 % figure, hold on
426 % plot(real(y))
427 % plot(imag(y))
428 % plot(abs(y))
429 % legend('Real Part','Imaginary Part','Absolute Value')
430 % title('Phase extracted from 3mHz signal of P2C2')
431
432 y = hilbert(fre4);
433 subplot(5,1,4),plot(angle(y));
434 title('4mHz Phase Extracted from bandpassed data from P4C1');
435
436 % figure, hold on
437 % plot(real(y))
438 % plot(imag(y))
439 % plot(abs(y))
440 % legend('Real Part','Imaginary Part','Absolute Value')
441 % title('Phase extracted from 4mHz signal of P2C2')
```

```
442
443 y = hilbert(fre5);
444 subplot(5,1,5),plot(angle(y));
445 title('5mHz Phase Extracted from bandpassed data from P4C1');
446
447 % figure, hold on
448 % plot(real(y))
449 % plot(imag(y))
450 % plot(abs(y))
451 % legend('Real Part','Imaginary Part','Absolute Value')
452 % title('Phase extracted from 5mHz signal of P2C2')
453
454 % legend('1mHz','2mHz','3mHz','4mHz','5mHz');
455
456 %% PLV
457
458 PlateauHilbert{1,1} = hilbert(Plateau{2,1}(1,:));
459 PlateauHilbert{2,1} = hilbert(Plateau{2,1}(2,:));
460 PlateauHilbert{3,1} = hilbert(Plateau{2,1}(3,:));
461 PlateauHilbert{4,1} = hilbert(Plateau{2,1}(4,:));
462 PlateauHilbert{5,1} = hilbert(Plateau{2,1}(5,:));
463 PlateauHilbert{6,1} = hilbert(Plateau{2,1}(6,:));
464 PlateauHilbert{7,1} = hilbert(Plateau{2,1}(7,:));
465 PlateauHilbert{8,1} = hilbert(Plateau{2,1}(8,:));
466 % PostHilbert{9,1} = hilbert(Post{2,1}(9,:));
467
468 PlateauAngle{1,1} = angle(PlateauHilbert{1,1});
469 PlateauAngle{2,1} = angle(PlateauHilbert{2,1});
470 PlateauAngle{3,1} = angle(PlateauHilbert{3,1});
471 PlateauAngle{4,1} = angle(PlateauHilbert{4,1});
```

```
472 PlateauAngle{5,1} = angle(PlateauHilbert{5,1});
473 PlateauAngle{6,1} = angle(PlateauHilbert{6,1});
474 PlateauAngle{7,1} = angle(PlateauHilbert{7,1});
475 PlateauAngle{8,1} = angle(PlateauHilbert{8,1});
476 % PostAngle{9,1} = angle(PostHilbert{9,1});
477
478 for i = 1:8
479     for j = 1:8
480
481         PLVPlateau{i,j} = exp(1i*(PlateauAngle{i,1}-
    PlateauAngle{j,1}));
482
483         PLVAveragePlateau(i,j) = abs(sum(exp(1i*(PlateauAngle{
    i,1}-PlateauAngle{j,1}))))/100;
484
485     end
486 end
487
488 %% phaaaaaase
489 for i = 1:6
490     AnglePre(i,:) = angle(hilbert(RawPre(i,:)));
491
492 end
493
494 for i = 1:9
495
496      AnglePost(i,:) = angle(hilbert(RawPost(i,:)));
497      AnglePlateau(i,:) = angle(hilbert(RawPlateau(i,:)));
498
499 end
```

```
500
501 %% PLV phase transirions
502
503 for i = 1:9
504     for j = 1:9
505
506         PLVPlateau{i,j} = exp(1i*(AnglePlateau(i,:)-
    AnglePlateau(j,:)));
507
508         PLVAveragePlateau(i,j) = abs(sum(exp(1i*(AnglePlateau(
    i,:)-AnglePlateau(j,:)))))/100;
509
510
511     end
512 end
513
514 %% signal against other phases
515
516 COI = 6;
517
518 for i = 1:9
519
520      PLVPrexPost{i,COI} = exp(1i*(AnglePre(COI,:)-AnglePost(i
    ,:)));
521
522      PLVAveragePrexPost(i,COI) = abs(sum(exp(1i*(AnglePre(COI
    ,:)-AnglePost(i,:)))))/100;
523 end
524
525 %% phase writer
```

```
526
527 for i = 1:6
528     PhasePre(i,:) = angle(hilbert(RawPre(i,:)));
529 end
530
531 for i = 1:9
532     PhasePost(i,:) = angle(hilbert(RawPost(i,:)));
533     PhasePlateau(i,:) = angle(hilbert(RawPlateau(i,:)));
534 end
535
536 %% adj matrix for phase and raw
537
538 for i = 1:6
539    for j = 1:6
540
541        use = normxcorr2(RawPre(i,:),RawPre(j,:));
542
543        AdjPre{1}(i,j) = use(100);
544        AdjPre{2}(i,j) = max(use);
545
546        use = normxcorr2(PhasePre(i,:),PhasePre(j,:));
547        AdjPre{3}(i,j) = use(100);
548        AdjPre{4}(i,j) = max(use);
549
550    end
551 end
552
553 %% elongation fft and graphing
554
555 figure;
```

```
556 hold on;
557 plot(Elongation{3,4});
558 plot(Elongation{1,4});
559 title('P2');
560 ylabel('Cell Length, pixels');
561 legend('Filtered Data', 'Raw Data');
562
563 figure;
564 spectrogram(Elongation{3,4},[],[],[],0.1,'yaxis');
565 title('P2');
566
567 %% correlation of spectrograms
568
569 % for i = 1:6
570 %     for j = 1:6
571 %
572 %         s1 = spectrogram(Elongation{3,i});
573 %         s2 = spectrogram(Elongation{3,j});
574 %
575 %         adj1(i,j) = max(max(normxcorr2(abs(s1(1:)),abs(s2
        (1,:))));
576 %
577 %
578 %     end
579 % end
580
581 %% plot elongation x filtered data
582 %1mHz signal
583 figure; hold on;
584 yyaxis left;
```

```
585 plot(n1{13});
586
587 yyaxis right;
588 plot(TP2C1e);
589 legend('1mHz','Cell Length');
590
591 yyaxis left;
592 ylabel('1mHz signal', 'FontSize', 16);
593 yyaxis right;
594 ylabel('Cell Length Through Time, pixels', 'FontSize', 16);
595 title('P4C1', 'FontSize', 24);
596
597 % 5mHz signal
598 figure; hold on;
599 yyaxis left;
600 plot(n5{13});
601
602 yyaxis right;
603 plot(TP2C1e);
604 legend('5mHz','Cell Length');
605
606 yyaxis left;
607 ylabel('5mHz signal', 'FontSize', 16);
608 yyaxis right;
609 ylabel('Cell Length Through Time, pixels', 'FontSize', 16);
610 title('P4C1', 'FontSize', 24);
611 %% loop through windowing
612
613 for ct = 1:421
614
```

```
615     ts = P1C2(ct:ct+499);
616     X = fftshift(fft(ts));
617     a(ct,:) = abs(X);
618 %     b(ct,:) = (abs(X))/median(abs(X));
619 
620 end
621 
622 %% stst
623 
624 for i = 1:203
625 
626     me(i) = median(a(i,:));
627     ra(i) = max(a(i,:))-min(a(i,:));
628     sn(i) = median(a(i,:))-min(a(i,:));
629     ns(i) = max(a(i,:)) - median(a(i,:));
630     mmn(i) = min(a(i,:));
631 
632 
633 end
634 % figure, hold on, plot(me/max(me)), plot(ra/max(ra));
635 % figure, plot(sn);
636 % hold on, plot(ns);
637 
638 %% freq delta
639 
640 for i = 251:500
641 
642     med(i) = median(a(:,i));
643     mx(i) = max(a(:,i));
644     mn(i) = min(a(:,i));
```

```
645     rg(i) = mx(i)-mn(i);
646
647     dx(i,:) = diff(a(:,i));
648
649 end
650 tscale = 52:100;
651 subplot(2,2,1),plot(med(tscale));
652 title('Median');
653 subplot(2,2,2),plot(mx(tscale));
654 title('Max');
655 subplot(2,2,3),plot(mn(tscale));
656 title('Min');
657 subplot(2,2,4),plot(rg(tscale));
658 title('Range');
659
660 %% dx plotter
661 % figure;
662 % hold on;
663
664 ii=0;
665 % title('Change in Frequency');
666
667
668 for i = 261:270
669     ii = ii+1;
670     subplot(10,1,ii),plot(a(:,i));
671
672 end
673 subplot(10,1,ii-9),plot(a(:,i-9));
674 title('Change in Frequency', 'FontSize', 38);
```

```
675
676 %% box plot
677
678 t = 1:100;
679 figure;
680 hold on;
681
682 for i = 1: 703
683
684     plot(t,a(i,:));
685
686 %      t = t+1;
687
688 end
689 %% dy
690
691 figure;
692 hold on;
693
694 for i = 51:60
695
696     boxplot(a(:,i),i);
697
698
699 end
700
701 %% fft on first 30k;
702
703 x1 = P1C1(551:802);
704
```

```
705 Fs = 0.1;
706
707 N = length(x1);
708
709
710 X = fftshift(fft(x1));
711 dt = 1/Fs;
712 dF = Fs/N;
713 f = -Fs/2:dF:Fs/2-dF;
714 figure;
715 plot(f,abs(X)/N);
716 xlabel('Frequency (in hertz)');
717 title('Magnitude Response of fourth quarter of time series');
718
719 %% fft on second 30k samples
720
721 x2 = eeg5(30001:60000);
722
723 Fs = 252;
724
725 N = length(x2);
726
727
728 X = fftshift(fft(x2));
729 dt = 1/Fs;
730 dF = Fs/N;
731 f = -Fs/2:dF:Fs/2-dF;
732 figure;
733 plot(f,abs(X)/N);
734 xlabel('Frequency (in hertz)');
```

```
735 title('Magnitude Response of first 30k samples');
736
737 %% fft test
738
739
740 t = 0:0.01:6.5;
741
742 x3 = sin(5*t*2*pi);
743
744 Fs = 1/0.01;
745
746 N = length(x3);
747
748
749 X = fftshift(fft(x3));
750 dt = 1/Fs;
751 dF = Fs/N;
752 f = -Fs/2:dF:Fs/2-dF;
753 figure;
754 plot(f,abs(X)/N);
755 xlabel('Frequency (in hertz)');
756 title('Magnitude Response of first 30k samples');
757
758 %% bulk spectrogram data pull
759
760 ii = 0;
761
762 for i = 1:126:length(eeg5)-((Fs*10)-1)
763     x = eeg5(i:i+Fs*10-1);
764     s = spectrogram(x,[],[],[],Fs);
```

```
765
766     ii = ii+1;
767
768     fr8(ii) = median(abs(s(:,8)));
769     fr7(ii) = median(abs(s(:,7)));
770     fr6(ii) = median(abs(s(:,6)));
771     fr5(ii) = median(abs(s(:,5)));
772     fr4(ii) = median(abs(s(:,4)));
773     fr3(ii) = median(abs(s(:,3)));
774     fr2(ii) = median(abs(s(:,2)));
775     fr1(ii) = median(abs(s(:,1)));
776
777 end
778
779 figure;
780 subplot(4,2,1),plot(fr1), title('first band');
781 subplot(4,2,2),plot(fr2), title('second band');
782 subplot(4,2,3),plot(fr3), title('third band');
783 subplot(4,2,4),plot(fr4), title('fourth band');
784 subplot(4,2,5),plot(fr5), title('fifth band');
785 subplot(4,2,6),plot(fr6), title('sixth band');
786 subplot(4,2,7),plot(fr7), title('seventh band');
787 subplot(4,2,8),plot(fr8), title('eight band');
788
789 %% plot inverse fft into spectrogram
790 Fs = 0.1;
791
792 % N = length(t);
793 N = 100;
794
```

```
795
796 X = fftshift(fft(t));
797 dt = 1/Fs;
798 dF = Fs/N;
799 f = -Fs/2:dF:Fs/2-dF;
800
801 figure, plot(f,Post{3,1}/N);
802 title('Post-division n0','fontsize',24);
803 xlabel('Frequency, Hz','fontsize',20);
804 figure, plot(f,Post{3,2}/N);
805 title('Post-division n+25','fontsize',24);
806 xlabel('Frequency, Hz','fontsize',20);
807 figure, plot(f,Post{3,3}/N);
808 title('Post-division n+50','fontsize',24);
809 xlabel('Frequency, Hz','fontsize',20);
810 figure, plot(f,Post{3,4}/N);
811 title('Post-division n+75','fontsize',24);
812 xlabel('Frequency, Hz','fontsize',20);
813
814 figure;
815 spectrogram(ifft(ifftshift(Post{3,1})),[],[],[],0.1,'yaxis');
816 title('Post-division n0','fontsize',24);
817 figure;
818 spectrogram(ifft(ifftshift(Post{3,2})),[],[],[],0.1,'yaxis');
819 title('Post-division n+25','fontsize',24);
820 figure;
821 spectrogram(ifft(ifftshift(Plateau{3,3})),[],[],[],0.1,'yaxis
      ');
822 title('Plateau n-50','fontsize',24);
823 figure;
```

```
824 spectrogram(ifft(ifftshift(Post{3,4})),[],[],[],0.1,'yaxis');
825 title('Post-division n+75','fontsize',24);
826
827 %% plot averaged signals
828
829 figure, hold on;
830 plot(ifft(ifftshift(Pre{3,1})));
831 plot(ifft(ifftshift(Pre{3,2})));
832 plot(ifft(ifftshift(Pre{3,3})));
833 plot(ifft(ifftshift(Pre{3,4})));
834 legend('n0','n-25','n-50','n-75');
835 title('Averaged Pre-division');
836
837 figure, hold on;
838 plot(ifft(ifftshift(Post{3,1})));
839 plot(ifft(ifftshift(Post{3,2})));
840 plot(ifft(ifftshift(Post{3,3})));
841 plot(ifft(ifftshift(Post{3,4})));
842 legend('n0','n+25','n+50','n+75');
843 title('Averaged Post-division');
844
845 figure, hold on;
846 plot(ifft(ifftshift(Plateau{3,1})));
847 plot(ifft(ifftshift(Plateau{3,2})));
848 plot(ifft(ifftshift(Plateau{3,3})));
849 plot(ifft(ifftshift(Plateau{3,4})));
850 legend('n0','n-25','n-50','n-75');
851 title('Averaged Plateau');
852
853
```

```
854 %% bandpass filter the averaged fft
855
856 rngs = [0.025 0.03];
857 numc = 6;
858
859 bPre{1,numc} = bandpass(ifft(ifftshift(Pre{3,1})),rngs,0.1);
860 bPre{2,numc} = bandpass(ifft(ifftshift(Pre{3,2})),rngs,0.1);
861 bPre{3,numc} = bandpass(ifft(ifftshift(Pre{3,3})),rngs,0.1);
862 bPre{4,numc} = bandpass(ifft(ifftshift(Pre{3,4})),rngs,0.1);
863
864 bPost{1,numc} = bandpass(ifft(ifftshift(Post{3,1})),rngs,0.1)
    ;
865 bPost{2,numc} = bandpass(ifft(ifftshift(Post{3,2})),rngs,0.1)
    ;
866 bPost{3,numc} = bandpass(ifft(ifftshift(Post{3,3})),rngs,0.1)
    ;
867 bPost{4,numc} = bandpass(ifft(ifftshift(Post{3,4})),rngs,0.1)
    ;
868
869 bPlateau{1,numc} = bandpass(ifft(ifftshift(Plateau{3,1})),
    rngs,0.1);
870 bPlateau{2,numc} = bandpass(ifft(ifftshift(Plateau{3,2})),
    rngs,0.1);
871 bPlateau{3,numc} = bandpass(ifft(ifftshift(Plateau{3,3})),
    rngs,0.1);
872 bPlateau{4,numc} = bandpass(ifft(ifftshift(Plateau{3,4})),
    rngs,0.1);
873
874 figure, hold on;
875 plot(bPre{1,numc});
```

```
876 plot(bPre{2,numc});
877 plot(bPre{3,numc});
878 plot(bPre{4,numc});
879 legend('n0','n-25','n-50','n-75');
880 title('Averaged Pre-division, bandpass filter 25-30mHz');
881
882 figure, hold on;
883 plot(bPlateau{1,numc});
884 plot(bPlateau{2,numc});
885 plot(bPlateau{3,numc});
886 plot(bPlateau{4,numc});
887 legend('n0','n-25','n-50','n-75');
888 title('Averaged Plateau, bandpass filter 25-30mHz');
889
890 figure, hold on;
891 plot(bPost{1,numc});
892 plot(bPost{2,numc});
893 plot(bPost{3,numc});
894 plot(bPost{4,numc});
895 legend('n0','n+25','n+50','n+75');
896 title('Averaged Post-division, bandpass filter 25-30mHz');
897
898
899
900 %% plot all signal
901
902 figure, hold on;
903 num = 4;
904
905 plot(Plateau{2,num}(1,:),'r--')
```

```
906 plot(Plateau{2,num}(2,:),'r--')
907 plot(Plateau{2,num}(3,:),'r--')
908 plot(Plateau{2,num}(4,:),'r--')
909 plot(Plateau{2,num}(5,:),'r--')
910 plot(Plateau{2,num}(6,:),'r--')
911 plot(Plateau{2,num}(7,:),'r--')
912 % plot(Plateau{2,num}(8,:),'r--')
913 % plot(Plateau{2,num}(9,:),'r--')
914 plot(Post{3,num}(1,:))
915 title('Plateau n-75','fontsize',24)
```

8.2 Quasi-2D BZ reaction

Initial experiments using the BZ reaction were conducted using a quasi-2D solution. The BZ solution was mixed and then poured into the 9cm diameter petri dish and recorded whilst subjected to varied external perturbations.

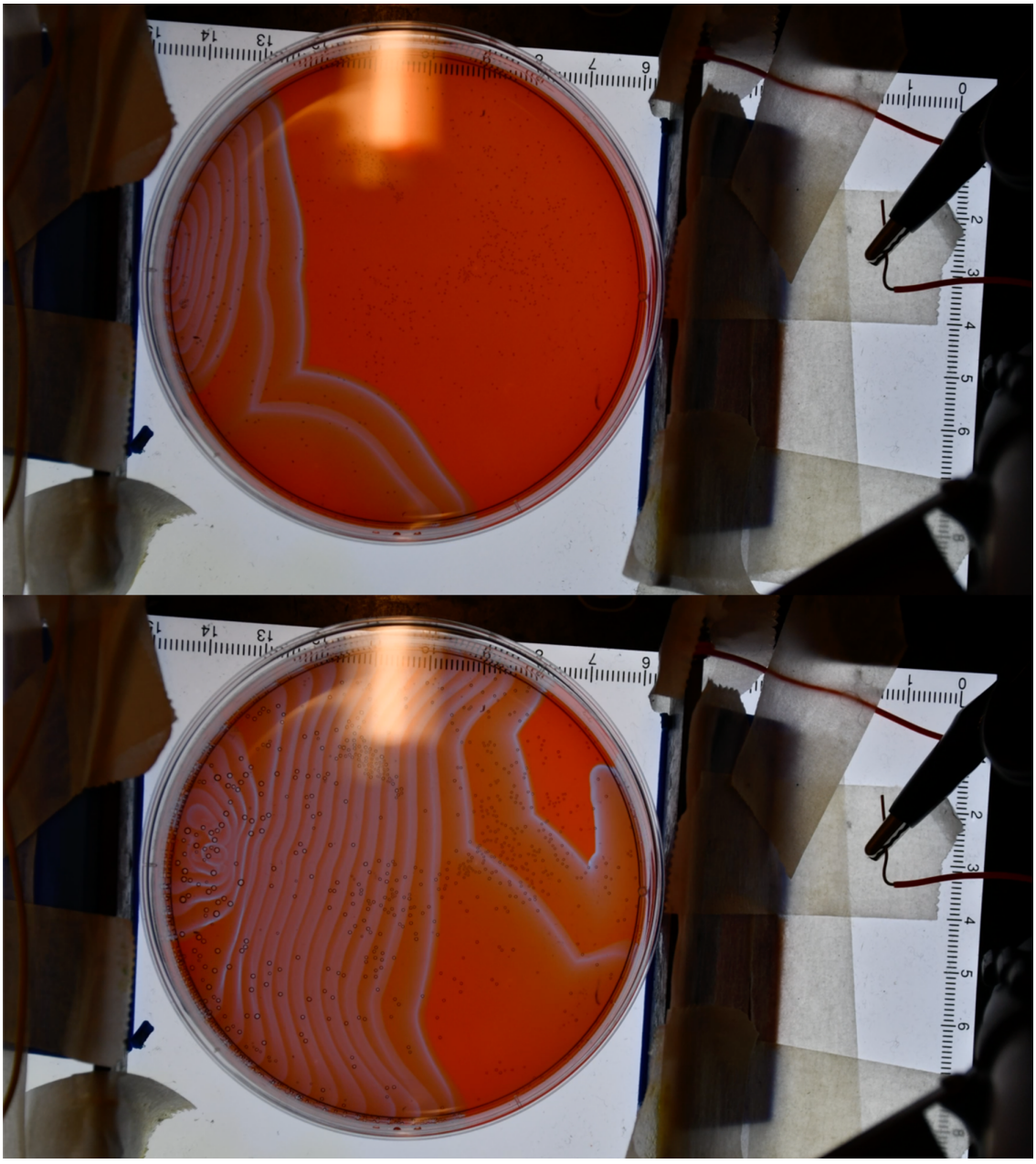

Figure 8.1: 2 snapshots of a representative example of applying an external DC field to the quasi-2D BZ reaction subject to static DC field. The positive electrode is placed on the left-hand side, and the negative is placed on the right-hand side, and a 30V field is applied. The formation of the LC is shown to occur nearest to the positive electrode.

Figure 8.1 shows a representative example of an experiment carried out on a quasi-2D solution of the BZ reaction. The 9cm diameter petri dish has a positive and negative electrode placed on either side. The LC formations occur closest to the positive electrode, due to the flow of the negative bromide ions towards the positive attractive force. The consumption of these bromide ions leads to the oxidation of the metal catalyst, ferroin solution. This causes the LC formation to occur, and leads to the propagation of a chemical wave across the quasi2D solution, in the direction towards the negative electrode.

t-test of elongation as a function of AC field period		
AC period	h-value	p-value
60 seconds	1	0.0031
90 seconds	1	0.0011
120 seconds	1	5.6422e-04
150 seconds	1	0.0033
180 seconds	1	0.0027
240 seconds	1	0.0079
300 seconds	0	0.514

Table 8.1: Results of T-test performed in the MATLAB computational environment, comparing the elongation of BZ droplets in the presence of an AC field, to the control group with no electric field stimulation.

t-test of width decrease as a function of AC field period		
AC period	h-value	p-value
60 seconds	0	0.3152
90 seconds	0	0.7002
120 seconds	0	0.5359
150 seconds	0	0.7936
180 seconds	0	0.8756
240 seconds	0	0.3696
300 seconds	0	0.3034

Table 8.2: Results of T-test performed in the MATLAB computational environment, comparing the decrease in width of BZ droplets in the presence of an AC field, to the control group with no electric field stimulation.

8.3 Statistical Tests of Droplet Elongation and width decrease as a function of AC field period

To determine the statistical significance of the experimentation, t-tests were performed on the elongation data using the MATLAB environment to compute the calculations. Each experimental group was tested against the control group to determine the significance of the findings. It was determined that the application of the electric field did prove to elongate the droplets in a significant manner.

It was discovered that the application of the AC field up to a period of 4 minutes was able to produce significant elongation of the BZ droplet, whilst the 5-minute period did not. However, no experimental condition here produced a significant decrease in width when compared to the control group.

8.4 Particle Image Velocimetry of Moving Particles Suspended Within Dividing Droplet

The following subsections contain particle image velocimetry (PIV) analysis of a dividing droplet. The droplet was doped with microspheres used to track the flow within the droplet. As the droplet produces LC formations, we observe shape deformation and elongation prior to the division event occurring, where 2 sub droplets are formed. Each plot describes the flow within the droplet during a successive stage in the division event. The stages were categorised by the change of shape in the droplet as it deforms and elongates whilst LC formations occur. The droplet was subject to an AC field for a period of 2 minutes and was submerged in an oil phase containing 0.9g SDS per litre of oleic acid. The outline of the plots was generated by tracing the shape of the droplet at the beginning of the time period the suspended particles were tracked for. The upper plot marked with μx represents a heatmap of the velocities of the tracked particles in the x direction. Where the positive direction follows left-to-right, shown with an arrow. The second plot represents the velocity in the y-direction and is marked with μy. The y-direction here is from the top to bottom, shown with a downward arrow. The legend for the heatmap is presented at the right hand of each figure. The final plot displays the streamlines of the flow captured by tracking multiple particles and aligning the flow directions. The droplets were studied as they underwent elongation in length, as well as shape deformation. This deformation was in the form of the width decreasing and the deformation of the elongating end of the droplet. There exists an argument about the nature of causality that can be made, as to whether the elongation is driven purely by the width decrease or vice versa. It is more likely that a combination of both factors forms positive feedback where the two variables act as factors in the increase in the other. Further work involving the adaptation of work completed by Bianco-Martinez *et al.* on the nature of causality and mutual information [394, 395]. This algorithm could be employed to determine the driving force between the stimulus. However, the current work takes the measure of uncertainty in future states in a bi-variable system and calculates the temporal notion of causality between the 2 variables. In our system, we have many locations in the droplet where deformation or width decrease occurs, which could be mapped to a singular variable measuring the elongation of the droplet. However, the elongation can be measured in differing manners as well, due to the deformation

resulting at the elongating end of the droplet, adding a tremendous amount of complexity to the system, thus the current causal mutual information algorithm is not fit for this analysis. The following plots were generated from the analysis of a single BZ droplet undergoing LC formation, leading to shape deformation, elongation, and finally division. From pipetting, the droplet took 13 minutes and 48 seconds to divide. The LC formations which induced the elongation and deformation that led to the division event started at the 8:49 minute mark, which is the point where the analysis begins. The time from the beginning of the LC formations to the division event occurring was 4 minutes and 59 seconds. Following the division event, the two sub-droplets form a spherical formation, following the minimum energy principle. The cylindrical ends form due to capillary action. We will be referring to the area within the droplet where we observe deformation and width decrease as an area with negative curvature, where positive curvature refers to the shape defined by the droplet acting under surface tension in normal conditions.

8.4.1 PIV 1 - Initial LC formations in BZ droplet

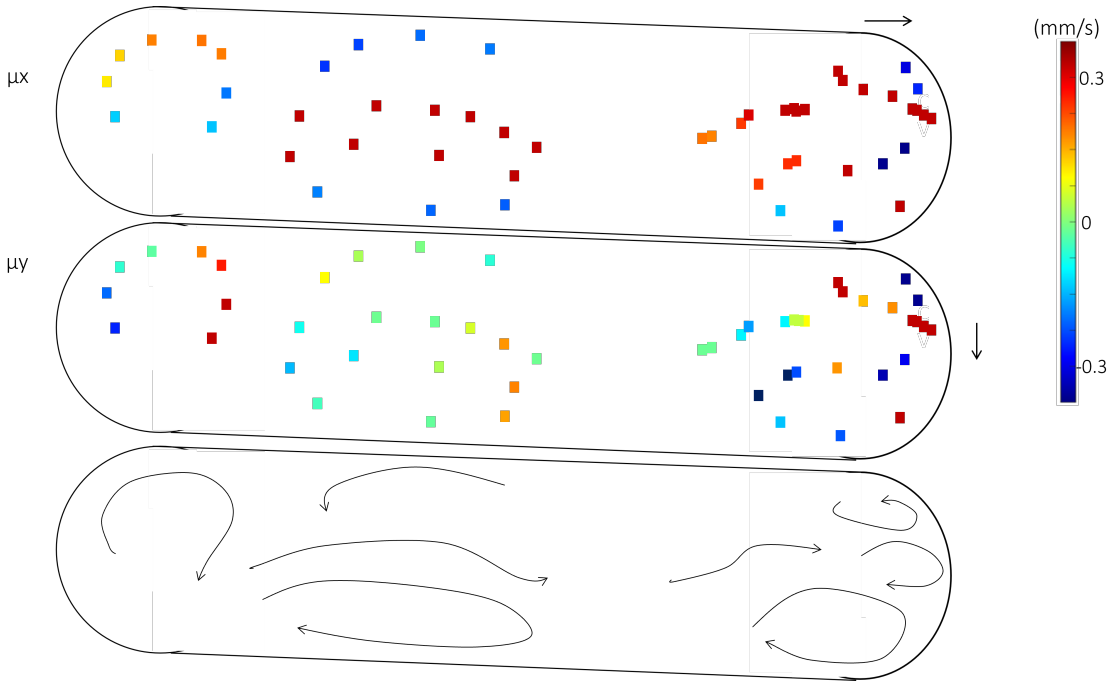

Figure 8.2: PIV analysis of initial stage in droplet division event. At this moment in time the droplet is not elongated, nor does it show any signs of deformation.

Here in figure 8.2 we can observe the internal flows created by many LC formations throughout the body of the droplet. The droplet currently shows no signs of deformation,

nor is it elongated. This is the first stage in the division event. There are multiple leading centre formations of which the flow is tracked and visualised in the PIV graph here. There is a cluster of flows around the right-most end of the droplet, which largely follow a clockwise direction as they travel. There is an accompanying anti-clockwise flow trajectory, however, at the top right of the droplet, which is likely to generate a pressure gradient around the body of the droplet, which will result in width reduction and the elongation of the droplet at this space of the droplet. To the left of this end, there is a flow stream seeming to move around the bottom-most clockwise vortex, which follows the mass transport from the centre of mass (CoM) of the droplet to the right-most end. There is a segment to the right of the CoM where no flows were tracked, this is not the case in the upcoming plots where the distribution of the microspheres changes through time. At the left-most end of the droplet, there exists a clockwise vortex-like flow, which is accompanied by another clockwise vortex formation near the bottom left, with a slight offset towards the CoM of the droplet. There is a mass transit flow above the accompanying vortex, which is likely to lead to the width decrease at the bottom left corner of the droplet due to the conservation of volume inside the droplet. The pressure build-up due to the colliding vortexes in correlation to the transit flow from the left end to the CoM will reduce the volume in this region. This will be reflected in the reduction in the width in the following outline of the droplet.

8.4.2 PIV 2 - Droplet Deformations

Figure 8.3 Represents the initial deformation stage in the droplet division lifecycle. There is a gradual increase in the length of the droplet, accompanied by a width reduction at either end. The reduction in width at the left end of the droplet only occurs on one side due to the arrangement of LC formations causing a bias in the flow states in the previous stage of the division process. Alternatively, at the right end of the droplet, there is deformation causing width decreases on both sides of the droplet. The prominent reason for this is due to the formation of clockwise and anticlockwise vortices forming in conjunction with the mass transit action forcing the droplet to elongate. The decreases in width act as a compensatory measure due to the conservation of mass as the droplet undergoes elongation. the droplet being pushed out of the minimum energy state is likely to have a profound effect on the

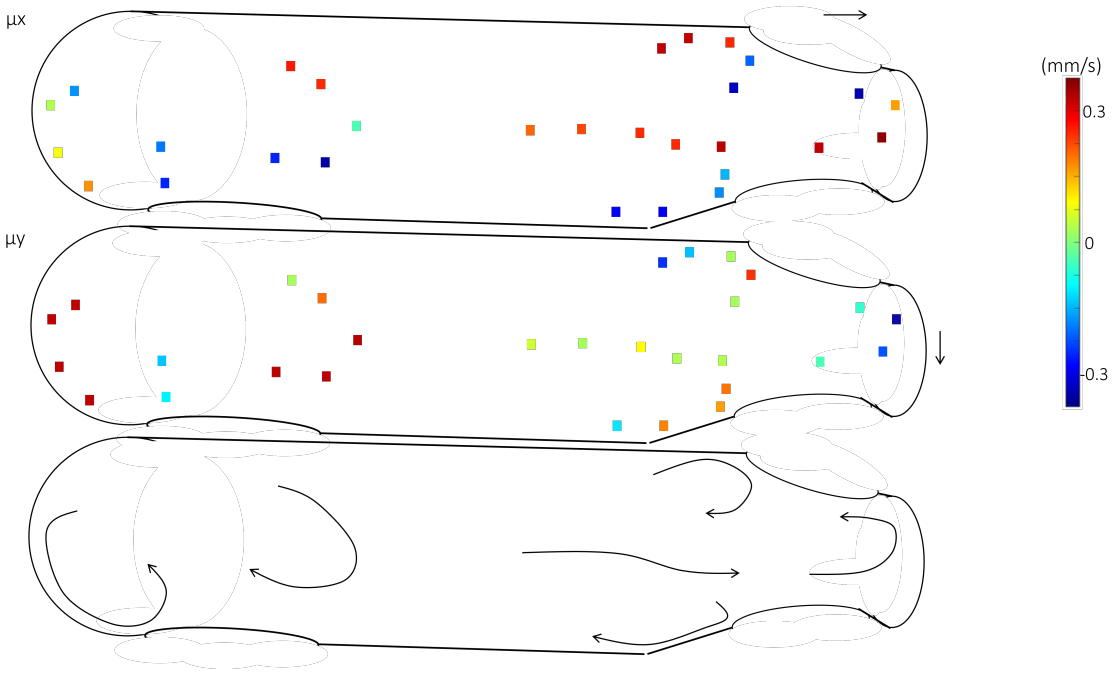

Figure 8.3: PIV analysis of a BZ droplet undergoing a division event. This figure represents the initial elongation of the droplet as the first LC formations have an impact on the droplet formation.

internal dynamics of the flow states. This is reflected in the PIV analysis, where we observe vortex flows around the deformation sites, along with a mass transit from the droplet CoM towards the elongating end, which will only further elongate the droplet during this procedure. It can be remarked that the velocity of the vortex flow at the left edge is relatively fast, which is likely to contribute to the deformation. To the right of this cortex, there is an opposing flow in the anti-clockwise coordination which will further exacerbate the decrease in width due to the conservation of mass, regarding the volume of the droplet. At the top right corner of the droplet, where elongation and deformation are taking place, a pair of antagonistic flows exist and likely contribute to the initial deformation and elongation, but here will only further it. These flows will work alongside the mass transit from the CoM to decrease the droplet volume at the centre and lead to two distinct regions of droplet volume.

8.4.3 PIV 3 - Initial Elongation

Figure 8.4 shows the results of the furthering elongation in correlation to width decrease. The deformation at the left-most end of the droplet has increased further due to the internal pressure generated by a pair of antagonistic vortex flows on either side of the deformation

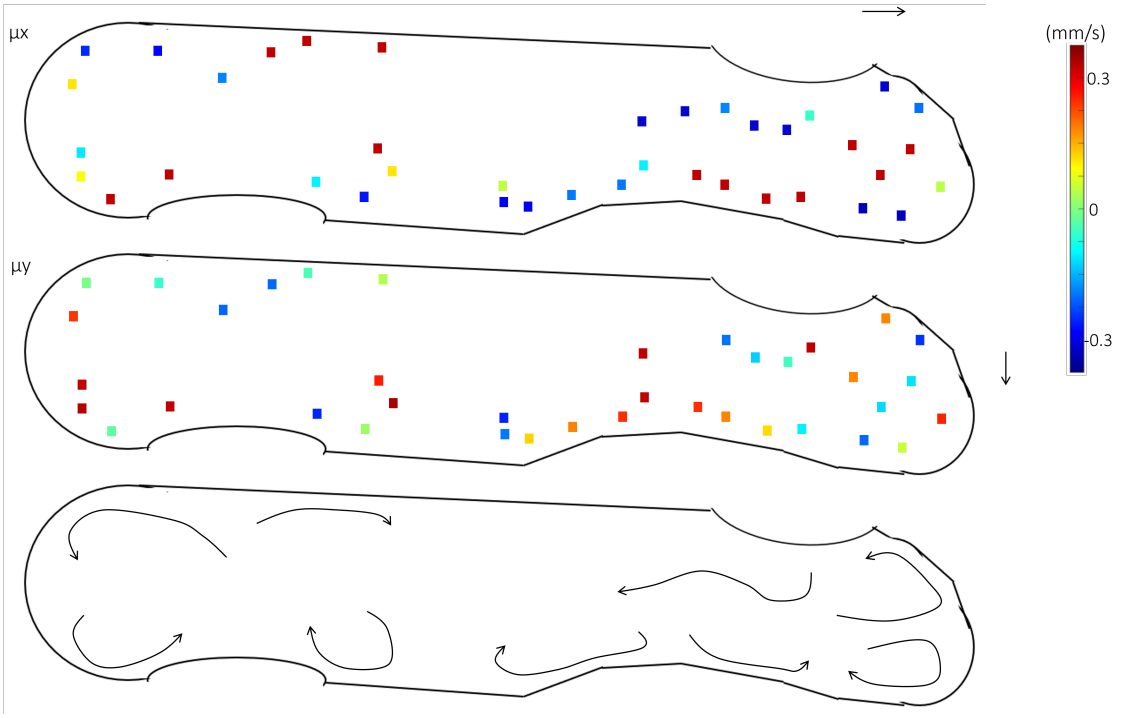

Figure 8.4: PIV analysis of am elongating droplet. The shape deformation on the droplet is beginning to increase due to the increase in flows within the droplet creating a disturbance to the droplet surface due to bulk flows within the droplet.

region. On the bottom right of the droplet, where the mirrored deformation is taking place, another pair of antagonistic vortices are prominent, however, this pair have formed in the opposing arrangement to the leftmost pair. The flow direction here acts in the opposing direction, creating a pull force inside the droplet. To the left of this pair, there is another vortex which is acting in the opposite direction to the right-hand vortex, which further acts as a driving force for elongation as there will be a compressive force acting at the point of convergence. This compression will act as a repulsive force and will drive the vortices further apart, leading to a greater elongation of the droplet. This elongation will subsequently cause greater deformation at the points already undergoing width decrease. The area of effect of the deformation will grow as the width decreases further. This will generate a stalk structure, or neck, in the droplet, as its structure will converge on a 'figure 8' arrangement prior to the division event occurring. The elongation of the droplet undergoing a division event is induced by the same mechanism for the regular elongation of a non-dividing droplet, however, the acceleration in the dividing droplet is much greater which can contribute to a negative curvature forming at the elongating end of the droplet. Another negative curvature is produced

at the right end of the droplet, where the bottom edge protrudes further than the top. This is due to friction from the oil phase creating a physical barrier for the droplet to overcome when elongating. Due to the sudden increase in droplet length an inhomogeneous elongation occurs where one side elongates further than the other. In this case where a division event is impending, the internal flows at the elongating end help to correct the structure into forming the spherical arrangement normally seen in droplets at minimum energy state. Here, the anti-clockwise flow at the top right will help to normalise the shape deformation and act as a sink for droplet volume, which will further accentuate the deformation at the droplet CoM, as the volume of the droplet must be conserved. This shape change will be corrected in the next figure and will show an enhanced elongation of the droplet. The effect of the positive pressure building up inside the droplet causes a driving force for a mass transit flow from the elongated end of the droplet back towards the CoM. This compensatory measure would largely be a form of self-regulation to minimise the droplet surface area. This is the effect that would inhibit the droplet division in the circumstance where the environmental perturbation was not sufficient enough to drive the internal mechanism to lead to droplet division events from occurring. A likely reason for this flow not causing the inhibition of droplet division is due to the opposing flow at the top left of the droplet, where there is a flow leading from the top left towards the droplet CoM. These flows would act as a repulsive force on each other and may interfere with other flows inside the CoM, and contribute to a turbulent flow within the droplet.

8.4.4 PIV 4 - Major Width Decrease

A pair of agonistic flows have formed at the left end of the droplet which acts as a sink for resources from the droplet CoM. There is one flow opposing this flow and is directed from the top left towards the droplet centre. The velocity of this flow may even be aided by the vortex to its left, where a pressure gradient created by the vortex acts as a pushing force towards the flow already initiated by LC formation. At the opposite end of the droplet, a pair of antagonistic flows have been generated, which in combination with the flow to the left of the deformed portion will create a driving force to further extenuate the deformation and elongation. The shape deformation at the elongating end which was caused by the accelerated droplet elongation has been corrected by the flows around the negative curvature. This has

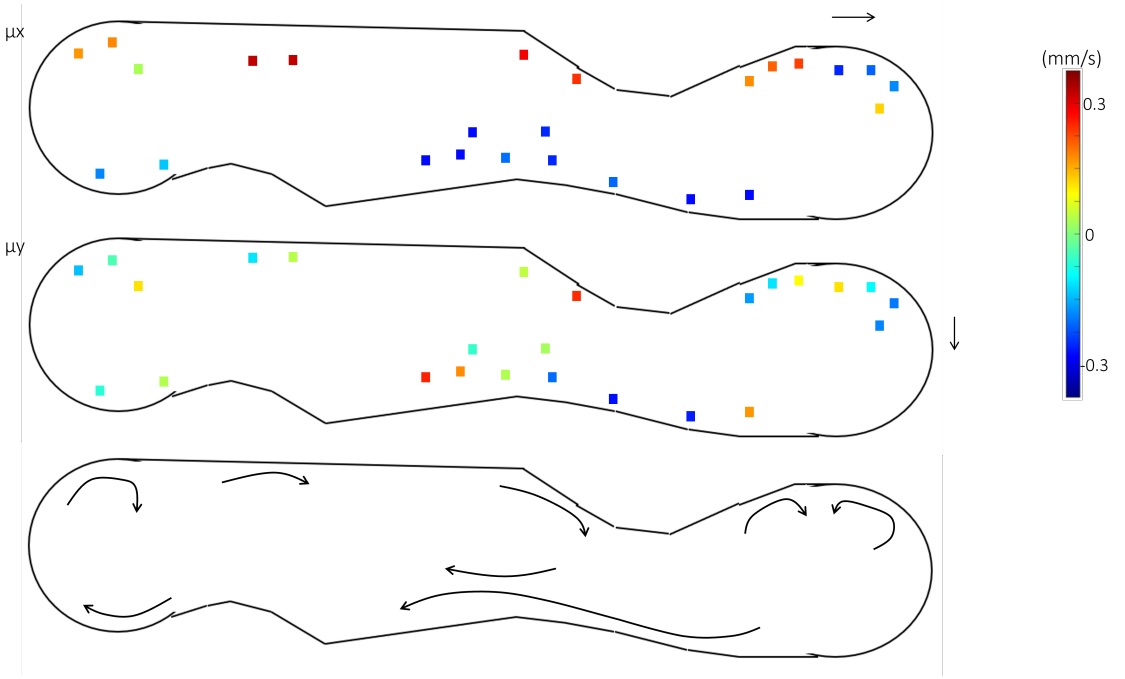

Figure 8.5: PIV analysis of a dividing droplet. The width decrease here is accelerating due to the elongation of the droplet. The negative curvature at the bottom right is set to merge with that on the bottom left, which will create a much greater decrease in width, and act as a mechanism to further the negative curvature of the droplet, as bulk flows will compensate within the droplet to try and decrease the surface tension.

also further enhanced the negative curvature at the top right, where the width decrease has increased. This also results in further elongation of the droplet, putting it further out from its minimum energy state by increasing the surface area even more. A pair of compensatory flows travel through the droplet CoM and are very possibly acting as a stability measure to retain the droplet in the minimum energy state [305]. The shape changes the droplet exhibits now are drastic, as two clear decreases in width are occurring at the top right, and bottom left of the droplet, the decrease in width at the bottom right of the droplet is appearing to be diminishing in magnitude, and whilst spreading out over a larger area. This deformation also appears to be merging with that in the bottom left, which will possibly generate the beginning of the stalk structure in the droplet prior to the division event occurring.

8.4.5 PIV 5 - Stalk Structure Formation Due To Elongation And Deformation

Figure 8.6 shows the beginning of the stalk formation taking place. The droplet is now elongated further and shows two distinct regions of deformation, rather than the previous 3.

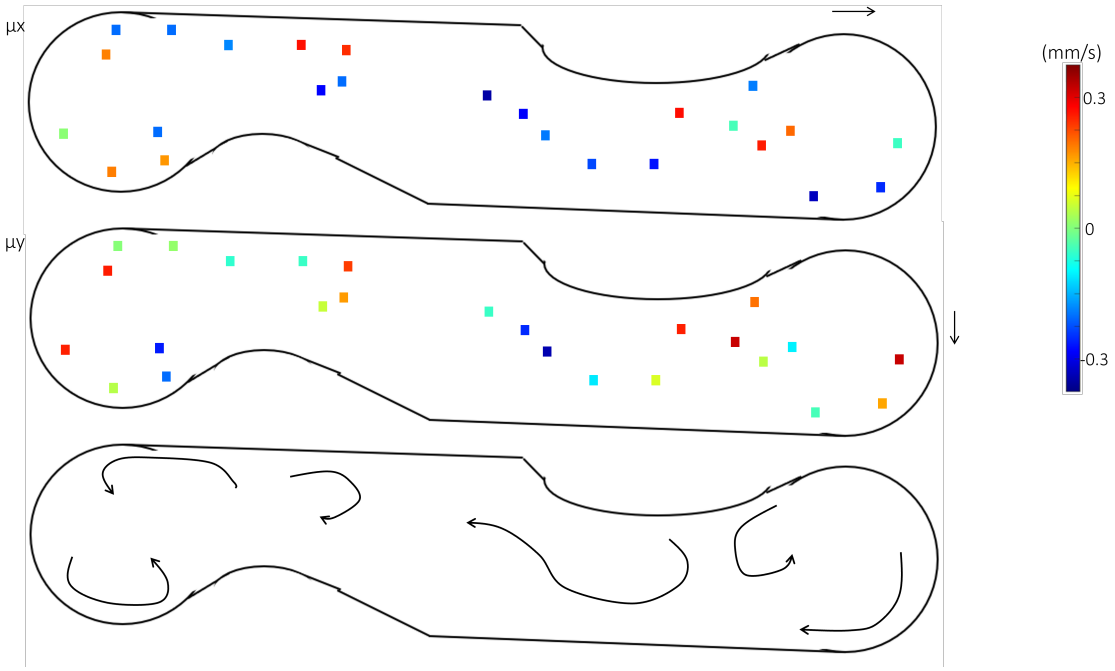

Figure 8.6: PIV analysis as the deformation sites on the lower side of the droplet have merged. Turbulent flows have formed at either end of the droplet, causing competition for resources at the CoM. This will result in a stalk structure forming, which will lead to the division event occurring.

The reduction in deformation at the negative curvature is due to the merging of 2 as the low right-hand site travelled down the droplet to the left and merged with the existing area with substantial negative curvature. This has the effect of increasing the deformation, resulting in a much greater width decrease than was previously visible. The opposing end of the droplet also shows a remarkable increase in the negative curvature, due to the elongation of the droplet. Around the deformation near the top right of the droplet, we observe a vortex flow following the anti-clockwise direction. The pressure generated by this flow will be both increasing the volume in the elongated end of the droplet, which will further increase the bulk flows at the droplet CoM, but also acts as a mechanism for generating a greater deformation on the droplet width, as the flow will act as a pulling force on the surface tension. This combination forms a push-pull mechanism inside the droplet, where the push force is directed towards elongating the droplet and increasing the internal turbulent flow at the CoM, whilst the pull force acts to decrease the width at the region with negative curvature. The combination of the reduction in width, with the disturbance due to the bulk flows compensating for the conservation of mass, act as agonistic actions with the effect of decreasing the width of the droplet even further. This is the basis of the positive feedback loop within the droplet which acts to overcome the

stabilising hydrodynamic forces seen in previous studies for maintaining droplet shape [305]. The deformation at the lower left end of the droplet has increased in size, causing a further decrease in width at this end of the droplet as a pair of flows in an anti-clockwise vortex arrangement to create a pressure build-up creating a reduction in the width. The turbulent flow at the droplet CoM will also play a crucial role in the deformation at this site, as there will be a smaller volume of the droplet to draw from when a vortex induces a push-pull mechanism. The maintenance of volume at the leftmost edge will be generated by the vortex flow at the end creating a pressure build-up to subside the flow at the centre towards the elongating end, however, it will not be great enough to counteract this motion, and thus the stalk formation will be formed.

8.4.6 PIV 6 - Division Event

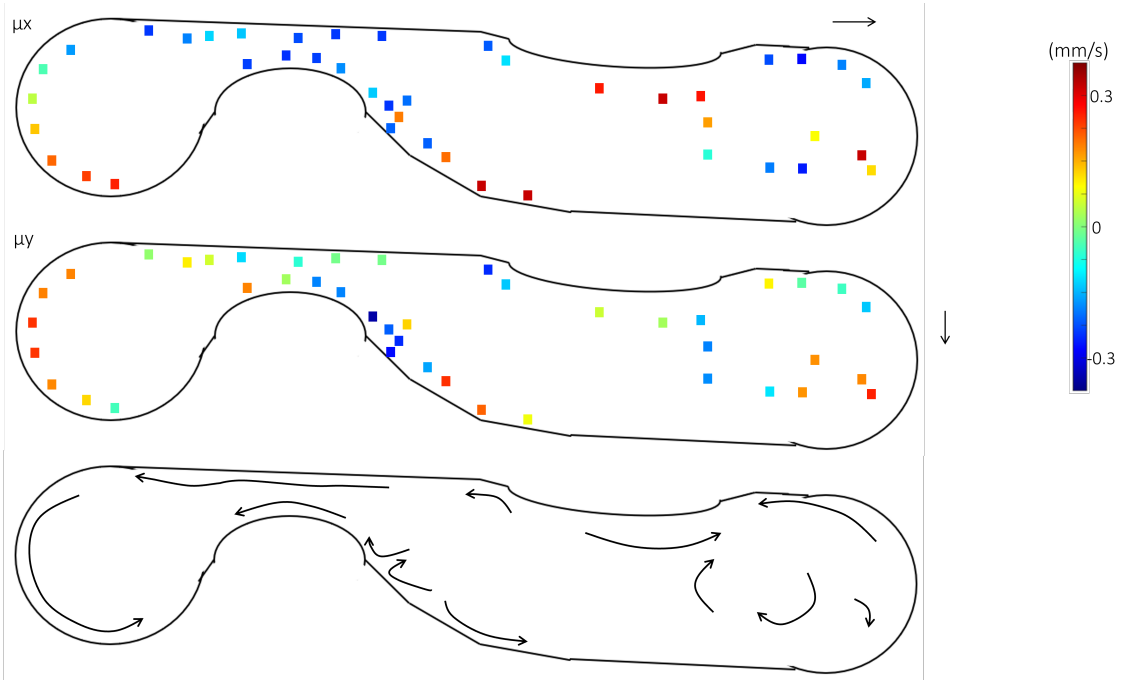

Figure 8.7: PIV analysis of a dividing droplet as the stalk structure has formed. There is no way for the droplet to return to its original shape, as the deformation and elongation has resulted in a stalk structure forming. The smallest energy cost action will be for the droplet to divide into 2 sub-droplets as a mechanism to reduce the surface area.

The final stage prior to the division is represented in figure 8.7 and shows the full formation of the neck, or stalk structure, as the droplet has fully elongated and has such a diminishing width towards the left of the droplet, that the division is inevitable. At this stage in the

division event, it is likely that no internal flows are required for the division to occur since there is such an elongation and the surface tension around the stalk structure may cause the division to occur as a method of reducing the volume to surface area ratio. Once the division occurs the two sub-droplets form spherical shapes due to the capillary effect to minimise the surface area.

8.5 Normalised Cross Correlation Graphs of Separated Droplets

In this section of appendices, we will look at other examples of the time-series data and normalised cross-correlation between a pair of droplets separated by 1cm, 2cm, or 3cm. The data here was extracted during the period after droplet B is introduced, so the data sets shown are droplet A-post and droplet B. The time series data was extracted by producing an average of a region of pixels from the RGB images taken from the recorded video of the droplets. The blue values were extracted from the RGB images and averaged in a 3x3 grid to reduce noise. The pair of time series data sets are plotted together to show the synchrony that occurs between them, along with the normalised cross-correlation function, to show the correlation between the pair of signals.

8.5.1 Normalised Cross-Correlation of 1cm Separation Droplets

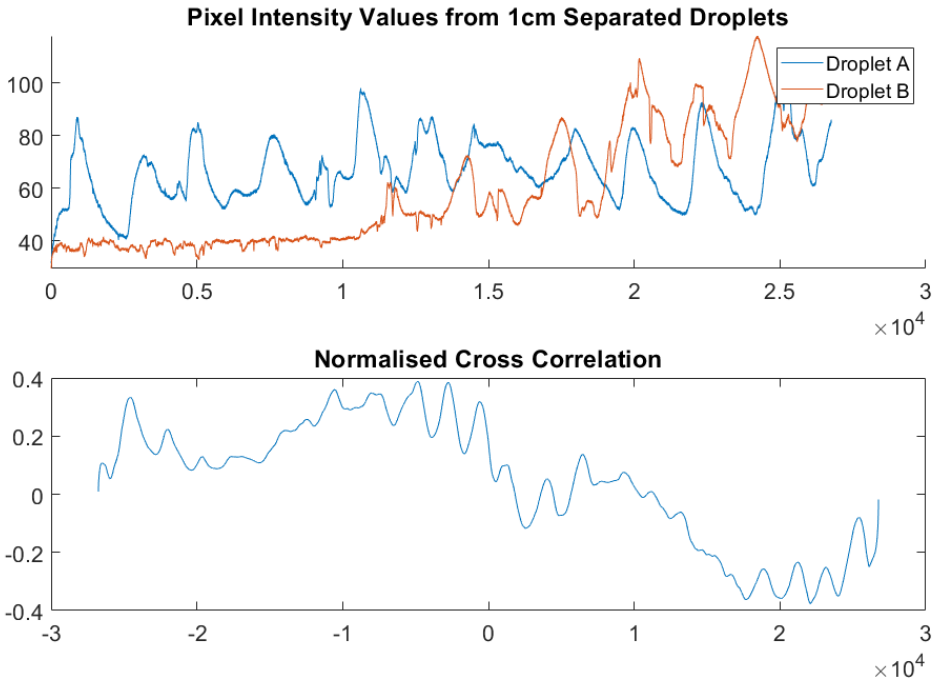

Figure 8.8: Pixel intensity values and the normalised cross-correlation of a pair of droplets separated by 1cm.

Figure 8.8 shows the time series dataset and the graph of the normalised cross-correlation function applied onto Droplet A-post introduction of Droplet B, with Droplet B. The time series data of droplet B shows the initial generation of chemical waves, where initially none

were produced. It is plausible to conclude that droplet A was producing LCs prior to droplet B due to mechanical perturbation from the surfactant, which also affected droplet B, upon its pipetting into the oil phase. An observation to be made regarding the beating frequency of droplet A, is the alteration of the frequency of which the peaks are produced as a result of the interactions with droplet B. The normalised cross-correlation has a very close resemblance of the correlation between a pair of perfect sinusoids, which alludes to the high degree of correlation between the pair of graphs. There is a slight offset visible, which would be due to the absence of chemical wave formation upon pipetting of droplet B.

8.5.2 Normalised Cross-Correlation of 1cm Separation Droplets

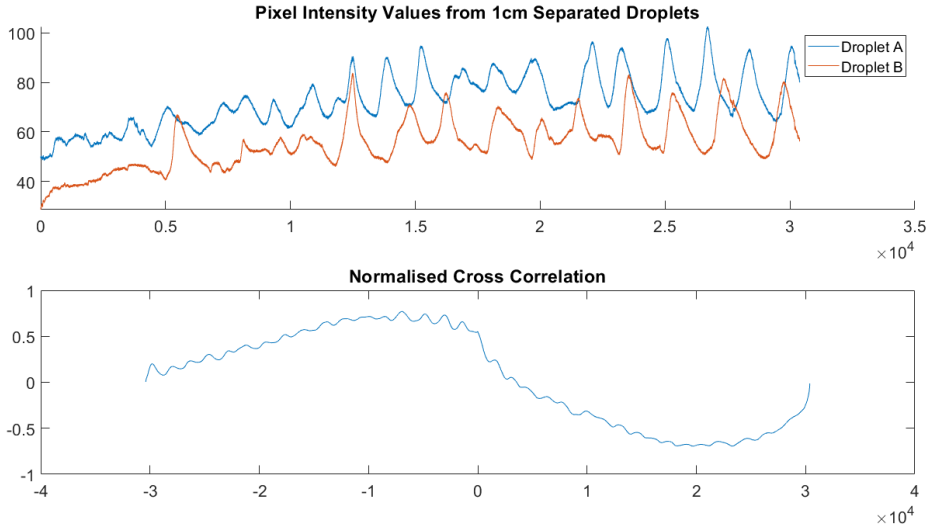

Figure 8.9: Pixel intensity values and the normalised cross-correlation of a pair of droplets separated by 1cm.

Figure 8.9 shows a very strong correlation between the graphs of droplet A, and droplet B. This is reflected in the graph of the normalised cross-correlation, where the peak in correlation happens very closely to τ=0. The correlation graph also appears to be very close to the correlation between 2 perfect sinusoids. It is observed that there is a small period at the beginning of the time series data set representing the pixel intensity values corresponding to droplet B, where no wave formation has begun to take place. Shortly, there are the first wave formations, which very quickly become synchronised with those produced by droplet A. The wave formations in droplet A also change behaviour, where they show a greater magnitude in the peaks, and also seem to become entrained with the peaks in droplet B.

8.5.3 Normalised Cross-Correlation of 1cm Separation Droplets

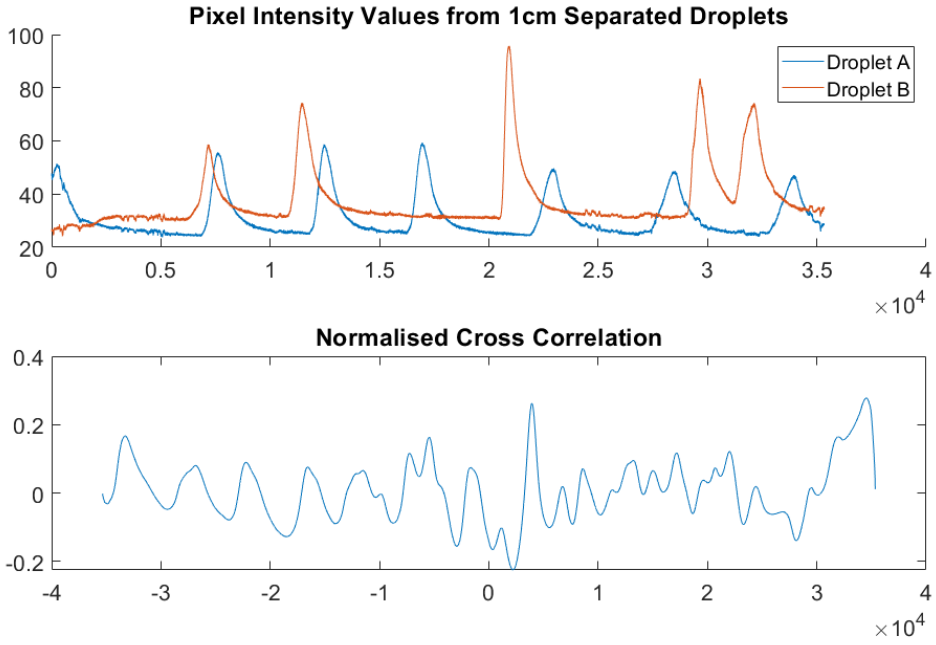

Figure 8.10: Pixel intensity values and the normalised cross-correlation of a pair of droplets separated by 1cm.

Figure 8.10 shows the time-series data set and normalised cross-correlation graph of a pair of droplets separated by 1cm. The pair of droplets did not produce a great number of chemical waves, which, however, did show a fairly large correlation. The correlation however does not resemble that of a pair of perfect sinusoids, but it is important to note that the peaks do align, showing that there has been influence from one droplet to the other, and visa versa.

8.5.4 Normalised Cross-Correlation of 1cm Separation Droplets

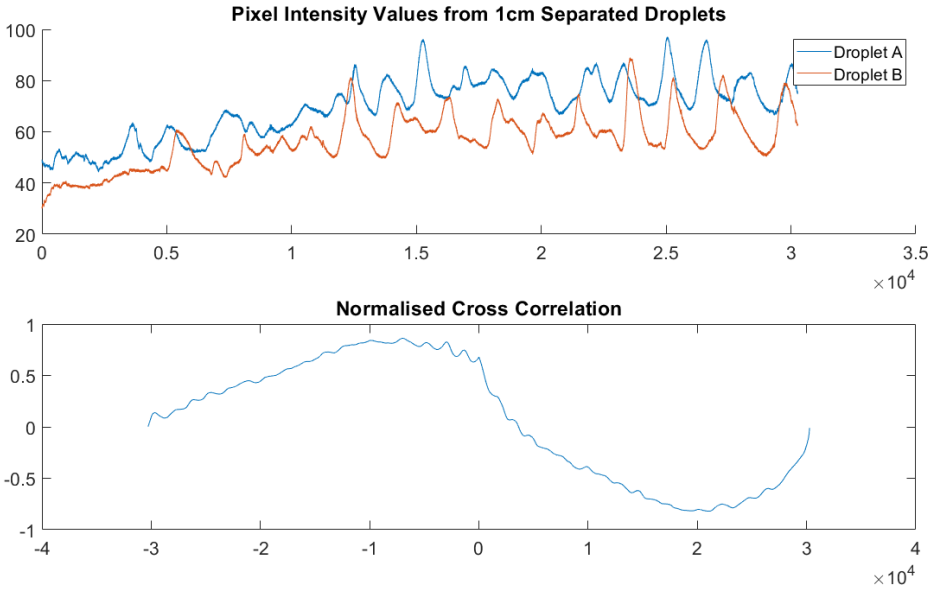

Figure 8.11: Pixel intensity values and the normalised cross-correlation of a pair of droplets separated by 1cm.

Figure 8.11 shows another example of a very strong correlation between droplets separated by a distance of 1cm. The graph of the normalised cross-correlation function shows a very close resemblance of the output from 2 perfect sinusoids. There is also a very large degree of synchrony observed in the time series data, where after a short induction period, the graphs of droplet A, and droplet B, show a very high correlation in their activity. This correlation also seems to strengthen over time, which is the nature of entrainment and information sharing between a pair of synchronous signals.

8.5.5 Normalised Cross-Correlation of 1cm Separation Droplets

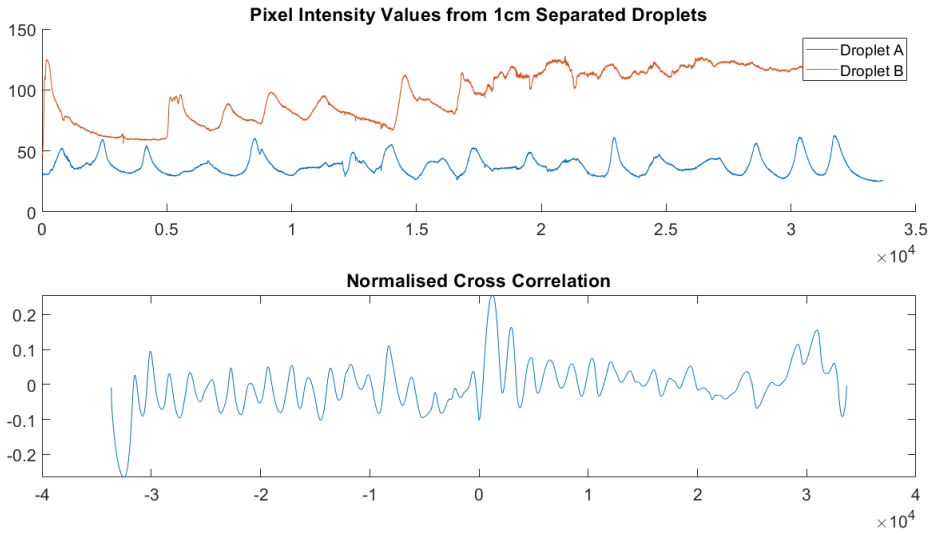

Figure 8.12: Pixel intensity values and the normalised cross-correlation of a pair of droplets separated by 1cm.

Figure 8.12 shows another pair of signals where the correlation graph doesn't demonstrate correlation in the same manner as that of a pair of perfect sinusoids. This can be explained by the presence of the induction period in droplet B, along with the trailing end at the time series, where the BZ reaction seems to have died out. This can be common in experiments, where the BZ lifecycle ends prematurely, and can be explained by thermodynamics and uncontrollable chaotic effects. The section of the time series in which we do observe wave formation does show a correlation between the pair of signals, this unfortunately could not be sustained due to the chemical wave formation in droplet B ending.

8.5.6 Normalised Cross-Correlation of 2cm Separation Droplets

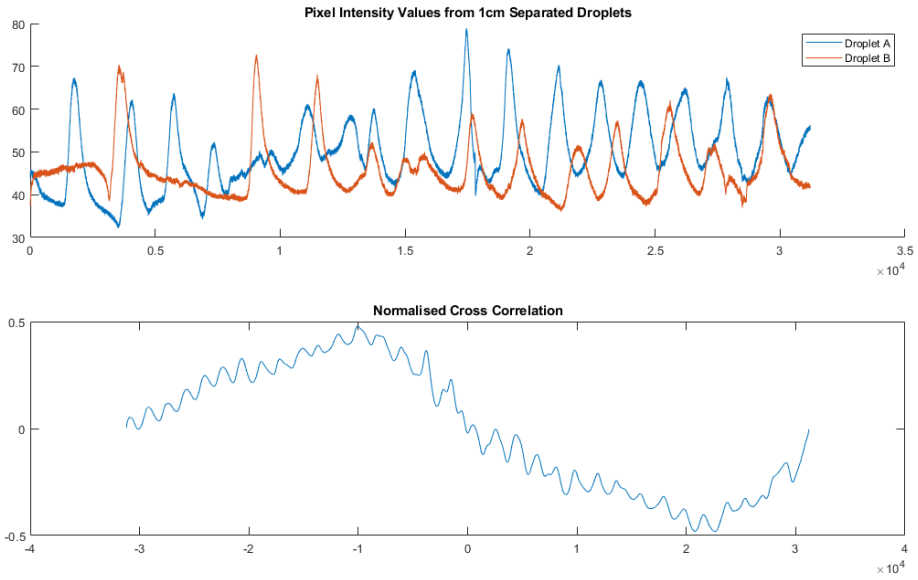

Figure 8.13: Pixel intensity values and the normalised cross-correlation of a pair of droplets separated by 2cm.

Figure 8.13 also shows a very high correlation, as demonstrated in the graph of the plotted normalised cross-correlation function. However, this does show a very large offset from τ=0, which represents a time shift in the correlation. This is supported by viewing the graphs of the time series data sets of the pixel intensity values extracted from the blue channel of the RGB image. The graph clearly shows that there is a correlation between the graphs, with an added time constraint, where a delay is found between the 2 graphs. This can be explained by the added distance between the pair of droplets, as this pair is subjected to a separation of 2cm, rather than 1cm as shown in figures 8.8 - 8.12. The time delay in the synchrony between the pair of droplets would be due to the increase in time that it takes for the longitudinal wave to travel between the droplets in the oil phase, creating a weaker entrainment, and therefore a shift in the correlation graph.

8.5.7 Normalised Cross-Correlation of 2cm Separation Droplets

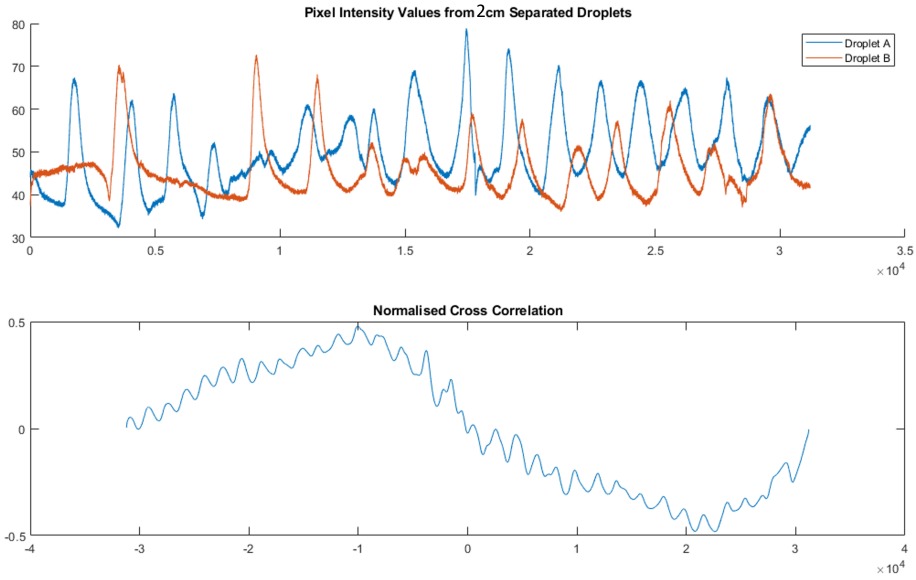

Figure 8.14: Pixel intensity values and the normalised cross-correlation of a pair of droplets separated by 2cm.

Another graph showing how the effect of one droplet on the other can cause the entrainment, even at a separation of 2cm, is shown in figure 8.14, where the initial stage in the interaction between droplet A, and droplet B, is remarked with little synchrony present in the oscillations. However, roughly a third of the way into the recording (around 5 minutes), the periodicity of the pair of signals appears to align, showing a very strong correlation, albeit with some time delay. This is supported in the graph of the normalised cross-correlation function, where there is a peak in correlation, shifted from τ=0.

8.5.8 Normalised Cross-Correlation of 2cm Separation Droplets

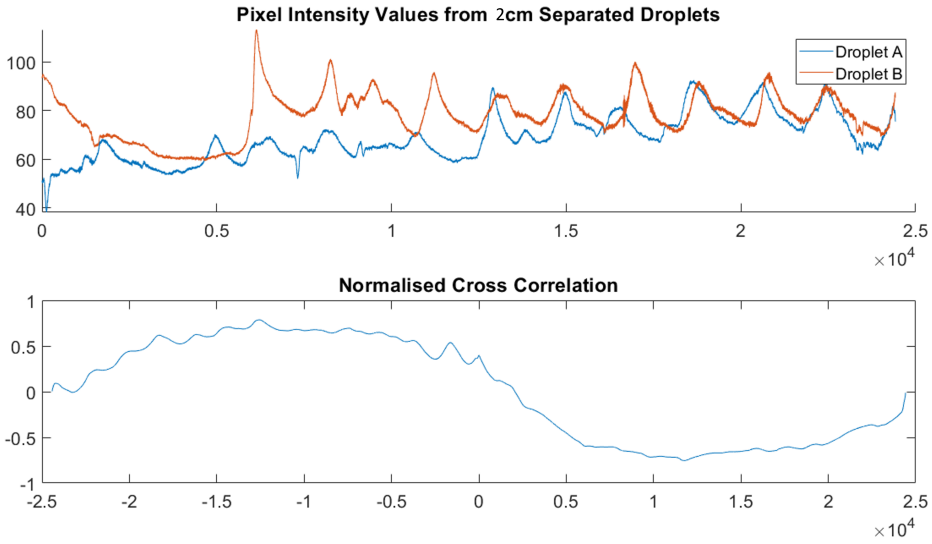

Figure 8.15: Pixel intensity values and the normalised cross-correlation of a pair of droplets separated by 2cm.

In figure 8.15, we can observe another example of the time delay in the appearance of synchrony between the pair of signals. This is again reflected in the timeshift from τ=0 in the plot of the normalised cross-correlation function. This is a great example of how the 2cm separation can produce syn between a pair of droplets, but also for how there is a time delay in such phenomenon occurring due to the spatial separation of the droplets.

8.5.9 Normalised Cross-Correlation of 2cm Separation Droplets

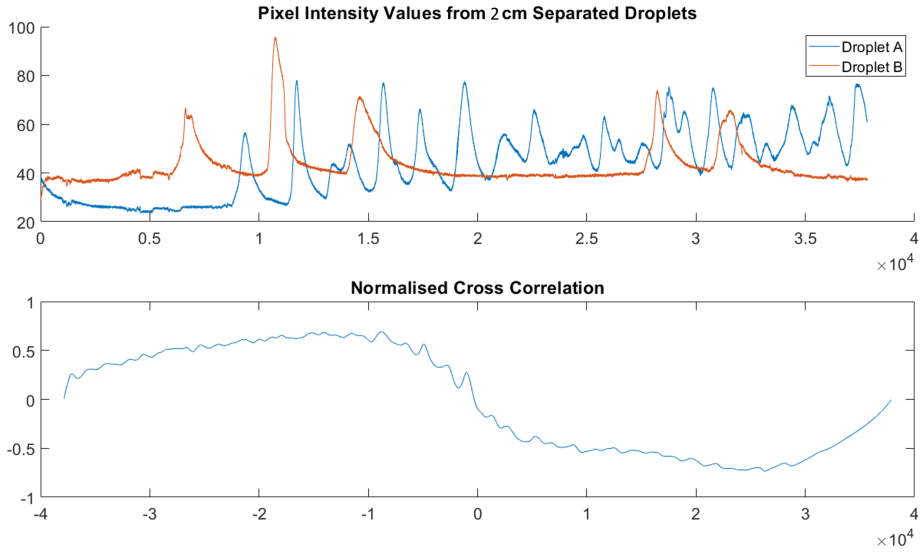

Figure 8.16: Pixel intensity values and the normalised cross-correlation of a pair of droplets separated by 2cm.

In figure

8.5.10 Normalised Cross-Correlation of 2cm Separation Droplets

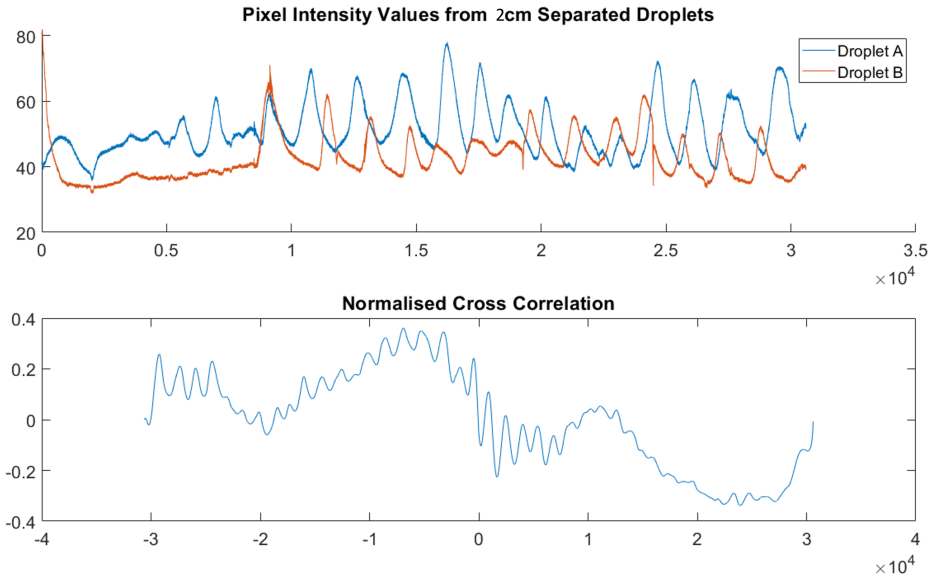

Figure 8.17: Pixel intensity values and the normalised cross-correlation of a pair of droplets separated by 2cm.

Figure 8.17 is another example of how the 2xm separated droplets can become synchronised, although weakly. The pair of droplets show a correlation in their activity, backed up by the peak in the correlation graph with a slight offset from τ=0. The dataset depicting the pixel values extracted from the blue channel of the RGB image shows us that whilst the droplet pairing did start to synchronise, this died out as the droplets appear to fall slightly out of synchrony. This is expected in this experimental condition, as there is a greater distance for the longitudinal wave to travel through, meaning that there is a time delay to the mechanical perturbation each droplet can have on one another. This will cause a weaker entrainment effect to be applied between the droplets, which results in what we see in figure 8.17, where the synchrony dies out.

8.5.11 Normalised Cross-Correlation of 3cm Separation Droplets

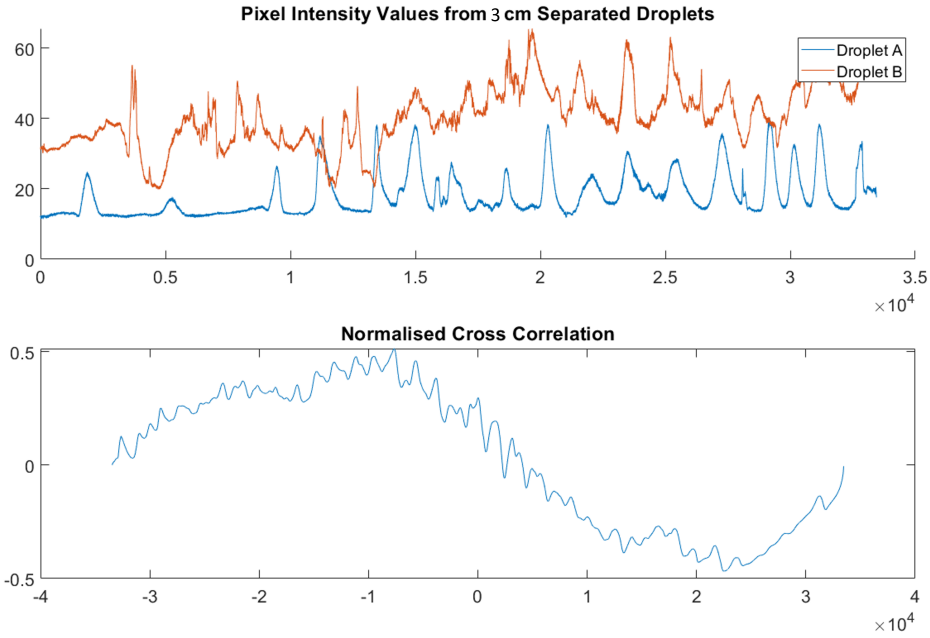

Figure 8.18: Pixel intensity values and the normalised cross-correlation of a pair of droplets separated by 3cm.

Figure 8.18 shows the time series and normalised cross-correlation function of a pair of droplets separated by 3cm. Whilst there is a peak in the normalised cross-correlation function, there is very little synchrony between the graphs of the time series data extracted from the RGB image. This is found to be commonplace for the droplets separated by 3cm, due to the diminished power of the mechanical perturbation applied from one droplet to another through the oil phase.

8.5.12 Normalised Cross-Correlation of 2cm Separation Droplets

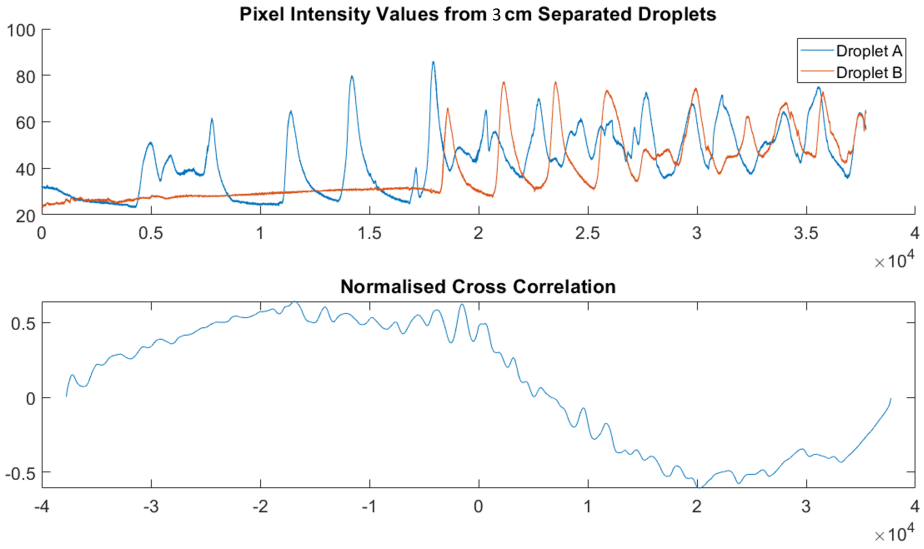

Figure 8.19: Pixel intensity values and the normalised cross-correlation of a pair of droplets separated by 3cm.

Figure 8.19 demonstrates an example of a time-delayed peak in the normalised cross-correlation function. There is a shift from τ=0, where similarities in the time series activity have produced a peak in the correlation graph, but upon inspecting the time series, it is evident that the 2 signals are operating at different frequencies, and merely have the occasional random aligning of peaks in the pixel intensity graphs.

8.5.13 Normalised Cross-Correlation of 3cm Separation Droplets

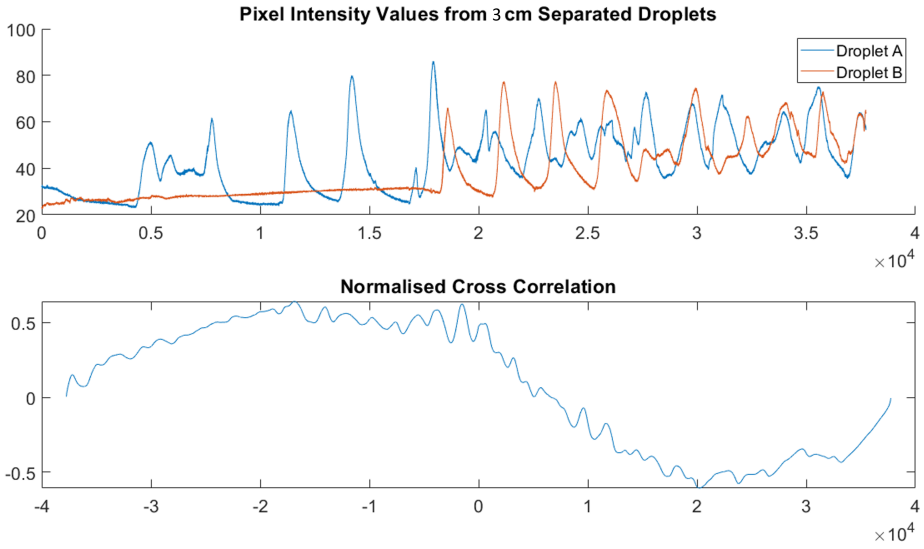

Figure 8.20: Pixel intensity values and the normalised cross-correlation of a pair of droplets separated by 3cm.

Figure 8.20 shows another example of a pair of signals showing very little correlation and no signs of synchrony. Droplet B also shows no wave generation in the first half of the time series, which crucial could be a factor in the limited entrainment observed between the droplets. However, in figures 8.8 - 8.17, the droplets are close enough to act as a source of mechanical perturbation on one another, which would explain why droplet B in these cases was active much sooner.

8.5.14 Normalised Cross-Correlation of 3cm Separation Droplets

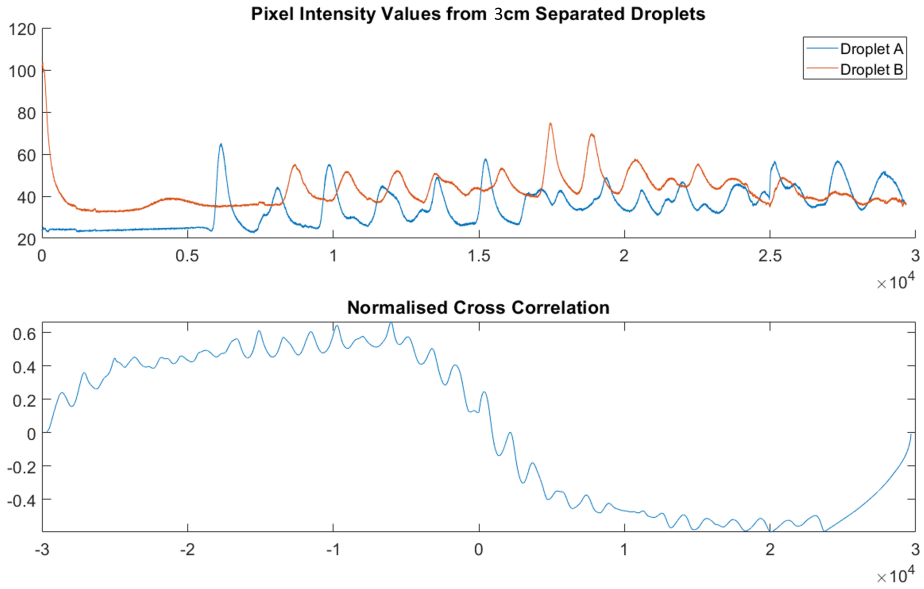

Figure 8.21: Pixel intensity values and the normalised cross-correlation of a pair of droplets separated by 3cm.

Figure 8.21 shows another example of a delay in wave production in droplet B, but also with droplet A. This is also reflected in the remainder of the time series graphs, as there is very little synchrony and correlation between the droplets. This is expected in the 3cm separated droplets, as the entrainment effect is found to be much lesser in magnitude, which would not lead to a synchronisation in the droplet pair. The correlation graph does show a time-delayed peak in correlation, due to some similarities in the signalling, but this does not imply sync.

8.5.15 Normalised Cross-Correlation of 3cm Separation Droplets

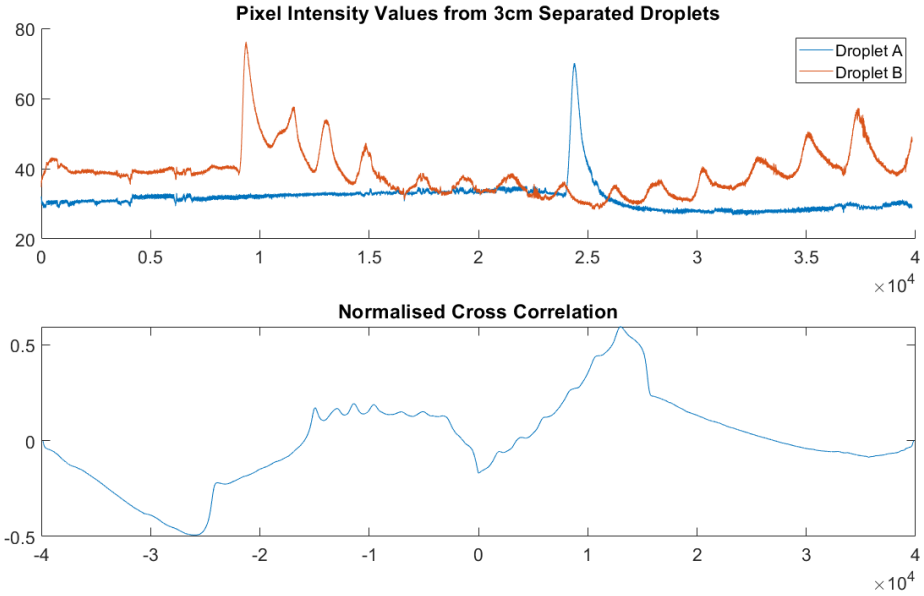

Figure 8.22: Pixel intensity values and the normalised cross-correlation of a pair of droplets separated by 3cm.

Figure 8.22 shows a pair of droplets with minimal activity. This is reflected in the cross-correlation graph, which shows no synchrony around the τ=0 region. The limited production of waves in the droplets would be an effect of minimal mechanical perturbation, due to the 3cm separation between the droplets.

8.5.16 Normalised Cross-Correlation of 3cm Separation Droplets

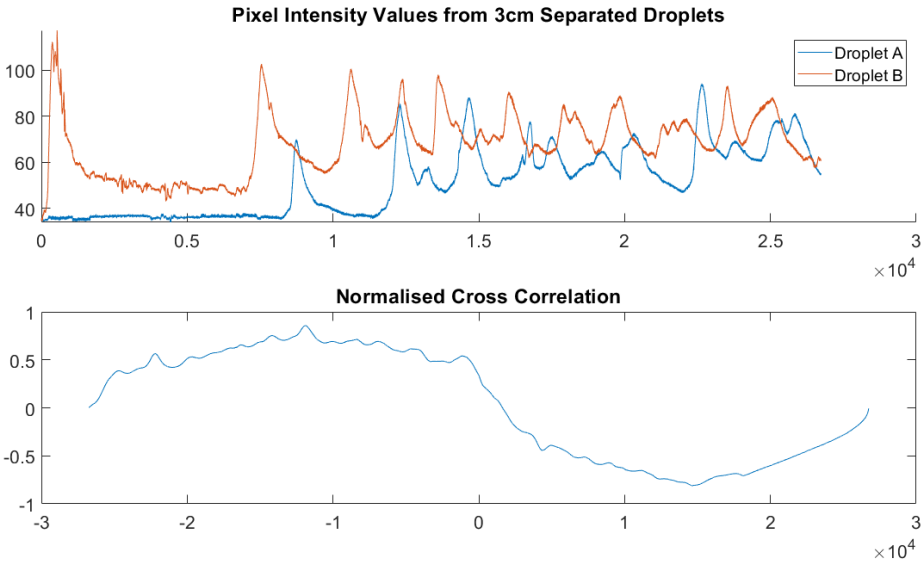

Figure 8.23: Pixel intensity values and the normalised cross-correlation of a pair of droplets separated by 3cm.

Figure 8.23 shows an example of when the activity in droplet A ceases prior to the introduction of droplet B, which in this case, immediately produced a wave formation. After some time, both droplets begin to produce chemical waves, at different frequencies. This is reflected in the cross-correlation graph, where the peak occurs at an offset from τ=0, whilst the time series shows no real sync, only some similarities in the wave formation.

8.5.17 Normalised Cross-Correlation of Perfect Sinusoids

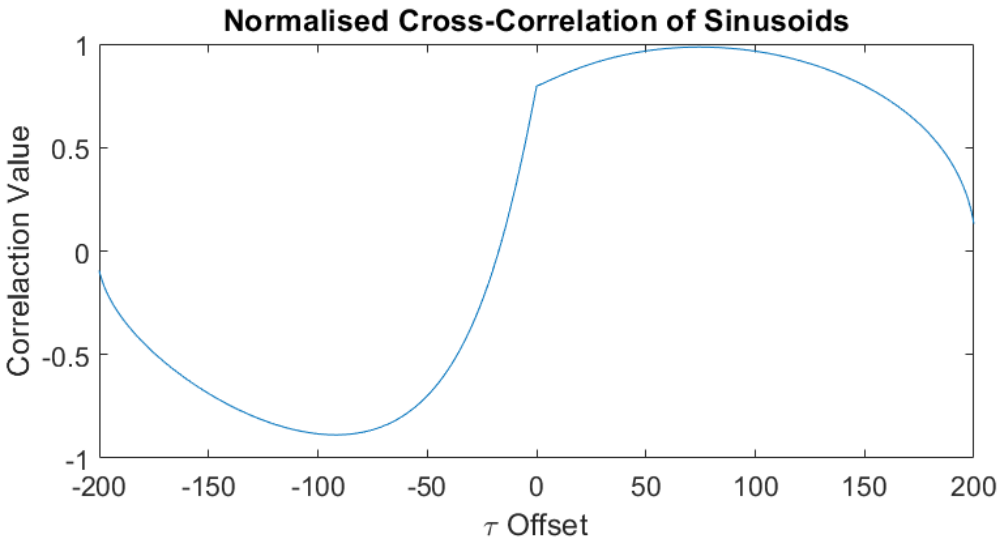

Figure 8.24: Normalised Cross-Correlation graph of perfect sinusoids. This graph is used to verify the correlation behaviour of the oscillating droplets.

Figure 8.24 shows the output of performing the normalised cross-correlation function on a pair of perfect sinusoids. The output shape is used to verify the correlation quality of the correlation values extracted from a pair of oscillating droplets.

8.6 Time Windowed Normalised Cross-Correlation Of Separated Droplets

The correlation of signals generated by droplets can change over time. To overcome this, we will observe the correlation values where there is no offset from τ=0, in a time segment extracted from the original series. This window will then be shifted in time, and the correlation value at τ=0 from there will be extracted. These values will be then plotted, to show how the correlation changes through time.

8.6.1 Normalised Cross-Correlation of 1cm Separation Droplets

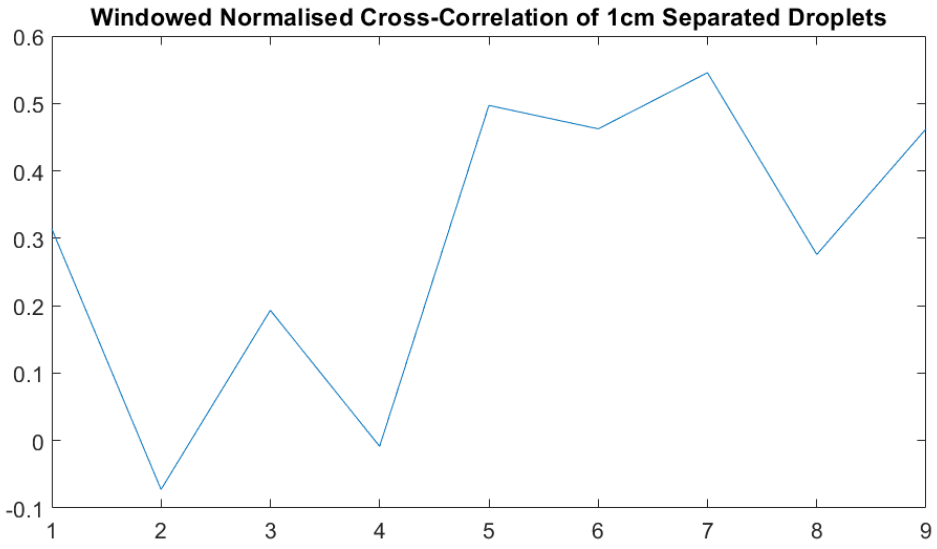

Figure 8.25: Plot of the change in the value at τ=0 through time. Values extracted from a shifting time windowed normalised cross-correlation function applied to the droplets post-introduction of droplet B.

Figure 8.25 shows the correlation increasing between the droplets through time. This is remarked by the increase in the output of the normalised cross-correlation function at τ=0 increasing as the time series increases.

8.6.2 Normalised Cross-Correlation of 1cm Separation Droplets

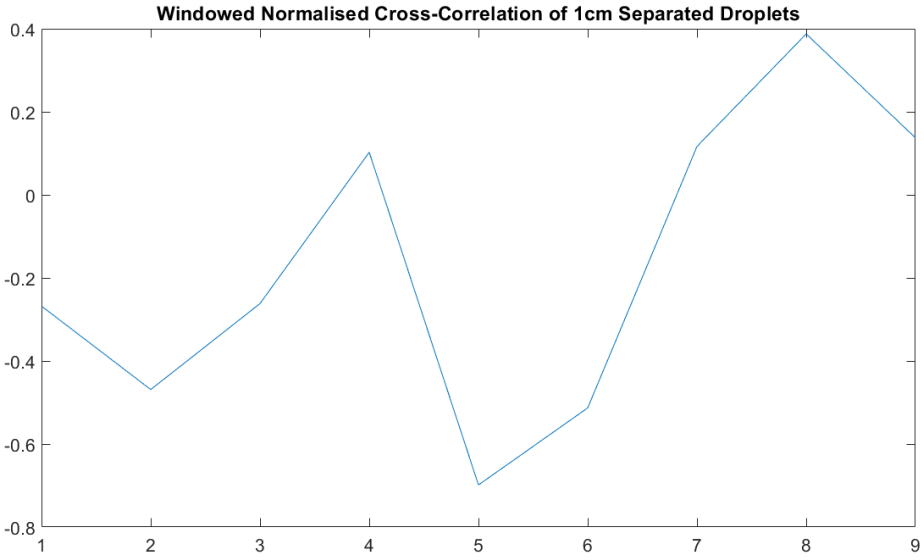

Figure 8.26: Plot of the change in the value at τ=0 through time. Values extracted from a shifting time windowed normalised cross-correlation function applied to the droplets post-introduction of droplet B.

Figure 8.26 shows the increase in synchrony through time observed between 2 droplets separated by 1cm. The signalling starts off with no sign of synchronous behaviour, which starts to increase with time. This is followed by a small swing to anti-sync, which can happen as the synchrony builds with entrainment. The droplets may initially appear to be in anti-phase with one another, then change to synchrony as the entrainment increases, as shown here.

8.6.3 Normalised Cross-Correlation of 1cm Separation Droplets

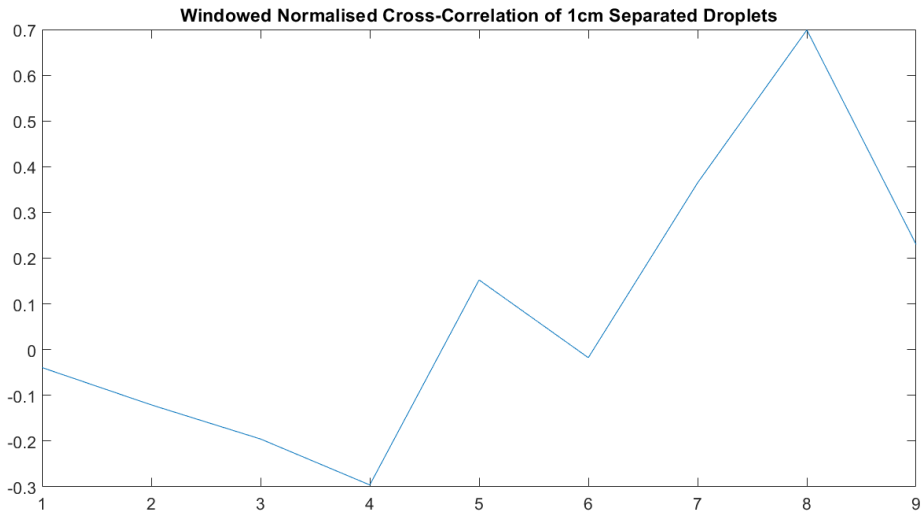

Figure 8.27: Plot of the change in the value at τ=0 through time. Values extracted from a shifting time windowed normalised cross-correlation function applied to the droplets post-introduction of droplet B.

Figure 8.27 shows another example of the signals between the droplets showing a small anti-sync swing before becoming in phase. This example also shows no synchrony at the beginning of the time series data set being windowed, showing how the synchronous behaviour forms over time, rather than simply randomly occurring.

8.6.4 Normalised Cross-Correlation of 1cm Separation Droplets

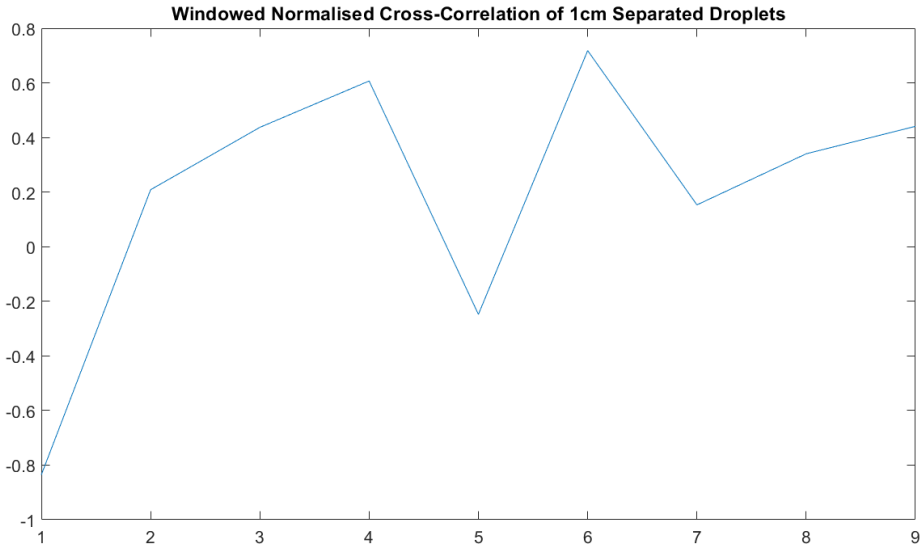

Figure 8.28: Plot of the change in the value at τ=0 through time. Values extracted from a shifting time windowed normalised cross-correlation function applied to the droplets post-introduction of droplet B.

Figure 8.28 shows a pair of droplets separated by 1cm which has a random anti-synchronous behaviour upon the introduction of droplet B. This could occur due to random signalling behaviour spontaneously showing similar activity. This is corrected for, however, as the droplets become entrained. The synchronous behaviour is displayed at the middle and end of the time windowed normalised cross-correlation function where the syn is found to be very strong between the 2 signals.

8.6.5 Normalised Cross-Correlation of 2cm Separation Droplets

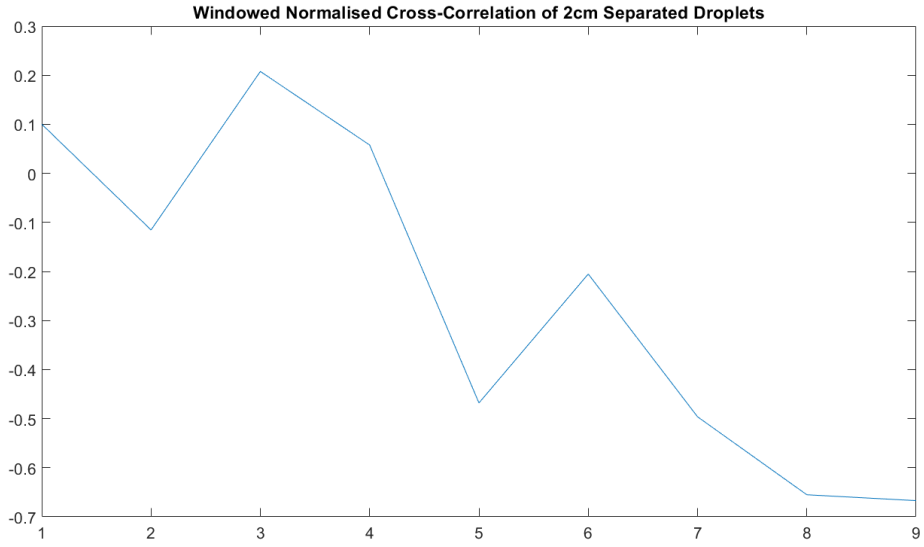

Figure 8.29: Plot of the change in the value at τ=0 through time. Values extracted from a shifting time windowed normalised cross-correlation function applied to the droplets post-introduction of droplet B.

Figure 8.29 shows the anti-synchronous behaviour of a pair of droplets separated by 2cm in an oil phase. The entrainment effect is still valid and robust between these droplets, however, it does not produce perfect synchrony, as shown by the formation of anti-sync in the graph of the value at τ=0 using a time-shifted window on the time series data sets. The strong anti-sync behaviour can be attributed to the entrainment effect between the droplets separated by 2cm not being strong enough to produce true synchrony, but strong enough that the anti-sync behaviour emerges.

8.6.6 Normalised Cross-Correlation of 2cm Separation Droplets

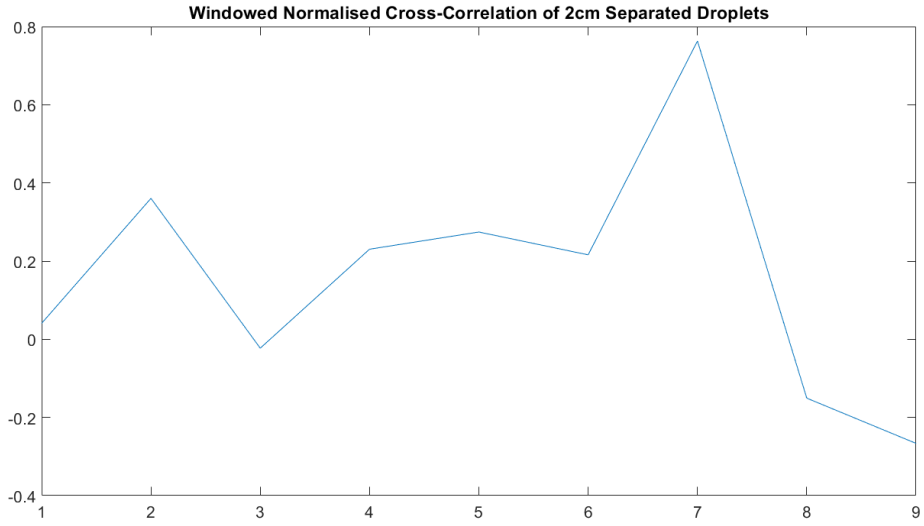

Figure 8.30: Plot of the change in the value at τ=0 through time. Values extracted from a shifting time windowed normalised cross-correlation function applied to the droplets post-introduction of droplet B.

Figure 8.30 presents the occurrence of minimal synchronisation between the pair of droplets. The droplets here are separated by 2cm and were found to show no signs of synchrony, or anti-synchrony until roughly two-thirds the way through the analysis, where there is a spike in synchrony, followed by a spike in anti-synchrony. This behaviour could be attributed to the emergence of anti-sync through time, exhibiting a small similarity at first great enough to register as a spike in synchrony behaviour, before devolving into an anti-sync regime. But it may also be a random chance responsible for this output in the windowed normalised cross-correlation function.

8.6.7 Normalised Cross-Correlation of 2cm Separation Droplets

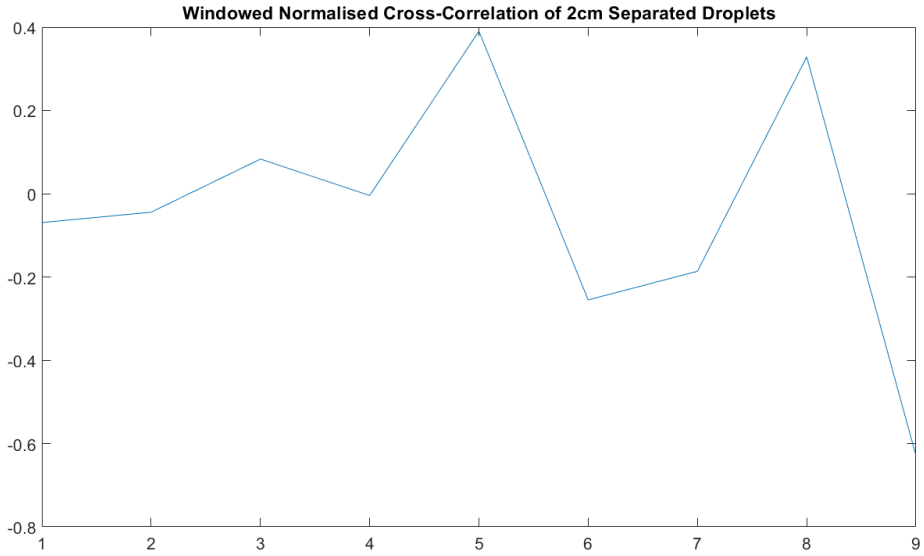

Figure 8.31: Plot of the change in the value at τ=0 through time. Values extracted from a shifting time windowed normalised cross-correlation function applied to the droplets post-introduction of droplet B.

Figure 8.31 presents an example of how slow the entrainment process is in the 2cm separated droplets. Here, the droplets only start showing signs of synchrony around midway through the analysis, and it is not until the end that the larger peak in the anti-sync is found.

8.6.8 Normalised Cross-Correlation of 2cm Separation Droplets

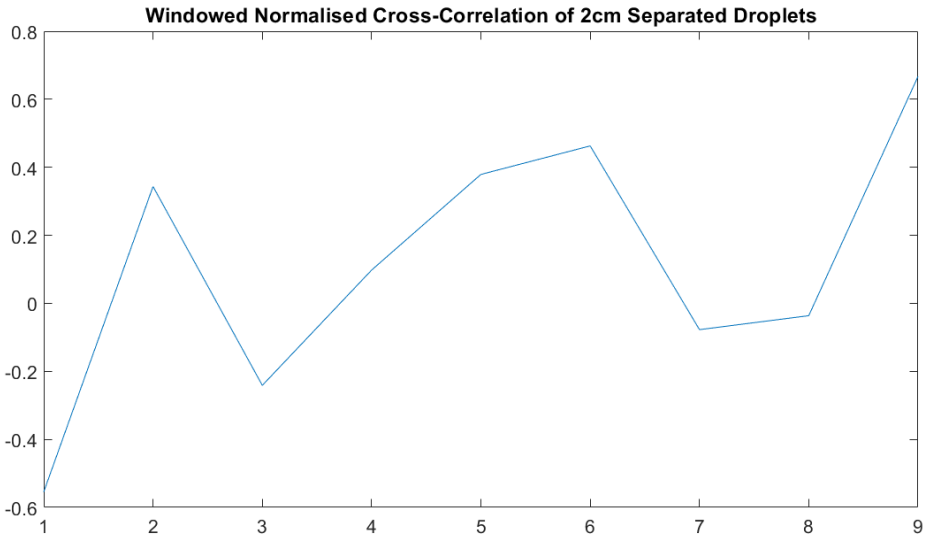

Figure 8.32: Plot of the change in the value at τ=0 through time. Values extracted from a shifting time windowed normalised cross-correlation function applied to the droplets post-introduction of droplet B.

Figure 8.32 shows a deviation from no sync at the very beginning which is very likely due to random signalling appearing as though anti-sync has developed between the droplets. When we observe the rest of the analysis, we find that there is a gradual build-up of synchrony between the droplets, occurring over a longer time period than shown in the 1cm separated droplets.

8.6.9 Normalised Cross-Correlation of 2cm Separation Droplets

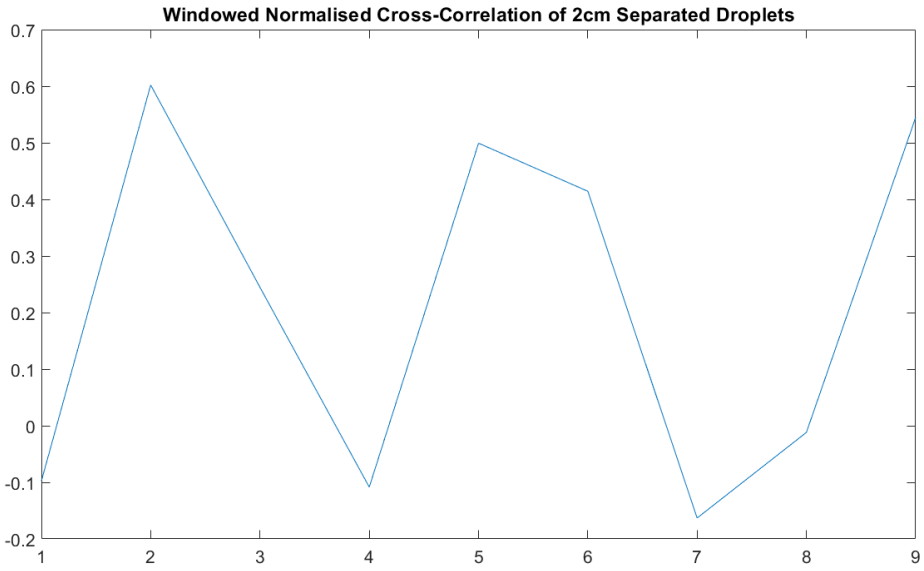

Figure 8.33: Plot of the change in the value at τ=0 through time. Values extracted from a shifting time windowed normalised cross-correlation function applied to the droplets post-introduction of droplet B.

Figure 8.33 shows an example of a pair of droplets separated by 2cm periodically dropping in and out of synchrony. This can be attributed to one droplet following the active role more frequently than the other. When this droplet would normally take the role of the passive droplet, with the other acting as active, there is no feedback from the paired droplet, meaning the synchrony becomes lost, and then the original droplet will start to produce more waveforms that act as perturbation onto the second droplet, bringing the pair back into sync, which is displayed in the plot as a high synchrony value found at τ=0. This type of behaviour can be produced by the hydrodynamic wave between the droplets not travelling perpendicular to the imaginary connecting line between the droplets, meaning a weaker mechanical perturbation is applied to the droplets.

8.6.10 Normalised Cross-Correlation of 3cm Separation Droplets

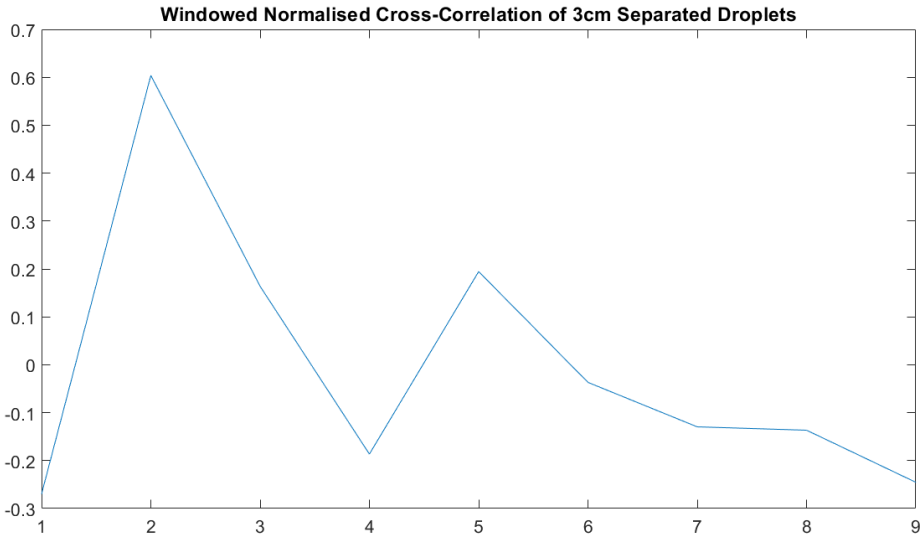

Figure 8.34: Plot of the change in the value at τ=0 through time. Values extracted from a shifting time windowed normalised cross-correlation function applied to the droplets post-introduction of droplet B.

Figure 8.34 shows a random spike of correlation early on, but no long-lasting synchrony is observed due to the 3cm separation not allowing the droplets to reach entrainment.

8.6.11 Normalised Cross-Correlation of 3cm Separation Droplets

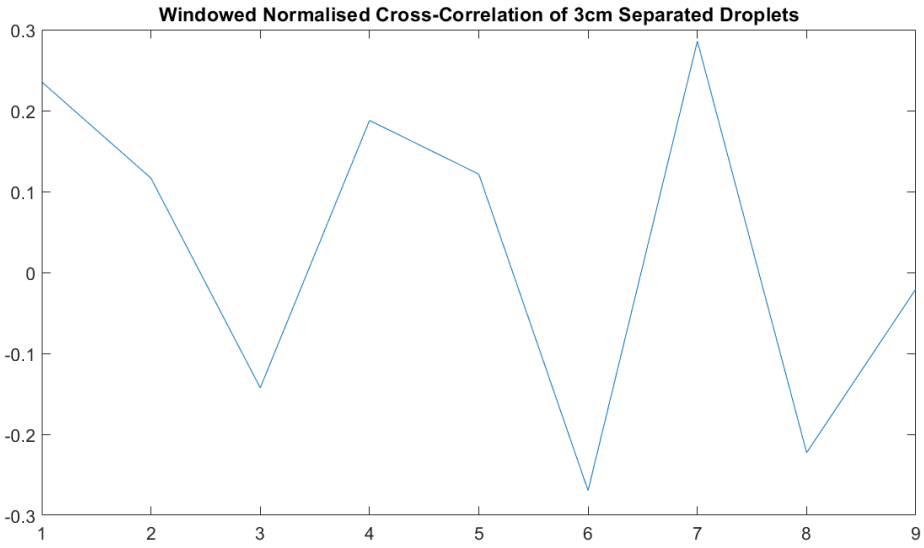

Figure 8.35: Plot of the change in the value at τ=0 through time. Values extracted from a shifting time windowed normalised cross-correlation function applied to the droplets post-introduction of droplet B.

Figure 8.35 shows a very similar shape graph to that of fig.8.33. However, a key difference is the magnitude of the correlation values. The 2 cm separated droplets in fig.8.33 show much greater sync when the spiking occurs. The relaxation also shows the neutral position around the origin, as opposed to dropping towards anti-sync in this example. This leads us to posit that this is purely random behaviour, rather than the droplets cycling between synchrony, and anti-synchrony.

8.6.12 Normalised Cross-Correlation of 3cm Separation Droplets

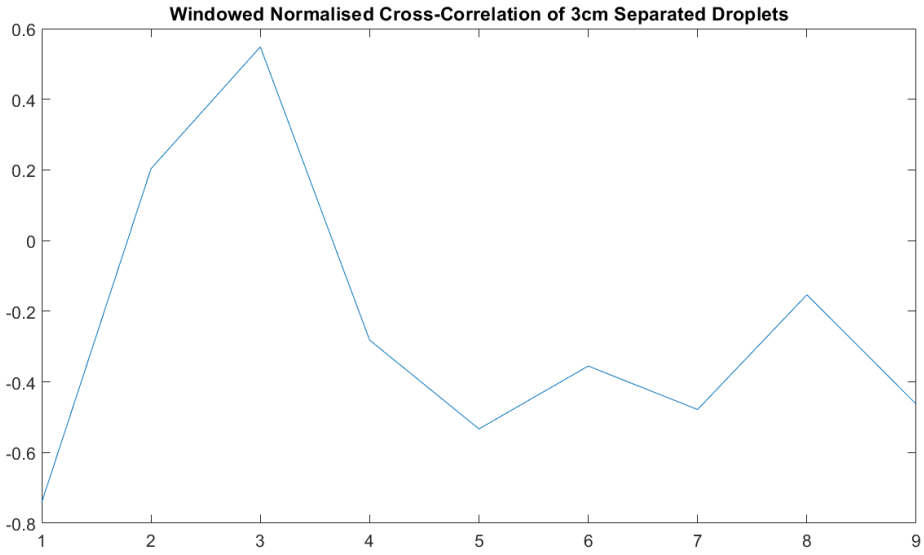

Figure 8.36: Plot of the change in the value at τ=0 through time. Values extracted from a shifting time windowed normalised cross-correlation function applied to the droplets post-introduction of droplet B.

Figure 8.36 shows another example of random behaviour appearing to produce synchrony when in reality we simply observe similarities in the waveforms produced, then no synchronous behaviour after this settles down. This is confirmed when the period of high sync values ends, there is no tendency for the behaviour to produce either sync nor anti-sync. This is common for droplets separated by 3cm, as there is too great of a distance between the oscillating droplets for the hydrodynamic flow to pass through, therefore, the entrainment power is inhibited and no synchrony will form between the pair of BZ droplets.

8.7 FHN model

8.7.1 FHN model

The experimentation with the FHN model was carried out using the below MATLAB file. Many iterations were experimented on, however, this version was used as the precursor to the model which showed entrainment between 2 signals.

```
Varray = zeros(400,1, 'double');
Warray = zeros(400,1, 'double');

%Excitation:

a = 0.8;
% b = 0.8;
c = 0.8;
dt = 0.001;
v=double(0.869601930608358-1.2);
w=double(-0.212002413260425);


%Relaxation:
%a = 0.8; b = 0.9; c = 0.8;
%dt = 0.00005;
%v=-0.075264;
%w=-0.240006;

count = 1;

for n = 1:120000


```

```
26    tempv = v-((v^3)/3)-w;
27    tempw = a*(v+b-(c*w));
28  % tempw = v + a -b*w;
29
30    v = v + 0.01*tempv;
31    w = w + 0.01*tempw;
32
33    if n==60000
34         %disp('n at 60000');
35        tempv = v+3.0;
36        tempw=w-0.2;
37
38        v = tempv;
39        w = tempw;
40
41    end
42
43  %   if mod(n,100)==0
44  %
45  %       Varray(count) = v;
46  %       Warray(count) = w;
47  %
48  %       count = count +1;
49  %
50  %   end
51        Varray(count) = v;
52        Warray(count) = w;
53
54        count = count +1;
55
```

```
56 end
57
58  figure, plot(Varray);
59  Title = ['a = ',num2str(a), ' b = ', num2str(b)];
60  title(Title);
```

8.7.2 Modified FHN to include Kuramoto Oscillator

The FHN model was modified to include the Kuramoto oscillator. The addition of the Kuramoto oscillator allows a pair of signals generated by the FHN model to become entrained. Different starting conditions will allow for the development of different behaviours, from synchrony, anti-synchrony, and chaotic out-of-phase behaviour.

```
a = 0.13;
b = 0.013;
c1 = 0.26;
c2 = 0.1;

K = 0.01;

u1 = 1;
u2 = 1;
v1 = 1;
v2 = 1;

tempu1 = 1;
tempu2 = 1;
tempv1 = 1;
tempv2 = 1;

D = 0.01;

for i = 1:2500

    dif = v2-v1;
    tempu1 = (c1*u1)*(u1-a)*(1-u1)-(c2*u1*v1)+(K*sin(dif))+D;
    u1 = u1 + tempu1;
    U1(i) = u1;
```

```
26
27      tempv1 = b*(u1-v1);
28      v1 = v1 + tempv1;
29      V1(i) = v1;
30
31      dif = v1-v2;
32      tempu2 = (c1*u2)*(u2-a)*(1-u2)-(c2*u2*v2)+(K*sin(dif));
33      u2 = u2 + tempu2;
34      U2(i) = u2;
35
36      tempv2 = b*(u2-v2);
37      v2 = v2 + tempv2;
38      V2(i) = v2;
39
40
41  %      if i == 1600
42  %
43  %          u1 = u1-0.5;
44  %          u2 = u2+2;
45  %
46  %      end
47
48  end
49
50   figure, hold on; plot(U1),plot(U2);
```

8.8 Brominated-SDS

Here the pair of BZ droplets are suspended freely in an oil phase over-saturated with surfactant. The image was taken during a pilot study, hence, no millifluidic device to anchor the droplets. The presence of a much greater surfactant concentration led to the leaching of bromine from the droplet, forming brominated-SDS within the oil phase. The visual formation of the brominated SDS appears to act as a halo surrounding the droplet, so will be referred to as such from here on. The droplets were subject to extreme deformation over the course of the BZ life cycle as the pair of droplets oscillated. The lower droplet is shown to be much more deformed than the upper droplet. However, the upper droplet began to deform as the pair of halos converge. This observation produced the idea of the cycling between active-inactive states, with the flux in the halo giving rise to the thought that the hydrodynamic flow between the pair of droplets is responsible for the entrainment.

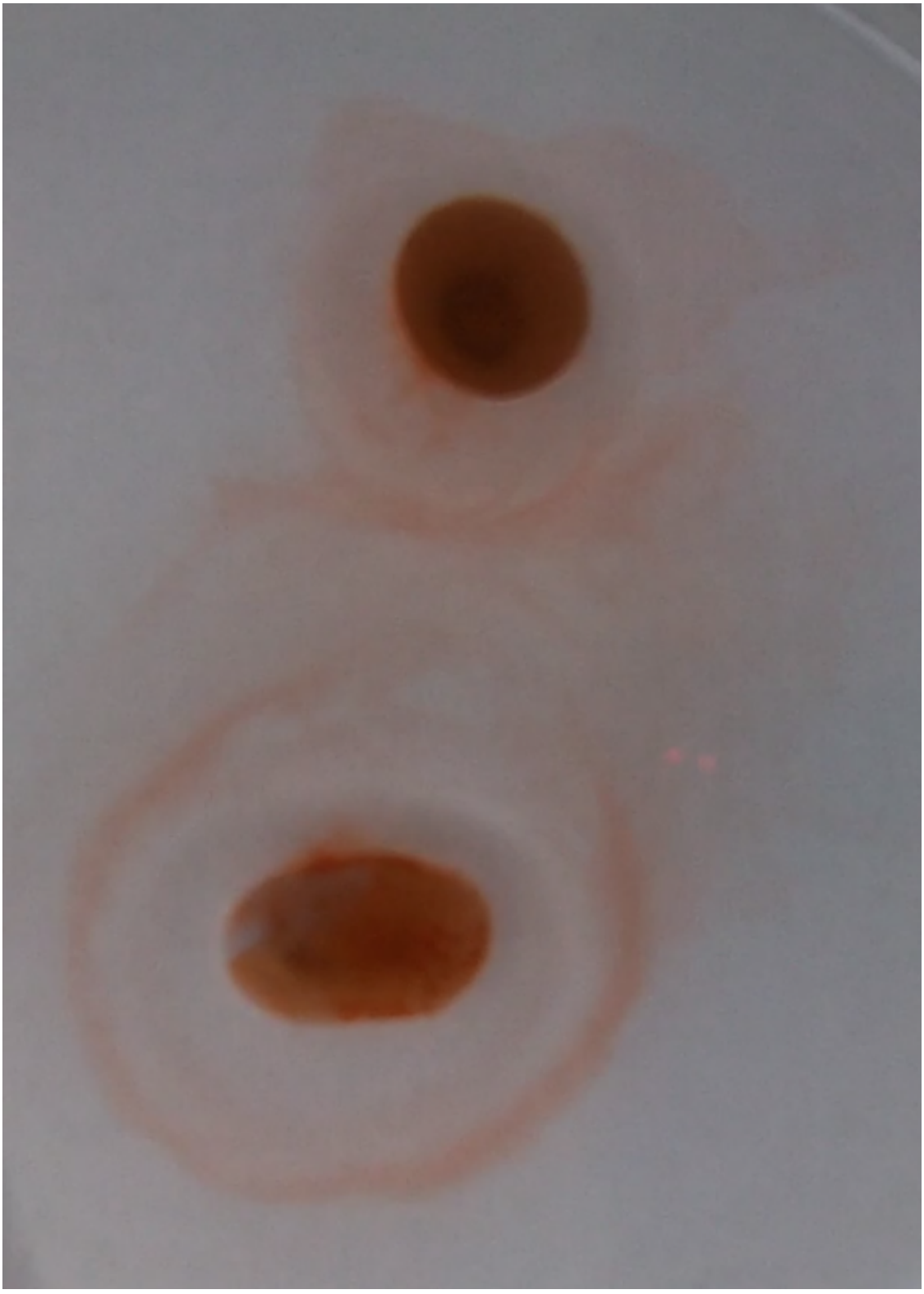

Figure 8.37: Brominated-SDS formation as a result of increased surfactant concentration leaching excitatory chemical species from the aqueous BZ droplet

References

[1] Jennifer H Fewell. "Social Biomimicry: what do ants and bees tell us about organization in the natural world?" In: *Journal of Bioeconomics* 17.3 (2015), pp. 207–216.

[2] Torben Anker Lenau and Thomas Hesselberg. "Biomimetic self-organization and self-healing". In: *Engineered Biomimicry*. Elsevier, 2013, pp. 337–362.

[3] Tzong-Zeng Wu, Yen-Ren Lo, and Err-Cheng Chan. "Exploring the recognized bio-mimicry materials for gas sensing". In: *Biosensors and Bioelectronics* 16.9-12 (2001), pp. 945–953.

[4] Woo-Dong Jang et al. "Bioinspired application of dendrimers: from bio-mimicry to biomedical applications". In: *Progress in Polymer Science* 34.1 (2009), pp. 1–23.

[5] Elena Lurie-Luke. "Product and technology innovation: What can biomimicry inspire?" In: *Biotechnology advances* 32.8 (2014), pp. 1494–1505.

[6] Mudit Tyagi et al. "Endoscopic visualization-assisted corneal bee sting removal". In: *Indian Journal of Ophthalmology* 69.2 (2021), p. 423.

[7] J Austin Lee, Eunice Singletary, and Nathan Charlton. "Methods of honey bee stinger removal: a systematic review of the literature". In: *Cureus* 12.5 (2020).

[8] P Kirk Visscher, Richard S Vetter, and Scott Camazine. "Removing bee stings". In: *The Lancet* 348.9023 (1996), pp. 301–302.

[9] T Rasheed et al. "Biomimetic nanostructures/cues as drug delivery systems: a review". In: *Materials Today Chemistry* 13 (2019), pp. 147–157.

[10] Valeria Rahamim and Aharon Azagury. "Bioengineered biomimetic and bioinspired noninvasive drug delivery systems". In: *Advanced Functional Materials* 31.44 (2021), p. 2102033.

[11] Zdenek Dvorak et al. "Weak microbial metabolites: a treasure trove for using biomimicry to discover and optimize drugs". In: *Molecular Pharmacology* 98.4 (2020), pp. 343–349.

[12] Davide Marin and Silvia Marchesan. "Self-assembled peptide nanostructures for ECM biomimicry". In: *Nanomaterials* 12.13 (2022), p. 2147.

[13] Ayomi S Perera and Marc-Olivier Coppens. "Re-designing materials for biomedical applications: from biomimicry to nature-inspired chemical engineering". In: *Philosophical Transactions of the Royal Society A* 377.2138 (2019), p. 20180268.

[14] Richard Taylor. *Reflecting the impossible*. 2009.

[15] Shane Kyi Hla Win et al. "An agile samara-inspired single-actuator aerial robot capable of autorotation and diving". In: *IEEE Transactions on Robotics* (2021).

[16] Yufeng Chen et al. "A biologically inspired, flapping-wing, hybrid aerial-aquatic microrobot". In: *Science robotics* 2.11 (2017), eaao5619.

[17] Alan A Berryman. "The orgins and evolution of predator-prey theory". In: *Ecology* 73.5 (1992), pp. 1530–1535.

[18] Russell D Fernald. "Evolution of eyes". In: *Current opinion in neurobiology* 10.4 (2000), pp. 444–450.

[19] Detlev Arendt. "Evolution of eyes and photoreceptor cell types." In: *International Journal of Developmental Biology* 47.7-8 (2003), pp. 563–571.

[20] Hannah M Ter Hofstede and John M Ratcliffe. "Evolutionary escalation: the bat–moth arms race". In: *Journal of Experimental Biology* 219.11 (2016), pp. 1589–1602.

[21] JOHN M Ratcliffe. "11 Predator-Prey Interaction in an Auditory World". In: *Cognitive ecology II* (2009), p. 201.

[22] David Steve Jacobs and Anna Bastian. *Predator-prey interactions: co-evolution between bats and their prey*. Springer, 2016.

[23] Christopher J Clark, Krista LePiane, and Lori Liu. "Evolutionary and ecological correlates of quiet flight in nightbirds, hawks, falcons, and owls". In: *Integrative and Comparative Biology* 60.5 (2020), pp. 1123–1134.

[24] Robert H Insall, Peggy Paschke, and Luke Tweedy. "Steering yourself by the bootstraps: how cells create their own gradients for chemotaxis". In: *Trends in Cell Biology* (2022).

[25] Johannes M Keegstra, Francesco Carrara, and Roman Stocker. "The ecological roles of bacterial chemotaxis". In: *Nature Reviews Microbiology* (2022), pp. 1–14.

[26] Panarat Arunrattiyakorn et al. "Biodegradation of polystyrene by three bacterial strains isolated from the gut of Superworms (Zophobas atratus larvae)". In: *Journal of Applied Microbiology* 132.4 (2022), pp. 2823–2831.

[27] Theodoros Grammenos et al. "Two-way chemotaxis-based communication for biological nanonetworks". In: *Proceedings of the 9th ACM International Conference on Nanoscale Computing and Communication*. 2022, pp. 1–2.

[28] Peter A Abrams. "Is predator-prey coevolutlon an arms race?" In: *Trends in Ecology & Evolution* 1.4 (1986), pp. 108–110.

[29] Peter A Abrams. "Adaptive responses of predators to prey and prey to predators: the failure of the arms-race analogy". In: *Evolution* 40.6 (1986), pp. 1229–1247.

[30] Peter A Abrams. "The evolution of predator-prey interactions: theory and evidence". In: *Annual Review of Ecology and Systematics* 31.1 (2000), pp. 79–105.

[31] Gary K Meffe. "Effects of abiotic disturbance on coexistence of predator-prey fish species". In: *Ecology* 65.5 (1984), pp. 1525–1534.

[32] Steve M Potter and Thomas B DeMarse. "A new approach to neural cell culture for long-term studies". In: *Journal of neuroscience methods* 110.1-2 (2001), pp. 17–24.

[33] Douglas J Bakkum et al. "Removing some 'A'from AI: Embodied cultured networks". In: *Embodied artificial intelligence*. Springer, 2004, pp. 130–145.

[34] Nina Louise Volstad and Casper Boks. "On the use of Biomimicry as a Useful Tool for the Industrial Designer". In: *Sustainable Development* 20.3 (2012), pp. 189–199.

[35] Olusegun Aanuoluwapo Oguntona and Clinton Ohis Aigbavboa. "Benefits of biomimicry adoption and implementation in the construction industry". In: *Advances in Human Factors, Sustainable Urban Planning and Infrastructure: Proceedings of the AHFE 2018 International Conference on Human Factors, Sustainable Urban Planning and*

Infrastructure, July 21-25, 2018, Loews Sapphire Falls Resort at Universal Studios, Orlando, Florida, USA 9. Springer. 2019, pp. 506–514.

[36] Elmira Jamei and Zora Vrcelj. "Biomimicry and the built environment, learning from nature's solutions". In: *Applied Sciences* 11.16 (2021), p. 7514.

[37] Mwila Isabel Nkandu and Halil Zafer Alibaba. "Biomimicry as an alternative approach to sustainability". In: *Architecture Research* 8.1 (2018), pp. 1–11.

[38] Jean-Marie Lehn. "Toward self-organization and complex matter". In: *Science* 295.5564 (2002), pp. 2400–2403.

[39] Scott Camazine et al. "Self-organization in biological systems". In: *Self-Organization in Biological Systems*. Princeton university press, 2020.

[40] Carlos Gershenson and Francis Heylighen. "When can we call a system self-organizing?" In: *Advances in Artificial Life: 7th European Conference, ECAL 2003, Dortmund, Germany, September 14-17, 2003. Proceedings 7*. Springer. 2003, pp. 606–614.

[41] Eric Bonabeau et al. *Swarm intelligence: from natural to artificial systems*. 1. Oxford university press, 1999.

[42] OB Shchekin, J Ahn, and DG Deppe. "High temperature performance of self-organised quantum dot laser with stacked p-doped active region". In: *Electronics Letters* 38.14 (2002), pp. 712–713.

[43] Yigit Altay et al. "Adaptive polymeric assemblies for applications in biomimicry and nanomedicine". In: *Biomacromolecules* 20.11 (2019), pp. 4053–4064.

[44] Assaf Zinger, John P Cooke, and Francesca Taraballi. "Biomimetic nano drug delivery carriers for treating cardiovascular diseases". In: *Nanomedicine: Nanotechnology, Biology and Medicine* 33 (2021), p. 102360.

[45] Yinfeng Zhang et al. "Self-assembled organic nanomaterials for drug delivery, bioimaging, and cancer therapy". In: *ACS Biomaterials Science & Engineering* 6.9 (2020), pp. 4816–4833.

[46] Matthew J Sis and Matthew J Webber. "Drug delivery with designed peptide assemblies". In: *Trends in pharmacological sciences* 40.10 (2019), pp. 747–762.

[47] Ian P Madden et al. "Hydrodynamically Controlled Self-Organization in Mixtures of Active and Passive Colloids". In: *Small* (2022), p. 2107023.

[48] Heinz Von Foerster. "On self-organizing systems and their environments". In: *Understanding understanding* (2003), pp. 1–19.

[49] Alberto Dinelli et al. "Self-organization of bacterial mixtures in the presence of quorum-sensing interactions". In: *arXiv preprint arXiv:2203.07757* (2022).

[50] Michael JB Krieger and Jean-Bernard Billeter. "The call of duty: Self-organised task allocation in a population of up to twelve mobile robots". In: *Robotics and Autonomous Systems* 30.1-2 (2000), pp. 65–84.

[51] Marco Dorigo, Guy Theraulaz, and Vito Trianni. "Swarm robotics: Past, present, and future [point of view]". In: *Proceedings of the IEEE* 109.7 (2021), pp. 1152–1165.

[52] Ziya Firat et al. "On self-organised aggregation dynamics in swarms of robots with informed robots". In: *Neural Computing and Applications* 32 (2020), pp. 13825–13841.

[53] Mauro S Innocente and Paolo Grasso. "Self-organising swarms of firefighting drones: Harnessing the power of collective intelligence in decentralised multi-robot systems". In: *Journal of Computational Science* 34 (2019), pp. 80–101.

[54] Agata Barciś, Michał Barciś, and Christian Bettstetter. "Robots that sync and swarm: A proof of concept in ROS 2". In: *2019 International Symposium on Multi-Robot and Multi-Agent Systems (MRS)*. IEEE. 2019, pp. 98–104.

[55] Steven Strogatz. "Sync: The emerging science of spontaneous order". In: (2004).

[56] David A Perry. "Self-organizing systems across scales". In: *Trends in Ecology & Evolution* 10.6 (1995), pp. 241–244.

[57] CHEN Jia. "The Ecological Ethical Implications of Latour's Gaia Theory". In: *Philosophy* 10.1 (2020), pp. 29–35.

[58] James Lovelock. "Gaia: the living Earth". In: *Nature* 426.6968 (2003), pp. 769–770.

[59] Hiro-Sato Niwa. "Self-organizing dynamic model of fish schooling". In: *Journal of theoretical Biology* 171.2 (1994), pp. 123–136.

[60] Martin Føre et al. "Modelling how the physical scale of experimental tanks affects salmon growth performance". In: *Aquaculture* 495 (2018), pp. 731–737.

[61] Christos C Ioannou. "Swarm intelligence in fish? The difficulty in demonstrating distributed and self-organised collective intelligence in (some) animal groups". In: *Behavioural processes* 141 (2017), pp. 141–151.

[62] Charlotte Hemelrijk. *Self-organisation and evolution of biological and social systems*. Cambridge University Press, 2005.

[63] Brian L Partridge. "The structure and function of fish schools". In: *Scientific american* 246.6 (1982), pp. 114–123.

[64] Jean-Louis Deneubourg and Simon Goss. "Collective patterns and decision-making". In: *Ethology Ecology & Evolution* 1.4 (1989), pp. 295–311.

[65] Wenlong Tang et al. "Genetic control of collective behavior in zebrafish". In: *IScience* 23.3 (2020), p. 100942.

[66] Marina Papadopoulou et al. "Self-organization of collective escape in pigeon flocks". In: *PLoS computational biology* 18.1 (2022), e1009772.

[67] Marina Papadopoulou et al. "Emergence of splits and collective turns in pigeon flocks under predation". In: *Royal Society Open Science* 9.2 (2022), p. 211898.

[68] Daniel WE Sankey et al. "Absence of "selfish herd" dynamics in bird flocks under threat". In: *Current Biology* 31.14 (2021), pp. 3192–3198.

[69] Charlotte K Hemelrijk and Hanno Hildenbrandt. "Some causes of the variable shape of flocks of birds". In: *PloS one* 6.8 (2011), e22479.

[70] Camille Curantz et al. "Cell shape anisotropy and motility constrain self-organised feather pattern fidelity in birds". In: *bioRxiv* (2021), pp. 2021–01.

[71] Herman Haken. "Synergetics". In: *Physics Bulletin* 28.9 (1977), p. 412.

[72] Hermann Haken. "Synergetics: an overview". In: *Reports on Progress in Physics* 52.5 (1989), p. 515.

[73] Hermann Haken et al. "Springer series in synergetics". In: *Editors: M. Cardona P. Fulde H.-J. Queisser* 269 (1983).

[74] Hermann Haken and Hermann Haken. "An introduction: nonequilibrium phase transitions and self-organization in physics, chemistry and biology". In: *Synergetics: Introduction and Advanced Topics* (2004), pp. 1–387.

[75] Steven H Strogatz. *Nonlinear dynamics and chaos: with applications to physics, biology, chemistry, and engineering*. CRC press, 2018.

[76] Joshua P Vandenbrink et al. "Turning heads: the biology of solar tracking in sunflower". In: *Plant Science* 224 (2014), pp. 20–26.

[77] Ian G McLachlan et al. "Diverse states and stimuli tune olfactory receptor expression levels to modulate food-seeking behavior". In: *Elife* 11 (2022), e79557.

[78] Rahul Jose and Varsha Singh. "Swarming in Bacteria: A tale of plasticity in motility behavior". In: *Journal of the Indian Institute of Science* 100.3 (2020), pp. 515–524.

[79] Payman Tohidifar et al. "The mechanism of bidirectional pH taxis in Bacillus subtilis". In: *Journal of bacteriology* 202.4 (2020), e00491–19.

[80] Antoine Wystrach et al. "Rapid aversive and memory trace learning during route navigation in desert ants". In: *Current biology* 30.10 (2020), pp. 1927–1933.

[81] Cody A Freas. "Learning, memory and cue choice in navigating ants". PhD thesis. Macquarie University, 2022.

[82] Valentino Braitenberg. *Vehicles: Experiments in synthetic psychology*. MIT press, 1986.

[83] Gottfried S Fraenkel and Donald L Gunn. "The orientation of animals: kineses, taxes and compass reactions." In: (1961).

[84] Jieyu Fan. "Simple Improvement of Braitenberg Vehicles". In: *International Core Journal of Engineering* 7.5 (2021), pp. 578–587.

[85] Ruikang Li, Yuxuan Wang, and Xue Yang. "Robot Following Function Based on Theoretical of Braitenberg Vehicles 3a". In: *2022 International Conference on Machine Learning and Intelligent Systems Engineering (MLISE)*. IEEE. 2022, pp. 231–235.

[86] Ran Cheng, Khalid B Mirza, and Konstantin Nikolic. "Neuromorphic robotic platform with visual input, processor and actuator, based on spiking neural networks". In: *Applied System Innovation* 3.2 (2020), p. 28.

[87] Cong Wang et al. "A Braitenberg vehicle based on memristive neuromorphic circuits". In: *Advanced Intelligent Systems* 2.1 (2020), p. 1900103.

[88] Gladys Alexandre, Suzanne Greer-Phillips, and Igor B Zhulin. "Ecological role of energy taxis in microorganisms". In: *FEMS microbiology reviews* 28.1 (2004), pp. 113–126.

[89] Fumi Takabatake, Kenichi Yoshikawa, and Masatoshi Ichikawa. "Communication: Mode bifurcation of droplet motion under stationary laser irradiation". In: *The Journal of Chemical Physics* 141.5 (2014), p. 051103.

[90] Daxing Sun et al. "Phototaxis Motion Behavior of a Self-propelled Submarine-like Water Droplet Robot in Oil Solvent". In: *ChemNanoMat* 6.11 (2020), pp. 1611–1616.

[91] Howard C Berg. "Chemotaxis in bacteria". In: *Annual review of biophysics and bioengineering* 4.1 (1975), pp. 119–136.

[92] Renate Lux and Wenyuan Shi. "Chemotaxis-guided movements in bacteria". In: *Critical Reviews in Oral Biology & Medicine* 15.4 (2004), pp. 207–220.

[93] Howard C Berg and Robert A Anderson. "Bacteria swim by rotating their flagellar filaments". In: *Nature* 245.5425 (1973), pp. 380–382.

[94] David F Blair. "How bacteria sense and swim". In: *Annual review of microbiology* 49.1 (1995), pp. 489–520.

[95] George H Wadhams and Judith P Armitage. "Making sense of it all: bacterial chemotaxis". In: *Nature reviews Molecular cell biology* 5.12 (2004), pp. 1024–1037.

[96] Nicholas Blackburn, Tom Fenchel, and Jim Mitchell. "Microscale nutrient patches in planktonic habitats shown by chemotactic bacteria". In: *Science* 282.5397 (1998), pp. 2254–2256.

[97] Birgit Scharf and Elmar K Wolff. "Phototactic behaviour of the archaebacterial Natronobacterium pharaonis". In: *FEBS letters* 340.1-2 (1994), pp. 114–116.

[98] Judith P Armitage and Klaas J Hellingwerf. "Light-induced behavioral responses ('phototaxis') in prokaryotes". In: *Discoveries in Photosynthesis*. Springer, 2005, pp. 985–995.

[99] Hedieh Sajedi and Fatemeh Mohammadipanah. "Developed Optimization Algorithms Based on Natural Taxis Behavior of Bacteria". In: *Cognitive Computation* 12.6 (2020), pp. 1187–1204.

[100] Charlotte Hurot et al. "Bio-inspired strategies for improving the selectivity and sensitivity of artificial noses: A review". In: *Sensors* 20.6 (2020), p. 1803.

[101] Matthew E Staymates et al. "Biomimetic sniffing improves the detection performance of a 3D printed nose of a dog and a commercial trace vapor detector". In: *Scientific reports* 6.1 (2016), pp. 1–10.

[102] Ozan Erol et al. "Transformer hydrogels: a review". In: *Advanced Materials Technologies* 4.4 (2019), p. 1900043.

[103] Yusen Zhao et al. "Soft phototactic swimmer based on self-sustained hydrogel oscillator". In: *Science Robotics* 4.33 (2019), eaax7112.

[104] Kyosuke Yoshimura et al. "Autonomous oil flow generated by self-oscillating polymer gels". In: *Scientific reports* 10.1 (2020), p. 12834.

[105] Alan Mathison Turing. "The chemical basis of morphogenesis". In: *Bulletin of mathematical biology* 52.1 (1990), pp. 153–197.

[106] Noboru Suzuki, Masashi Hirata, and Shigeru Kondo. "Traveling stripes on the skin of a mutant mouse". In: *Proceedings of the National Academy of Sciences* 100.17 (2003), pp. 9680–9685.

[107] Shigeru Kondo and Takashi Miura. "Reaction-diffusion model as a framework for understanding biological pattern formation". In: *science* 329.5999 (2010), pp. 1616–1620.

[108] Hans Meinhardt. "Models of biological pattern formation". In: *New York* 118 (1982).

[109] James D Murray. *Mathematical biology II: spatial models and biomedical applications*. Vol. 3. Springer New York, 2001.

[110] P. Gray and S. K. Scott. In: *Chemical Engineering Science* 39 (1983), p. 29.

[111] Peter Gray and Stephen K Scott. *Chemical oscillations and instabilities: non-linear chemical kinetics*. 1990.

[112] Martin M Hanczyc et al. "Fatty acid chemistry at the oil- water interface: Self-propelled oil droplets". In: *Journal of the American Chemical Society* 129.30 (2007), pp. 9386–9391.

[113] Takahiko Ban et al. "Anionic control of autonomous motion of oil/water interface with cationic surfactant". In: *Chemistry letters* 36.8 (2007), pp. 1040–1041.

[114] Peter Constantin and Ciprian Foias. *Navier-stokes equations*. University of Chicago Press, 2020.

[115] Alexandre Joel Chorin. "Numerical solution of the Navier-Stokes equations". In: *Mathematics of computation* 22.104 (1968), pp. 745–762.

[116] Sergey V Ershkov et al. "Towards understanding the algorithms for solving the Navier–Stokes equations". In: *Fluid Dynamics Research* 53.4 (2021), p. 044501.

[117] Terence Tao. "Searching for singularities in the Navier–Stokes equations". In: *Nature Reviews Physics* 1.7 (2019), pp. 418–419.

[118] Charles S Peskin. "Numerical analysis of blood flow in the heart". In: *Journal of computational physics* 25.3 (1977), pp. 220–252.

[119] Sauro Succi. *The lattice Boltzmann equation: for fluid dynamics and beyond*. Oxford university press, 2001.

[120] Carlo Cercignani and Gilberto Medeiros Kremer. "Relativistic boltzmann equation". In: *The Relativistic Boltzmann Equation: Theory and Applications*. Springer, 2002, pp. 31–63.

[121] Shiyi Chen and Gary D Doolen. "Lattice Boltzmann method for fluid flows". In: *Annual review of fluid mechanics* 30.1 (1998), pp. 329–364.

[122] Amir H Hedjripour, David P Callaghan, and Tom E Baldock. "Generalized transformation of the lattice Boltzmann method for shallow water flows". In: *Journal of Hydraulic Research* 54.4 (2016), pp. 371–388.

[123] Sriram Ramaswamy. "Active matter". In: *Journal of Statistical Mechanics: Theory and Experiment* 2017.5 (2017), p. 054002.

[124] Sriram Ramaswamy. "The mechanics and statistics of active matter". In: *Annu. Rev. Condens. Matter Phys.* 1.1 (2010), pp. 323–345.

[125] M Cristina Marchetti et al. "Hydrodynamics of soft active matter". In: *Reviews of modern physics* 85.3 (2013), p. 1143.

[126] Isabel Schick et al. "Inorganic Janus particles for biomedical applications". In: *Beilstein journal of nanotechnology* 5.1 (2014), pp. 2346–2362.

[127] Shikuan Yang et al. "Microfluidic synthesis of multifunctional Janus particles for biomedical applications". In: *Lab on a Chip* 12.12 (2012), pp. 2097–2102.

[128] Haiyang Su et al. "Janus micro/nanorobots in biomedical applications". In: *Advanced Healthcare Materials* (2022), p. 2202391.

[129] Xiangyu Jiao et al. "NIR powered Janus nanocarrier for deep tumor penetration". In: *Applied Materials Today* 18 (2020), p. 100504.

[130] Xiang Zhou et al. "Light/gas cascade-propelled Janus micromotors that actively overcome sequential and multi-staged biological barriers for precise drug delivery". In: *Chemical Engineering Journal* 408 (2021), p. 127897.

[131] S Swann. "Magnetron sputtering". In: *Physics in technology* 19.2 (1988), p. 67.

[132] Y Sumino and K Yoshikawa. "Amoeba-like motion of an oil droplet". In: *The European Physical Journal Special Topics* 223.7 (2014), pp. 1345–1352.

[133] Prateek Dwivedi, Dipin Pillai, and Rahul Mangal. "Self-propelled swimming droplets". In: *Current Opinion in Colloid & Interface Science* (2022), p. 101614.

[134] Hiroyuki Kitahata et al. "Convective and periodic motion driven by a chemical wave". In: *The Journal of chemical physics* 116.13 (2002), pp. 5666–5672.

[135] Caleb H Meredith et al. "Chemical design of self-propelled Janus droplets". In: *Matter* 5.2 (2022), pp. 616–633.

[136] Fei Wang et al. "Progress report on phase separation in polymer solutions". In: *Advanced Materials* 31.26 (2019), p. 1806733.

[137] Chengxiang He et al. "Self-assembly of droplet swarms and its feedback on droplet generation in a step-emulsification microdevice with parallel microchannels". In: *Chemical Engineering Science* 256 (2022), p. 117685.

[138] Caleb H Meredith et al. "Predator–prey interactions between droplets driven by non-reciprocal oil exchange". In: *Nature Chemistry* 12.12 (2020), pp. 1136–1142.

[139] Zheng Yuan Luo, Xing Long Shang, and Bo Feng Bai. "Effect of soluble surfactant on the motion of a confined droplet in a square microchannel". In: *Physics of Fluids* 31.11 (2019), p. 117104.

[140] Hongping Wang et al. "The motion of respiratory droplets produced by coughing". In: *Physics of Fluids* 32.12 (2020), p. 125102.

[141] Takahiro Tanabe, Takuto Ogasawara, and Nobuhiko J Suematsu. "Effect of a product on spontaneous droplet motion driven by a chemical reaction of surfactant". In: *Physical Review E* 102.2 (2020), p. 023102.

[142] Gaojin Li. "Swimming dynamics of a self-propelled droplet". In: *Journal of Fluid Mechanics* 934 (2022), A20.

[143] Yutaka Sumino et al. "Chemosensitive running droplet". In: *Physical Review E* 72.4 (2005), p. 041603.

[144] J. R. Blake. "A spherical envelope approach to ciliary propulsion". In: *Journal of Fluid Mechanics* 46.1 (1971), pp. 199–208. DOI: 10.1017/S002211207100048X.

[145] Xin Wang et al. "Active motion of multiphase oil droplets: emergent dynamics of squirmers with evolving internal structure". In: *Soft Matter* 17.10 (2021), pp. 2985–2993.

[146] Christopher A Azaldegui, Anthony G Vecchiarelli, and Julie S Biteen. "The emergence of phase separation as an organizing principle in bacteria". In: *Biophysical journal* 120.7 (2021), pp. 1123–1138.

[147] Jizhou Zhao and Lorenz Ratke. "Kinetics of Phase Separation in a Hypermonotectic Al–Pb Alloy". In: *International Journal of Materials Research* 89.4 (2021), pp. 241–246.

[148] Detlef Lohse and Xuehua Zhang. "Physicochemical hydrodynamics of droplets out of equilibrium". In: *Nature Reviews Physics* 2.8 (2020), pp. 426–443.

[149] Dong Liu et al. "Life-Like Motion of Oil Drops at the Air–Liquid Interface". In: *Langmuir* 35.49 (2019), pp. 16146–16152.

[150] Pornprapa Bol et al. "The Kinetics of Phase Separation in Liquid-Liquid Extraction: Modeling of Droplet Swarm Coalescence". In: *Chemie Ingenieur Technik* 93.10 (2021), pp. 1502–1508.

[151] Md Rifat Hassan and Cheng Wang. "Ferro-hydrodynamic interactions between ferrofluid droplet pairs in simple shear flows". In: *Colloids and Surfaces A: Physicochemical and Engineering Aspects* 602 (2020), p. 124906.

[152] Muneyuki Matsuo et al. "Sequentially Selective Coalescence of Binary Self-Propelled Droplets upon Collective Motion". In: *Langmuir* (2023).

[153] AG Islamova et al. "Droplet-droplet, droplet-particle, and droplet-substrate collision behavior". In: *Powder Technology* 403 (2022), p. 117371.

[154] IM Bugarin and TF Oliveira. "Droplet motion in confined natural convection flows". In: *International Journal of Heat and Mass Transfer* 173 (2021), p. 121249.

[155] D Ferraro et al. "Controlling the distance of highly confined droplets in a capillary by interfacial tension for merging on-demand". In: *Lab on a Chip* 19.1 (2019), pp. 136–146.

[156] Donald E Woodmansee and Thomas J Hanratty. "Mechanism for the removal of droplets from a liquid surface by a parallel air flow". In: *Chemical Engineering Science* 24.2 (1969), pp. 299–307.

[157] Bing Xiahou et al. "Simulation and experimental research on droplet flow characteristics and deposition in airflow field". In: *International Journal of Agricultural and Biological Engineering* 13.6 (2020), pp. 16–24.

[158] Brian Dincau, Emilie Dressaire, and Alban Sauret. "Pulsatile flow in microfluidic systems". In: *Small* 16.9 (2020), p. 1904032.

[159] Karin Schroen et al. "Droplet microfluidics for food and nutrition applications". In: *Micromachines* 12.8 (2021), p. 863.

[160] Rahil N Valani, Anja C Slim, and Tapio Simula. "Superwalking droplets". In: *Physical Review Letters* 123.2 (2019), p. 024503.

[161] Prateek Dwivedi et al. "Solute induced jittery motion of self-propelled droplets". In: *Physics of Fluids* 33.2 (2021), p. 022103.

[162] Prateek Dwivedi et al. "Mode-switching of active droplets in macromolecular solutions". In: *arXiv preprint arXiv:2207.13318* (2022).

[163] Sebastien Michelin. "Self-Propulsion of Chemically Active Droplets". In: *Annual Review of Fluid Mechanics* 55 (2022).

[164] Brian E McKenzie et al. "Drop deformation during diffusiophoresis". In: *Journal of Fluid Mechanics* 949 (2022), A17.

[165] AN Zaikin and AM Zhabotinsky. "Concentration wave propagation in two-dimensional liquid-phase self-oscillating system". In: *Nature* 225.5232 (1970), pp. 535–537.

[166] Richard J Field. *Oscillations and traveling waves in chemical systems*. Wiley, 1985.

[167] John J Tyson. "What everyone should know about the Belousov-Zhabotinsky reaction". In: *Frontiers in mathematical biology*. Springer, 1994, pp. 569–587.

[168] Boris Belousov. "Periodically acting reaction and its mechanism". In: 147.145 (1959).

[169] A. M. Zhabotinsky. "Periodical oxidation of malonic acid in solution (a study of the Belousov reaction kinetics)". In: *Biofizika* 9 (1964), pp. 306–311.

[170] Arthur T Winfree. *The geometry of biological time*. Vol. 12. Springer Science & Business Media, 2001.

[171] R.J. Field and R.M Noyes. "Oscillations in chemical systems. IV. Limit cycle behavior in a model of a real chemical reaction". In: *The Journal of Chemical Physics* 60.5 (1974), pp. 1877–1884.

[172] Richard J Field and Richard M Noyes. "Oscillations in chemical systems. IV. Limit cycle behavior in a model of a real chemical reaction". In: *The Journal of Chemical Physics* 60.5 (1974), pp. 1877–1884.

[173] László Györgyi and Richard J Field. "A three-variable model of deterministic chaos in the Belousov–Zhabotinsky reaction". In: *Nature* 355.6363 (1992), pp. 808–810.

[174] Richard J Field, Joana G Freire, and Jason AC Gallas. "Quint points lattice in a driven Belousov–Zhabotinsky reaction model". In: *Chaos: An Interdisciplinary Journal of Nonlinear Science* 31.5 (2021), p. 053124.

[175] Lanre Akinyemi. "A fractional analysis of Noyes–Field model for the nonlinear Belousov–Zhabotinsky reaction". In: *Computational and Applied Mathematics* 39.3 (2020), pp. 1–34.

[176] Victor V Yashin and Anna C Balazs. "Theoretical and computational modeling of self-oscillating polymer gels". In: *The Journal of chemical physics* 126.12 (2007), p. 124707.

[177] Hiroyuki Kitahata et al. "Dynamics of Droplets". In: *Pattern Formations and Oscillatory Phenomena*. Elsevier, 2013, pp. 85–118.

[178] Olga Kuksenok, Victor V Yashin, and Anna C Balazs. "Three-dimensional model for chemoresponsive polymer gels undergoing the Belousov-Zhabotinsky reaction". In: *Physical Review E* 78.4 (2008), p. 041406.

[179] Niall Shanks. "Modeling biological systems: the Belousov–Zhabotinsky reaction". In: *Foundations of Chemistry* 3.1 (2001), pp. 33–53.

[180] John J Tyson. "From the Belousov–Zhabotinsky reaction to biochemical clocks, traveling waves and cell cycle regulation". In: *Biochemical Journal* 479.2 (2022), pp. 185–206.

[181] Alan L Hodgkin and Andrew F Huxley. "A quantitative description of membrane current and its application to conduction and excitation in nerve". In: *The Journal of physiology* 117.4 (1952), pp. 500–544.

[182] AL Hodgkin and AF Huxley. "A quantitative description of membrane current and its application to conduction and excitation in nerve". In: *Bulletin of mathematical biology* 52.1-2 (1990), pp. 25–71.

[183] B Van der Pol. "A theory of the amplitude of free and forced triode vibrations, Radio Rev. 1 (1920) 701-710, 754-762". In: *Selected Scientific Papers* 1 (1960).

[184] Balth Van der Pol. "LXXXVIII. On "relaxation-oscillations"". In: *The London, Edinburgh, and Dublin Philosophical Magazine and Journal of Science* 2.11 (1926), pp. 978–992.

[185] Ikuko N Motoike and Andrew Adamatzky. "Three-valued logic gates in reaction–diffusion excitable media". In: *Chaos, Solitons & Fractals* 24.1 (2005), pp. 107–114.

[186] Jinichi Nagumo, Suguru Arimoto, and Shuji Yoshizawa. "An active pulse transmission line simulating nerve axon". In: *Proceedings of the IRE* 50.10 (1962), pp. 2061–2070.

[187] Eugene M Izhikevich and Richard FitzHugh. "Fitzhugh-nagumo model". In: *Scholarpedia* 1.9 (2006), p. 1349.

[188] Richard FitzHugh. "Impulses and physiological states in theoretical models of nerve membrane". In: *Biophysical journal* 1.6 (1961), pp. 445–466.

[189] Yong Liu et al. "A new photosensitive neuron model and its dynamics". In: *Frontiers of Information Technology & Electronic Engineering* 21.9 (2020), pp. 1387–1396.

[190] Sundarapandian Vaidyanathan. "Anti-synchronization of the FitzHugh-Nagumo chaotic neuron models via adaptive control method". In: *International Journal of PharmTech Research* 8.7 (2015), pp. 71–83.

[191] Dejun Fan and Ling Hong. "Hopf bifurcation analysis in a synaptically coupled FHN neuron model with delays". In: *Communications in Nonlinear Science and Numerical Simulation* 15.7 (2010), pp. 1873–1886.

[192] Malik Muhammad Ibrahim et al. "Lag synchronization of coupled time-delayed FitzHugh–Nagumo neural networks via feedback control". In: *Scientific reports* 11.1 (2021), pp. 1–15.

[193] Peggy Marie Wood and John Ross. "A quantitative study of chemical waves in the Belousov–Zhabotinsky reaction". In: *The Journal of chemical physics* 82.4 (1985), pp. 1924–1936.

[194] Gareth Jones et al. "Autonomous droplet architectures". In: *Artificial life* 21.2 (2015), pp. 195–204.

[195] Kai Ming Chang, Maurits RR de Planque, and Klaus-Peter Zauner. "Towards functional droplet architectures: A Belousov-Zhabotinsky medium for networks". In: *Scientific reports* 8.1 (2018), pp. 1–12.

[196] Michael J Booth et al. "Functional aqueous droplet networks". In: *Molecular BioSystems* 13.9 (2017), pp. 1658–1691.

[197] Horst Dieter Försterling et al. "Stoichiometry of bromide production from ceric oxidation of bromomalonic acid in the Belousov-Zhabotinskii reaction". In: *The Journal of Physical Chemistry* 97.11 (1993), pp. 2623–2627.

[198] Marta Dueñas-Dıez and Juan Pérez-Mercader. "How chemistry computes: language recognition by non-biochemical chemical automata. From finite automata to turing machines". In: *Iscience* 19 (2019), pp. 514–526.

[199] Noam Chomsky. "Three models for the description of language". In: *IRE Transactions on information theory* 2.3 (1956), pp. 113–124.

[200] KI Agladze and P De Kepper. "Influence of electric field on rotating spiral waves in the Belousov-Zhabotinskii reaction". In: *The Journal of Physical Chemistry* 96.13 (1992), pp. 5239–5242.

[201] SV Amrutha et al. "Mechanism of Spiral Wave Unpinning in the Belousov–Zhabotinsky Reaction with a DC Electric Field". In: *The Journal of Physical Chemistry C* (2022).

[202] Luciana Sciascia et al. "Oscillatory dynamics of the Belousov–Zhabotinsky system in the presence of a self-assembling nonionic polymer. Role of the reactants concentration". In: *Physical Chemistry Chemical Physics* 12.37 (2010), pp. 11674–11682.

[203] Anumita Paul. "Observations of the Effect of Anionic, Cationic, Neutral, and Zwitterionic Surfactants on the Belousov- Zhabotinsky Reaction". In: *The Journal of Physical Chemistry B* 109.19 (2005), pp. 9639–9644.

[204] Daisuke Suzuki and Ryo Yoshida. "Effect of initial substrate concentration of the Belousov- Zhabotinsky reaction on self-oscillation for microgel system". In: *The Journal of Physical Chemistry B* 112.40 (2008), pp. 12618–12624.

[205] James P Keener and John J Tyson. "Spiral waves in the Belousov-Zhabotinskii reaction". In: *Physica D: Nonlinear Phenomena* 21.2-3 (1986), pp. 307–324.

[206] Vladimir S Zykov, Oliver Steinbock, and Stefan C Müller. "External forcing of spiral waves". In: *Chaos: An Interdisciplinary Journal of Nonlinear Science* 4.3 (1994), pp. 509–518.

[207] Amrutha SV et al. "Theory and experiments of spiral unpinning in the Belousov-Zhabotinsky reaction using a circularly polarized electric field". In: *arXiv preprint arXiv:2301.01040* (2023).

[208] Mario Markus, Zsuzsanna Nagy-Ungvarai, and Benno Hess. "Phototaxis of spiral waves". In: *Science* 257.5067 (1992), pp. 225–227.

[209] Oliver Steinbock, Vladimir Zykov, and Stefan C Müller. "Control of spiral-wave dynamics in active media by periodic modulation of excitability". In: *Nature* 366.6453 (1993), pp. 322–324.

[210] Vladimir K Vanag and Irving R Epstein. "Inwardly rotating spiral waves in a reaction-diffusion system". In: *Science* 294.5543 (2001), pp. 835–837.

[211] W Hanke et al. "Microgravity dependence of excitable biological and physicochemical media". In: *Protoplasma* 229.2 (2006), pp. 235–242.

[212] Irving R Epstein, John A Pojman, and Oliver Steinbock. "Introduction: Self-organization in nonequilibrium chemical systems". In: *Chaos: An Interdisciplinary Journal of Nonlinear Science* 16.3 (2006), p. 037101.

[213] Brian J Welsh. "Pattern formation in the Belousov-Zhabotinsky reaction". PhD thesis. Glasgow College of Technology, 1984.

[214] Anna Zhyrova et al. "Construction the model of Belousov-Zhabotinsky reaction by means of the state trajectory creation". In: ().

[215] Claire Fullarton et al. "Belousov–Zhabotinsky reaction in liquid marbles". In: *Journal of Physics: Materials* 2.1 (2019), p. 015005.

[216] Rita Tóth et al. "Wave initiation in the ferroin-catalysed Belousov–Zhabotinsky reaction with visible light". In: *Physical Chemistry Chemical Physics* 2.3 (2000), pp. 413–416.

[217] Michail-Antisthenis Tsompanas, Claire Fullarton, and Andrew Adamatzky. "Belousov-Zhabotinsky liquid marbles in robot control". In: *Sensors and Actuators B: Chemical* 295 (2019), pp. 194–203.

[218] Andrew Adamatzky et al. "Liquid marble photosensor". In: *ChemPhysChem* 21.1 (2020), pp. 90–98.

[219] Ryo Yoshida et al. *Self-oscillating gels*. 1997.

[220] Ryo Yoshida et al. "In-phase synchronization of chemical and mechanical oscillations in self-oscillating gels". In: *The Journal of Physical Chemistry A* 104.32 (2000), pp. 7549–7555.

[221] Ryo Yoshida, Keigo Takei, and Tomohiko Yamaguchi. "Self-beating motion of gels and modulation of oscillation rhythm synchronized with organic acid". In: *Macromolecules* 36.6 (2003), pp. 1759–1761.

[222] Ryo Yoshida. "Self-oscillating gels driven by the Belousov–Zhabotinsky reaction as novel smart materials". In: *Advanced Materials* 22.31 (2010), pp. 3463–3483.

[223] Shigeo Sasaki et al. "Mechanical oscillation coupled with the Belousov- Zhabotinsky reaction in gel". In: *Langmuir* 19.14 (2003), pp. 5595–5600.

[224] Shingo Maeda et al. "Self-walking gel". In: *Advanced Materials* 19.21 (2007), pp. 3480–3484.

[225] Ryo Yoshida et al. "Self-oscillating gel as novel biomimetic materials". In: *Journal of controlled release* 140.3 (2009), pp. 186–193.

[226] Yoko Murase et al. "Design of a mass transport surface utilizing peristaltic motion of a self-oscillating gel". In: *Langmuir* 25.1 (2009), pp. 483–489.

[227] Osamu Tabata et al. "Ciliary motion actuator using self-oscillating gel". In: *Sensors and Actuators A: Physical* 95.2-3 (2002), pp. 234–238.

[228] Yoshihiro Ito, Masayuki Nogawa, and Ryo Yoshida. "Temperature Control of the Belousov- Zhabotinsky Reaction Using a Thermoresponsive Polymer". In: *Langmuir* 19.23 (2003), pp. 9577–9579.

[229] Daisuke Suzuki and Ryo Yoshida. "Temporal control of self-oscillation for microgels by cross-linking network structure". In: *Macromolecules* 41.15 (2008), pp. 5830–5838.

[230] H. Kitahata et al. "Convective and periodic motion driven by a chemical wave". In: *The Journal of chemical physics* 116.13 (2002), pp. 5666–5672.

[231] H. Kitahata et al. "Spontaneous motion of a droplet coupled with a chemical wave". In: *Physical Review E* 84.1 (2011), p. 015101.

[232] S. Kitawaki et al. "Control of the Self-Motion of a Ruthenium-Catalyzed Belousov–Zhabotinsky Droplet". In: *The Journal of Physical Chemistry C* 116.51 (2012), pp. 26805–26809.

[233] D Kumar, Kabeer Jasuja, and Pratyush Dayal. "Spontaneous locomotion of nano-catalysed BZ droplets". In: *Bulletin of the American Physical Society* 65 (2020).

[234] Nobuhiko J Suematsu et al. "Spontaneous mode switching of self-propelled droplet motion induced by a clock reaction in the Belousov–Zhabotinsky medium". In: *The Journal of Physical Chemistry Letters* 12.31 (2021), pp. 7526–7530.

[235] Kanala Venkata Sravana Chaithanya, Shreyas A Shenoy, and Pratyush Dayal. "Hydrodynamics of a confined active Belousov-Zhabotinsky droplet". In: *Physical Review E* 106.6 (2022), p. 065103.

[236] Kristian Torbensen et al. "Chemical communication and dynamics of droplet emulsions in networks of Belousov–Zhabotinsky micro-oscillators produced by microfluidics". In: *Lab on a Chip* 17.7 (2017), pp. 1179–1189.

[237] Rahul Kumar et al. "Past, present and future of blood pressure measuring instruments and their calibration". In: *Measurement* 172 (2021), p. 108845.

[238] John Canny. "A computational approach to edge detection". In: *IEEE Transactions on pattern analysis and machine intelligence* 6 (1986), pp. 679–698.

[239] Daya Shankar Gupta et al. "Temporal Structure of Neural Processes Coupling Sensory, Motor and Cognitive Functions of the Brain". In: *Frontiers in Computational Neuroscience* 14 (2020).

[240] N. Ando and R. Kanzaki. "A simple behaviour provides accuracy and flexibility in odour plume tracking–the robotic control of sensory-motor coupling in silkmoths". In: *Journal of Experimental Biology* 218.123 (2015), pp. 3845–3854.

[241] Daniel J Webre, Peter M Wolanin, and Jeffry B Stock. "Bacterial chemotaxis". In: *Current Biology* 13.2 (2003), R47–R49.

[242] Robert R Kay et al. "Changing directions in the study of chemotaxis". In: *Nature reviews Molecular cell biology* 9.6 (2008), pp. 455–463.

[243] Edward F DeLong, Richard B Frankel, and Dennis A Bazylinski. "Multiple evolutionary origins of magnetotaxis in bacteria". In: *Science* 259.5096 (1993), pp. 803–806.

[244] Ann M Rajnicek, COLIN D McCAIG, and NA Gow. "Electric fields induce curved growth of Enterobacter cloacae, Escherichia coli, and Bacillus subtilis cells: implications for mechanisms of galvanotropism and bacterial growth." In: *Journal of bacteriology* 176.3 (1994), pp. 702–713.

[245] Naoko Ogawa et al. "A physical model for galvanotaxis of Paramecium cell". In: *Journal of theoretical biology* 242.2 (2006), pp. 314–328.

[246] Chenyu Jin, Carsten Krüger, and Corinna C Maass. "Chemotaxis and autochemotaxis of self-propelling droplet swimmers". In: *Proceedings of the National Academy of Sciences* 114.20 (2017), pp. 5089–5094.

[247] István Lagzi et al. "Maze solving by chemotactic droplets". In: *Journal of the American Chemical Society* 132.4 (2010), pp. 1198–1199.

[248] Jitka Cejkova et al. "Dynamics of chemotactic droplets in salt concentration gradients". In: *Langmuir* 30.40 (2014), pp. 11937–11944.

[249] Gábor Holló et al. "Electric field assisted motion of a mercury droplet". In: *Scientific reports* 11.1 (2021), pp. 1–11.

[250] Shuichi Kinoshita. *Pattern formations and oscillatory phenomena*. Newnes, 2013.

[251] Shashi Thutupalli, Ralf Seemann, and Stephan Herminghaus. "Swarming behavior of simple model squirmers". In: *New Journal of Physics* 13.7 (2011), p. 073021.

[252] A. N. Zaikin and A. M. Zhabotinsky. In: *Nature* 225 (1970), p. 535.

[253] Richard J Field. "Limit cycle oscillations in the reversible Oregonator". In: *The Journal of Chemical Physics* 63.6 (1975), pp. 2289–2296.

[254] P. Gray and S. K. Scott. In: (1990).

[255] Vladimir K Vanag, Anatol M Zhabotinsky, and Irving R Epstein. "Pattern Formation in the Belousov- Zhabotinsky Reaction with Photochemical Global Feedback". In: *The Journal of Physical Chemistry A* 104.49 (2000), pp. 11566–11577.

[256] J. Guckenheimer and P. Holmes. *Nonlinear oscillations, dynamical systems, and bifurcations of vector fields*. Vol. 42. Springer Science & Business Media, 2013.

[257] Irving R Epstein and John A Pojman. *An introduction to nonlinear chemical dynamics: oscillations, waves, patterns, and chaos*. Oxford University Press, 1998.

[258] P.C. Fife. "Understanding the patterns in the BZ reagent". In: *Journal of Statistical Physics* 39.5-6 (1985), pp. 687–703.

[259] S.A. Levin and L.A. Segel. "Pattern generation in space and aspectt". In: *SIAM Review* 27.1 (1985), pp. 45–67.

[260] O. Steinbock and S. C. Müller. In: *The Journal of Physical Chemistry* 102 (1998), p. 6485.

[261] M. Blank and I. Soo. In: *Bioelectrochemistry* 61 (2003), p. 93.

[262] Martin Blank and Lily Soo. "Electromagnetic acceleration of electron transfer reactions". In: *Journal of cellular biochemistry* 81.2 (2001), pp. 278–283.

[263] Masakazu Kuze et al. "Chemical Wave Propagation in the Belousov–Zhabotinsky Reaction Controlled by Electrical Potential". In: *The Journal of Physical Chemistry A* 123.23 (2019), pp. 4853–4857.

[264] Hideyuki Okano et al. "The Influence of a gradient static magnetic field on an unstirred Belousov–Zhabotinsky reaction". In: *Bioelectromagnetics: Journal of the Bioelectromagnetics Society, The Society for Physical Regulation in Biology and Medicine, The European Bioelectromagnetics Association* 29.8 (2008), pp. 598–604.

[265] S. J. S. Jamaluddin et al. "Photochemical motion control of surface active Belousov–Zhabotinsky droplets". In: *Chaos: An Interdisciplinary Journal of Nonlinear Science* 30.8 (2020), p. 083143.

[266] K. Yoshikawa et al. "Generation of periodic force with oscillating chemical reaction". In: *Chemical physics letters* 211.2-3 (1993), pp. 211–213.

[267] Walter F Paxton et al. "Catalytic nanomotors: autonomous movement of striped nanorods". In: *Journal of the American Chemical Society* 126.41 (2004), pp. 13424–13431.

[268] M. Gunji and M. Washizu. "Self-propulsion of a water droplet in an electric field." In: *Journal of Physics D: Applied Physics* 38.14 (2005).

[269] Masahiko Hase, Shun N Watanabe, and Kenichi Yoshikawa. "Rhythmic motion of a droplet under a dc electric field". In: *Physical Review E* 74.4 (2006), p. 046301.

[270] Tunde Geher-Herczegh et al. "Delayed Mechanical Response to Chemical Kinetics in Self-Oscillating Hydrogels Driven by the Belousov–Zhabotinsky Reaction". In: *Macromolecules* 54.13 (2021), pp. 6430–6439.

[271] James M Denegre et al. "Cleavage planes in frog eggs are altered by strong magnetic fields". In: *Proceedings of the National Academy of Sciences* 95.25 (1998), pp. 14729–14732.

[272] Min Zhao, John V Forrester, and Colin D McCaig. "A small, physiological electric field orients cell division". In: *Proceedings of the National Academy of Sciences* 96.9 (1999), pp. 4942–4946.

[273] Juan Shong Khaw et al. "Electrical stimulation of titanium to promote stem cell orientation, elongation and osteogenesis". In: *Acta Biomaterialia* 139 (2022), pp. 204–217.

[274] Sarah Sundelacruz, Michael Levin, and David L Kaplan. "Role of membrane potential in the regulation of cell proliferation and differentiation". In: *Stem cell reviews and reports* 5.3 (2009), pp. 231–246.

[275] Douglas J Blackiston, Kelly A McLaughlin, and Michael Levin. "Bioelectric controls of cell proliferation: ion channels, membrane voltage and the cell cycle". In: *Cell cycle* 8.21 (2009), pp. 3527–3536.

[276] Dany S Adams and Michael Levin. "Endogenous voltage gradients as mediators of cell-cell communication: strategies for investigating bioelectrical signals during pattern formation". In: *Cell and tissue research* 352.1 (2013), pp. 95–122.

[277] Carlo M Croce. "Causes and consequences of microRNA dysregulation in cancer". In: *Nature reviews genetics* 10.10 (2009), pp. 704–714.

[278] Emilia Kansanen et al. "The Keap1-Nrf2 pathway: Mechanisms of activation and dysregulation in cancer". In: *Redox biology* 1.1 (2013), pp. 45–49.

[279] Paulius Gibieža and Vilma Petrikaitė. "The regulation of actin dynamics during cell division and malignancy". In: *American Journal of Cancer Research* 11.9 (2021), p. 4050.

[280] Pavan Vedula and Anna Kashina. "The makings of the 'actin code': regulation of actin's biological function at the amino acid and nucleotide level". In: *Journal of cell science* 131.9 (2018), jcs215509.

[281] Aleksandra Simiczyjew et al. "Effect of overexpression of β-and γ-actin isoforms on actin cytoskeleton organization and migration of human colon cancer cells". In: *Histochemistry and cell biology* 142.3 (2014), pp. 307–322.

[282] Daniel Riveline et al. "Acting on actin: the electric motility assay". In: *European biophysics journal* 27.4 (1998), pp. 403–408.

[283] Sreeja B Asokan et al. "Two-dimensional manipulation and orientation of actin- myosin systems with dielectrophoresis". In: *Nano Letters* 3.4 (2003), pp. 431–437.

[284] Changsong Yang and Tatyana M Svitkina. "Ultrastructure and dynamics of the actin-myosin II cytoskeleton during mitochondrial fission". In: *Nature cell biology* 21.5 (2019), pp. 603–613.

[285] Bing Song et al. "Electric signals counterbalanced posterior vs anterior PTEN signaling in directed migration of Dictyostelium". In: *Cell & bioscience* 11.1 (2021), pp. 1–18.

[286] Deborah Huber et al. "Hydrodynamics in cell studies". In: *Chemical reviews* 118.4 (2018), pp. 2042–2079.

[287] Ajit P Yoganathan et al. "Review of hydrodynamic principles for the cardiologist: applications to the study of blood flow and jets by imaging techniques". In: *Journal of the American College of Cardiology* 12.5 (1988), pp. 1344–1353.

[288] M Mason Guest et al. "Red blood cells: change in shape in capillaries". In: *Science* 142.3597 (1963), pp. 1319–1321.

[289] Sergei Trofimchuk and Vitaly Volpert. "Traveling waves in delayed reaction-diffusion equations in biology". In: *Mathematical Biosciences and Engineering* 17.6 (2020), pp. 6487–6514.

[290] Nikolai Bessonov et al. "Nonlocal reaction–diffusion model of viral evolution: Emergence of virus strains". In: *Mathematics* 8.1 (2020), p. 117.

[291] Angela M Jarrett et al. "Incorporating drug delivery into an imaging-driven, mechanics-coupled reaction diffusion model for predicting the response of breast cancer to neoadjuvant chemotherapy: theory and preliminary clinical results". In: *Physics in Medicine & Biology* 63.10 (2018), p. 105015.

[292] Angela M Jarrett et al. "Mathematical models of tumor cell proliferation: a review of the literature". In: *Expert review of anticancer therapy* 18.12 (2018), pp. 1271–1286.

[293] Tiago Yuzo Miyaoka, Suzanne Lenhart, and João FCA Meyer. "Optimal control of vaccination in a vector-borne reaction–diffusion model applied to Zika virus". In: *Journal of mathematical biology* 79.3 (2019), pp. 1077–1104.

[294] Arthur Prindle et al. "Ion channels enable electrical communication in bacterial communities". In: *Nature* 527.7576 (2015), pp. 59–63.

[295] AiSun Tseng and Michael Levin. "Cracking the bioelectric code: probing endogenous ionic controls of pattern formation". In: *Communicative & Integrative Biology* 6.1 (2013), pp. 13192–200.

[296] Akiko Nakamasu et al. "Interactions between zebrafish pigment cells responsible for the generation of Turing patterns". In: *Proceedings of the National Academy of Sciences* 106.21 (2009), pp. 8429–8434.

[297] Amit N Landge et al. "Pattern formation mechanisms of self-organizing reaction-diffusion systems". In: *Developmental biology* 460.1 (2020), pp. 2–11.

[298] Masafumi Inaba, Hiroaki Yamanaka, and Shigeru Kondo. "Pigment pattern formation by contact-dependent depolarization". In: *Science* 335.6069 (2012), pp. 677–677.

[299] Bela Novak et al. "Mathematical model of the cell division cycle of fission yeast". In: *Chaos: An Interdisciplinary Journal of Nonlinear Science* 11.1 (2001), pp. 277–286.

[300] Benno Schwikowski, Peter Uetz, and Stanley Fields. "A network of protein–protein interactions in yeast". In: *Nature biotechnology* 18.12 (2000), pp. 1257–1261.

[301] Sea Pitre et al. "Global investigation of protein–protein interactions in yeast Saccharomyces cerevisiae using re-occurring short polypeptide sequences". In: *Nucleic acids research* 36.13 (2008), pp. 4286–4294.

[302] Taraknath Mandal, Peter H Koenig, and Ronald G Larson. "Nonmonotonic scission and branching free energies as functions of hydrotrope concentration for charged micelles". In: *Physical review letters* 121.3 (2018), p. 038001.

[303] Charlotte de Blois et al. "Swimming droplets in 1D geometries: an active Bretherton problem". In: *Soft matter* 17.27 (2021), pp. 6646–6660.

[304] Charlotte de Blois et al. "Flow field around a confined active droplet". In: *Physical Review Fluids* 4.5 (2019), p. 054001.

[305] Rabea Seyboldt and Frank Jülicher. "Role of hydrodynamic flows in chemically driven droplet division". In: *New journal of physics* 20.10 (2018), p. 105010.

[306] Andrew W Murray. "The genetics of cell cycle checkpoints". In: *Current opinion in genetics & development* 5.1 (1995), pp. 5–11.

[307] RF Kayser. "Effect of capillary waves on surface tension". In: *Physical Review A* 33.3 (1986), p. 1948.

[308] M Pasandideh-Fard et al. "Capillary effects during droplet impact on a solid surface". In: *Physics of fluids* 8.3 (1996), pp. 650–659.

[309] Gábor Holló et al. "Shape changes and budding of giant vesicles induced by an internal chemical trigger: an interplay between osmosis and pH change". In: *Physical Chemistry Chemical Physics* 23.7 (2021), pp. 4262–4270.

[310] Masahide Okada et al. "Spontaneous deformation and fission of oil droplets on an aqueous surfactant solution". In: *Physical Review E* 102.4 (2020), p. 042603.

[311] Xiaoming Luo et al. "Breakup modes and criterion of droplet with surfactant under direct current electric field". In: *Chemical Engineering Research and Design* 132 (2018), pp. 822–830.

[312] Zhikun Xu, Tianyou Wang, and Zhizhao Che. "Droplet deformation and breakup in shear flow of air". In: *Physics of Fluids* 32.5 (2020), p. 052109.

[313] Hua-Shu Dou. "No existence and smoothness of solution of the Navier-Stokes equation". In: *Entropy* 24.3 (2022), p. 339.

[314] Timo Schorlepp et al. "Spontaneous symmetry breaking for extreme vorticity and strain in the three-dimensional Navier–Stokes equations". In: *Philosophical Transactions of the Royal Society A* 380.2226 (2022), p. 20210051.

[315] Hiroyuki Kitahata et al. "Convective and periodic motion driven by a chemical wave". In: *The Journal of chemical physics* 116.13 (2002), pp. 5666–5672.

[316] K. H. Nagai H. Kitahara N. Yoshinaga and Y. Sumino. In: *Physical Review E* 84 (2011), p. 015101.

[317] Oliver Back et al. "Electrotaxis behavior of droplets composed of aqueous Belousov-Zhabotinsky solutions suspended in oil phase". In: *Scientific Reports* (2023).

[318] Martin Blank and Lily Soo. "Electromagnetic acceleration of the Belousov–Zhabotinski reaction". In: *Bioelectrochemistry* 61.1-2 (2003), pp. 93–97.

[319] Kai Ming Chang, Maurits RR de Planque, and Klaus-Peter Zauner. "Fabricating millifluidic reaction-diffusion devices: Droplet-in-oil networks structured by laser cutting". In: *2016 IEEE Symposium Series on Computational Intelligence (SSCI)*. IEEE. 2016, pp. 1–7.

[320] Adrian Melling. "Tracer particles and seeding for particle image velocimetry". In: *Measurement science and technology* 8.12 (1997), p. 1406.

[321] Sharda Pasricha. "Aqueous Phase Bromination by Micellar Solution of Sodium Dodecyl Sulfate (SDS): An Undergraduate Chemistry Experiment". In: *Current Catalysis* 10.3 (2021), pp. 214–218.

[322] Lalit Kumar, Tanu Mahajan, and Dau Dayal Agarwal. "Aqueous bromination method for the synthesis of industrially-important intermediates catalyzed by micellar solution of sodium dodecyl sulfate (SDS)". In: *Industrial & engineering chemistry research* 51.5 (2012), pp. 2227–2234.

[323] Meng Wang and Xin Yi. "Bulging and budding of lipid droplets from symmetric and asymmetric membranes: competition between membrane elastic energy and interfacial energy". In: *Soft Matter* 17.21 (2021), pp. 5319–5328.

[324] Reinhard Lipowsky. "Domain-induced budding of fluid membranes". In: *Biophysical Journal* 64.4 (1993), pp. 1133–1138.

[325] Allan R Willms, Petko M Kitanov, and William F Langford. "Huygens' clocks revisited". In: *Royal Society open science* 4.9 (2017), p. 170777.

[326] Henrique M Oliveira and Luıs V Melo. "Huygens synchronization of two clocks". In: *Scientific reports* 5.1 (2015), pp. 1–12.

[327] Michael Rosenblum and Arkady Pikovsky. "Synchronization: from pendulum clocks to chaotic lasers and chemical oscillators". In: *Contemporary Physics* 44.5 (2003), pp. 401–416.

[328] J Peña Ramirez et al. "An improved model for the classical Huygens experiment on synchronization of pendulum clocks". In: *Journal of Sound and Vibration* 333.26 (2014), pp. 7248–7266.

[329] Alex Arenas et al. "Synchronization in complex networks". In: *Physics reports* 469.3 (2008), pp. 93–153.

[330] Hiroya Nakao. "Phase reduction approach to synchronisation of nonlinear oscillators". In: *Contemporary Physics* 57.2 (2016), pp. 188–214.

[331] Piero Mella. "Synchronization and Self-Organization in Organizations. The Combinatory System© View." In: *Economia Aziendale Online-* 4 (2012), pp. 1–18.

[332] Sylvain Rama, Mickael Zbili, and Dominique Debanne. "Signal propagation along the axon". In: *Current opinion in neurobiology* 51 (2018), pp. 37–44.

[333] A. Vujic et al. "Mitochondrial redox and TCA cycle metabolite signaling in the heart". In: *Free Radical Biology and Medicine* 166 (2021), pp. 287–296.

[334] Joseph W Larkin et al. "Signal percolation within a bacterial community". In: *Cell systems* 7.2 (2018), pp. 137–145.

[335] Monika A Gorzelak, Benjamin H Ellert, and Leho Tedersoo. *Mycorrhizas transfer carbon in a mature mixed forest*. 2020.

[336] Monika A Gorzelak et al. "Inter-plant communication through mycorrhizal networks mediates complex adaptive behaviour in plant communities". In: *AoB plants* 7 (2015).

[337] Yuan Yuan Song et al. "Interplant communication of tomato plants through underground common mycorrhizal networks". In: *PloS one* 5.10 (2010), e13324.

[338] Miguel Segundo-Ortin and Paco Calvo. "Consciousness and cognition in plants". In: *Wiley Interdisciplinary Reviews: Cognitive Science* 13.2 (2022), e1578.

[339] František Baluška and Stefano Mancuso. "Individuality, self and sociality of vascular plants". In: *Philosophical Transactions of the Royal Society B* 376.1821 (2021), p. 20190760.

[340] DA Bratsun and Anne De Wit. "On Marangoni convective patterns driven by an exothermic chemical reaction in two-layer systems". In: *Physics of fluids* 16.4 (2004), pp. 1082–1096.

[341] D Jaya Prasanna Kumar, Chaitra Borkar, and Pratyush Dayal. "Fast-Moving Self-Propelled Droplets of a Nanocatalyzed Belousov–Zhabotinsky Reaction". In: *Langmuir* 37.43 (2021), pp. 12586–12595.

[342] Ryotaro Hirabayashi et al. "Silver plasmonic colour change due to chemical/mechanical reactions". In: *Colloids and Surfaces A: Physicochemical and Engineering Aspects* 627 (2021), p. 127221.

[343] Miao Yuqing, Chen Jianrong, and Fang Keming. "New technology for the detection of pH". In: *Journal of biochemical and biophysical methods* 63.1 (2005), pp. 1–9.

[344] Kohta Suzuno et al. "Maze solving using fatty acid chemistry". In: *Langmuir* 30.31 (2014), pp. 9251–9255.

[345] Kohta Suzuno et al. "Marangoni flow driven maze solving". In: *Advances in Unconventional Computing*. Springer, 2017, pp. 237–243.

[346] AM Reynolds. "Maze-solving by chemotaxis". In: *Physical Review E* 81.6 (2010), p. 062901.

[347] Jie Zhang, Bartosz A Grzybowski, and Steve Granick. "Janus particle synthesis, assembly, and application". In: *Langmuir* 33.28 (2017), pp. 6964–6977.

[348] Shan Jiang et al. "Janus particle synthesis and assembly". In: *Advanced materials* 22.10 (2010), pp. 1060–1071.

[349] Andreas Walther and Axel HE Müller. "Janus particles". In: *Soft matter* 4.4 (2008), pp. 663–668.

[350] Haiyang Su et al. "Janus particles: design, preparation, and biomedical applications". In: *Materials today bio* 4 (2019), p. 100033.

[351] Tu C Le et al. "Janus particles: recent advances in the biomedical applications". In: *International journal of nanomedicine* 14 (2019), p. 6749.

[352] Jan Guzowski et al. "Microfluidic platform for reproducible self-assembly of chemically communicating droplet networks with predesigned number and type of the communicating compartments". In: *Lab on a Chip* 16.4 (2016), pp. 764–772.

[353] Philip H King et al. "Interdroplet bilayer arrays in millifluidic droplet traps from 3D-printed moulds". In: *Lab on a chip* 14.4 (2014), pp. 722–729.

[354] Philip H King et al. "Excitability modulation of oscillating media in 3D-printed structures". In: *Artificial life* 21.2 (2015), pp. 225–233.

[355] Florian Mormann et al. "Mean phase coherence as a measure for phase synchronization and its application to the EEG of epilepsy patients". In: *Physica D: Nonlinear Phenomena* 144.3-4 (2000), pp. 358–369.

[356] Marcello A Budroni et al. "Synchronization scenarios induced by delayed communication in arrays of diffusively coupled autonomous chemical oscillators". In: *Physical Chemistry Chemical Physics* 23.32 (2021), pp. 17606–17615.

[357] Jorge Delgado et al. "Coupled oscillations in a 1D emulsion of Belousov–Zhabotinsky droplets". In: *Soft Matter* 7.7 (2011), pp. 3155–3167.

[358] Xinzhe Li et al. "EEG dynamical network analysis method reveals the neural signature of visual-motor coordination". In: *PloS one* 15.5 (2020), e0231767.

[359] Thomas C Draper, Marta Dueñas-Dıez, and Juan Pérez-Mercader. "Exploring the symbol processing 'time interval'parametric constraint in a Belousov–Zhabotinsky operated chemical turing machine". In: *RSC advances* 11.37 (2021), pp. 23151–23160.

[360] Ashmita Bose and Jerzy Gorecki. "Computing With Networks of Chemical Oscillators and its Application for Schizophrenia Diagnosis". In: *Frontiers in Chemistry* 10 (2022).

[361] Vladimir K Vanag and Irving R Epstein. "A model for jumping and bubble waves in the Belousov–Zhabotinsky-aerosol OT system". In: *The Journal of chemical physics* 131.10 (2009), p. 104512.

[362] Hidetoshi Miike et al. "Accelerating chemical waves accompanied by traveling hydrodynamic motion and surface deformation". In: *Physical Review E* 48.3 (1993), R1627.

[363] Masahiro Toiya, Vladimir K Vanag, and Irving R Epstein. "Diffusively coupled chemical oscillators in a microfluidic assembly". In: *Angewandte Chemie* 120.40 (2008), pp. 7867–7869.

[364] Jan Szymanski, Jerzy Gorecki, and Marcus JB Hauser. "Chemo-mechanical coupling in reactive droplets". In: *The Journal of Physical Chemistry C* 117.25 (2013), pp. 13080–13086.

[365] John Happel and Howard Brenner. *Low Reynolds number hydrodynamics: with special applications to particulate media*. Vol. 1. Springer Science & Business Media, 2012.

[366] C. A. Sterling and L. E. Scriven. In: *AIChE Journal* 5 (1959), p. 514.

[367] Nobuhiko J Suematsu et al. "Oscillation of speed of a self-propelled Belousov–Zhabotinsky droplet". In: *The journal of physical chemistry letters* 7.17 (2016), pp. 3424–3428.

[368] Shashi Thutupalli, Stephan Herminghaus, and Ralf Seemann. "Bilayer membranes in micro-fluidics: from gel emulsions to soft functional devices". In: *Soft Matter* 7.4 (2011), pp. 1312–1320.

[369] Shashi Thutupalli and Stephan Herminghaus. "Tuning active emulsion dynamics via surfactants and topology". In: *The European Physical Journal E* 36.8 (2013), pp. 1–10.

[370] Irene Chou Chen. "Chemomechanics of self-oscillating gels". PhD thesis. Massachusetts Institute of Technology, 2013.

[371] Lin Ren et al. "Chemomechanical origin of directed locomotion driven by internal chemical signals". In: *Science advances* 6.18 (2020), eaaz9125.

[372] Baptiste Blanc et al. "Active gels: from chemical microreactor to polymeric actuator". In: *arXiv preprint arXiv:2201.08273* (2022).

[373] Yanqiu Che et al. "Parameter estimation of the FitzHugh-Nagumo model using noisy measurements for membrane potential". In: *Chaos: An Interdisciplinary Journal of Nonlinear Science* 22.2 (2012), p. 023139.

[374] Yoshiki Kuramoto. "Self-entrainment of a population of coupled non-linear oscillators". In: *International symposium on mathematical problems in theoretical physics*. Springer. 1975, pp. 420–422.

[375] Yoshiki Kuramoto. *Chemical oscillations, waves, and turbulence*. Courier Corporation, 2003.

[376] Juan A Acebrón et al. "The Kuramoto model: A simple paradigm for synchronization phenomena". In: *Reviews of modern physics* 77.1 (2005), p. 137.

[377] Qingyun Wang et al. "Bifurcation and synchronization of synaptically coupled FHN models with time delay". In: *Chaos, Solitons & Fractals* 39.2 (2009), pp. 918–925.

[378] Miguel A Barrón and Mihir Sen. "Synchronization of four coupled van der Pol oscillators". In: *Nonlinear Dynamics* 56.4 (2009), pp. 357–367.

[379] Xiaoyan Fang, Shukai Duan, and Lidan Wang. "Memristive FHN spiking neuron model and brain-inspired threshold logic computing". In: *Neurocomputing* 517 (2023), pp. 93–105.

[380] Dong Yu et al. "Synchronization mode transition induced by bounded noise in multiple time-delays coupled FitzHugh–Nagumo model". In: *Chaos, Solitons & Fractals* 147 (2021), p. 111000.

[381] Jüri Engelbrecht, Kert Tamm, and Tanel Peets. "Modeling of complex signals in nerve fibers". In: *Medical Hypotheses* 120 (2018), pp. 90–95.

[382] Ali Soleimanizadeh, Mohammad Ali Nekoui, and Mahdi Aliyari Shoorehdeli. "Synchronization between two coupled fractional order neuron models using the optimized fuzzy logic controller in the presence of external disturbances". In: *International Journal of Nonlinear Analysis and Applications* (2022).

[383] Sina G Yazdi et al. "A review of arterial phantom fabrication methods for flow measurement using PIV techniques". In: *Annals of Biomedical Engineering* 46.11 (2018), pp. 1697–1721.

[384] Constantine M Megaridis et al. "Internal droplet circulation induced by surface-driven rotation". In: *International journal of heat and fluid flow* 15.5 (1994), pp. 364–377.

[385] R Hain and CJ Kähler. "Fundamentals of multiframe particle image velocimetry (PIV)". In: *Experiments in fluids* 42.4 (2007), pp. 575–587.

[386] Jerry Westerweel. "Digital particle image velocimetry: Theory and application." In: (1995).

[387] Ronald J Adrian and Jerry Westerweel. *Particle image velocimetry*. 30. Cambridge university press, 2011.

[388] Fahrettin Gökhan Ergin, Bo Beltoft Watz, and Nicolai Fog Gade-Nielsen. "A review of planar PIV systems and image processing tools for lab-on-chip microfluidics". In: *Sensors* 18.9 (2018), p. 3090.

[389] Haruyuki Kinoshita et al. "Three-dimensional measurement and visualization of internal flow of a moving droplet using confocal micro-PIV". In: *Lab on a Chip* 7.3 (2007), pp. 338–346.

[390] Luming Fan et al. "Laser-induced incandescence particle image velocimetry (LII-PIV) for two-phase flow velocity measurement". In: *Experiments in Fluids* 59.10 (2018), pp. 1–14.

[391] RS Volkov and PA Strizhak. "Research of temperature fields and convection velocities in evaporating water droplets using planar laser-induced fluorescence and particle image velocimetry". In: *Experimental Thermal and Fluid Science* 97 (2018), pp. 392–407.

[392] RS Volkov and PA Strizhak. "Using Planar Laser Induced Fluorescence and Micro Particle Image Velocimetry to study the heating of a droplet with different tracers and schemes of attaching it on a holder". In: *International Journal of Thermal Sciences* 159 (2021), p. 106603.

[393] Kai-Yang Tung, Chih-Chieh Li, and Jing-Tang Yang. "Mixing and hydrodynamic analysis of a droplet in a planar serpentine micromixer". In: *Microfluidics and Nanofluidics* 7.4 (2009), pp. 545–557.

[394] Ezequiel Bianco-Martinez and Murilo S Baptista. "Space-time nature of causality". In: *Chaos: An Interdisciplinary Journal of Nonlinear Science* 28.7 (2018), p. 075509.

[395] Nicolás Rubido et al. "Exact detection of direct links in networks of interacting dynamical units". In: *New Journal of Physics* 16.9 (2014), p. 093010.